

GEOTECHNICAL, GEOLOGICAL AND EARTHQUAKE ENGINEERING

# GEOTECHNICAL EARTHQUAKE ENGINEERING

Simplified Analyses with Case Studies  
and Examples

MILUTIN SRBULOV

 Springer

@Seismicisolation

CD-Rom  
included

## GEOTECHNICAL EARTHQUAKE ENGINEERING

@Seismicisolation

# GEOTECHNICAL, GEOLOGICAL AND EARTHQUAKE ENGINEERING

---

Volume 9

---

## *Series Editor*

Atilla Ansal, *Kandilli Observatory and Earthquake Research Institute,  
Boğaziçi University, Istanbul, Turkey*

## *Editorial Advisory Board*

Julian Bommer, *Imperial College London, U.K.*

Jonathan D. Bray, *University of California, Berkeley, U.S.A.*

Kyriazis Pitilakis, *Aristotle University of Thessaloniki, Greece*

Susumu Yasuda, *Tokyo Denki University, Japan*

For other titles published in this series, go to  
[www.springer.com/series/6011](http://www.springer.com/series/6011)

@Seismicisolation

# Geotechnical Earthquake Engineering

Simplified Analyses with Case Studies  
and Examples

*by*

MILUTIN SRBULOV

*United Kingdom*

with Foreword of  
E.T.R. Dean



@Seismicisolation

Dr. Milutin Srbulov  
United Kingdom  
[srbuluv@aol.com](mailto:srbuluv@aol.com)

ISBN: 978-1-4020-8683-0      e-ISBN: 978-1-4020-8684-7

Library of Congress Control Number: 2008931592

© 2008 Springer Science+Business Media B.V.

No part of this work may be reproduced, stored in a retrieval system, or transmitted in any form or by any means, electronic, mechanical, photocopying, microfilming, recording or otherwise, without written permission from the Publisher, with the exception of any material supplied specifically for the purpose of being entered and executed on a computer system, for exclusive use by the purchaser of the work.

Printed on acid-free paper

9 8 7 6 5 4 3 2 1

[springer.com](http://springer.com)

The logo consists of the word "Seismic" in a bold, blue, sans-serif font. The letter "S" is stylized with a circular arrow around it, and the "e" has a small circle to its left. To the left of "Seismic" is a smaller, semi-transparent "isolation".

# Foreword

Measurable earthquakes occur very frequently in many parts of the world. For example, Shepherd (1992) lists 7283 earthquakes recorded in the Caribbean Antilles in the 22-year period 1964 to 1985, a rate of about 1 earthquake per day. Some were due to movements of highly stressed rock at more than 100 km below the ground surface (Shepherd and Aspinall, 1983). Similar high levels of activity are found in all seismically active regions of the world.

As the earthquake vibrations travel from the source towards the ground surface, the energy spreads out and also dissipates, so that energy density reduces with distance from source. For the majority of events, shaking has reduced to levels that people cannot feel by the time it reaches the ground surface. For some events, sufficient energy reaches the surface for people to feel minor effects. For a few, the energy reaching the surface is sufficient to cause major damage.

Since earthquake shaking is transmitted through ground, and since ground also supports buildings and other structures, the art and science of geotechnical engineering is an important part of earthquake engineering. A variety of concepts and techniques are detailed by Kramer (1996), Day (2002), Chen and Scawthorne (2003), and others. Some of the important geotechnical aspects are:

- The particle mechanical nature of soil (Mitchell and Soga, 2005; Lambe and Whitman, 1979)
- Terzaghi's Principle of Effective Stress (Terzaghi et al, 1996)
- Linear, isotropic elastic models (Davis and Selvadurai, 1996)
- The theory of soil plasticity (Drucker et al., 1957; Davis and Selvadurai, 2002; Loret, 1990)
- The Mohr-Coulomb failure envelope (Lambe and Whitman, 1979; Das, 2004)
- The characterization of soil properties, and theories of compressibility, flow of water through soils, fluidization, and consolidation of soils (Florin and Ivanov, 1961; Lambe and Whitman, 1979; Heidari and James, 1982; Wroth and Housby, 1985; Terzaghi et al, 1996; Das, 2004)
- Critical state soil mechanics, which seeks to incorporate soil elasticity, plasticity, strength, density, and consolidation into a single unifying theoretical framework (Schofield and Wroth, 1968; Atkinson and Bransby, 1978; Muir-Wood, 1992; Schofield, 2005)

- Advanced site investigation and laboratory testing techniques (Hunt, 2005; Head, 2006)
- Advanced methods for slope stability assessment (Abramson et al, 1996; Cornforth, 2005), and bearing capacity and lateral earth pressure (eg. Choudhary et al, 2004; Kumar and Ghosh, 2006)
- Liquefaction and the steady state concept (Castro, 1969; Seed and Idriss, 1971; Poulos, 1981; Vaid and Chern, 1985; Seed, 1988; Ishihara, 1995; Jefferies and Been, 2006)
- Shaking table and centrifuge model testing (Schofield, 1980; Arulanandan and Scott, 1994; Taylor, 1994)
- The developing theories of unsaturated soil mechanics (Fredlund and Rahardjo, 1993)
- The use of advance constitutive models (Loret, 1990; Yamamoto and Kaliakin, 2005) with finite element methods (Zienkiewicz and Taylor, 1989, 1991; Britto and Gunn, 1987; Finn, 1999; Potts, 2003)
- The global gathering, processing, and use of collective experience (Youd and Idriss, 2001)

Based on these and other factors, advances in understanding have been incorporated in design codes including the Uniform Building Code (UBC, 1997), the International Building Code (IBC, 2006), Eurocode 8 (2004), API RP2A (2005), ISO 19901 (2004), and many others.

To support these developments, it can be highly desirable to document some simplified models that are easier to understand, retain and explain the fundamental physics involved, and provide ways of assessing the relevance, reliability, and applicability of more sophisticated approaches. It is also rather useful to be able to identify the most significant publications in a technical literature that is now very extensive indeed. The monograph presents some of the Author's descriptions, case histories, experiences and comments on a variety of simplified models for engineering design and analysis. This is valuable both for persons new to the subject who will learn of the wide-ranging considerations involved, and to other experienced practitioners who will be able to compare experiences with those shared here.

Senior Lecturer in Geotechnical Engineering,  
University of the West Indies

E.T.R. Dean

# Preface

This monograph contains descriptions of numerous methods aimed at ease and speed of use for major problems in geotechnical earthquake engineering. Comments on assumptions, limitations, and factors affecting the results are given. Case studies and examples are included to illustrate the accuracy and usefulness of simplified methods. A list of references is provided for further considerations, if desired. Microsoft Excel workbooks referred to in Appendices and provided on an accompanying CD are for the case studies and examples considered in the monograph. Some of the reasons for using this monograph are mentioned below.

Many codes and standards contain recommendations on best practice but compliance with them does not necessarily confer immunity from relevant statutory and legal requirements (as stated in British Standards). Some seismic codes and standards were revised after major events such as the 1995 Hyogo-ken Nambu and the 1994 Northridge earthquakes. Codes contain clauses without references to the original sources for more detailed considerations when cases that require such consideration appear in practice. Codes do not contain explanations of the statements expressed in them. Codes are brief regarding ground properties and ground response. For example, Eurocode 8 – Part 5 requires assessment of the effects of soil-structure interaction in certain circumstances but does not specify the details of the analyses. Therefore, the use of codes and standards alone may not be sufficient in engineering practice.

In engineering practice, there is often rather little interaction between structural and foundation disciplines. Structural engineers often consider ground in a simplified way using equivalent springs. Geotechnical engineers consider often only loading from structures on foundations. Dynamic soil-structure interaction is very complex and analyzed mainly by specialist in geotechnical earthquake engineering. This monograph should help geotechnical and structural engineers to communicate effectively to better understand solutions of many problems in geotechnical earthquake engineering.

Specialists in non-linear dynamics analyses need to recognize that the motion of a non-linear system can be chaotic and the outcomes can be unrepeatable and unpredictable. Baker and Gollub (1992), for example, show that two conditions are sufficient to give rise to the possibility of chaotic motion: the system has at least three independent variables, and the variables are coupled by non-linear

relations. Equivalent linear and simplified non-linear dynamic analysis described in this monograph can be used to avoid possible chaotic outcomes of a complex non-linear dynamic analysis. Ground motion caused by earthquakes is chaotic and therefore greater accuracy of sophisticated methods loses its advantage. Expected ground motion can be predicted only approximately, and simplified analyses are faster and easier tools for parametric studies compared to sophisticated methods.

United Kingdom

Milutin Srbulov

## Acknowledgements

Professor Maksimovic persuaded me to switch profession from concrete structures to geotechnics right after my graduation. He pioneered studies of soil mechanics paid by Energoprojekt Co. at Imperial College in the U.K. The MSc soil mechanics study in 1984/85 enabled me to obtain the position of a research assistant later.

I was honored and privileged to work with Professor Ambraseys on a number of research projects supported by the Engineering and Physical Science Research Council of the United Kingdom and by the EPOCH program of the Community of European Countries at Imperial College in London during the period 1991–1997. The simplified approach used in our research is directly applicable to routine engineering practice.

Dr E.T.R. Dean reviewed several of my papers and was of great help with his detailed and precise comments for the improvement of the initial versions of the papers. He kindly reviewed the monograph and made a significant contribution towards the improvement of the clarity and readability of the text.

Elsevier publishers kindly granted permission to reproduce Fig. 5B, Fig. 10, Fig. 11, 2/3 of Discussion, and Appendix A of the paper by Ambraseys and Srbulov (1995) in print and electronic format in all languages and editions. Elsevier publishers kindly granted permission to reproduce pages 255 to 268 of the paper by Srbulov (2001) in print and English version.

Patron Editore publishers kindly granted permission to reproduce parts of my papers published in the journal European Earthquake Engineering.

The American Society of Civil Engineers kindly granted permission to reproduce in print and electronic version Table 2 from Zhang et al. (2005) paper.

# Contents

<b>1 Well Known Simplified Models .....</b>	1
1.1 Introduction .....	1
1.2 Source Models of Energy Release by Tectonic Fault .....	1
1.2.1 A Simplified Point-Source Model .....	1
1.2.2 An Alternative, Planar Source Model .....	4
1.2.3 Case Study Comparisons of the Point and Planar Source Models .....	5
1.3 Sliding Block Model of Co-Seismic Permanent Slope Displacement	6
1.3.1 Newmark's (1965) Sliding Block Model .....	6
1.3.2 Comments on Newmarks's (1965) Sliding Block Model ...	7
1.4 Single Degree of Freedom Oscillator for Vibration of a Structure on Rigid Base .....	10
1.4.1 Description of the Model .....	10
1.4.2 Comments on the Model .....	11
1.5 Summary .....	12
<b>2 Soil Properties .....</b>	13
2.1 Introduction .....	13
2.2 Cyclic Shear Stiffness and Material Damping .....	14
2.2.1 Shear Stiffness and Damping Ratio Dependence on Shear Strain .....	16
2.3 Static Shear Strengths of Soils .....	18
2.4 Cyclic Shear Strengths of Soils .....	20
2.5 The Equivalent Number of Cycles Concept .....	23
2.5.1 An Example of Equivalent Harmonic Time Histories .....	25
2.6 Water Permeability and Volumetric Compressibility .....	26
2.7 Summary .....	28
<b>3 Seismic Excitation .....</b>	29
3.1 Introduction .....	29
3.2 Seismic Hazard .....	29
3.2.1 Types of Earthquake Magnitudes .....	30
3.2.2 Types of Source-to-Site Distances .....	31

3.2.3	Types of Earthquake Recurrence Rates . . . . .	31
3.2.4	Representations of Seismic Hazard . . . . .	32
3.2.5	Sources of Earthquake Data . . . . .	39
3.3	Factors Affecting Seismic Hazard . . . . .	41
3.3.1	Earthquake Source and Wave Path Effects . . . . .	41
3.3.2	Sediment Basin Edge and Depth Effects . . . . .	45
3.3.3	Local Soil Layers Effect . . . . .	54
3.3.4	Topographic Effect . . . . .	57
3.3.5	Space and Time Clustering (and Seismic Gaps) . . . . .	58
3.4	Short Term Seismic Hazard Assessment . . . . .	60
3.4.1	Historic and Instrumental Seismic Data Based . . . . .	60
3.4.2	Observational Method . . . . .	62
3.5	Long Term Seismic Hazard Assessment . . . . .	65
3.5.1	Tectonic Data Based . . . . .	65
3.5.2	Paleoseismic Data Based . . . . .	67
3.6	Summary . . . . .	70
<b>4</b>	<b>Slope Stability and Displacement . . . . .</b>	<b>73</b>
4.1	Introduction . . . . .	73
4.2	Slope Stability . . . . .	73
4.2.1	Limit Equilibrium Method for Two-Dimensional Analysis by Prismatic Wedges . . . . .	74
4.2.2	Single Tetrahedral Wedge for Three-Dimensional Analysis of Translational Stability . . . . .	84
4.3	Shear Beam Model for Reversible Displacement Analysis . . . . .	86
4.3.1	Two-Dimensional Analysis . . . . .	86
4.3.2	Three-Dimensional Effect . . . . .	88
4.4	Sliding Block Models for Permanent Displacement Analysis . . . . .	89
4.4.1	Co-Seismic Stage . . . . .	89
4.4.2	Post-Seismic Stage . . . . .	94
4.5	Bouncing Ball Model of Rock Fall . . . . .	99
4.5.1	Case Study of Bedrina 1 Rock Fall in Switzerland . . . . .	103
4.5.2	Case Study of Shima Rock Fall in Japan . . . . .	105
4.5.3	Case Study of Futamata Rock Fall in Japan . . . . .	106
4.6	Simplified Model for Soil and Rock Avalanches, Debris Run-Out and Fast Spreads Analysis . . . . .	107
4.6.1	Equation of Motion . . . . .	108
4.6.2	Mass Balance . . . . .	110
4.6.3	Energy Balance . . . . .	111
4.7	Summary . . . . .	117
<b>5</b>	<b>Sand Liquefaction and Flow . . . . .</b>	<b>119</b>
5.1	Introduction . . . . .	119
5.2	Conventional Empirical Methods . . . . .	120
5.2.1	Liquefaction Potential Assessment . . . . .	120

5.2.2	Flow Consideration .....	122
5.3	Rotating Cylinder Model for Liquefaction Potential Analysis of Slopes.....	123
5.3.1	Model for Clean Sand .....	123
5.3.2	Model for Sand with Fines .....	126
5.4	Rolling Cylinder Model for Analysis of Flow Failures.....	135
5.4.1	Model for Clean Sand .....	135
5.4.2	Model for Sand with Fines .....	136
5.5	Summary .....	139
<b>6</b>	<b>Dynamic Soil – Foundation Interaction .....</b>	<b>141</b>
6.1	Introduction .....	141
6.2	Advanced and Empirical Methods .....	142
6.2.1	Numerical Methods, Centrifuge and Shaking Table Testing ..	142
6.2.2	System Identification Procedure.....	142
6.3	Discrete Element Models .....	143
6.3.1	Lumped Mass Model Formula .....	143
6.3.2	Closed Form Solution in Time .....	150
6.3.3	Time Stepping Procedure .....	156
6.4	Single Degree of Freedom Oscillator on Flexible Base for Piled Foundations and Flexural Retaining Walls .....	168
6.4.1	Ground Motion Averaging for Kinematic Interaction Effect Consideration .....	170
6.4.2	Acceleration Response Spectra Ratios for Inertial Interaction Effect Consideration .....	172
6.5	Summary .....	185
<b>7</b>	<b>Bearing Capacity And Additional Settlement of Shallow Foundation ..</b>	<b>187</b>
7.1	Introduction .....	187
7.2	Bearing Capacity: Pseudo-Static Approaches .....	187
7.3	Bearing Capacity: Effects of Sub-Surface Liquefaction .....	188
7.4	Bearing Capacity: Effects of Structural Inertia and Eccentricity of Load .....	189
7.4.1	An Example of Calculation of Bearing Capacity of Shallow Foundation in Seismic Condition .....	190
7.5	Additional Settlement in Granular soils .....	191
7.5.1	Examples of Estimation of Additional Settlement Caused by Sand Liquefaction .....	192
7.6	Summary .....	193
<b>8</b>	<b>Seismic Wave Propagation Effect on Tunnels and Shafts .....</b>	<b>195</b>
8.1	Introduction .....	195
8.2	Wave Propagation Effect on Cut and Cover Tunnels and Shafts .....	195
8.2.1	Case Study of the Daikai Station Failure in 1995.....	196
8.2.2	Case Study of a Ten Story Building in Mexico City .....	199

8.3	Wave Refraction Effect on Deep Tunnels and Shafts .....	201
8.4	Summary .....	202
<b>9</b>	<b>Comments on Some Frequent Liquefaction Potential Mitigation Measures .....</b>	<b>203</b>
9.1	Introduction .....	203
9.2	Stone Columns .....	203
9.3	Soil Mixing .....	204
9.4	Excess Water Pressure Relief Wells .....	205
9.4.1	An Example for Pressure Relief Wells .....	208
9.5	Summary .....	208
<b>Appendices – Microsoft Excel Workbooks on Compact Disk .....</b>		<b>211</b>
A.1	Coordinates of Earthquake Hypocentre and Site-to-Epicentre Distance .....	211
A.2	Limit Equilibrium Method for Northolt Slope Stability .....	212
A.3	Single Wedge for Three-Dimensional Slope Stability .....	214
A.4	Co-Seismic Sliding Block .....	215
A.5a	Post-Seismic Sliding Blocks for Maidipo Slip in Frictional Soil .....	215
A.5b	Post-Seismic Sliding Blocks for Catak Slip in Cohesive Soil .....	216
A.6	Bouncing Block Model of Rock Falls .....	216
A.7	Simplified Model for Soil and Rock Avalanches, Debris Run-Out and Fast Spreads .....	216
A.8	Closed-Form Solution for Gravity Walls .....	219
A.9a	Time Stepping Procedure for Kobe Wall .....	219
A.9b	Time Stepping Procedure for Kalamata Wall .....	219
A.10	Accelerogram Averaging and Acceleration Response Spectra .....	219
A.11	Bearing Capacity of Shallow Foundation .....	223
A.12	Excess Pore Water Pressure Dissipation .....	223
<b>References .....</b>		<b>225</b>
<b>Index .....</b>		<b>241</b>

# List of Symbols

<b>Symbol</b>	<b>Description</b>
$\partial\sigma_h/\partial h$	horizontal axial stress gradient in horizontal direction
$\partial\tau_{hn}/\partial n$	gradient of shear stress in vertical plane in direction normal to the plane
$\partial\tau_{hv}/\partial v$	gradient of shear stress in vertical plane in vertical direction
$\partial^2 u_{(1)}/\partial t^2$	second gradient of horizontal displacement in time (1-down slope)
$\partial u/\partial v$	horizontal displacement gradient in vertical direction
$\bar{c}$	apparent cohesion of reinforced soil
$\bar{\phi}$	equivalent friction angle along sliding block base
$\bar{\sigma}$	average compressive stress on sliding block base
$\bar{\theta}$	inclination to the horizontal of sliding block base
$\ddot{\theta}$	rotational acceleration of a cylinder around a point
$\ddot{u}$	horizontal acceleration
$\dot{\theta}_{1n}$	rotational velocity of a gravity wall
$\ddot{\theta}_{on}, \ddot{u}_{on}$	rotational and horizontal accelerations of a gravity wall
$\bar{\alpha}$	exponent of the ratio $\gamma \gamma_r^{-1}$
$\bar{\alpha}$	angle of sliding block inclination to horizontal
$\bar{k}$	exponent of the ratio $\sigma'_m P_a^{-1}$
$(N_1)_{60}$	normalized blow count to an overburden pressure of 100kPa and corrected to an energy ratio of 60%
$a$	an exponent
$a_{(i)}$	acceleration (initial)
$a, b, c$	coefficients calculated from measured incremental displacements $\Delta u, \Delta v, \Delta w$
$a_1$	rate of ground acceleration increment during a time interval
$A_{1,2}$	seismic wave amplitudes 1 and 2
$A_b$	area of the mass contact with the base and sides
$a_{c(h,r)}$	critical horizontal acceleration in sliding (h) or rocking (r)
$a_{cr}$	critical acceleration

$A_f$	foundation area
$a_{f,p}$	horizontal peak foundation acceleration
$A_{fault}$	tectonic fault area
$A_g$	amplitude of ground displacement
$a_{g,t}$	horizontal ground acceleration
$a_h$	horizontal acceleration (for a harmonic load)
$a_i$	peak input acceleration of a SDOFO
$a_l$	ground acceleration at depth $l$ along the pile/wall at time $t$
$A_{loop}$	the area of the hysteretic loop
$a_o$	ground acceleration at the beginning of a time interval
$a_{peak,depth}$	peak horizontal ground acceleration at depth
$a_{ph}$	peak horizontal ground surface acceleration
$a_{peak,surface}$	
$a_{pv}$	peak vertical ground surface acceleration
$a_r$	rock fall acceleration just before the impact
$A_s$	area of slope sliding surface
$A_{u(d)}$	upstream (downstream) vertical cross section area
$b$	horizontal distance between the back of a wall and the wall centroid
$b_{(i)}$	breadth of wedge base (interface $i$ )
$B_b$	width of an equivalent ball of rock fall
$b_c$	breadth of a rectangular pile cap
$B_f$	diameter of an equivalent circular foundation
$b_j$	breadth of joint $j$
$B_s$	number of (sub) basements in a building
$B_w$	wall base width
$c$	soil shear strength (cohesion) at zero compressive stress
$C$	translational dashpot coefficient
$c'_{(j)}$	soil cohesion in drained condition (at joint $j$ )
$C_{0,1,2}$	constants
$c_h$	horizontal coefficient of inertia force induced by ground motion
$c_n$	amplitude of the nth harmonic of the Fourier series
$c_p$	ground longitudinal wave velocity
$C_s$	soil constant in the shear strength and shear strain relationship
$c_s$	soil characteristic wave velocity
$c_t$	ground transversal wave velocity
$c_u$	undrained shear strength of liquefied sand layer
$c_{u(1)}$	undrained cohesion (in one cycle)
$c_{ur}$	residual undrained shear strength of liquefied sand
$c_{v(r)}$	coefficient of consolidation (in radial direction)
$c_{vm}$	vertical coefficient of inertia force induced by ground motion
$C_\theta$	rotational soil dashpot coefficient

$d$	minimal distance from the location of interest to the surface projection of a fault
$D_{50}$	an average diameter of soil particles
$d_c$	depth factor
$d_e$	distance between wells centre to centre
$D_f$	foundation depth below ground level
$d_{g,t}$	horizontal ground displacement in time
$d_h$	horizontal distance between the location where the load $F$ is acting and the location where the stress is calculated
$D_l$	depth of liquefied soil layer
$d_p$	pile diameter
$d_{ph}$	peak horizontal ground surface displacement
$d_r$	radial distance measured from centre of the well
$d_s$	straight-line (slant) distance between the earthquake hypocenter and a recording site
$D_s$	maximum surface displacement of tectonic fault
$dt$	change of thickness of wedge joint
$dt_{j,e}$	joint ( $j$ ) thickness change
$e$	distance between wall centroid and its base
$E$	Young modulus
$E_d$	energy density at a hypocentral distance
$E_{ff}$	theoretical free-fall energy of hammer
$E_{loss}$	energy loss due to plastic deformation of impacted surface
$E_m$	actual energy delivered by hammer
$E_o$	total energy released at the earthquake source
$E_p$	Young modulus of pile
$E_s$	an average lateral earth force
$E_t$	total energy released at the earthquake source per unit area of the source
$f$	frequency of shear stress reversal
$F_{avr}$	average factor of safety of a group of wedges
$F_g$	ground resisting force to rock fall penetration on impact
$F_{i,j}$	local factors of safety along wedge joints i, j
$F_m$	modification factor of sediments transversal wave velocities
$F_N$	normal and strike-slip fault indicator
$F_O$	unspecified fault indicator
$F_p$	point load
$F_r$	soil reaction force at wall base
$FS$	factor of safety of slope stability
$F_T$	reverse (thrust) fault indicator
$F_v$	vertical foundation capacity
$G$	shear modulus
$g$	gravitational acceleration
$G_b$	average transversal wave velocity range $360 < v_t < 750$ m/s to 30 m depth indicator

$G_c$	average transversal wave velocity range $180 < v_t <$ 360 m/s to 30 m depth indicator
$G_{max}$	maximum shear modulus
$G_{secant}$	secant shear modulus
$GW$	ground water force acting in the direction that is perpendicular to the surface of a wedge base or interface
$h$	horizontal direction
$H$	soil layer thickness
$h_c$	distance of the centre of gravity above foundation level
$H_d$	dam height
$h_f$	focal depth
$h_h$	free column height
$H_l$	distance from foundation level to the level of liquefied layer below
$h_o$	distance of the centre of gravity above ground level
$h_s$	depth below surface
$H_s$	distance between storeys
$H_w$	retaining wall height
$I$	wall mass moment of inertia around the centre of gravity
$i$	hydraulic gradient
$I_{(o)}$	polar moment of mass inertia (around the centroid)
$i, j$	wedge joint indices
$I_a$	second moment of area
$K$	translational static stiffness coefficient
$k$	coefficient of soil permeability
$k_{,k^I}$	exponents in soil shear strength and strain relationship
$K'_o$	coefficient of soil lateral pressure
$k_c$	ratio between the critical horizontal acceleration at which the factor of safety of slope stability is 1 and the gravitational acceleration
$k_d$	an average material damping coefficient (about 0.001 to 0.01)
$k_h$	ratio between horizontal inertial and the gravitational acceleration
$k_h$	coefficient of permeability of soil in the horizontal direction
$k_p$	ratio between the peak horizontal ground acceleration and the gravitational acceleration
$k_s$	coefficient of lateral stiffness of pile(s)/wall
$K_s$	coefficient of punching shear
$K_\theta$	rotational soil stiffness coefficient
$L$	distance from pile/wall top to a referent point under the pile/wall
$L'$	length of slip surface in the cross section
$l_c$	length of a rectangular pile cap
$L_d$	dam length at its crest

$L_f$	tectonic fault length
$L_l$	thickness of liquefied layer in meters
$L_o$	initial length of two sliding blocks
$L_p$	length of sedimentation path
$L_r$	length of surface rupture by tectonic fault
$L_s$	length along pile/wall over which ground motion is averaged
$M$	earthquake magnitude
$m_*$	mass (of *)
$m_b$	body wave earthquake magnitude
$M_d$	soil deformation modulus
$M_{E+\Delta E}$	rotational moment around the wall center of gravity from the average seismic earth force $E_s$ and the transient part $\Delta E$
$M_L$	local earthquake magnitude
$M_o$	seismic moment
$M_r$	soil reaction moment at structure/wall base
$M_s$	surface wave earthquake magnitude
$m_v$	coefficient of volume compressibility of soil
$M_w$	moment earthquake magnitude
$M_{\Delta(\Theta)}$	bending moment at the top of the column due to the horizontal displacement $\Delta$ and rotation $\theta$
$N$	standard penetration resistance blow count
$n$	direction of normal to a plane and number of wedges
$N_a$	axial force between a sand grain model and a fines model in the static condition
$N_c$	bearing capacity factor
$n_d$	number of standard deviations from an average value
$N_{eqv}$	equivalent number of uniform stress cycles
$N_{i(j)}$	axial force at wedge base i (interface j)
$N_L$	number of cycles required to produce $r_u=1$
$N_l$	number of loading cycles
$n_m$	mode of free vibration of an infinite layer
$n_s$	initial sand porosity
$n_w$	number of wedges
$OCR$	soil over consolidation ratio
$p$	number of standard deviations from an average value
$P$	average of interface forces
$P[N \geq 1]$	probability of at least one exceedance of a particular earthquake magnitude in a period of $t$ years
$P_a$	atmospheric pressure
$P_b$	soil resisting force acting at the base
$P_f$	axial component of rock fall impact force
$PI$	soil plasticity index
$p_n$	characteristic axial stress

$p_o'$	effective overburden stress at the foundation depth
$P_r$	soil reinforcement force
$P_s$	improvement in shearing resistance from soil reinforcement force $P_r$
$R$	radius of an equivalent ball of rock fall
$r$	cylinder radius
$r_1$	radius of the fines model
$R_b$	ratio between the horizontal distances from a station to sediment basin edge and the depth of sediments at the location of the station
$r_c$	correlation coefficient
$r_d$	stress factor with depth
$r_e$	a half of the distance $d_e$
$r_f$	source slant distance
$r_h$	radius of an equivalent disks for the horizontal motion
$r_{MC}$	radius of Mohr – Coulomb circle defined by Equation (9.1)
$r_{pile}$	a half of pile diameter
$r_r$	radius of an equivalent disks for the rotational motion
$r_{u(j)}$	excess pore water pressure ratio (at joint $j$ )
$r_v$	radius of an equivalent disks for the vertical motion
$r_w$	radius of a well
$S$	sliding force at the base of a rigid retaining wall
$s$	axis to axis spacing between soil-cement mixture walls
$S_A$	stiff soil site indicator
$s_c$	shape factor
$S_f$	average slip on the fault during an earthquake
$S_S$	soft soil site indicator
$S_t$	number of storeys above ground level
$S_u$	minimal uniaxial compressive strength of samples taken from mixed soil
$T$	period of vibration
$t$	time
$T_{i(j)}$	force acting in the direction that is parallel to the surface of a wedge base $i$ (interface $j$ )
$t_1$	time when cylinder will start rotation
$t_{ach}$	time corresponding to $a_{ch}$
$T_d$	period of the first mode of free vibration of a dam
$T_{eqv}$	period of equivalent harmonic cycle
$T_f$	transversal component of rock fall impact force
$T_i$	shear force at wedge joint $i$
$T_M$	return period of earthquakes exceeding magnitude $M$
$T_p$	age of tectonic plate subduction
$T_r$	earthquake recurrence period
$T_s$	the time (in seconds) necessary for a seismic wave to pass along $L_s$

$T_v$	time factor
$t_w$	thickness of soil-cement mixture walls
$T_{\Delta(\Theta)}$	transversal force at the top of the column due to the horizontal displacement $\Delta$ and rotation $\theta$
$u$	horizontal displacement
$U_{(z,r)}$	overall degree of consolidation (at depth $z$ , radius $r$ )
$u_1$	one-way permanent horizontal component of displacements on sloping ground
$u_2$	two-way permanent displacements of level (horizontal) ground
$u_f$	flow distance
$u^f(\omega)$	surface amplitude of the free field ground motion
$u_o$	horizontal wall displacement
$u_t$	excess pore water pressure at time $t$
$v$	vertical direction
$V$	volume of moving mass along travel path
$v_1$	lower soil wave propagation velocity
$v_h$	horizontal base velocity
$v_{in}$	incoming velocity of rock fall
$v_l$	velocity of propagation of the longitudinal waves
$v_m$	moving mass velocity
$v_o$	initial velocity
$v_{out}$	velocity of bounced rock fall
$V_p$	velocity of a particle
$v_{ph}$	peak horizontal ground surface velocity
$V_r$	rate of tectonic plate subduction
$v_t$	velocity of propagation of the transversal waves
$v_{tp}$	ground velocity below the pile/wall tip at time $t$
$v_{t-T_s}$	ground velocity below the pile/wall tip at time $t - T_s$
$W$	weight
$W_1$	weight of the fines model
$W_D$	dissipated energy by material (hysteretic) damping
$W_f$	tectonic fault width
$W_s$	strain energy
$x$	shortest distance between the force $N$ and point A in Figure 5.5
$y$	shortest distance (level arm) between the force $N \tan\phi$ and point A in Figure 5.5
$y_{pile}$	shortest distance between pile centroid and the neutral axis of rotation
$z$	depth
$z_m$	datum above moving mass at rest position
$\tau_{a(i)}$	available soil shear strength (at joint i)
$\tau_e$	shear stress necessary to maintain limit equilibrium
$B$	Constant of proportionality between $\gamma_{i(j),e}$ and $\Delta_{i(j),e}$

$\Delta_{(i(j),e)}$	relative horizontal displacement of a beam end (magnitudes of kinematically possible tangential displacements along joints $i, j$ of wedges)
$\Delta E$	transient part of lateral earth force
$\Delta_{i(j),e}$	kinematically possible shear strain along joint $i$ or $j$
$\Delta M_\theta$	mass moment of inertia of the trapped soil beneath wall for Poisson's ratio greater than 1/3
$\Delta s$	foundation settlement
$\Delta t$	time step
$\Delta t_w$	time lag between arrival of longitudinal and transversal waves
$\Delta u$	increment of ground surface displacement in x direction
$\Delta v$	increment of ground surface displacement in y direction
$\Delta w$	increment of ground surface displacement in z direction
$\Delta_x$	incremental horizontal distance along rock fall trajectory just before the impact
$\Delta x$	horizontal length over which change of thickness of moving mass has been achieved
$\Delta_y$	incremental vertical distance along rock fall trajectory just before the impact
$\Delta_z$	change of thickness of moving mass
$\Delta \varepsilon$	incremental axial strain
$\Delta \phi$	difference between angle of soil friction at zero effective stress and basic angle of soil friction
$\Delta \gamma$	incremental shear strain
$\Delta \sigma_v$	additional vertical stress at a depth $z>0$ caused by point load $F$ at the ground surface
$\Sigma$	sum of energy loss over a travel path of moving mass
$\Sigma N$	axial component of the resultant of all forces acting on the slip surface
$\Sigma T$	shear component of the resultant of all forces acting on the slip surface
$\alpha$	angle in Figure 5.4 and 5.11
$\alpha_{1(2)}$	angle between normal to the interface and direction of propagation of wave paths on two sides of an interface
$\alpha_j$	angle of inclination of tangential displacement vector with respect to joint direction
$\alpha_l$	local angle of inclination to the horizontal at the impact place of rock fall
$\beta$	inclination to the horizontal
$\beta_l$	larger inclination of the ground surface slope or the slope of the lower boundary of the liquefied zone in percent
$\beta_{rf}$	angle (positive upwards) with the horizontal at the beginning of rock fall
$\beta_t$	tuning ratio

$\delta_b$	friction angle between soil and wall back
$\delta_{i(j),a}$	shear displacement in direct shear apparatus corresponding to available shear stress $\tau_a$ at a joint $i$ (i.e. $j$ )
$\delta_{i(j),e}$	shear displacement in direct shear apparatus corresponding to mobilized shear stress $\tau_e$ at a joint $i$ (i.e. $j$ )
$\delta_p$	plastic deformation in direction perpendicular to the impact surface
$\delta_r$	residual angle of soil friction
$\varepsilon_{i(j),a}$	axial strain in triaxial apparatus corresponding to available shear stress $\tau_a$ at a joint $i$ (i.e. $j$ )
$\varepsilon_{i(j),e}$	axial strain in triaxial apparatus corresponding to mobilized shear stress $\tau_e$ at a joint $i$ (i.e. $j$ )
$\phi$	friction angle in cyclic condition
$\phi'_{(j)}$	soil friction angle (at joint $j$ ) in drained condition
$\phi_1$	peak frictional angle in static condition
$\phi_b$	basic angle of soil friction
$\phi_n$	phase angle respectively of the $n^{th}$ harmonic of the Fourier series
$\gamma$	shear strain
$\gamma'$	submerged unit weight of non-liquefied soil
$\gamma_{hv}$	shear strain in vertical plane
$\gamma_{i(j),a}$	shear strain corresponding to available shear stress $\tau_a$ at a joint $i$ (i.e. $j$ )
$\gamma_{i(j),e}$	shear strain corresponding to mobilized shear stress $\tau_e$ at a joint $i$ (i.e. $j$ )
$\gamma_r$	referent shear strain
$\gamma_s$	unit weight of soil particle
$\gamma_{soil}$	unit weight of soil
$\gamma_w$	unit weight of water
$\eta$	viscosity of soil
$\eta_{aw}$	absolute viscosity of water
$\eta_w$	angle of inclination to the horizontal of backfill behind a retaining wall
$\kappa, \kappa_1$	exponent to shear strain in the shear strength and shear strain relationship
$\lambda$	average rate of occurrence of the event with considered earthquake magnitude
$\mu$	shear modulus of the Earth's crust
$\nu$	Poisson's ratio
$\sigma$	angle of inclination to the vertical of the back of a wall
$\theta$	rotation angle
$\theta_1$	an additional internal rotational degree of freedom
$\theta_b$	relative rotation of a beam end
$\theta_o$	angle of wall rotation

$\theta_r$	angle between the reinforcement direction and a normal to wedge joint
$\theta_\alpha$	difference between angles $\alpha_1$ and $\alpha_2$
$\rho$	soil unit density
$\rho_1$	lower soil unit density
$\rho_w$	water unit density
$\sigma'_m$	mean effective confining stress
$\sigma'_v$	vertical effective stress (from overburden)
$\sigma'_3$	lateral confining effective pressure
$\sigma_d$	horizontal compressive stresses acting on the downstream vertical cross sections of moving mass
$\sigma_h$	axial stress, positive when tensile
$\sigma_u$	horizontal compressive stress acting on the upstream vertical cross sections of moving mass
$\sigma_v$	total overburden pressure (at depth $v$ below wall top)
$\sigma^{(')}$	axial (effective) stress, positive when compressive
$\tau$	shear stress
$\tau_b$	shear stress at the base and sides
$\tau_d$	vertical shear stress acting on the downstream vertical cross sections of the mass
$\tau_{hn}$	shear stress in the plane perpendicular to the plane within which horizontal displacement occurs
$\tau_{hv}$	shear stress in the vertical plane (behind wall at depth $v$ )
$\tau_p$	peak shear strength
$\tau_u$	vertical shear stress acting on the upstream vertical cross sections of the mass
$\omega_{(n)}$	circular frequency (of $n^{\text{th}}$ harmonic of the Fourier series)
$\omega_d$	circular frequency of an input motion
$\omega_e$	fundamental circular frequency of undamped coupled linear elastic SDOFO
$\omega_g$	ground circular frequency
$\omega_h$	circular frequency of horizontal motion
$\omega_o$	circular frequency of the output motion
$\omega_r$	natural frequency corresponding to the rotational motion of a dynamic model
$\omega_s$	natural circular frequency of pile(s)/wall in fixed base condition
$\xi$	damping ratio
$\xi_e$	equivalent hysteretic damping ratio
$\xi_g$	soil hysteretic damping ratio
$\xi_h$	radiation damping ratio of a pile group in horizontal direction
$\xi_{min}$	minimum damping ratio
$\xi_r$	radiation damping ratio of a pile group in rotation
$\xi_s$	structural hysteretic damping ratio

# Chapter 1

## Well Known Simplified Models

### 1.1 Introduction

Simplified models have been used historically in geotechnical earthquake engineering, and in other branches of engineering, primarily due to lack of computers and available data. Such models continue to be used for quick assessment when data, time, and other resources are limited. As more sophisticated methods become available through the increase of computing power and software development, simplified models will be used for rough checks on those models.

Wolf (1994) proposed that simplified models should satisfy several requirements. They should offer conceptual clarity and physical insight. They should be simple in physical description and in application, permitting an analysis with a hand calculator or a spreadsheet in many cases. Yet they should have sufficient scope of application (for different shapes, soil profiles, ground properties). They should also offer acceptable accuracy, as demonstrated by comparing the results of the simplified models with those of rigorous methods. They should be adequate to explain the main physical phenomena involved, and have direct use in engineering practice for everyday design. They need to be useable for checking the results of more sophisticated analyses. Finally, there should be a potential generalization of the concept with clear links to the rigorous methods.

The objective of this chapter is to introduce the reader to three well known simplified models used in practice and in subsequent sections of this monograph.

### 1.2 Source Models of Energy Release by Tectonic Fault

#### 1.2.1 A Simplified Point-Source Model

Earthquakes consist of ground waves radiating energy from a source. The amount of energy transmitted to a location away from the source decreases with distance from the source. This is because the wave front spreads so that the total energy along the wave front equals the source energy less the energy lost in the ground as the waves

pass. The lost energy heats the ground, though by very little. The heating is caused by friction due to the relative motions of soil particles during wave propagation.

The energy transmitted to the ground surface is thus decreased the farther a location is from the source. The energy can cause damage and destruction of structures, lifelines and ground slopes. For this reason, it is necessary to estimate the amount of energy that arrives at the ground surface.

An earthquake source is usually a tectonic fault, often associated with the subduction zone of a tectonic plate. Other sources of ground shaking include volcanic activity, ground failures (such as large landslides or cavity collapse), explosions (from mining and military), and meteorite impact (e.g. Kramer, 1996). The rupture of a tectonic fault starts at one location and propagates over the fault area in time. Forecasting of dynamic fault rupture propagation is rather complex and therefore simplified models are used. The simplest of these is the point source model. The reasons why an earthquake source has been considered as a point, with its focus or hypocentre at a depth and the epicentre at the Earth's surface, are small fault area (for earthquake magnitudes up to 5), great source-to-site distance and lack of recording seismic stations historically.

Figure 1.1 depicts a point source model with its hypocentre and epicentre, three wave fronts of spherical shapes in times and the source-to-site distance  $d_s$  to the hypocentre.

The usual method of calculating the location of an earthquake hypocentre is based on the relative arrival times of the longitudinal and transversal seismic waves at a set of at least three locations. Longitudinal seismic waves travel faster than the transversal waves and therefore there will be a time lag  $\Delta t_w$  between their arrivals. The time lag is estimated from the ground motion record. Let  $d_s$  represent the straight-line (slant) distance from the earthquake hypocenter and a recording site on the Earth's surface. If  $v_t$  and  $v_l$  denote the velocities of propagation of the transversal and longitudinal waves respectively, then the transversal waves take a time  $d_s v_t^{-1}$  to arrive at the site, and the longitudinal waves take a time  $d_s v_l^{-1}$  to arrive. Hence by measuring the difference  $\Delta t_w$  between these arrival times, and inverting the relationship, one arrives at:

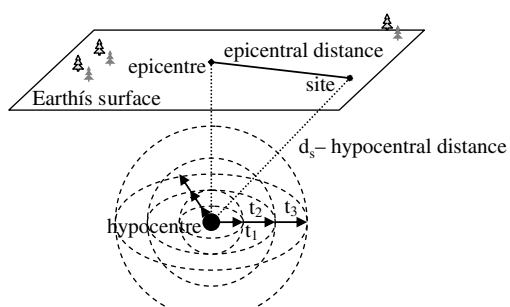


**Fig. 1.1** Point source model with spheres of wave's front propagation from the hypocentre in times  $t_1-t_3$

$$d_s = \frac{\Delta t_w}{1/v_t - 1/v_l} \quad (1.1)$$

The distance  $d_s$  can be estimated if the velocities are known and the interval  $\Delta t_w$  can be measured. The equation is strictly correct for homogeneous ground, without ground wave refraction at the boundaries of zones with different wave propagation velocities. Earth's interior is heterogeneous and therefore the equation is just a first approximation in the calculation of the slant distance to an earthquake hypocentre. This model does not account also for a number of other source and wave path effects described in Section 3.3.1.

Anderson (1989) compiled available data and indicated that a typical range of the longitudinal wave velocity is 6–7 km/s at depths greater than 1 km. The corresponding typical range of the transversal wave velocity is 3.5–4 km/s. The wave propagation through Earth's interior causes mainly elastic (small strain) deformations because material damping (energy transformed into heat by friction between particles due to their motion during wave propagation) is small and amounts to less than 1% of the energy transmitted by waves. Longitudinal and transversal wave velocities are coupled by a factor called Poisson's ratio. The ratio range for rock at depths greater than 1 km is from 0.24 to 0.26.

A Microsoft Excel spreadsheet for calculating the location of the hypocentre of an earthquake from the slant distances to three recording seismic stations on rock is described in Appendix A.1. The same appendix contains also procedure for calculation of distance between a site and earthquake epicentre when the locations of the site and the epicentre are given as geographic latitude and longitude in degrees.

The point source model assumes that the wave front propagates from the source as concentric spheres. In this case, the ground motion at a hypocentral distance  $d_s$  will be inversely proportional to the square root of the energy density, i.e.

$$\sqrt{\frac{E_d}{E_o}} \sim \sqrt{\frac{1}{e^{k_d \cdot d_s} \cdot 4 \cdot \pi \cdot d_s^2}} \quad (1.2)$$

where  $E_o$  is the total energy released at the earthquake source,  $E_d$  is the energy density at a hypocentral distance  $d_s$ ,  $k_d$  is an average material damping coefficient (about 0.001–0.01), e.g. Ambraseys and Srbulov (1998). The term  $e^{k_d}$ , determined by both experiments and theory, describes the effect of material damping (i.e. the energy dissipation because of internal friction). The term  $4\pi d_s^2$  (i.e. the surface of a sphere with the radius  $d_s$ ) describes the effect of radiation damping on seismic energy dissipation with distance  $d_s$  to the source. Equation (1.2) is the basic expression used in the derivation of almost all attenuation relationships that assume a point source model. It is strictly valid for distances from the source where the body seismic waves dominate the ground motion at the surface. At distances greater than a few tens of kilometers from the source (e.g. Kramer, 1996), where the surface seismic waves (Rayleigh, Love) appear at the surface and predominate the ground

motion, the radiation damping may be proportional to  $d_s^{-0.5}$ , because the circumference of the surface wave propagation front is  $\pi d_s$ .

### 1.2.2 An Alternative, Planar Source Model

Ambraseys and Srbulov (1998) showed that on average the planar model fits better the recorded peak ground accelerations than the point source model. Their calculations assumed that a planar tectonic fault radiates the energy as a wave train uniformly in all directions in a medium with an average material damping coefficient  $k_d$ . However, their model requires knowledge of the fault plane size and location as well as of the attitude and thickness of the non-seismogenic zone, information that has to be assumed by the engineer a priori. For known faults (identified based on the past strong motion records, micro seismic activity observations and geological studies) the use of the planar source model is not much complicated than the use of the point source model.

To model a planar fault, Srbulov (2004) used a four-Gauss-point integration scheme. The locations of four integration points on a fault plane and distances to the site are shown in Fig. 1.2.

For this model, Eq. (1.2) is replaced by:

$$\sqrt{\frac{E_d}{E_t}} \sim \sqrt{L_f \cdot W_f \cdot \sum_{i=1}^4 \frac{1}{e^{k_d \cdot d_i} \cdot 4 \cdot \pi \cdot d_i^2}} \quad (1.3)$$

where  $E_t = E_o(L_f W_f)^{-1}$  is the total energy released at the earthquake source per unit area of the source,  $L_f$  is tectonic fault length,  $W_f$  is tectonic fault width. This is again valid for distances up to source-to-site distances of a few tens of kilometers, where the body seismic waves dominate the ground motion at the surface. At greater distances, where the surface waves dominate the ground motion at the surface, Equation (1.3) may be replaced by

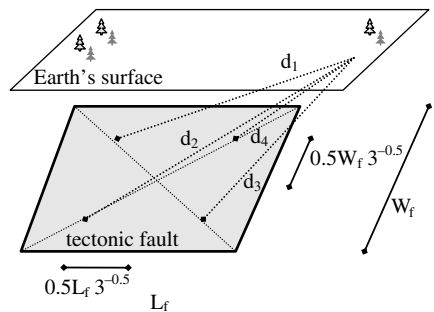


**Fig. 1.2** The locations of four Gauss integration points on a fault plane and slant distances  $d_{1-4}$  to the site (Srbulov, 2004, by permission of Patron Editore)

$$\sqrt{\frac{E_d}{E_t}} \sim \sqrt{L_f \cdot W_f \cdot \sum_{i=1}^4 \frac{1}{e^{k_d \cdot d_i} \cdot 2 \cdot \pi \cdot d_i}} \quad (1.4)$$

### 1.2.3 Case Study Comparisons of the Point and Planar Source Models

Data for the case study comparisons are from Ambraseys et al. (2004). Basic data are given in Table 1.1. Ambraseys et al. (2004) provide also the projections of the causative faults on the Earth's surface, the epicentral distances, the hypocentral depths and the fault plane inclinations to the horizontal (trends) so that Equations (1.2) to (1.4) can be used.

For each earthquake listed in Table 1.1, horizontal ground accelerations were measured at a number of different recording stations, at various distances from the earthquake source. Ratios between the peak horizontal accelerations at two recording stations can therefore be calculated. If the most remote recording station is used as the reference, then the ratio for this station itself is one.

Ratios of peak horizontal accelerations for the three earthquakes listed in Table 1.1 are shown in Fig. 1.3. Filled circles and squares represent ratios based on source-to-site distances reported by Ambraseys et al. (2004). Empty circles and squares in Fig. 1.3 represent ratios calculated using Equations (1.2) to (1.4). Fault distance used is the shortest distance from a recording station to the Earth's surface projection of a tectonic fault.

From Fig. 1.3 it follows that there is a good agreement between predicted peak acceleration ratios based on the planar source model and the best fit of ratios (shown by thick dashed line) calculated from recorded peak accelerations using the fault distances as well as between predicted peak acceleration ratios based on the point source model and the best fit of ratios (shown by thick dotted line) calculated from recorded peak accelerations using the epicentral distances.

In Fig. 1.3, it is possible to notice a number of outliers, i.e. values that are significantly different from the best fit, at the site-to-source distances greater than about 20 km particularly when the epicentral distances are considered. This suggests that the use of epicentral distances is not always appropriate when considering attenuation of peak accelerations associated with radiation damping.

**Table 1.1** Basic earthquake source data in the example

No	Earthquake	Date	Time	Magnitude M <sub>w</sub> <sup>#</sup>	Causative fault type*
1	Tabas – Iran	16 September 1978	15:35:57	7.35	Oblique
2	Montenegro	15 April 1979	06:19:41	7.0	Thrust
3	Campano Lucano – Italy	23 November 1980	18:34:52	6.93	Normal

Notes: # Description of earthquake magnitudes is given in Section 3.2.1. \*Description of tectonic fault types is given in Section 3.3.1.

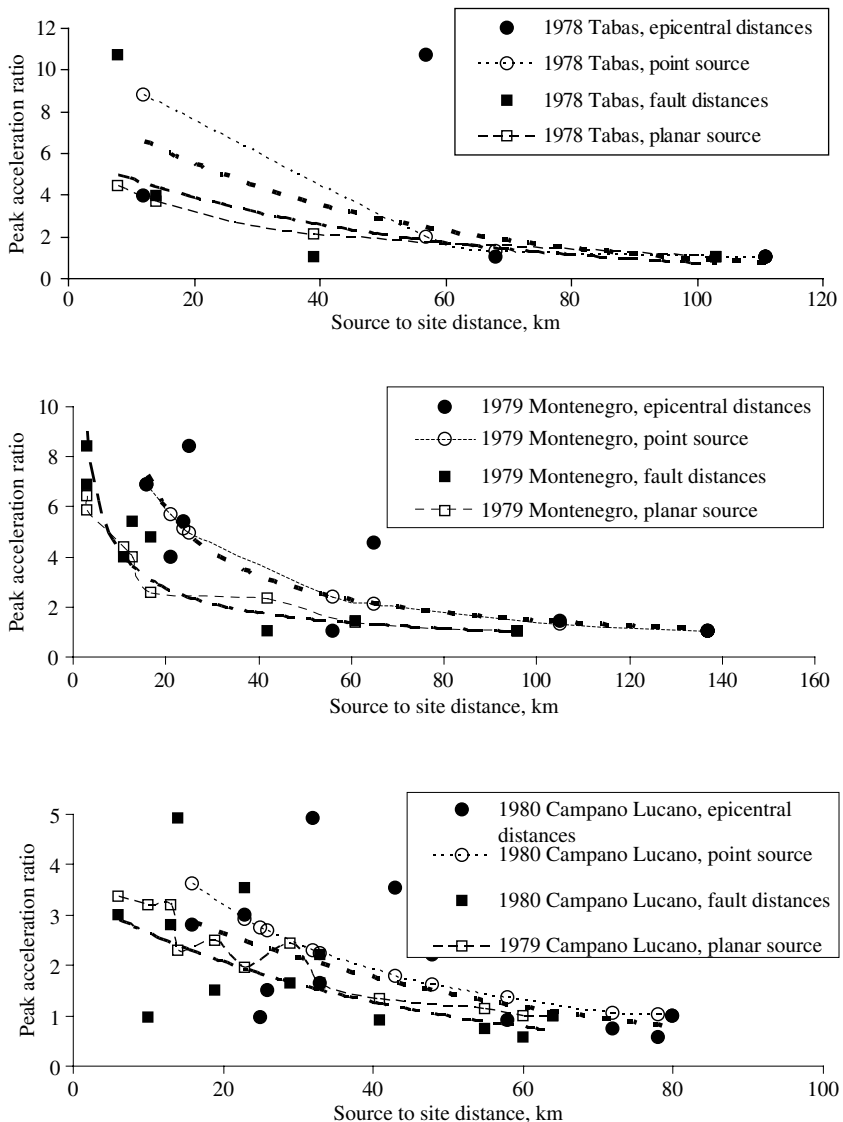


**Fig. 1.3** Peak acceleration ratios versus source to site distances in the example

### 1.3 Sliding Block Model of Co-Seismic Permanent Slope Displacement

#### 1.3.1 Newmark's (1965) Sliding Block Model

It is not always economic to ensure that natural and even made slopes have factor of safety against sliding greater than one during strong earthquakes. For this reason it

is necessary to estimate permanent ground displacement of slopes caused by strong earthquakes. If such displacements are deemed acceptable for safety and serviceability reasons then the slope inclination might be considered acceptable. If not, remediation measures may be needed such as the decrease of the slope inclination.

Slope displacements occur during and after strong earthquakes. Co-seismic displacements are those that start immediately, during the earthquake, and are a direct result of the dynamic ground shaking. Post-earthquake displacements occur after the earthquake and result from other reasons such as decrease of soil shear strength in cyclic condition, soil consolidation, or other causes.

Slope failures induced by earthquakes in cohesive soil occur frequently along distinct slip surfaces. The existence of discontinuities within a slope can create a non-linear, possibly chaotic, response, which is rather complex to analyze in routine engineering practice. Therefore, simplified methods are employed. Newmark (1965) used a rigid sliding block model for prediction of co-seismic permanent displacement of slope parts subjected to base motion. His model assumes that permanent displacement starts when base acceleration exceeds the critical acceleration that can be sustained by the slip surface. The permanent displacement continues until the base acceleration decreases below the critical acceleration and the relative velocity of the sliding block decreases to zero.

### ***1.3.2 Comments on Newmarks's (1965) Sliding Block Model***

As noted by Newmark (1965), the sliding block model is based on a number of simplifying assumptions. These include:

- Soil behaves as a rigid perfectly plastic material.
- Permanent displacement occurs along a single, well-defined slip surface.
- Soil does not change its shear strength as a result of shaking.

In practice, additional assumptions may be added such as:

- Permanent displacement occurs only in the down slope direction.
- Vertical accelerations may be ignored.

In any particular situation, the inclination of sliding block to the horizontal for any shape of slip surface can be inferred from equilibrium of the forces acting on the slip surface under consideration. The procedure is indicated in Fig. 1.4. The forces acting on the parts of the slip surface in Fig. 1.4.a are sorted into the polygon of forces with their resultants in Fig. 1.4.b. The inclination of the resultant of transversal forces to the horizontal equals to the inclination of the equivalent sliding block shown in Fig. 1.4.c.

Some computer programs for slope stability analysis contain procedure for determination of the inclination of the sliding block. An example of the use of an automatic procedure for determination of inclination of an equivalent sliding block is given for the case study in Section 6.3.3.

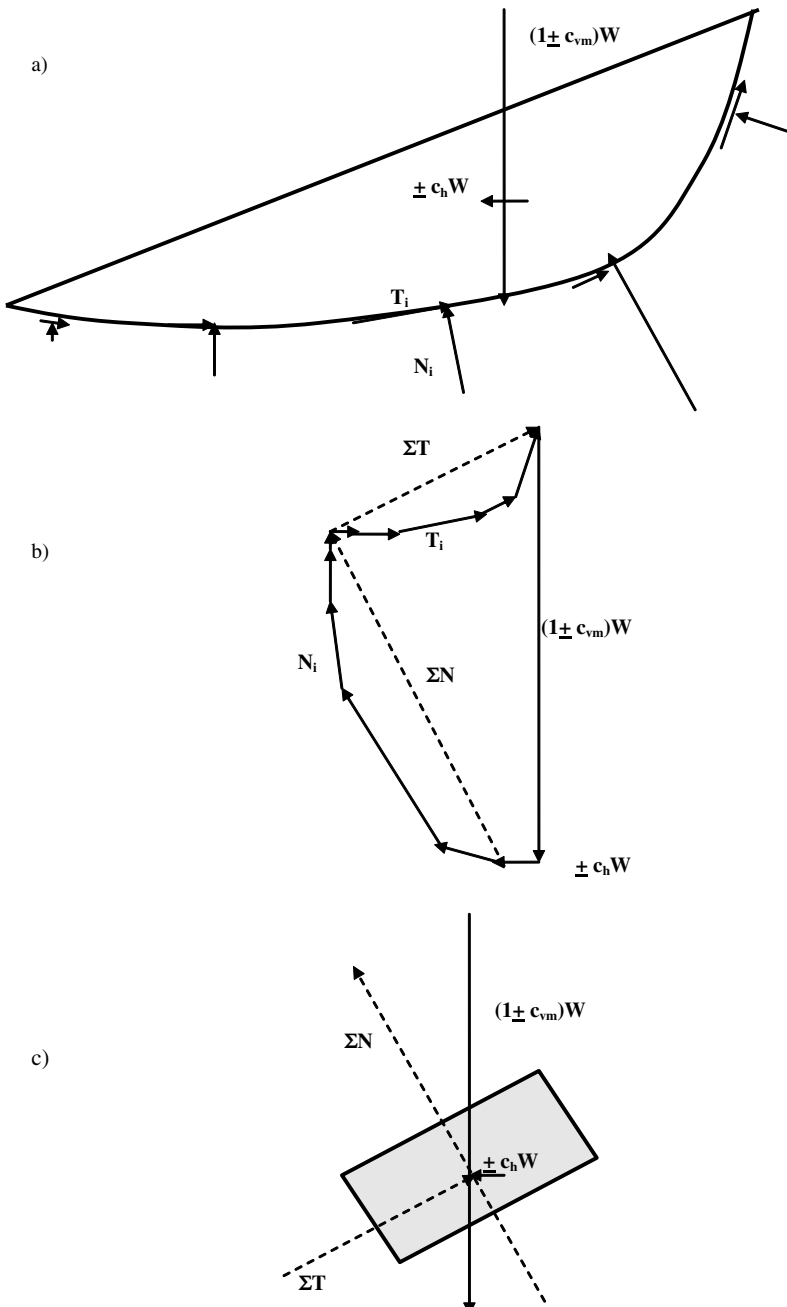


**Fig. 1.4** (a) Forces acting on a slope part, (b) an equilibrium polygon of the forces, (c) the equivalent sliding block of the slope (Srbulov, 2003b, by permission of Patron Editore)

In Fig. 1.4,  $T_i$  and  $N_i$  are shear and axial force respectively acting at base  $i$  of a wedge,  $W$  is the weight of soil slope above the slip surface,  $c_h$  and  $c_{vm}$  are the horizontal and vertical coefficient respectively of the mass inertia induced by ground motion,  $\Sigma T$  and  $\Sigma N$  are the shear and axial component of the resultant of all forces acting on the slip surface. Eurocode 8–5 (2004) specifies that the coefficient  $c_h$  in pseudo-static analyses shall be taken as 0.5 of the ratio between design horizontal ground acceleration and the gravitational acceleration and  $c_{vm}$  as 0.33 to 0.5 of  $c_h$ .

Newmark (1965) considered only a circular and a planar slip surface as examples. It is arguable that the procedure is applicable not only to soils which have nearly the same static and cyclic shear resistances, but also to soil which properties change in cyclic condition, providing that the shear strength and excess pore pressure induced by cyclic loading (Section 2.4) are used in the analysis. Newmark (1965) considered both a square acceleration pulse and a suite of earthquake motions to develop simplified engineering design charts. Subsequently, other researches considered triangular, sinusoidal and actual recorded acceleration pulses, soil shear strength variation, vertical accelerations, and other variations. The results of some recent researches are mentioned here.

Wartman et al. (2003) found that the rigid sliding block procedure was generally not on the safe side when the predominant frequency of the input motion is somewhat less or about equal to the natural frequency of the sliding mass. Contrary, the sliding block procedure is generally on the safe side when the predominant frequency of the input motion exceeds the natural frequency of the mass.

Kramer and Lindwall (2004) compared the common practice of applying one dimensional input motion in the direction of block sliding with the application of two and three dimensional input motions to sliding block model and found both small and large effects of two and three dimensional input motions in comparison with one dimensional input motion. The effect of slope orientation on Newmark sliding block displacements was also investigated. Computed displacements were found to be very sensitive to the assumed orientation of the input motion, particularly for cases of high yield acceleration.

Wartman et al. (2005) performed shaking table tests on clayey slope models and found that the results of the rigid sliding block analysis ranged from 27 to 225% of maximum measured displacements, and averaged about 75% of measured displacements for the test series. The Newmark type analyses were most appropriate for model tests that experienced large deformations, where the sliding resistance was controlled principally by post peak to residual strengths.

Bray and Travasarou (2007) utilized a nonlinear fully coupled stick-slip sliding block model for estimating permanent displacements due to earthquake induced deviatoric deformations. Their model considers the system's yield coefficient, its initial fundamental period and the ground motion's spectral acceleration at a degraded period. The use of the seismic displacement model is validated by reexamining 16 case histories of earth dam and solid waste landfill performances.

The number of comparative studies of actual permanent displacements and the sliding block model results is limited. Further consideration and the results of rigid sliding block method are given in Section 4.4.1.

## 1.4 Single Degree of Freedom Oscillator for Vibration of a Structure on Rigid Base

### 1.4.1 Description of the Model

Earthquake induced multi-directional ground shaking with different frequencies causes a multitude of structural vibration modes. The most important structural vibration is in the horizontal direction because structures are designed to carry vertical loads primarily. A detailed dynamic analysis of each structure is not economical and therefore simplified models of vibrations of structures are used in practice.

A single degree of freedom oscillator (SDOFO) on a rigid base is one of the simplest ways of modeling the vibrations of a structure, Fig. 1.5.

Not all structures can be approximated by a SDOFO. Single-storey building frame, bridge with hinged columns and multi-storey structure responding in rigid base condition are typical examples of structures that can be represented as a SDOFO. The main assumptions of this model are:

- The first and only possible vibration mode is the most significant.
- Soil-foundation interaction effect is not significant and is not considered.
- Horizontal and vertical ground motions caused by earthquakes are considered separately.

The SDOFO model has been frequently considered for generation of response spectra, since their introduction by Benioff (1934) and Biot (1941). The response spectrum describes the maximum response of a SDOFO to a particular ground input motion as a function of the fundamental frequency (or the fundamental period) and damping of the SDOFO, Fig. 1.6. When the frequency/period of an SDOFO is close to the frequency/period of the base motion, the SDOFO tends to go into resonance with base motion, and exhibits larger accelerations (peaks in the spectral shape).

The SDOFO's damping is usually considered in terms of a percentage of critical damping. The critical damping is defined as the damping that just prevents oscillations of the SDOFO. If dampers in Fig. 1.5 are so strong to be able to resist inertial forces acting on the SDOFO due to base motion then the SDOFO would be critically damped and not oscillate.

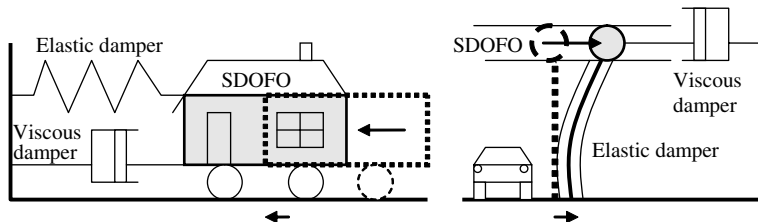


**Fig. 1.5** Single degree of freedom oscillator (SDOFO) models of a rigid (*box like*) and a flexible (*beam like*) structure with elastic (*spring/beam*) and viscous (*dash pot*) dampers

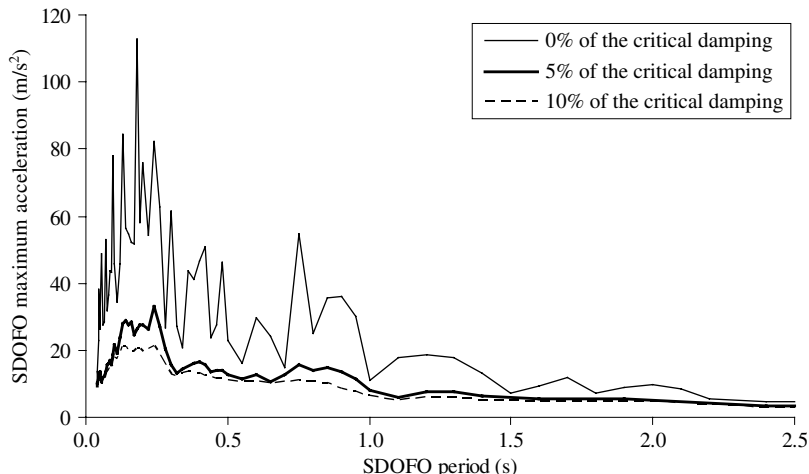


**Fig. 1.6** Example of elastic acceleration response spectra of a SDOFO

Smoothed envelope of many response spectra are used in engineering codes for routine design of structures.

From Fig. 1.6, it can be seen that, for the particular earthquake time history used here, the peak response of a SDOFO occurs at the predominant period of the earthquake acceleration time history of 0.2 s and that structural damping has a significant influence on the spectral accelerations. Therefore, selection of structural damping is an important issue.

#### 1.4.2 Comments on the Model

Only a lumped mass can oscillate in one mode only. However, Eurocode 8, Part 5 (2004) requires that the effects of dynamic soil-structure i.e. soil-foundation interaction shall be taken into account for structures where their displacements are significant so that the axial forces within structural parts can cause significant bending moments in these parts; structures with massive or deep-seated foundations, such as bridge piers, offshore caissons and silos; slender tall structures, such as towers and industrial chimneys; and structures supported on very soft soil, with average transversal wave velocity less than 100 m/s to a depth of 30 m below the ground surface.

Recent examination of different elastic SDOFOs for horizontal structural response to combined horizontal and vertical ground motion caused by earthquakes was done by Ambraseys and Douglas (2003). Their main findings are:

- Bending and hinging SDOFOs have three main types of behavior: normal, parametric resonance and instability.

- The type of behavior that a system exhibits is controlled by the combination of system parameters and the vertical input acceleration. As a consequence of variation of input acceleration, a system can exhibit all three types of behaviors.

Further consideration of SDOFO is provided in Section 6.4.

## 1.5 Summary

Three simplified models, which are frequently used in practice, have been described and commented on in this chapter.

- The point source model of tectonic energy radiation is applicable to earthquakes of smaller size (with earthquake magnitude less than 5) and distant earthquakes (with little differences among distances between a site and parts of a tectonic fault). The model assumes homogeneous Earth's crust and the spherical shapes of the fronts of seismic wave's propagation. It does not account for the effects of tectonic fault type and direction of rupture propagation in near-fault zone.
- Newmark's (1965) sliding block model of permanent displacements of ground slopes is applicable to rigid ground with distinct slip surfaces. It can involve consideration of soil shear strength dependence on rate and slip distance as well as the vertical component of ground motion. The effect of vertical ground motion needs to be considered for very steep slopes (cliffs) and reinforced retaining walls.
- A single-degree-of-freedom oscillator (SDOFO) with a rigid base is frequently used to generate acceleration response spectra defined in codes for design of engineering structures. The model allows for a single vibration mode and that the horizontal and vertical vibrations caused by ground motions are considered separately. It can include simplified consideration of soil-foundation interaction effects and soil properties dependence on deformation amount, i.e. soil non-linear behavior.

These three simplified models also contain initial indications of necessary input parameters for their use (soil properties, seismic excitation) as well as the effects of ground motion (energy input, permanent displacements, accelerations) on natural soil (slopes) and engineering structures, which are considered in the following chapters.

# Chapter 2

## Soil Properties

### 2.1 Introduction

Ground motion during earthquakes is influenced by and affects properties of ground. The main materials involved in construction practice are manufactured concrete, steel, plastic, timber, and natural rock and soil.

Manufactured materials are well controlled concerning their content and properties and they are frequently assumed to behave linearly and elastically under non-extreme loading, i.e. the loading and deformations are linearly proportional and deformations are fully recoverable on unloading, unless deliberately or incidentally develop cracks and hinges under extreme loadings during earthquakes.

Rock has a substantial rigidity, which is comparable to manufactured materials, but also planes of weakness (cracks/joints) caused by tectonic stresses, rock exposure to atmosphere and weathering, heat from the sun or from the earth's core, freezing, tree roots expansion, and other factors. The strength on shearing of rock mass under gravity and earthquake forces is often controlled by its joints, which are frequently filled by soil and/or water near the rock surface. Hoek (1983), for example, provides more details on the influence of joints on rock properties.

Soil is a mixture of solid grains, gasses and fluids (e.g. Bear, 1988). Soil grains are derived from parent rock by physical (freeze/thaw/erosion) and chemical (mainly oxidation) weathering and grinding/shaping by transportation (by wind/glaciers/surface streams/ocean currents and waves) and sedimentation (in lakes and oceans). Gasses in soil arise either from soil contact with air or from underlying decomposition of rock (e.g. radon in granite) or other chemical processes, which create methane, hydro sulfides and other harmful gasses. Fluids in soil originate mainly from surface water or deep reservoirs and other sources. Fluids can include hydrocarbon and other contaminants from man-made or natural sources. Soil is frequently considered as two-phase material (grains and fluid), or a one-phase material if dry. In the case of rapid deformations, such as during fast earthquake motions, the so-called undrained condition may apply when ground water cannot escape or freely move within soil. In this case, some analyses can be carried out in terms of total stresses, taking the soil to be a single-phase continuum. Soil creation processes cause soil layering (heterogeneity) and anisotropy (different behaviors in the horizontal and vertical direction). Besides inherent soil anisotropy by formation,

induced soil anisotropy is a result of different loading/unloading in the horizontal and vertical direction (e.g. Tatsuoka et al., 1997; Hashiguchi, 2001).

Soil grains are a complex set of particles of different sizes, shapes and minerals. Under load, the slip of particles causes a non-linear relationship between applied load and resulting displacement i.e. between stresses and strains. Stresses and strains within soil are frequently calculated as for continuous instead of discrete materials. For continuum, stress is defined as the ratio between acting load and the area on which it is applied; axial strain is the ratio between achieved displacement under load and the length over which it has been achieved; shear strain is equivalent to a change in previously right angle within a continuum. Under sufficient loads (which may be small), soil exhibits irreversible (plastic) deformation due to a combination of permanent slip of soil particles relative to one another, small amounts of crushing of asperities at grain contacts, and sometimes fracture or shattering of some grains. When such irreversible deformations are developed during strong earthquakes, the number of cycles of earthquake shaking is an important factor affecting soil behavior.

If drainage is allowed, a change of loads on soil tend to cause soil to contract if loose or expands if dense. If the voids of a soil body are filled completely with water, with no air present, and if drainage is prevented, the soil develops excess pore water pressures when attempting to contract, or suction when attempting to expand. Soil strength under shearing and stiffness under axial loads are dependent on effective stress, which is the difference between the total applied stress induced by external load (self-weight, applied weights, and dynamic inertial loads) and pore water pressure in soil (consisting of equilibrium pressure plus excess pressure). A decrease in soil effective stress due to excess pore water pressure increase causes decrease of soil shear strength and stiffness, i.e. softening.

In fine grained soil, with particle diameters less than about  $5\text{ }\mu\text{m}$ , chemically bonded water of high density causes viscous, rate-dependent effects (e.g. Leroueil and Marques, 1996). Earthquakes cause great loading rates and hence noticeable viscous effects in fine grained soil.

A very comprehensive review of dynamic soil properties and dynamic soil testing methods is given in Kramer (1996). An advantage of simplified analyses is that they require simplified soil properties. The objective of this chapter is to describe the soil properties, which will be referred to in following chapters.

## 2.2 Cyclic Shear Stiffness and Material Damping

Atkinson (2000) shows that soil is neither linear nor elastic, even at very small strains. Moreover, a variety of authors have shown that, even if linearity and elasticity are assumed, soil is not isotropic (e.g. Tatsuoka et al., 1997; Hashiguchi, 2001). Nevertheless, isotropic, linear-elastic models are still used in practice.

Laboratory tests have shown that soil stiffness and soil damping (energy dissipation) is influenced by cyclic strain amplitude, density and acting mean principal effective stress of coarse grained soil, plasticity index and over consolidation ratio of

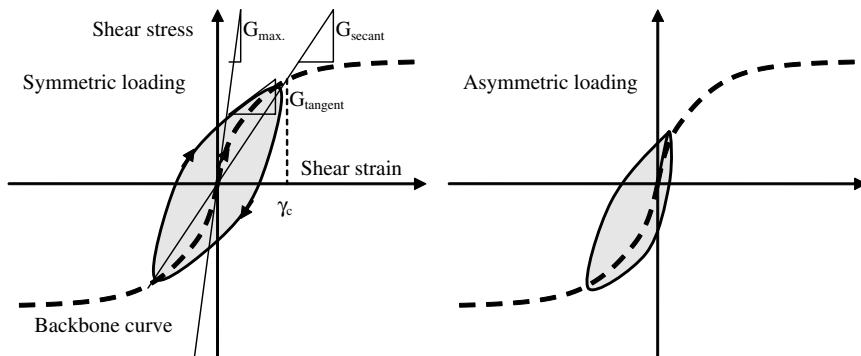


**Fig. 2.1** A hysteretic loop in one cycle of soil shearing

fine grained soil, and number of loading cycles (e.g. Seed and Idriss (1970), Hardin and Drnevich (1972), Vucetic and Dobry (1991), Ishibashi (1992), etc.). A typical relationship between applied shear stress and induced shear strain, within soil under symmetric cyclic loading, exhibits a hysteretic loop as sketched in Fig. 2.1. The same figure also contains a sketch for the case of a non-symmetrical cyclic loading.

A shear modulus  $G$  is a ratio between incremental shear stress and shear strain. Several different measures of shear modulus are shown in Fig. 2.1. When the increments are related to the origin (zero values) then so called secant modulus is obtained. If the increments are related to the change in values from previous values then the tangent modulus is obtained. Shear modulus dependence on shear strain amplitude and other factors is determined by laboratory tests (e.g. ASTM D4015, ASTM D3999) or from formulae given in Section 2.2.1.

With increases in shear stress and strain, slippage between grains causes a weakening of the soil structure, and a decrease of its shear strength and stiffness. This process results in rotation of hysteretic loop towards horizontal axis. The locus of points corresponding to the tips of hysteretic loops of various cyclic strain amplitudes is called a backbone (or skeleton) curve (e.g. Kramer, 1996). It should be noted that the backbone curve shown in Fig. 2.1 is for one cycle of loading/unloading. Backbone curve for greater number of cycles may change if soil strength and stiffness change (decrease) with increase in number of cycles or with excess pore water pressure increase. For elastic materials, the hysteretic loop and the backbone curve are straight and coincidental lines.

At very small shear strains, less than about  $10^{-6}$ , hysteresis is virtually absent, and the behavior of the soil is often approximated as linear-elastic. When the soil indeed behaves as an isotropic linear elastic body, the shear modulus  $G_{\max}$  is related to other quantities by:

$$G_{\max} = \rho \cdot v_t^2 \quad (2.1)$$

where  $\rho$  is soil unit density ( $\text{kg}/\text{m}^3$ ) and  $v_t$  is soil transversal wave velocity. The latter can be determined using field geophysical methods (e.g. ASTM D4428, ASTM

D5777) or seismic cone (e.g. Lunne et al., 2001) to avoid possible problems caused by sample disturbance, size and orientation effects and measurements of very small strain in the laboratory. Disturbance of loose sample causes their artificial compaction and of dense samples their artificial loosening. Sample disturbance can be minimized by using thin walled soil samplers, pushing instead of hammering of soil samplers and by rapid freezing of soil before sampling. The later technique is very expensive and not widely used in practice. Several researches (e.g. Hardin, 1978; Seed and Idriss, 1970) suggested formulae for calculation of  $G_{\max}$  based on empirical correlations with other soil properties.

The width of the hysteretic loop is related to the area, which is a measure of internal energy dissipation. The dissipation involves the transformation of energy or work into heat, by particles friction due to their movements. A damping ratio  $\xi$  is frequently used as a measure of the energy dissipation (e.g. Kramer, 1996).

$$\xi = \frac{W_D}{4 \cdot \pi \cdot W_s} = \frac{1}{2 \cdot \pi} \cdot \frac{A_{loop}}{G_{secant} \cdot \gamma_c^2} \quad (2.2)$$

where  $W_D$  is the dissipated energy,  $W_s$  is the maximum strain energy, i.e. the area of the triangle in Fig. 2.1 bordered by  $G_{secant}$  line, the vertical at  $\gamma_c$  and shear strain axis; and  $A_{loop}$  is the area of the hysteretic loop. Soil parameters  $G_{secant}$  and  $\xi$  are often referred to as equivalent linear soil parameters. Soil damping is determined by laboratory tests (e.g. ASTM D3999, D4015) or from formulae given in Section 2.2.1.

### 2.2.1 Shear Stiffness and Damping Ratio Dependence on Shear Strain

Several authors proposed different expression for shear modulus  $G$  and damping ratio  $\xi$ , e.g. Vucetic and Dobry (1991), Ishibashi (1992). Recently, Zhang et al. (2005) provided the following relationships for  $G = G_{secant}$  and  $\xi$  based on a modified hyperbolic model and a statistical analysis of existing resonant column and torsional shear test results from 122 specimens.

$$\begin{aligned} G &= \frac{G_{\max}}{\left[ 1 + \left( \frac{\gamma}{\gamma_r} \right)^{\alpha} \right]} \\ \gamma_r &= \gamma_{r1} \cdot \left( \frac{\sigma'_m}{P_a} \right)^k \\ \sigma'_m &= \sigma'_v \cdot \frac{1 + 2 \cdot K'_o}{3} \\ \xi &= 10.6 \cdot \left( \frac{G}{G_{\max}} \right)^2 - 31.6 \cdot \frac{G}{G_{\max}} + 21.0 + \xi_{\min} \end{aligned} \quad (2.3)$$

**Table 2.1** Recommended mean values of  $\alpha$ ,  $k$ ,  $\gamma_{r1}$ , and  $\xi_{\min}$  at  $\sigma'_m = 100$  kPa (Zhang et al., 2005, with permission from ASCE)

Geologic age	Parameter	Plasticity index, PI (%)					
		0	15	30	50	100	150
Quaternary	$\alpha$	0.83	0.87	0.90	0.94	1.04	1.15 <sup>a</sup>
	$k$	0.316	0.255	0.207	0.156	0.077	0.038 <sup>a</sup>
	$\gamma_{r1}$ (%)	0.075	0.092	0.108	0.13	0.186	0.241 <sup>a</sup>
	$\xi_{\min}$ (%)	0.82	0.94	1.06	1.23	1.63	2.04 <sup>a</sup>
Tertiary and older	$\alpha$	1.03	1.04	1.05	1.07	1.11 <sup>a</sup>	—
	$k$	0.316	0.268	0.227	0.182	0.105 <sup>a</sup>	—
	$\gamma_{r1}$ (%)	0.031	0.037	0.43	0.051	0.072 <sup>a</sup>	—
	$\xi_{\min}$ (%)	0.82	0.94	1.06	1.23	1.63 <sup>a</sup>	—
Residual/saprolite soil	$\alpha$	0.79	0.86	0.92	1.01 <sup>a</sup>	—	—
	$k$	0.42	0.212	0.107	0.043 <sup>a</sup>	—	—
	$\gamma_{r1}$ (%)	0.039	0.053	0.067	0.086 <sup>a</sup>	—	—
	$\xi_{\min}$ (%)	0.82 <sup>b</sup>	0.94 <sup>b</sup>	1.06 <sup>b</sup>	1.23 <sup>b</sup>	—	—

<sup>a</sup>Tentative value; extrapolated from the range of available test data<sup>b</sup>Tentative value; no small-strain torsional shear damping measurements available

— Little or no data available.

where  $G_{max}$  is according to Equation (2.1),  $\gamma_r$  is referent shear strain (which depends on  $\gamma_{r1}$  and  $\sigma'_m$ );  $\gamma_{r1}$  depends on soil plasticity index  $PI$  and geologic age, and is given in Table 2.1 by Zhang et al. (2005) together with other constants ( $\alpha$ ,  $k$ ,  $\xi_{\min}$ );  $P_a$  is atmospheric pressure,  $\sigma'_m$  is the mean effective confining stress,  $\sigma'_v$  is the vertical effective stress,  $K'_o$  is coefficient of soil lateral pressure (typically approximated as  $1 - \sin\phi'$  following simplified expression by Jaky (1944), for normally consolidated soils, where  $\phi'$  is soil friction angle. The coefficient  $K'_o$  is the ratio between the horizontal and vertical soil effective stresses under conditions of zero lateral strains.

Geological ages considered by Zhang et al. (2005) include the Quaternary (covering the last about two millions years), the Tertiary (from about two millions years ago to 65 millions years ago) and older as well as residual/saprolite soils. It is found that the Quaternary soil exhibits more linearity than soil of other two groups (Tertiary and residual/saprolite).

Shapes of  $G/G_{max}$  and damping ratio  $\xi$  versus logarithm of shear strain  $\gamma$  for Quaternary formations and  $\sigma'_m = P_a$  are shown in Fig. 2.2, for example.

Lin et al. (2000) performed a test program with measurements of transversal wave velocity by the down-hole method and large-scale dynamic triaxial tests and resonant-column tests of gravelly deposit from Taichung area of Taiwan. They found that the shear modulus ratio  $G/G_{max}$  of the gravelly cobble deposits does not decrease below a value of about 0.5 for shear strain greater than  $10^{-4}$ , in contrast to sandy soil. They suggested the following relationship for  $G_{max}$ :

$$G_{max} = 305 \cdot \exp(0.0025 \cdot \sigma_3) \quad (2.4)$$

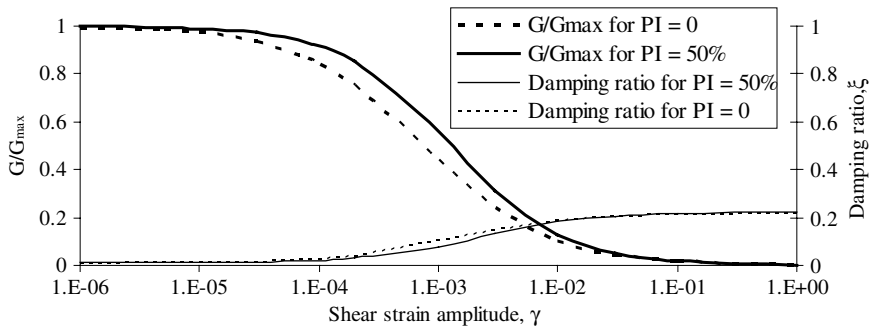


**Fig. 2.2** Typical  $G/G_{\max}$  and damping ratio  $\xi$  versus logarithm of shear strain  $\gamma$  for Quaternary soil

where  $\sigma'_3$  is confining effective pressure in kPa and  $G_{\max}$  is in MPa. Other specific soil such as highly organic peat may exhibit different shear modulus and damping ratio relationships (e.g. Kramer, 2000).

Shear strain is frequently not known in advance and depends on the severity of ground motion, which depends on soil shear modulus, which in turn depends on shear strain, so that a recursive relationship arises. Averaged shear modulus and damping ratios are given in Table 4.1 of Eurocode 8-5 depending on the ratio between ground and the gravitational acceleration up to maximum of 0.3 g. Srbulov (2003a) made proposals for the shear modulus and damping ratios for the ground acceleration ratio (i.e. ground to gravitational acceleration ratio) of up to 0.5. Table 2.2 contains a combination of the ratios from Eurocode 8-5 (2004) and Srbulov (2003a), who used a SDOFO for back analyses of 66 case histories of recorded peak horizontal ground accelerations at the ground surface and at depths.

**Table 2.2** Average soil damping ratios and average shear modulus ratios ( $\pm$  one standard deviation) within 20 m depth, based on Table 4.1 in Eurocode 8-5 (2004) for ground acceleration ratio up to 0.3 and from Srbulov (2003a) for ground acceleration ratio of 0.5

Ground acceleration ratio	Damping ratio $\xi$	$G/G_{\max}$
0.1	0.03	0.80 ( $\pm 0.1$ )
0.2	0.06	0.50 ( $\pm 0.2$ )
0.3	0.1	0.36 ( $\pm 0.2$ )
0.5	0.125	0.20 ( $\pm 0.15$ )

### 2.3 Static Shear Strengths of Soils

The shear strength of soil in static conditions depends on many factors, of which the most important are density (or porosity) of coarse grained soil; degree of over consolidation, plasticity in drained condition and consistency in undrained condition of fine grained soil. The critical states model provides a useful framework in which to study the static strength of fine-grained soils (e.g. Schofield and Wroth, 1968). The

steady-state approach (e.g. Castro, 1969; Poulos, 1981) provides a useful framework for coarse-grained materials.

Soil shear strength can be determined by laboratory tests. The following formulae have been proposed as first approximations in static conditions, when the soil parameters are within the limits of the variables used in the formulae.

Bjerrum et al. (1961) proposed that the peak frictional angle in static condition  $\phi_1$  in degrees can be expressed as a function of initial sand porosity  $n_s$  (for  $n_s$  range from 36% to 47.5%). According to their results:

$$\phi_1 = 12 + \sqrt{27^2 - \left[ \frac{27}{11.5} \cdot (n_s - 36) \right]^2} \quad (2.5)$$

Peck et al. (1974) proposed a correlation between angle  $\phi_1$  and the standard penetration resistance blow count  $N$ . For the range of  $N$  from 10 to 40, for medium dense to dense sand, their results can be expressed as:

$$\phi_1 = 30 + \frac{10}{35} \cdot (N - 10) \quad (2.6)$$

Kulhawy and Mayne (1990) subsequently suggested to take into account the influence of effective overburden stress  $\sigma'_v$  on angle  $\phi_1$  and proposed the following relationship

$$\phi_1 \approx \arctan \left( \frac{N}{12.2 + 20.3 \cdot \frac{\sigma'_v}{100}} \right)^{0.34} \quad (2.7)$$

where the effective overburden stress  $\sigma'_v$  is in kPa,  $N$  is the blow count from the standard penetration test in blows/foot.

Kenney (1959) plotted the values of  $\sin \phi_1$  versus plasticity index  $PI$  (%) for normally consolidated clay. The results showed some scatter. From that plot it follows that for the average values:

$$\phi_1 = \arcsin \left[ 0.6 - \frac{0.25}{90} \cdot (PI - 10) \right] \quad (2.8)$$

Skempton (1957) suggested a correlation between the undrained shear strength for normally consolidated natural clay and the overburden pressure in one cycle as:

$$\frac{c_{u1}}{\sigma'_v} = 0.11 + 0.0037 \cdot PI \quad (2.9)$$

where  $c_{u1}$  is undrained cohesion in one cycle,  $\sigma'_v$  is effective overburden pressure,  $PI$  is soil plasticity index in percents.

Ladd and Foot (1974), among others, found that the undrained shear strength of over consolidated clay in one cycle is approximately proportional to:

$$\frac{c_{u1}}{\sigma'_v} \cdot OCR^{0.8} \quad (2.10)$$

where the ratio  $c_{u1} \sigma_v^{-1}$  is given in Equation (2.9),  $OCR$  is soil over consolidation ratio (between previous effective overburden pressure and existing overburden pressure). Apparent  $OCR$  can be caused by soil cementation and desiccation.

## 2.4 Cyclic Shear Strengths of Soils

Soil shear strength in cyclic condition depends also on number of cycles, cyclic stress or strain amplitude and for fine grained soil on frequency due to the rate effect.

The cyclic strength should ideally be determined using bi-direction simple shear tests (e.g. Ishihara and Nagase, 1985) because ground motion caused by earthquakes is three dimensional instead of one-dimensional. For example, when one-directional horizontal component of ground motion, which time history is shown in Fig. 2.9, is combined with corresponding perpendicular one-directional horizontal component of the ground motion, the resulting is bi-directional motion in the horizontal plane as shown in Fig. 2.3. Multi-directional motion causes greater deformation and greater loads on soil than one-dimensional motion.

Seed and Lee (1965) showed for medium dense sand, Lee and Focht (1976) showed for clay and Boulanger and Idriss (2007) for silt and clay that the soil shear strength in cyclic condition decreases to about a half of undrained cohesion/friction angle for a static condition. Figure 2.4 indicates the upper and lower boundaries for clay and the ratios for other soil types according to the reported results by various authors.

Consistently with the critical and steady state approaches mentioned earlier, loose saturated sandy soil can completely lose its shear strength in cyclic condition and liquefy when dissipation of built up excess pore water pressure is prevented. Dense sand and stiff clay tends to expand on shearing and build up a negative

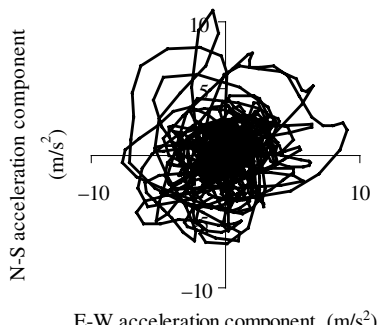


**Fig. 2.3** Ground acceleration projection in horizontal plane

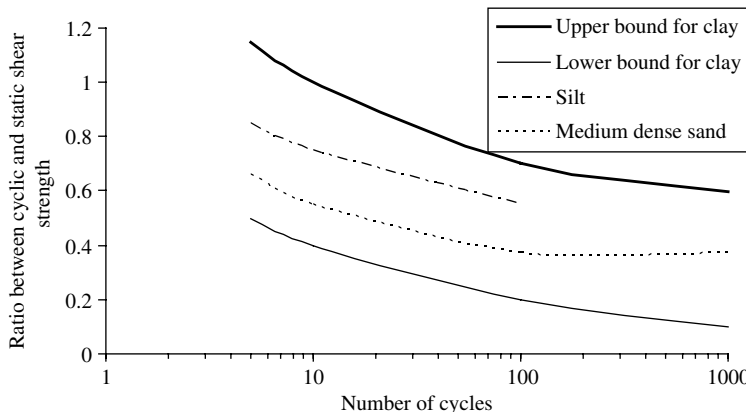


**Fig. 2.4** Soil shear strength decrease with number of cycles from test data

pore water pressure at the beginning of cycling with apparent increase of its shear strength. Fine soil exhibits also rate of shear effect and an increase of soil shear strength with relation to the strength in static condition.

Parathiras (1995), among others, tested London clay, with plasticity index  $PI = 49\%$  and clay content of  $60\%$ , and Cowden till, with plasticity index  $PI = 21\%$  and clay content of  $31\%$ , in a ring shear apparatus. Parathiras (1995) reported an increase of the residual friction angle of  $6^\circ$  at  $50$  kPa compressive stress and  $3.5^\circ$  at  $400$  kPa compressive stress for both soil when the rate of displacement increased from  $0.2$  to  $1.5$  cm/s. The increase of the residual friction angle at  $50$  kPa stress was  $48.4\%$  for London clay and  $15.2\%$  for Cowden till while at  $400$  kPa stress was  $62.5\%$  for London clay and  $10.5\%$  for Cowden till.

Hungr and Morgenstern (1984) found slight rate of shear dependence of shear strength of sand. However, loose to medium dense sand tends to develop positive excess pore water pressure with an increase of number of cycles.

Srbulov (2005a) used a simple model described in Section 5.3 with data from Moss (2003), for the cases when soil liquefaction did not occur, and from Olson (2001), for the cases when soil liquefaction occurred, to back calculate the friction angles of sandy soil in cyclic condition as shown in Fig. 2.5. One standard deviation from the average value shown in Fig. 2.5 is  $1.6^\circ$ ,  $r_c$  is the correlation coefficient of the linear least square regression used. The value of  $(N_1)_{60}$  is defined in equation (5.2).

Soil shear strength in cyclic condition can be written as  $(1 - r_u)\sigma' \tan \phi_1$ , where cyclic excess pore water pressure ratio  $r_u = \Delta u / \sigma'^{-1}$ ,  $\Delta u$  is cyclic excess pore water pressure,  $\sigma'$  is axial effective stress,  $\phi_1$  according to Equation (2.6) is independent of  $\sigma'$ . Increase in cyclic excess pore water pressure occurs on loading of loose soil (which volume tends to decrease because of the existence of large amount of pores not filled with grains) when drainage of excess pore water pressure is slow or prevented in cyclic condition. As soil shear strength in cyclic condition is proportional to  $\sigma' \tan \phi$  then the increase in  $r_u$  in cyclic condition is calculated from the following formula.

$$r_u = 1 - \frac{\tan \phi}{\tan \phi_1} \quad (2.11)$$

where  $\phi$  is according to Fig. 2.5. The results are shown in Fig. 2.6.

For stress-controlled cyclic tests with uniform loading, Lee and Albaisa (1974) and De Alba et al. (1975) found that the pore water pressure ratio  $r_u$  is related to the number of loading cycles  $N_c$  as:

$$r_u = \frac{1}{2} + \frac{1}{\pi} \cdot \arcsin \left[ 2 \left( \frac{N_c}{N_L} \right)^{1/\alpha} - 1 \right] \quad (2.12)$$

where  $r_u$  is the ratio between excess pore water pressure and the effective confining stress  $\sigma'_3$ ,  $N_L$  is the number of cycles required to produce  $r_u = 1$  and  $\alpha$  is a function of the soil properties and test conditions. The functional relationship given in Equation (2.12) is shown in Fig. 2.7.

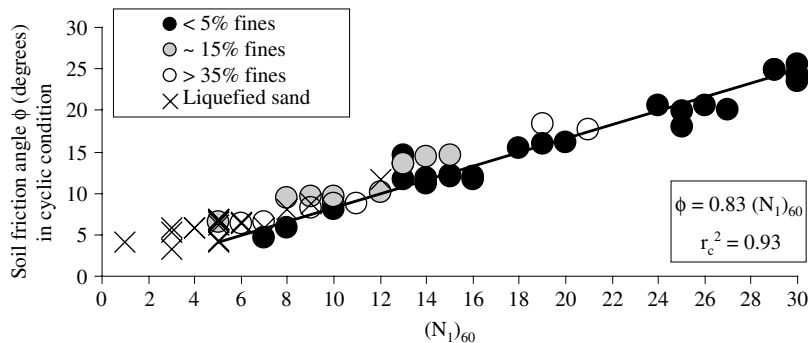


**Fig. 2.5** Correlation between soil friction angles in cyclic condition and the normalized number of blow counts in the standard penetration tests from the 43 case histories (*circles*) with no liquefaction observed compiled by Moss (2003) using the simple model described in Section 5.3. The crosses are for the 19 case histories with observed liquefaction compiled by Olson (2001) (Srbulov, 2005a, by permission of Patron Editore)

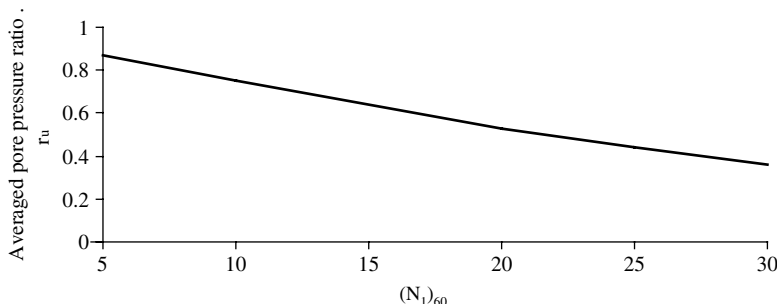


**Fig. 2.6** Average excess pore pressure ratio based on the simple model described in Section 5.3

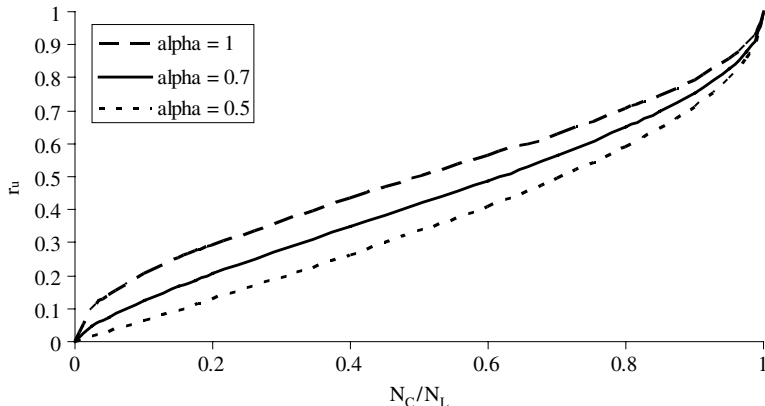


Fig. 2.7 Rate of excess pore pressure generation in cyclic tests ( $\alpha = \alpha$  in equation 2.12)

## 2.5 The Equivalent Number of Cycles Concept

The duration of strong ground motion can have a strong influence on earthquake damage, due partly to a degradation of stiffness and strength of some structures and of some soil, and to a build-up of excess pore pressure in loose and saturated sandy soil. There are different definitions of the duration of strong ground motion:

- Bolt (1969) proposed bracketed duration, which is defined as the time between the first and last exceedance of threshold acceleration (usually 0.05 of the gravitational acceleration).
- Trifunac and Brady's (1975) definition of duration is based on the time interval at which 5% and 95% of the total energy has been recorded.

Many other definitions of duration exist (e.g. Kramer, 1996; Hancock and Bommer, 2004). Bracketed duration is most easy to use because it is based directly on the properties of acceleration records. Duration has also been expressed in terms of equivalent cycles of ground motion.

Seed et al. (1975) developed the concept of an equivalent number of significant stress cycles to represent an irregular time history of shear stresses (caused by the horizontal ground accelerations) by a uniform series of harmonic stress cycles. The equivalent number of uniform stress cycles  $N_{eqv}$  was selected to cause pore pressure build-up equivalent to that of an actual shear stress time history at harmonic stress amplitude of 65% of the maximum actual shear stress (caused by the peak horizontal ground acceleration). Seed et al. (1975) data can be approximated by a simple formula.

$$N_{eqv} = 0.0008 \cdot M_L^{4.88} \quad (2.13)$$

where  $M_L$  is local earthquake magnitude, which is defined in Section 3.2.1.

Green and Terri (2005) examined the implications of using a high cycle fatigue hypothesis to compute the number of equivalent cycles for evaluating liquefaction

by Seed et al. (1975) based on Palmgren – Miner cumulative damage hypothesis developed for metal fatigue evaluations in the elastic range of material behavior. The results of a parametric study using a procedure that equates energy dissipated in soil subjected to earthquake motions show that the number of equivalent cycles varies as a function of earthquake magnitude, site-to-source distance and depth below ground level.

Hancock and Bommer (2004) reviewed, classified and compared various definitions of the effective number of cycle's concept. They found that measurement and hence predictions are particularly different for accelerograms with broad banded frequency content, which contain a significant number of non-zero crossing peaks. While the number of effective cycles depend on earthquake magnitude, its dependence on fault distance is small, approximately one cycle in 30 km. Fault rupture directivity effect (which is described in Section 3.3.1) has an important influence on the number of cycles in near-field ground motions. Based on data by Hancock and Bommer (2004), the number of effective acceleration cycles  $N_{cycles}$  can be expressed as:

$$N_{cycles} = 3 + \frac{7}{4} \cdot (M_W - 4) \pm (M_W - 3), \quad M_W > 4 \quad (2.14)$$

where  $M_W$  is earthquake moment magnitude, which is described in Section 3.2.1. Sarma and Srbulov (1998) obtained similar results to Hancock and Bommer (2004). The number of equivalent cycles in Equation (2.13) represents the upper bound values.

Final parameter of an equivalent harmonic motion is its period  $T$ . The predominant periods of actual ground acceleration, velocity and displacement are different, as shown in the following example, but the periods of an equivalent harmonic motion are the same. For a simple harmonic motion of period  $T$ , the ratio between the peak velocity and acceleration is  $T(2\pi)^{-1}$ .

$$\begin{aligned} Displacement &= A_g \cdot \sin\left(\frac{2\pi}{T} \cdot t\right) \\ Velocity &= A_g \cdot \frac{2 \cdot \pi}{T} \cdot \cos\left(\frac{2 \cdot \pi}{T} \cdot t\right) \\ Acceleration &= -A_g \cdot \frac{4 \cdot \pi^2}{T^2} \cdot \sin\left(\frac{2 \cdot \pi}{T} \cdot t\right) \end{aligned} \quad (2.15)$$

where  $A_g$  is amplitude of ground displacement and  $t$  is time. Using Fourier series, a periodic function such as time history of ground motion can be described as:

$$c_o + \sum_{n=1}^{\infty} c_n \cdot \sin(\omega_n + \phi_n) \quad (2.16)$$

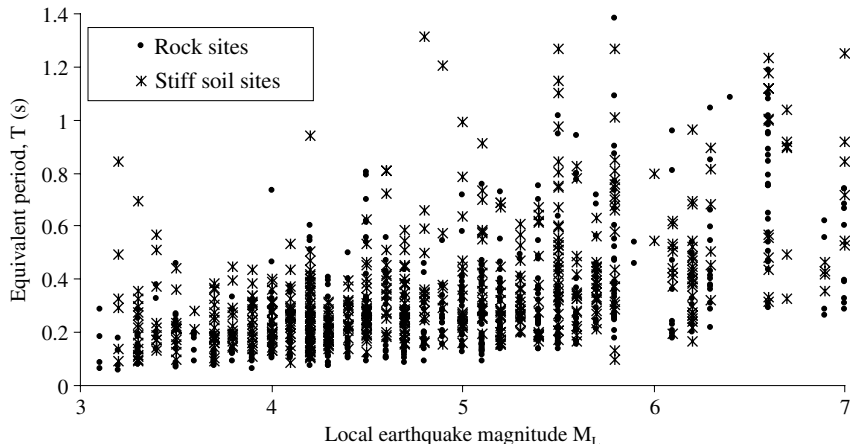


**Fig. 2.8** Dependence of the equivalent period on local earthquake magnitude  $M_L$

where  $c_n$  and  $\phi_n$  are the amplitude and phase angle respectively of the  $n^{\text{th}}$  harmonic of the Fourier series. The Fourier series provides a complete description of the ground motion only for an infinite number of members of the series.

Seed and Idriss (1982) suggested representative average values of the peak velocity to acceleration ratios for different site conditions less than 50 km from the source. These ratios can be interpreted as the periods of equivalent harmonic waves for the rock, stiff soil, and deep stiff soil site conditions of 0.35 s, 0.70 s and 0.87 s respectively. However, ground motion exhibits a significant variation from the average values as shown in Fig. 2.8 from Srbulov (2004).

### 2.5.1 An Example of Equivalent Harmonic Time Histories

Figure 2.9 shows that the predominant periods from the elastic response spectra of the ground acceleration is 0.2 s, of the ground velocity 4.8 s, and of the ground displacement 5.5 s. Comparisons between the actual ground motion time histories and the equivalent harmonic time histories are shown in Fig. 2.10 based on  $N_{\text{eqv}} = 15$  from Equation (2.13) for magnitude 7.5 and  $T_{\text{eqv}} = 0.87$  s from Seed and Idriss (1982) for deep stiff soil. The period of an equivalent harmonic motion calculated from the ratio between the actual peak velocity and acceleration is 0.60 s and from the ratio between the actual peak displacement and velocity is 0.76 s.

A further estimate of the peak horizontal velocity to acceleration ratio of rock and soft soil is shown in Fig. 3.6. Alternatively, the period  $T_{\text{eqv}}$  of an equivalent harmonic motion can be calculated from Equation (2.15)

$$\frac{4 \cdot \pi^2}{T_{\text{eqv}}^2} \cdot A_g = 0.65 \cdot \text{Peak ground acceleration} \quad (2.17)$$

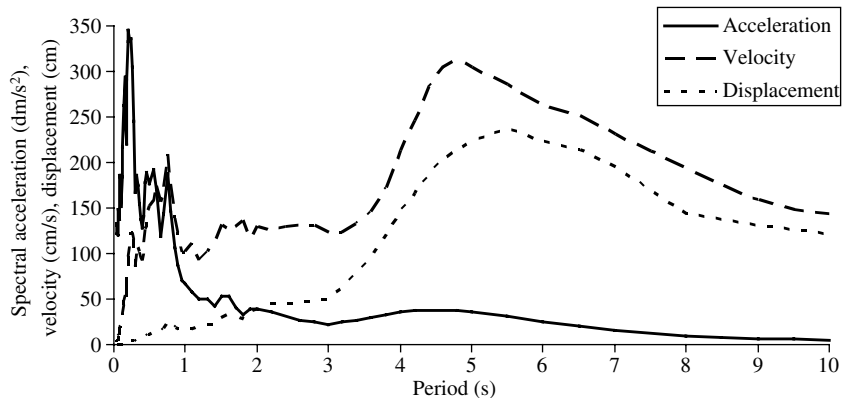


**Fig. 2.9** Elastic response spectra of acceleration, velocity and displacement for 5% of the critical damping in the example

where  $A_g$  is the amplitude of ground displacement. In this example,  $T_{\text{eqv}} = 2.29$  s. From Fig. 2.10 it follows that the velocity and displacement amplitudes can not be similar to the actual values simultaneously if a single harmonic motion is considered.

This analysis demonstrates that the choice of the equivalent period is dependent on the problem at hand, i.e. if equivalent harmonic velocity or displacement is more important.

## 2.6 Water Permeability and Volumetric Compressibility

Soil coefficient of water permeability, defined as the quantity of flow through unit area of soil under a unit pressure gradient, and volumetric compressibility have a major influence on dissipation and generation of excess pore water pressure during earthquakes respectively.

Soil permeability of water depends on many factors of which soil grain sizes (fine or coarse), soil porosity and degree of saturation are the most influential ones. Fine grained soil, of low porosity and partially saturated has smaller permeability to water than coarse, porous and fully saturated soil (e.g. Das, 1985).

Water permeability can be determined by field water pumping tests performed in boreholes to avoid problems with samples disturbance, size and orientation. Field permeability tests are standardized (e.g. ASTM 6391, BS 5930). Their primary advantages are that the soil is not disturbed, and that the field tests can also provide information to validate inferences about soil layering. However, they have several disadvantages. They generally measure horizontal permeability, which can be several times larger than the vertical permeability values that may be directly relevant to seismic post-seismic analysis. Also, they provide permeability at ambient confining stress and not increased stresses during strong ground motion (although water

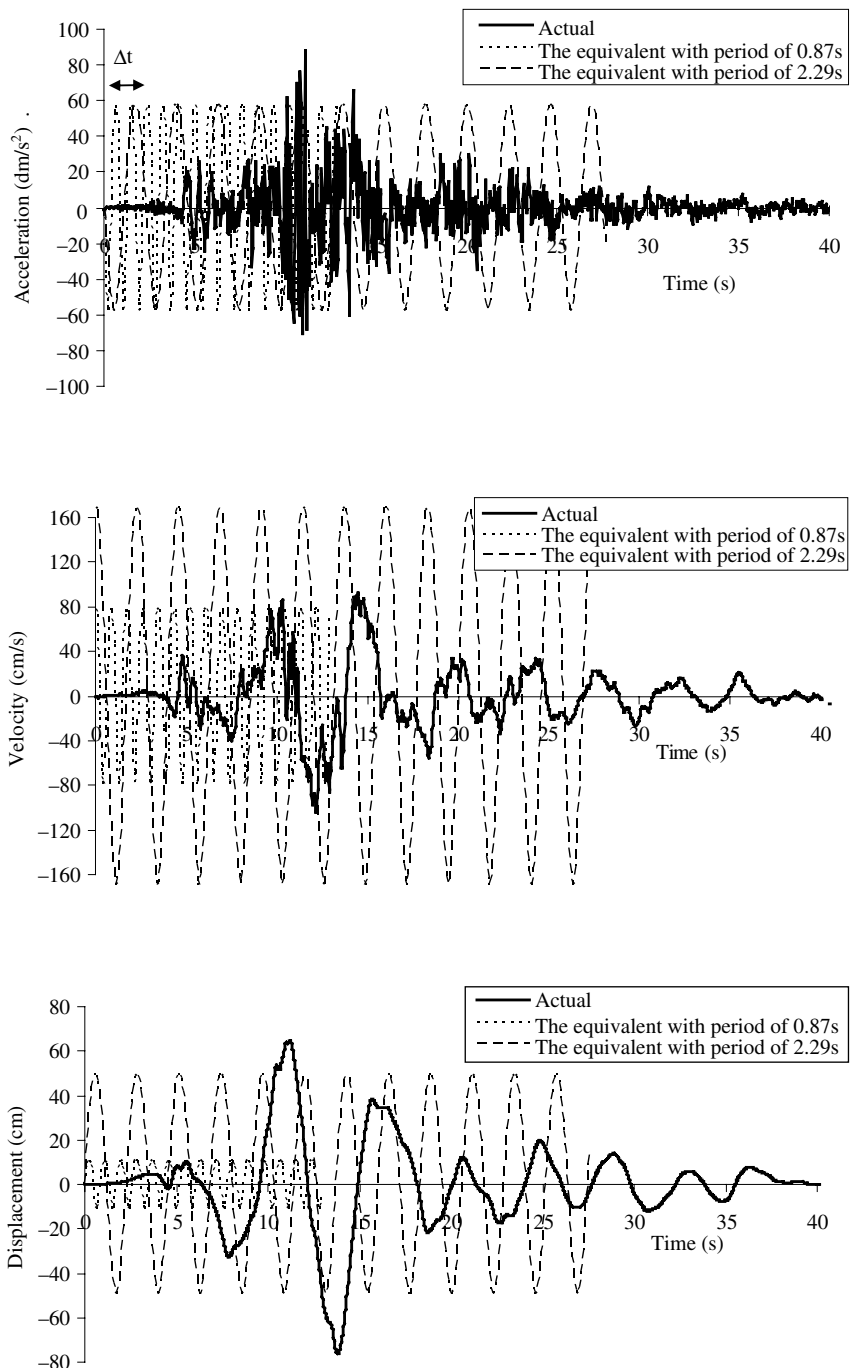


Fig. 2.10 A comparison between an actual and the equivalent harmonic ground motions

pumping from borehole causes a decrease of ground water level and an increase of in-situ effective stress). Another difficulty in field testing is that a smear zone formed along borehole wall may affect the test results unless wash boring or bore-hole washing is performed. Additional problem could appear in layered fine and coarse grained soil if fine grains suspended in water within a borehole move towards more permeable coarser grained soil and form so called filter cake, which apparently decreases permeability of coarser grained soil.

Volumetric compressibility of soil is traditionally determined using field tests in coarse-grained soil and oedometer tests on small specimens of fine-grained soil. However, it has been recognized that laboratory tests overestimate soil compressibility at small strain with the exception in soft clay and loose sand (e.g. Jardine et al., 1985; Burland 1989; Tatsuoka et al. 1997). Therefore, it is recommended to determine soil volume compressibility based on back analyses of data obtained from prototype structures, if possible. If this is not possible then triaxial tests with local measurements of strain on soil specimens can improve assessment of soil volumetric compressibility over a wide range of strain. Such tests are not standardized and are performed by specialist soil testing laboratories (e.g. Jardine et al., 1985; Burland 1989; Tatsuoka et al. 1997).

## 2.7 Summary

Soil properties required for the simplified analyses include:

- Soil density or unit weight
- Shear stiffness and material damping (energy dissipation) of soil during cyclic loading. These properties are influenced mainly by amplitude of shear strain, effective confining pressure and plasticity index. Because of dependence of soil stiffness and damping on strain amplitude and strain amplitude dependence on soil stiffness and damping, simplified estimates of shear stiffness and soil damping dependence on peak ground acceleration are provided in Table 2.2.
- Shear strength of soil and excess pore water pressure generation in cyclic condition. These properties are mainly depended on soil type, number of cycles, cyclic amplitude and soil density/stiffness. If the results of cyclic tests on soil samples are not available then, as a first estimation, soil shear strength in cyclic condition may be assumed to be equal to a half of soil shear strength in static condition.
- Soil water permeability and volumetric compressibility have a major influence on dissipation and generation of excess pore water pressure respectively. These soil properties can be determined using field tests and back analyses of case histories.
- Equivalent harmonic cycles concept greatly simplifies analysis of complex ground motion during earthquakes. The amplitude and frequency of an equivalent harmonic ground motion can be related to the peak values of actual ground acceleration, velocity and displacement.

# **Chapter 3**

## **Seismic Excitation**

### **3.1 Introduction**

Ground motion caused by earthquakes is chaotic (e.g. Goltz, 1998), i.e. unpredictable and unrepeatable. It is possible to estimate boundaries within which the ground motion parameters are expected to occur. Analyses performed using sophisticated methods with various input parameters can be expensive and time consuming. Therefore, simplified methods can be more suitable for parametric studies. A postulated greater accuracy of sophisticated methods is not an advantage if the input parameters can be determined only approximately.

The objective of this chapter is to describe ground motion parameters used in simplified analyses, to provide a basis for their selection or checking, and to discuss some aspects of complexity and the risks involved.

### **3.2 Seismic Hazard**

Seismic hazard is considered to be severity and repeatability of ground shaking at a location causing inertial forces, ground deformation and failure, soil liquefaction, Earth's surface rupture and tsunami. While the inertial forces always occur, tsunamis are relatively rare. This section looks at the most important factors affecting seismic hazard at a location, which are:

- earthquake magnitude
- the source-to-site distance
- earthquake rate of occurrence (return period)
- duration of ground shaking (Section 2.5)

Other factors are mentioned in Section 3.3. Because of the complexity of the problem, an integrated approach is preferable using all available data and comparisons between results of different procedures.

### 3.2.1 Types of Earthquake Magnitudes

Earthquake magnitude is a measure of tectonic energy released at the source. A part of this energy radiated to Earth's surface can cause serious damage/destruction of structures depending on earthquake magnitude and, therefore, earthquake magnitude is the first parameter of strong ground motion to consider. Different earthquake magnitudes are used. The most frequent are:

- Local magnitude  $M_L$  is defined as the logarithm of the maximum trace amplitude (in micrometers) recorded on a Wood-Anderson seismometer located 100 km from the epicentre of the earthquake. This magnitude scale becomes insensitive to the actual size of an earthquake for magnitudes of 6.8 or greater, and hence is not useful for very strong earthquakes (Idriss, 1985).
- Body wave magnitude  $m_b$  (Gutenberg, 1945) is based on the longitudinal wave amplitude (in micrometers) and their period (usually about one second). This magnitude scale becomes insensitive to the actual size of an earthquake for magnitudes of 6.4 or greater, and hence is not useful for very strong earthquakes (Idriss, 1985).
- Surface wave magnitude  $M_s$  (Gutenberg and Richter, 1936) is based on the amplitude of maximum ground displacement (in micrometers) caused by Rayleigh (near surface) waves with a period of about 20 seconds and the epicentral distance of the seismometer measured in degrees. This magnitude scale becomes insensitive to the actual size of an earthquake for magnitudes of 8.4 or greater, and hence is not useful for very strong earthquakes (Idriss, 1985). Gutenberg and Richter (1956) estimated the relationship between the total seismic energy released during an earthquake and the magnitude  $M_s$  as:

$$\log_{10} E_o = 4.8 + 1.5 \cdot M_s \quad (3.1)$$

where energy  $E_o$  is expressed in joules.

- Moment magnitude  $M_w$  (Hans and Kanamori, 1979) is based on the seismic moment  $M_o$  (in Nm). This magnitude does not have an upper limit.

$$\begin{aligned} M_w &= \frac{2}{3} \cdot \log_{10}(M_o) - 6.1 \\ M_o &= L_f \cdot W_f \cdot S_f \cdot \mu \end{aligned} \quad (3.2)$$

where  $L_f$  and  $W_f$  are the length and width of a fault area,  $S_f$  is the average slip on the fault during an earthquake in meters (which is typically about  $5 \times 10^{-5} L_f$  for intraplate earthquakes, Scholz et al., 1986),  $\mu$  is shear modulus of the Earth's crust (which is usually taken as  $3.3 \times 10^{10}$  N/m<sup>2</sup>).

Present practice appears to be moving towards the use of moment magnitude in preference to other magnitudes. Many earthquake magnitudes are defined using different magnitude scales and, therefore, a conversion between magnitudes is applied (e.g. Idriss, 1985). The conversion relationships are usually specified when different

magnitude scales are used. Ambraseys (1990) derived the following relationships between various common earthquake magnitude scales:

$$\begin{aligned} 0.77 \cdot m_b - 0.64 \cdot M_L &= 0.73 \\ 0.86 \cdot m_b - 0.49 \cdot M_s &= 1.94 \\ 0.80 \cdot M_L - 0.60 \cdot M_s &= 1.04 \end{aligned} \quad (3.3)$$

Chen and Chen (1989) provided the following relationships between  $\log_{10}(M_o)$  and  $M_s$ .

$$\begin{aligned} \log_{10}(M_o) &= M_s + 12.2 \quad \text{for } M_s \leq 6.4 \\ \log_{10}(M_o) &= 1.5 \cdot M_s + 9.0 \quad \text{for } 6.4 < M_s \leq 7.8 \\ \log_{10}(M_o) &= 3.0 \cdot M_s - 2.7 \quad \text{for } 7.8 < M_s \leq 8.5 \end{aligned} \quad (3.4)$$

When  $\log_{10}(M_o)$  is replaced from Equation (3.2) into Equation (3.4), it is possible to obtain the correlation between  $M_w$  and  $M_s$  magnitudes.

### 3.2.2 Types of Source-to-Site Distances

Only a part of tectonic energy released at the source arrives at Earth's surface depending on the source-to-site distance. This distance is the second parameter of ground motion to consider. Several definitions of the source to site distance exist, the most frequently used being:

- Epicentral distance between the site and the Earth's surface projection of the hypocentre of an earthquake, shown in Fig. 1.1.
- Closest distance to the vertical projection of a fault plane on the Earth's surface (Joyner and Boore, 1981a,b).
- Closest distance to the fault rupture (Campbell, 1981) or the closest distance to the “zone of seismogenic rupture” (Campbell, 1997).

Case study results, discussed in Chapter 1 and shown in Fig. 1.3, indicate that the use of epicentral distance is not always appropriate as it may not indicate correctly the source energy dissipation with radiation damping. Epicentral distance is used mainly for earthquakes with their magnitude smaller than 5, for distant earthquakes, and when other distances are not known.

### 3.2.3 Types of Earthquake Recurrence Rates

Frequency of earthquakes recurrence is important because frequent earthquakes are likely to cause more cumulative damage than the same size rare earthquakes, which usually occur within interiors of tectonic plates (i.e. within the continents). Different earthquake rates of occurrence are proposed but most frequently referred are:

- Poisson process in which earthquakes occurs randomly, with no regard to the time, size or location of any preceding event. This model does not account for time clustering of earthquakes and may be appropriate only for large areas containing many tectonic faults. The probability of at least one exceedance of a particular earthquake magnitude in a period of  $t$  years  $P[N \geq 1]$  is given by the expression:

$$P[N \geq 1] = 1 - e^{-\lambda \cdot t} \quad (3.5)$$

where  $\lambda$  is the average rate of occurrence of the event with considered earthquake magnitude. Cornell and Winterstein (1986) have shown that the Poisson model should not be used when the seismic hazard is dominated by a single source for which the return period is greater than the average return period and when the source displays strong characteristic-time behavior.

- Time predictable, which specifies a distribution of the time to the next earthquake that depends on the magnitude of the most recent earthquake (e.g. Scholz, 1990).
- Slip predictable, which considers the distribution of earthquake magnitude to depend on the time since the most recent earthquake (e.g. Scholz, 1990).

Earthquake recurrence rate models are only approximate. For example, the Park-field earthquakes in California along the San Andreas Fault were of about magnitude  $M_w = 6.0$  and happened in 1857, 1881, 1901, 1922, 1934, 1966 and 2004 (e.g. <http://earthquake.usgs.gov/research/parkfield/index.php>) with time intervals of 24, 20, 21, 12, 32 and 38 years. These earthquakes were neither time predictable nor size variable depending on the time since the most recent earthquake. Different earthquake recurrence rates, and the chaotic nature of earthquakes, are discussed by Scholz (1990).

### ***3.2.4 Representations of Seismic Hazard***

Seismic hazard can be represented in different ways but most frequently in terms of values or probability distributions of accelerations, velocities, or displacements of either bedrock or the ground surface:

- The peak ground acceleration, ground acceleration time history or response spectral acceleration are useful because the product of a mass and the acting acceleration equals the magnitude of inertial force acting on the mass. However, peak acceleration occurs in high frequency pulses at infrequent intervals during the time history of ground vibration, and thus contains only a small fraction of the emitted seismic energy. For this reason peak acceleration is not suitable as a single measure of ground motion representation (e.g. Sarma and Srbulov, 1998).
- The peak ground velocity, ground velocity time history or response spectral velocity are useful because the product of square of velocity and a half of mass

equals the amount of kinetic energy of the mass. Ground motions of smaller amplitude but longer duration frequently results in larger ground velocity and more severe destruction capability of ground shaking (e.g. Ambraseys and Srbulov, 1994).

- The peak ground displacement, ground displacement time history or response spectral displacement of a structure are useful since damage of structures subjected to earthquakes is certainly expressed in deformations (e.g. Bommer and Elnashai, 1999).

Ground acceleration, velocity and displacement are related among them because integration or differentiation in time of one of them produces another.

Time histories of ground motions are often used in practice for non-linear analyses when damage caused by ground shaking can accumulate in time. Single peak values are poor indicators of earthquake destructiveness, so time histories of ground motion are usually considered for important, large, expensive and unusual structures and ground conditions. Response spectral values are a compromise between the singular values and a complete ground motion definition in time. Some of the sources of the peak values of ground motion, of the time histories and of the response spectra are described in Section 3.2.5.

### 3.2.4.1 Comments on Attenuation Relationships

Peak ground motion for a given location is traditionally assessed based on empirical attenuation relationships derived by least square regression from peak values of ground motion recorded at nearby sites. Attenuation relationships are then used to determine the consequential motions at the location of interest. The main cause of attenuation is radiation damping i.e. spread of seismic waves as they propagate through Earth's interior. A secondary cause of ground attenuation is material damping i.e. transfer of wave energy into heat by ground particle friction caused by wave movement. Equation (1.2) is used in the derivation of almost all attenuation relationships that assume a point source model.

The attenuation relationships define dependence of the peak or spectral ground motion parameter on earthquake magnitude and the site-to-source distance. Recent attenuation relationships may include also consideration of soil type at a site and type of causative tectonic fault. Attenuation relationships usually provide not only average peak or spectral values but also standard deviation from the average values i.e. likely scatter of individual data, which can be quite considerable.

A large number of the attenuation relationships exists because they are derived based on limited data bases and/or they consider only a limited number of factors affecting ground motion. Douglas (2004, 2006), for example, provided a summary of the relationships for peak ground acceleration and spectral ordinates. Examples of some recent attenuation relationships are as follows.

### 3.2.4.2 Examples of the Peak Horizontal Ground Acceleration Attenuation Relationships

Ambraseys et al. (2005a) proposed the following relation between the peak horizontal ground acceleration  $a_{ph}$  in  $\text{m/s}^2$ , the earthquake moment magnitude  $M_w$ , and the minimal distance  $d$  from the location of interest to the surface projection of a fault (or epicentral distance where the location of the causative fault has not been reported):

$$\begin{aligned}\log_{10}(a_{p,h}) = & 2.522 - 0.142 \cdot M_w + (-3.184 + 0.314 \cdot M_w) \cdot \log_{10} \sqrt{d^2 + 7.62} \\ & + 0.137 \cdot S_S + 0.05 \cdot S_A - 0.084 \cdot F_N + 0.062 \cdot F_T - 0.044 \cdot F_O\end{aligned}\quad (3.6)$$

where  $S_S=1$  for soft soil sites (with the transversal wave velocity range between 180 and 360 m/s to a depth of 30 m) and 0 otherwise,  $S_A=1$  for stiff soil sites (with the transversal wave velocity range between 360 and 750 m/s to a depth of 30 m) and 0 otherwise,  $F_N=1$  for normal and strike-slip faulting earthquakes and 0 otherwise,  $F_T=1$  for reverse (thrust) faulting earthquakes and 0 otherwise,  $F_O=1$  for unspecified faulting earthquakes and 0 otherwise. Fault types are described in Section 3.2.1.

Ambraseys et al. (2005a) reported that the intra-earthquake (a single event) standard deviation for the above equation, indicating the statistical scatter, is 0.665–0.065  $M_w$ , and that the inter-earthquake (multiple events) standard deviation is 0.222–0.022  $M_w$ . Standard deviation is used as a measure of data spread from the average value. For Gauss (normal) distribution of data samples, 84% of data are contained within average plus one standard deviation range and 98% percent of data are contained within average plus two standard deviation range. Based on Equation (3.6), the average peak horizontal accelerations of rock and soft soil from unspecified faulting earthquakes are shown in Fig. 3.1.

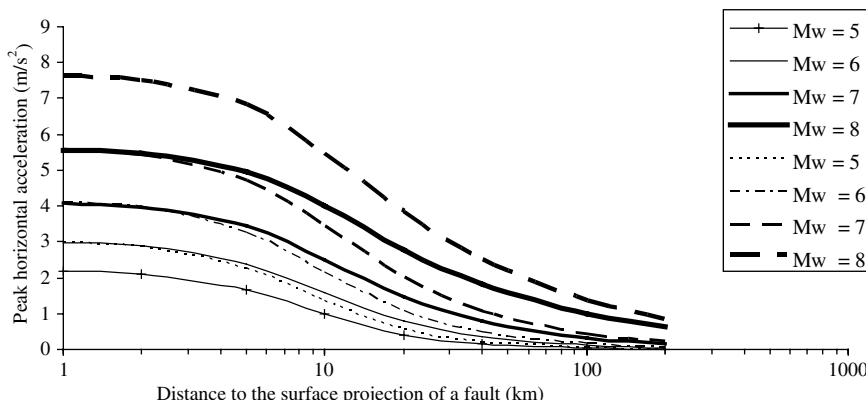


**Fig. 3.1** The average peak horizontal accelerations of rock (continuous lines) and soft soil sites (dashed lines) from unspecified faulting according to Equation (3.6)

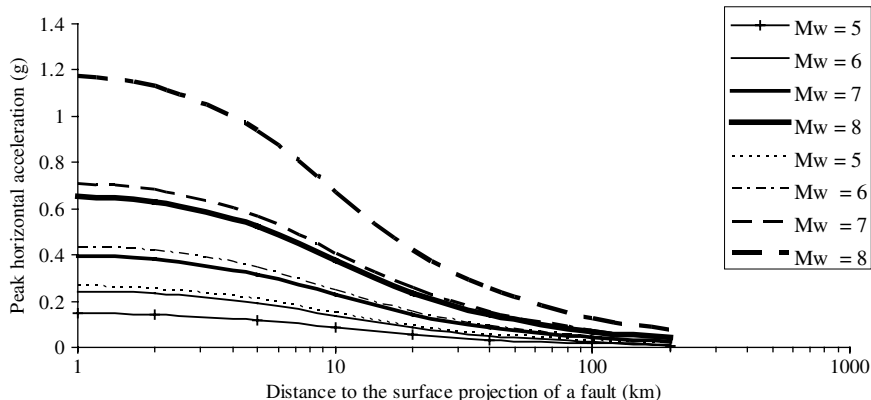


**Fig. 3.2** The average peak horizontal accelerations of rock (*continuous lines*) and soft soil sites (*dashed lines*) according to Equation (3.7)

For western North America, Boore et al. (1997) proposed Equation (3.7) for the horizontal component with largest peak acceleration:

$$\log_{10}\left(\frac{a_{p,h}}{g}\right) = -0.038 + 0.216 \cdot (M_w - 6) - 0.777 \cdot \log_{10} \sqrt{d^2 + 5.48^2} + 0.158 \cdot G_b + 0.254 \cdot G_c \quad (3.7)$$

where  $M_w$  is moment magnitude,  $d$  is the minimal distance to the surface projection of the fault or epicentral distance where the location of the causative fault has not been reported, the standard deviation is 0.23,  $G_b = 1$  for the average transversal wave velocity range  $360 < v_t < 750$  m/s to 30 m depth and 0 otherwise,  $G_c = 1$  for the average transversal wave velocity range  $180 < v_t < 360$  m/s to 30 m depth and 0 otherwise. The average peak horizontal accelerations of rock and soft soil are shown in Fig. 3.2.

Differences in the attenuation relationships described by Equations (3.6) and (3.7) and shown in Figs. 3.1 and 3.2 are caused by different data sets used, particularly in the near field zone of a few kilometers from the source.

Empirical attenuation relationships have not been developed to predict the effect of seismic wave bounce from the Moho surface (i.e. the Earth's crust and mantle boundary). The effect tends to occur from larger magnitude earthquakes at the site-to-source distance range from about 60 to 120 km and can produce motions across all site conditions as high as one standard deviation above the average value (Stewart et al., 2001).

### 3.2.4.3 An Example of the Peak Vertical Ground Acceleration Attenuation Relationship

Ambraseys et al. (2005b) proposed the following relation between the peak vertical ground acceleration  $a_{pv}$  in  $\text{m/s}^2$ , the earthquake moment magnitude  $M_w$ , and the

minimal distance  $d$  from the location of interest to the surface projection of the fault (or epicentral distance where the location of the causative fault has not been reported):

$$\begin{aligned} \log_{10}(a_{p,v}) = & 0.835 + 0.083 \cdot M_w + (-2.489 + 0.206 \cdot M_w) \cdot \log_{10} \sqrt{d^2 + 5.6^2} \\ & + 0.078 \cdot S_S + 0.046 \cdot S_A - 0.126 \cdot F_N + 0.005 \cdot F_T - 0.082 \cdot F_O \end{aligned} \quad (3.8)$$

where  $S_S=1$  for soft soil sites (with the transversal wave velocity range between 180 and 360 m/s to a depth of 30 m) and 0 otherwise,  $S_A=1$  for stiff soil sites (with the transversal wave velocity range between 360 and 750 m/s to a depth of 30 m) and 0 otherwise,  $F_N=1$  for normal and strike-slip faulting earthquakes and 0 otherwise,  $F_T=1$  for reverse (thrust) faulting earthquakes and 0 otherwise,  $F_O=1$  for unspecified faulting earthquakes and 0 otherwise. Fault types are described in Section 3.3.1.

The intra-earthquake (a single event) standard deviation for the above equation (i.e. the scatter of data at different locations from a single earthquake source) was reported as 0.262. The inter-earthquake (multiple events) standard deviation (i.e. the scatter of data from different earthquake sources) was 0.100. The average peak vertical accelerations of rock and soft soil from unspecified faulting earthquakes are shown in Fig. 3.3.

Different vertical and horizontal peak accelerations are caused by different longitudinal and transversal ground waves respectively.

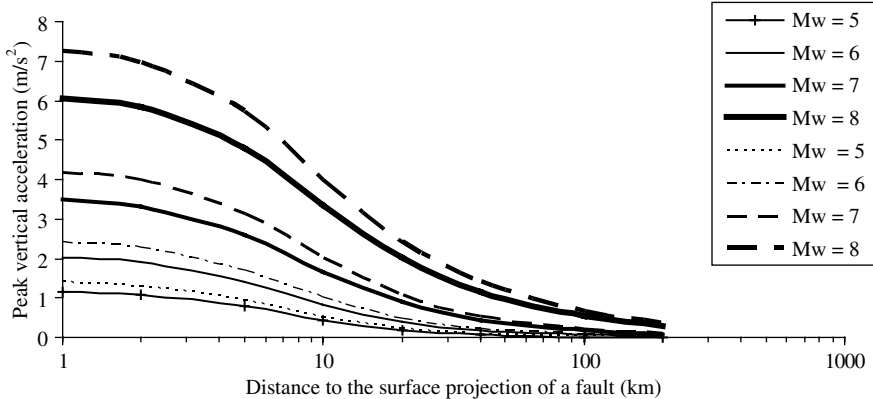


**Fig. 3.3** The average peak vertical accelerations of rock (*continuous lines*) and soft soil sites (*dashed lines*) from unspecified faulting

### 3.2.4.4 An Example of the Peak Vertical to Horizontal Ground Acceleration Ratio Attenuation Relationship

Sometimes, only horizontal ground acceleration is specified and the vertical component is taken as a part of the horizontal component. In this case, it is useful to know the peak vertical to horizontal ground acceleration ratio. The ratio between the peak

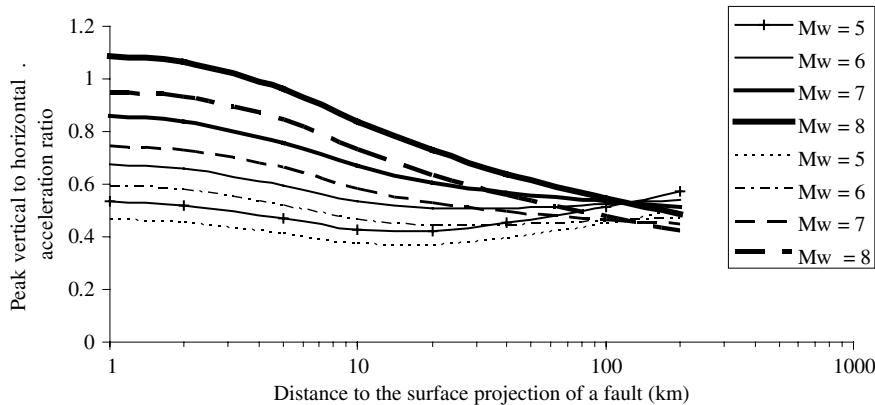


**Fig. 3.4** The average peak vertical to horizontal acceleration ratio for rock (*continuous lines*) and soft soil sites (*dashed lines*) from unspecified faulting

vertical and horizontal acceleration, from Equations (3.8) and (3.6), for rock and soft soil from unspecified faulting earthquakes is shown in Fig. 3.4.

While the peak vertical acceleration is about  $2/3$  to  $1/2$  of the peak horizontal acceleration in the far field from the source, as assumed previously in designs and older seismic codes, it is evident from Fig. 3.4 that it can be the same or even slightly greater than the horizontal peak acceleration in the near field from the source. For example, Eurocode 8-1 (2004) recommends the ratio between vertical and horizontal peak rock acceleration of 0.9 for surface wave magnitudes greater than 5.5 and 0.45 for the magnitudes smaller than 5.5.

### 3.2.4.5 An Example of the Peak Horizontal Ground Velocity Attenuation Relationship

Akkar and Bommer (2007) proposed the following attenuation relationship between the peak horizontal ground velocity  $v_{p,h}$  in cm/s, the earthquake moment magnitude  $M_w$ , and the minimal distance  $d$  from the location of interest to the surface projection of the fault (or the epicentral distance where the location of the causative fault has not been reported).

$$\begin{aligned} \log_{10}(v_{p,h}) &= -1.26 + 1.103 \cdot M_w - 0.085 \cdot M_w^2 + (-3.103 + 0.327 \cdot M_w) \cdot \\ &\log_{10} \sqrt{d^2 + 5.5^2} + 0.226 \cdot S_S + 0.079 \cdot S_A - 0.083 \cdot F_N + 0.0116 \cdot F_R \end{aligned} \quad (3.9)$$

where  $S_S=1$  for soft soil sites (with the transversal wave velocity range between 180 and 360 m/s to a depth of 30 m) and 0 otherwise,  $S_A=1$  for stiff soil sites (with the transversal wave velocity range between 360 and 750 m/s to a depth of 30 m) and 0 otherwise,  $F_N=1$  for normal and strike-slip faulting earthquakes and 0

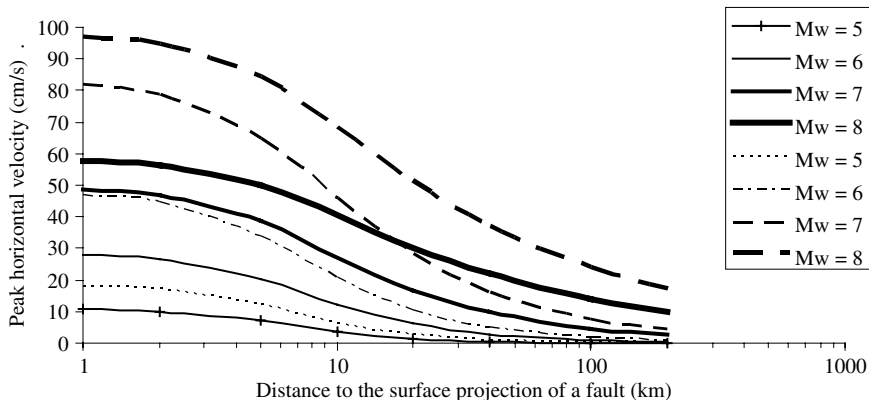


**Fig. 3.5** The average peak horizontal velocity of rock (*continuous lines*) and soft soil sites (*dashed lines*) from unspecified faulting

otherwise,  $F_R=1$  for reverse (thrust) faulting earthquakes and 0 otherwise. Fault types are described in Section 3.2.1.

The intra-earthquake (a single event) standard deviation for the above proposal was reported as  $0.88\text{--}0.102M_w$ . The inter-earthquake (multiple events) standard deviation was  $0.344\text{--}0.04M_w$ . The average peak horizontal velocities of rock and soft soil from unspecified faulting earthquakes are shown in Fig. 3.5.

### 3.2.4.6 An Example of the Peak Horizontal Ground Velocity to Acceleration Ratio Attenuation Relationship

The use of this ratio for estimation of the period of equivalent harmonic ground motion is described in Section 2.5. The ratio between the peak horizontal velocity and acceleration for rock and soft soil from unspecified faulting earthquakes is calculated from Equations (3.9) and (3.6) and shown in Fig. 3.6.

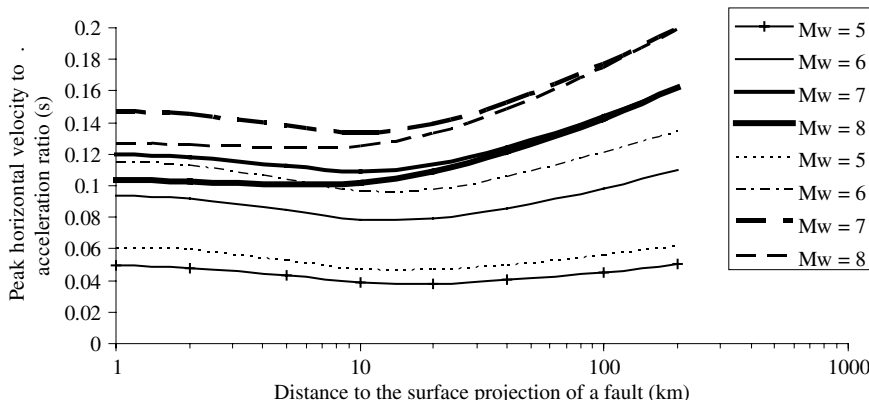


**Fig. 3.6** The average peak horizontal velocity to acceleration ratio for rock (*continuous lines*) and soft soil sites (*dashed lines*) from unspecified faulting

### 3.2.4.7 An Example of the Peak Horizontal Ground Displacement Attenuation Relationship

Bommer and Elnashai (1999) proposed the following attenuation relation between peak horizontal ground displacement  $d_{p,h}$  in cm, the surface wave magnitude  $M_s$ , and the minimal distance  $d$  to the surface projection of the fault (or epicentral distance where the location of the causative fault has not been reported):

$$\begin{aligned} \log_{10}(d_{p,h}) = & -1.757 + 0.526 \cdot M_s - 1.135 \cdot \log_{10} \sqrt{d^2 + 3.5^2} \\ & + 0.114 \cdot S_A + 0.217 \cdot S_S + 0.32 \cdot P \end{aligned} \quad (3.10)$$

where,  $S_S=1$  for soft soil sites (with the transversal wave velocity range between 180 and 360 m/s to a depth of 30 m) and 0 otherwise,  $S_A=1$  for stiff soil sites (with the transversal wave velocity range between 360 and 750 m/s to a depth of 30 m) and 0 otherwise,  $P$  is a variable that takes a value of 0 for mean peak displacement and 1 for 84-percentile values of exceedance of the mean peak displacement.

Based on the above equation, the average peak horizontal displacements for rock and soft soil are shown in Fig. 3.7.

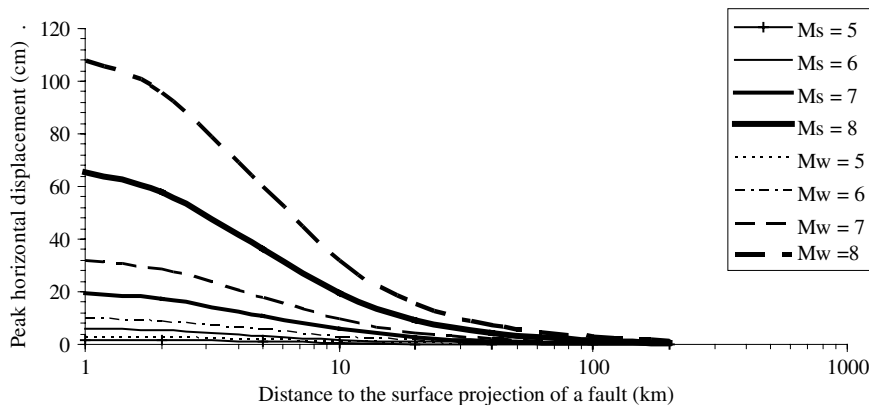


**Fig. 3.7** The average peak horizontal displacement of rock (*continuous lines*) and soft soil sites (*dashed lines*) from unspecified faulting

### 3.2.5 Sources of Earthquake Data

Peak bedrock accelerations are defined in many local seismic codes and on maps. Two examples of international maps are:

- Global seismic hazard map produced by the global seismic hazard assessment program (GSHAP) as a part of UN International Decade of Natural Disaster Reduction (1999) (<http://www.seismo.ethz.ch/GSHAP/>)
- European-Mediterranean seismic hazard map produced by European Seismological Commission (2003) (<http://wija.ija.csic.es/gt/earthquakes/>)

Strong ground motion time histories are selected from several available databases using a number of earthquake and site parameters, such as earthquake magnitude, site-to-source distance and ground type at the recording station. Examples of such databases are:

- In the USA

The United States Geological Survey – USGS

([http://nsmp.wr.usgs.gov/nsmn\\_eqdata.html](http://nsmp.wr.usgs.gov/nsmn_eqdata.html) for time histories of ground motion and <http://earthquake.usgs.gov/eqcenter/> for earthquake data)

The Pacific Earthquake Engineering Research Center – PEER

(<http://peer.berkeley.edu/smcat/>)

The National Geophysical Data Center – NGDC

(<http://www.ngdc.noaa.gov/nndc/struts/form?t=101650&s=1&d=1>)

- In Europe

European Earthquake Data Base (at <http://www.isesd.cv.ic.ac.uk/>)

- In Japan

Kyoshin Network K-NET (at <http://www.k-net.bosai.go.jp/>)

Time histories in these databases are corrected by the standard processing techniques that remove low and high frequency noise from them. Raw records may contain also non-standard errors and therefore uncorrected records should not be used for the analyses. Non-standard errors are (e.g. Douglas, 2003):

- insufficient digitizer resolution
- transversal wave trigger
- insufficient sampling rate
- multiple baselines
- spikes
- multiple shocks
- early termination during coda
- clipping

Douglas (2003) considered the effects of late triggering of the instrument and also strong-motion records from digital instruments with low analog/digital converter resolution and concluded that good response spectral ordinates can be obtained from such ‘poor-quality’ records within the period range of most engineering interest.

Response spectral values, described in Section 1.4, are usually obtained from the existing engineering international and local seismic codes. Examples of such codes are:

- Eurocode 8: Design of structures for earthquake resistance, Part 1: General rules, seismic actions and rules for buildings (2004)
- Uniform Building Code, Volume 2: Structural Engineering Design provisions (1997)
- International Building Code (2006)
- Building Center of Japan: The seismic code: guidelines for structural calculations

A number of procedures exist for generating artificial ground motion time histories in order to perform just one time history analyses (e.g. Stewart et al., 2001). Many of such procedures are based on matching the response spectrum of an artificial motion with design response spectra from codes. Because response spectra from codes are envelopes of many actual response spectra, there are dangers that artificial ground motion time histories

- may look different from actual time histories,
- may have inappropriate velocity and/or displacement response spectra, even while matching the acceleration response spectra
- may have an inappropriate energy content

It is normally possible to select about three actual ground motion time histories so that the envelope of their response spectral accelerations matches rather closely the target spectrum.

### 3.3 Factors Affecting Seismic Hazard

Selection of ground motion parameters (peak values, time histories or response spectral) for the simplified analyses should be guided by knowledge and understanding of various factors affecting seismic hazard at a particular location. The main factors described in this subsection are:

- source and wave path effects
- sediment basin edge and depth effects
- local soil layers effects
- topographic effects
- space and time clustering, and seismic gaps

Seismic hazard assessment at a particular location is normally done by a specialist in engineering seismology. Nevertheless, the user of the results of the assessment should have a good understanding of the accuracy and reliability of data provided. Assessment is not simple. Models that use ground motion data as their input parameters may be simplified but are not necessarily simple.

#### 3.3.1 Earthquake Source and Wave Path Effects

Of different possible earthquake sources mentioned in Section 1.2, the subduction zones (with ocean trenches) and transform boundaries between major tectonic plates (Fig. 3.8) as well as intra-plate faults are the most frequent and strongest sources of earthquakes. The sites near such earthquake sources are likely to experience increased seismic hazard.

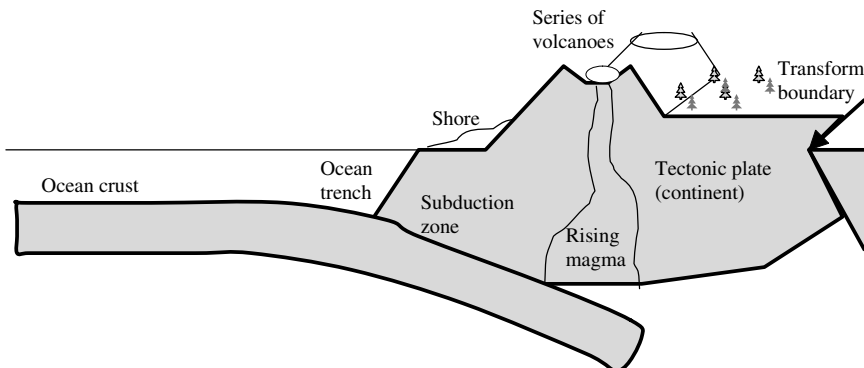


**Fig. 3.8** Cross section through a subduction zone (with ocean trench); transform boundary and a tectonic plate (continent)

Fowler (1990), for example, refers to a number of subduction zones (i.e. ocean trenches) and transform boundaries between tectonic plates, which locations are shown in Fig. 3.9.

*“One of the largest earthquakes ever was the Chile event of 22 May 1960 with moment magnitude  $M_w$  of 9.5. Around 75% of the world’s seismic energy is released at the edge of the Pacific, where the thinner Pacific plate is forced beneath thicker continental crust along subduction zones. This 40,000 km band of seismicity stretches up the west coasts of South and Central America and from the Northern USA to Alaska, the Aleutians, Japan, China, the Philippines, Indonesia and Australasia. Around 15% of the total seismic energy is released where the Eurasian and African plates are colliding, forming a band of seismicity which stretches from Burma, westwards to the Himalayas to the Caucasus and the Mediterranean”. (e.g. <http://www.moorlandschool.co.uk/earth/images/Earthquakefaq.htm#FAQ03>).*

A complete classification of types of tectonic faults is given by Mandl (2000), for example. The principal classifications depend on the direction of movements of one mass relative to the other, as shown in Fig. 3.10:

- Normal faults occur when the movements along the fault surface is downward.
- Reverse faults occur when the movements along the fault surface is upward. A particular type of a reverse fault is thrust fault, which occurs when the fault plane has a small inclination angle to the horizontal.
- Strike-slip faults occur when the movements along the fault surface is horizontal.
- Oblique faults occur when the movements along the fault surface is both horizontal and up or downward.

Somerville et al. (1996), for example, reported that median ground motions from reverse faults are greater than those from strike-slip. The effect of faulting type on the peak ground acceleration and velocity is considered in Equations (3.6), (3.8) and (3.9) for example.

The near-fault zone is usually assumed to be within a distance of about 20–60 km from a ruptured fault because Earth body waves rather than near surface waves

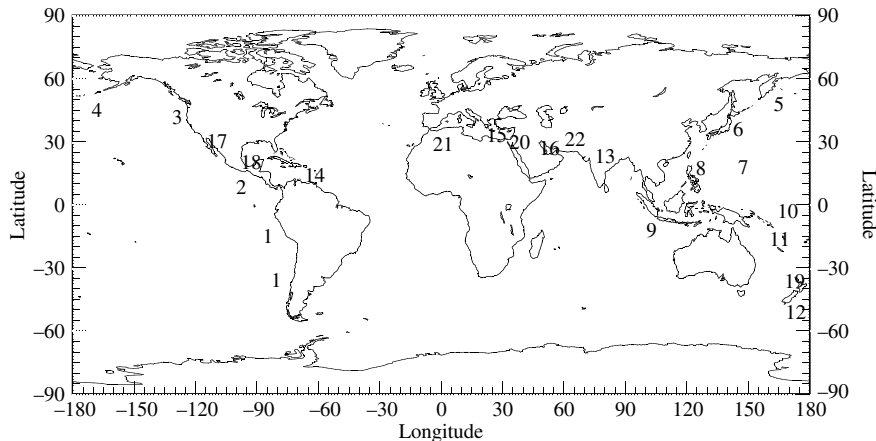


**Fig. 3.9** Subduction zones (i.e. ocean trenches) and transform boundaries between tectonic plates (based on Fowler, 1990)

*Legend:* 1. Peru-Chile trench along the west coast of South America, 2. Mexico trench along the west coast of Central America, 3. Cascadian trench off the coast of Washington and British Columbia, 4. Aleutian trench along Aleutian islands and across the north side of Pacific ocean, 5. Kuril trench along the east coast of Kuril island, 6. Japan trench along the east coast of Japan's islands, 7. Mariana's trench along the east border of Philippine plate, 8. The trench along the west border of Philippine plate, 9. Java trench along the west coast of Indonesia, 10. New Hebrides trench, 11. Kermadec-Tonga trench north of New Zealand, 12. Macquarie ridge in New Zealand, 13. The subduction zone of Indian sub-continent under Eurasia plate along Himalayas, 14. The trench east of Caribbean islands, 15. East Mediterranean sea trench south of Italy, Greece and Cyprus, 16. The trench in Persian/Arabian Gulf.

The transform boundaries between tectonic plates: 17. The San Andreas zone in California, 18. The Montague zone between North American and Caribbean plates, 19. The Alpine zone of New Zealand, 20. The Dead Sea zone, 21. The west Mediterranean zone along North Africa, 22. The Afghanistan-Pakistan zone

dominate ground motion. Within this near-fault zone, ground motions can be significantly influenced by:

- The rupture mechanism, i.e. fault type.
- The direction of rupture propagation relative to the site.
- Possible permanent ground displacement resulting from the fault slip.

Somerville et al. (1996) stated “*The ground motions from the Northridge earthquake and our simulations of these ground motions have a similar pattern of departure from empirical attenuation relations for thrust earthquakes: the peak accelerations are at about the 84th percentile level for distances within 20–30 km and follow the median level for larger distances*”. In other words, the peak accelerations generated by thrust earthquakes can be equal to average plus one standard deviation of the peak accelerations predicted by empirical attenuation relationships.

The last two factors result in effects termed as ‘rupture-directivity’ and ‘fling step’ (e.g. Somerville et al., 1997):

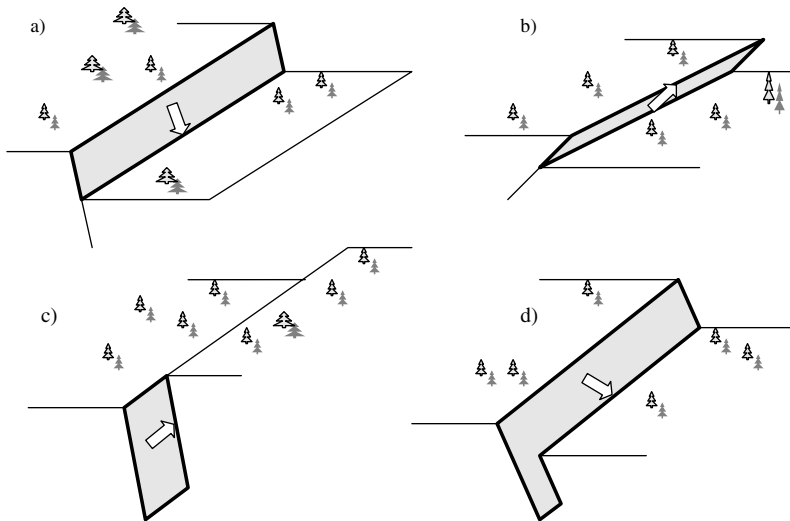


**Fig. 3.10** Types of tectonic fault movements: (a) normal, (b) reverse, (c) strike-slip, (d) oblique

- ‘Rupture directivity’ occurs when fault rupture propagates towards a site and the direction of slip on the fault is also toward the site. This seems to occur because the velocity of fault rupture is close (about 80%) to the transversal wave velocity propagation through the rock near the source. The large impulsive motions occur only in the fault-normal direction and only away from the epicentre.
- ‘Fling step’, occurs over a discrete time interval of several seconds as the fault slip is developed. Fling step displacements occur in the direction of fault slip, and therefore are not strongly coupled with the dynamic displacements referred to as the ‘rupture directivity’ pulse.

The available strong motion data that can be used to quantify these effects are limited. The effects can be taken into account approximately by adding one or two standard deviations to the average peak and response spectra values defined by attenuation relationships.

In a simplified interpretation, the effects of rupture directivity and fling step can be considered as the case of directed instead of dissipated seismic waves. An analogy could be made between a laser and sunlight. Directed seismic waves have minimal radiation damping because of their near parallel propagation as shown in Fig. 3.11. For this situation to occur, a straight fault zone and homogenous rock between the source and the site are necessary conditions.

In the far-field zone (a few tens of kilometers from the source, e.g. Kramer, 1996), the ground motion is dominated by near-surface propagating Rayleigh and Love waves instead of the body longitudinal and transversal waves, as mentioned also in Section 1.2.

In far fault zones, near-shore structures could be affected by tsunami formed as a result of the uplift of ocean floor by a reverse fault, which also uplifts a large volume

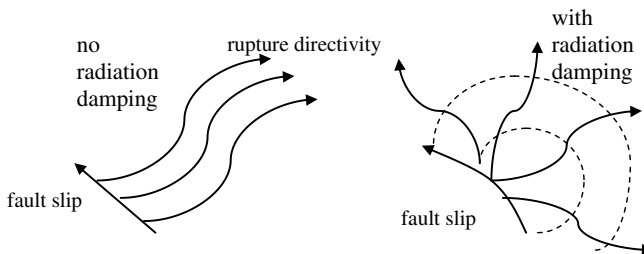


**Fig. 3.11** Plan view Sketches of cases with and without radiation damping effects

of water above the sea level. The uplifted water tends to spread around because of a spill-over effect and propagates over large distances by large period and low amplitude waves until the waves reach near shore when their amplitude increases significantly as the water depth decreases (e.g. <http://en.wikipedia.org/wiki/Tsunami>).

### 3.3.2 *Sediment Basin Edge and Depth Effects*

#### 3.3.2.1 The Phenomena

Stewart et al. (2001), for example, reviewed available knowledge about the effects of deep sediment-filled basins, with thickness ranging from a 100 m to over 10 km (Fig. 3.12), on strong ground motion during earthquakes. Seismic waves that become trapped in deep sedimentary basins can produce up to 50% greater amplitudes at intermediate and low frequencies ( $<1$  Hz) and their durations can be twice as long as those recorded on comparable near surface soil outside basins. Also, basin edges may focus energy (like a lens) in spatially restricted areas on the surface, Stephenson et al. (2000), Davis et al. (2000). The conditions (basin curvature) for such a focusing are quite specific and therefore should be rare.

Many structures are located in alluvial valleys and the structural damages were concentrated near the basin edges. Significant differences between the peak horizontal surface accelerations at the centre and near edges of the valleys were recorded

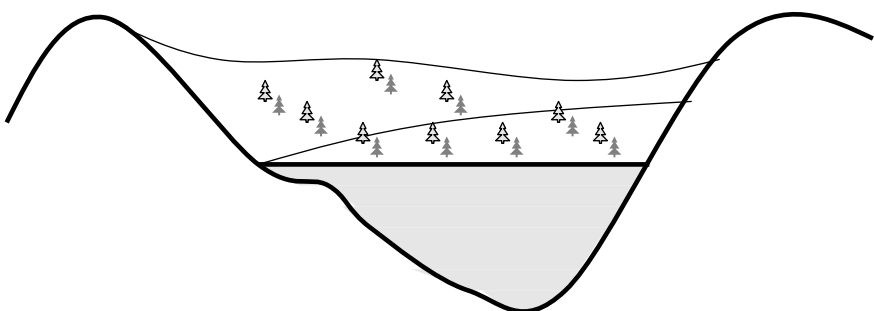


**Fig. 3.12** Cross section through a sediment basin

(e.g. King and Tucker, 1984). Back analyses assuming one-dimensional wave propagation in the vertical direction indicated a good agreement between the computed and recorded peak horizontal surface accelerations near the centers of valleys but not near the edges (e.g. King and Tucker, 1984).

Curved basin edges impose a three-dimensional stress state in their vicinity. Two and three-dimensional analyses of wave propagation are based on finite difference and finite element methods. Using workstation computer, it is currently feasible to compute 3D ground motions reliably up to frequencies of about 0.5–1 Hz in large urban regions (Stewart et al., 2001). The peak acceleration may occur at higher frequencies and therefore not be predicted by the model. Another factor affecting the frequency resolution is that, in many areas, the seismic velocity model has limited spatial resolution, which places a limit on the frequencies that can be modeled (Stewart et al., 2001).

### 3.3.2.2 A Simplified Approach to Basin Edge Effects

One way to address the issues of basin edge effects is to define and use modification factors for one-dimensional analyses near basin edges. The factors would be used in conjunction with one-dimensional analyses, to determine site specific seismic hazards caused by local ground layers.

The equation of motion in the horizontal direction for a three-dimensional elastic solid is developed in many textbooks (e.g. Kramer, 1996).

$$\rho \frac{\partial^2 u}{\partial t^2} = \frac{\partial \tau_{hv}}{\partial v} + \frac{\partial \sigma_h}{\partial h} + \frac{\partial \tau_{hn}}{\partial n} \quad (3.11)$$

where  $\rho$  is unit soil mass density,  $u$  is horizontal displacement,  $t$  is time,  $\tau_{hv}$  is shear stress in the vertical plane within which horizontal displacement occurs,  $\sigma_h$  is axial stress (positive when tensile) in direction of displacement  $u$ ,  $\tau_{hn}$  is shear stress in the plane perpendicular to the plane within which horizontal displacement occurs,  $v, h, n$  are the vertical, horizontal and normal direction respectively.

If one-dimensional wave propagation is considered instead of three-dimensional propagation then the stress gradients  $\partial \sigma_h / \partial h$  and  $\partial \tau_{hn} / \partial n$  are zero and only the stress gradient  $\partial \tau_{hv} / \partial v$  exists. Using zero stress gradients  $\partial \sigma_h / \partial h$  and  $\partial \tau_{hn} / \partial n$  in one-dimensional analysis causes inevitably under prediction of the horizontal acceleration  $\partial^2 u / \partial t^2$  near basin edges. An apparent increase in  $\partial \tau_{hv} / \partial v$  is necessary in one-dimensional analysis to compensate for the ignored stress gradients  $\partial \sigma_h / \partial h$  and  $\partial \tau_{hn} / \partial n$  near basin edges.

Equation (3.11) is valid for any stress-strain relationship but cannot be solved directly because it mixes stresses with displacements (e.g. Kramer, 1996). In real materials, part of the elastic energy of a traveling wave is always converted to heat. Viscous damping is often used to represent this dissipation of elastic energy because of its mathematical convenience. For the purposes of visco elastic wave propagation analysis, soil is usually represented as Kelvin-Voigt model (e.g. Kramer, 1996). The stress-strain relationship for a Kelvin-Voigt soil in shear can be expressed as

$$\tau_{hv} = G \cdot \gamma_{hv} + \eta \cdot \frac{\partial \gamma_{hv}}{\partial t} \quad (3.12)$$

where  $G$  is shear modulus, shear strain  $\gamma_{hv} = \partial u / \partial v$  and  $\eta$  is the viscosity of soil  $G = \xi(\pi f)^{-1}$ ,  $\xi$  is damping ratio,  $f$  is the frequency of shear stress reversal and  $t$  is time. The equation for one-dimensional wave propagation becomes (e.g. Schnabel et al., 1972)

$$\rho \cdot \frac{\partial^2 u}{\partial t^2} = G \cdot \frac{\partial^2 u}{\partial v^2} + \eta \cdot \frac{\partial^3 u}{\partial v^2 \partial t} \quad (3.13)$$

The analysis is usually performed in frequency domain because of its high speed in comparison with time domain analysis. Ground motion is represented by a Fourier series for a number of frequencies  $f$ . Soil viscosity  $\eta$  is related to the damping ratio  $\xi$  (Equation 2.2) as  $\eta = G \cdot \xi(\pi \cdot f)^{-1}$ . Because of the modulus and damping ratio non-linear dependence on shear strain magnitude, an equivalent linear approach is used in the computation in frequency domain (e.g. Schnabel et al., 1972).

An increase in  $\partial^2 u / \partial t^2$  in equivalent one-dimensional analyses is considered by factoring actual transversal wave velocities of soil layers in one-dimensional analyses.

### 3.3.2.3 Case Studies of Sediment Basins

The correction factors of transversal wave velocities are determined using computer program SHAKE (Schnabel et al., 1972) and the available case histories given in Table 3.1. Srbulov (2006a) used acceleration records, which basic data are given in Table 3.2, for the calculation of the factors. An increase in transversal wave velocities increases soil shear modulus  $G$  and consequently increases calculated peak acceleration. Such approach also increases the fundamental frequency of vibration and therefore affects the spectral accelerations.

The case studies of sediment basins, which data are summarized in Table 3.1, are described below. They were investigated for the purpose of determining correction coefficient of transversal wave velocity near basin edges for 1D SHAKE analyses.

- 1. Caracas Basin during the 1967 Caracas Earthquake.** Papageorgiou and Kim (1991) studied the anti-plane response of a 2D model of the basin in Caracas, Venezuela with reference to the 29th July 1967 earthquake offshore Caracas. A significant feature of the earthquake was the concentration of damage to multi-storey buildings in the Palos Grandes suburb of East Caracas. Their 2D boundary element model in frequency domain indicated the existence of a fairly uniform peak surface acceleration from 0.15 to 0.21 g across the basin. The depth of sediments under Palos Grandes district is about 280 m and the width at the surface about 3 km. The distance between the district and the basin edge is about 1 km so that the ratio between the length and the depth is about 3.6. The earthquake moment magnitude was 6.6 and epicentral distance of 25 km. No strong motion instrument was operational in the area at the time of the earthquake. There was

**Table 3.1** Data for sediment basins (Srbulov, 2006a, by permission of Patron Editore)

N <sub>o</sub>	Basin	Reference	Horizontal distance to the basin edge (m)	Sediment layers depth range (m)	Sediment transversal wave velocity v <sub>t</sub> (m/s)	Sediment unit density ρ(g/cm <sup>3</sup> )	Peak surface acceleration (m/s <sup>2</sup> )
1	Caracas during the 1967 Caracas earthquake	Papageorgiou and Kim (1991)	1000	0–20 20–280	310 950	1.7 1.8	1.5–2.1
2	Kirovakan during the 1988 Armenia earthquake	Bielak et al. (1999)	412.5	0–10 10–20 20–50 50–165	200 280 490 710	1.78 1.80 1.90 2.00	1.5
3	The marina during the 1989 Loma Prieta earthquake	Zhang and Papageorgiou (1996)	400	0–13 13–45 45–63 63–72	190 225 265 335	1.80 1.83 1.88 1.88	1.6
4	Santa Clara during the 1984 Morgan Hill and 1989 Loma Prieta earthquake	Pei and Papageorgiou (1996)	1785	0–200 200–321	300 700	2 2.2	1.6–2.1 (1984) 3.2–3.7 (1989)
5	Los Angeles during the 1994 Northridge earthquake	Graves et al. (1998)	6200	0–380 380–1180 1180–1900	500–600 800–1200 1300–1600	1.7–1.75 1.85–2.0 2.05–2.2	3.7–8.7
6	Kobe during the 1995 Hyogo-ken Nambu earthquake	Kawase (1996)	317	0–41 41–177.5 177.5–382 382–983	450 550 650 1000	1.75 1.85 1.95 2.05	6.0–8.2
7	Dinar during the 1995 Dinar earthquake	Bakir et al. (2002)	93.6	0–2 2–4 4–14 14–17 17–23.4	140 170 225 275 320	1.6 1.65 1.7 1.75	2.8–2.9

a seismoscope at the Cajigal Observatory, located on rock outcrop west of Palos Grandes that was operational during the earthquake. Fielder (1968) estimated that the peak acceleration at the rock site of the observatory was 0.16 g. A substitute two-component acceleration record of rock motion at Bagnoli-Irpino station is used as the input base motion for the calculation of the correction coefficient of transversal wave velocity.

2. **Kirovakan Basin during the 1988 Armenia Earthquake.** Bielak et al. (1999) considered the problem of soil amplification and structural damage due to

**Table 3.2** Basic data of input base acceleration records used for the case histories (Srbulov, 2006a, by permission of Patron Editore)

N <sub>o</sub>	Reference	Earthquake	Hypocentral depth (km)	Date & Time	Station	Source to site distance (km)	Ground acceleration component direction	Peak horizontal acceleration m/s <sup>2</sup>	Amplitude scaling factor
1	Ambraseys et al. (2000)	Campano Lucano	6.6 (M <sub>L</sub> )	16 18:34:52	Bagnoli- Ipinio	23 (epic.)	N-S E-W	1.36 1.78	1
2	Ambraseys et al. (2000)	Spitak	3.3 (M <sub>s</sub> )	5 11/1/1991 21:28:51	Spitak - Karadzor	6 (epic.)	N-S E-W	0.941 1.298	1
3	PEER	Loma Prieta	7.1 (M <sub>s</sub> )	- 18/10/1989 00:05	Pacific Heights	81 (fault)	270 360	0.60 0.46	1
4	PEER	Morgan Hill	6.2 (M <sub>L</sub> )	- 24/04/1984 21:15	Gilroy 6	11.8 (fault)	000	2.178	1
5	PEER	Loma Prieta	7.1 (M <sub>s</sub> )	- 18/10/1989 00:05	Gilroy 1	11.2 (fault)	000	2.864 4.032	1
6	PEER	Northridge	6.7 (M <sub>s</sub> )	- 17/01/1994	Mt Wilson - CIT	36 (fault)	000	4.640 2.29	1
7	Ambraseys et al. (2000)	Hyogo-ken Nambu	6.9	- 04/03/1977 19:21:54	JMA	0.6 (fault)	000	8.05	0.69 <sup>#</sup>
		Bucharest	6.4 (M <sub>L</sub> )		Vrancea	4 (epic.)	N-S E-W	5.88 1.91	0.75 <sup>#</sup> 1
		Valnerina	5.5 (M <sub>L</sub> )	4 19/09/1979 21:35:37	Cascia	4 (epic.)	N-S E-W	1.51 2.01	1

\*  $1.2 = 10^{(\log_{10}(0.234) \times \log_{10}(22.6)) / \log_{10}(36)}$ .\*\*  $1.3 = 10^{(\log_{10}(0.134) \times \log_{10}(22.6)) / \log_{10}(36)}$ .

# For the peak velocity of 55 cm/s.

local site condition in a small valley in Kirovakan, for which 1D wave propagation analyses have failed to provide adequate answers for the large extent and spatial distribution of damage during the 1988 Armenia (Spitak) earthquake. Two-dimensional finite element analysis was performed using as input an inferred rock accelerogram for a vertically incident SH-wave and linear elastic soil properties with damping. Bielak et al. (1999) calculated that the peak ground acceleration of about 0.55 g in the central part of the basin was about 50% larger than for the 1D model and the 2D model exhibited an additional set of resonant frequencies, which caused the ground amplification ratio to oscillate very rapidly both spatially and with frequency. The width of triangularly shaped sedimentary basin considered is only about five times its depth. The basin contains a thin layer of medium stiff clay on top of stiffer clay down to about 165 m depth. The mid valley profile is analyzed so that the ratio between distance to the basin edge and the depth is about 2.5. Only one set of good quality strong motion records was obtained in the town of Ghoukasian on the 7th December 1988 Armenia (Spitak) earthquake, with magnitude  $M_s=6.8$ . The station is located on top of an extended shallow deposit of alluvium and lake-bed clay layers underlain by rock about 30 km northwest from the epicentre. Yegian et al. (1994a) estimated that the peak horizontal ground acceleration in Kirovakan during the 1988 Armenia (Spitak) earthquake did not exceed 0.15 g based on their observations of grave markers in cemeteries in the city and shaking table tests on model blocks. A substitute two-component acceleration record of rock motion at Spitak-Karadzor station is used as the input base motion for the calculation of the correction coefficient of transversal wave velocity.

3. **The Marina Basin during the 1989 Loma Prieta Earthquake.** Zhang and Papageorgiou (1996) used a 2D model of a SW-NE trending cross section of the Marina Basin, San Francisco – California, to estimate the intensity of ground motion experienced during the Loma Prieta earthquake on the 18th October 1989. The effect of soil nonlinear behavior during straining was simulated by an iterative procedure called the “equivalent linear approach”, which is also used by the computer program SHAKE (Schnabel et al., 1972). Zhang and Papageorgiou’s (1996) results showed that the peak horizontal ground accelerations and velocities may have reached values as high as 0.23 g and 34 cm/s respectively. The peak ground horizontal acceleration of 156 cm/s<sup>2</sup> was recorded at Treasure Island, overlaying ‘bay mud’, some 6 km east from Marina District. The sediments at the bottom consist of stiff Pleistocene bay clay which is overlain by a dense Pleistocene (silty to clayey) sand layer, soft to medium stiff (normally consolidated) bay sediments, loose to dense Holocene beach and dune sand, and artificial fill. The ground properties at Point 11, in the paper by Zhang and Papageorgiou (1996) are used in the analysis. The distance to the basin edge from the location of Point 11 is about 0.4 km and the maximum depth at the location of Point 11 is about 72 m so that the distance to depth ratio is about 5.5. There existed no ground motion recording instruments in the Marina District at the time of the Loma Prieta earthquake. Two-component acceleration record of rock

motion obtained at nearby Pacific Height station is used for the input base motion for the calculation of the correction coefficient of transversal wave velocity. The same records were used by Zhang and Papageorgiou (1996).

4. **Santa Clara Basin during the 1984 Morgan Hill and 1989 Loma Prieta Earthquake.** Pei and Papageorgiou (1996) analyzed the motions recorded by the Gilroy array of instruments on the surface across the Santa Clara Basin, California, for evidence of valley induced surface waves. Their analysis of the recorded motions of the 1989 Loma Prieta earthquake revealed existence of the fundamental and first and second higher modes of Rayleigh waves, while the recorded motions of the 1984 Morgan Hill earthquake showed an additional fundamental Love mode. To reinforce their interpretation of the recorded motion, they used a 2D hybrid boundary – finite element method, which input data are used in this paper for 1D analysis. The Gilroy array extends 10 km from Franciscan rocks (the station 1) across Quaternary alluvium of the Santa Clara basin to Crataceous rocks (the station 6) of the Great Valley sequence. Seismic refraction studies of the Santa Clara basin indicated that the basin is wedge shaped in cross section with the basement dipping about  $10^\circ$  (1 vertical to 5.7 horizontal) beneath the Quaternary alluvium of the valley to a maximum depth of about 1 km. The Gilroy array stations G2, G3, G4 are located at the distances of about 1785, 3570 and 5355 m from the station 1, according the model by Pei and Papageorgiou (1996). Two-component acceleration records of rock motions at the stations Gilroy 6 and 1 are used as the input base motion for the calculation. The fault to station 2, 3, 4 distances during the 1984 Morgan Hill earthquake were 15.1, 14.6, 12.8 km respectively and during the 1989 Loma Prieta earthquake 12.7, 14.4, 16.1 km respectively according to PEER.
5. **Los Angeles Basin during the 1994 Northridge Earthquake.** Graves et al. (1998) used 2D simulations by finite-difference technique to analyze the ground motions induced by the 1994 Northridge earthquake in the Santa Monica area, where numerous structures were heavily damaged or destroyed by the strong ground shaking. Their simulation indicated that the edge structure of the shallow basin (about 1 km deep) formed by the active strand of the Santa Monica fault created a large amplification in motions immediately south of the fault scarp, in very good agreement with main shock damage patterns, recorded ground motions, and locations of elevated site response. Graves et al. (1998) considered that this large amplification resulted from constructive interference of direct waves with the basin-edge generated surface waves. They found that focusing effects created by the deeper basin structure (3–4 km deep) cannot explain the large motions observed immediately south of the fault scarp. The greatest peak ground horizontal acceleration of 0.87 g was recorded at SMCH station in tangential direction with respect to the epicentre at 22.6 km distance from the station. SMCH station is located at a distance of about 6200 m from the basin edge. The ratio between the station horizontal distance to the basin edge and the depth of basin at the location of the station is about 3.3. Two-component acceleration record of rock motion obtained on rock at Mt Wilson – CIT Seismological station during

the 1994 Northridge earthquake (PEER) is used for the input base motion for the calculation of the correction coefficient of transversal wave velocity.

6. **Kobe Basin during the 1995 Hyogoken-Nanbu Earthquake.** Kawase (1996) used 2D finite element model to analyze the basin edge effect on observed so-called “damage belt” oriented WSW-ENE across the city of Kobe during the Hyogoken Nanbu earthquake on the 17th January 1995. The damage belt is located from 500 to 1000 meters away from the Rokko geological faults. Kawase (1996) concluded that the amplification of the ground motion 1 km away from the basin edge was caused by the coincidental interference of the primary S-waves with the basin-induced diffracted/surface waves, which were generated at the basin edge and radiated horizontally into the basin. The nearby Suma and Egeyama faults were modeled as vertical by Kawase (1996). The ground and layer surfaces are gently sloping offshore and are considered horizontal in this section. The ratio between JMA station horizontal distance to the edge of the basin and the basin depth at the location of the station is about 0.32. Kawase (1996) performed a deconvolution of the accelerogram recorded at the JMA station to define equivalent outcrop bedrock motion and compared the results with the record obtained at Kobe University station on granite rock. He obtained different velocity waveforms but concluded that the amplitudes and predominant frequencies of these two records are similar. The peak velocity of the deconvoluted bedrock motion and at Kobe University station was 55 cm/s. The peak horizontal ground acceleration recorded at JMA station was 8.05 m/s<sup>2</sup>.
7. **Dinar Basin during the 1995 Dinar earthquake.** Bakir et al. (2002) analyzed the strong ground motion in Dinar town, located near the edge of an alluvial basin in Southeast Anatolia – Turkey, during the Dinar earthquake, with magnitude  $M_L=5.9$ , which occurred on the 1st October 1995. Inflicted structural damage throughout the town was highly concentrated in a region up to 1 km wide located on the alluvium and adjacent to the rock outcrop bounding the eastern side of the town. Bakir et al. (2002) found that the 1D analysis by SHAKE considerably under predicted the spectral response in the area of heavily damaged structures. Differences between the spectral responses obtained from the 1D and 2D analyses by QUAD4M decreased with increasing distance from the rock outcrop. Dinar basin is about 4.8 km wide at the location of Dinar town. The slope of the basin is about 1 vertical to 4 horizontal inclined to a depth of about 100 m below the town, according to Bakir et al. (2002). The basin is filled with alluvial sediments of sand, gravel, clay and silt. The epicentral distance of the earthquake was 2–3 km north of Dinar city and the hypocentral depth at 24 km. Ground motion induced by the earthquake was recorded at the meteorological station in Dinar, which is located on the alluvium approximately 93 m away from the basin edge. Recorded peak ground accelerations in horizontal directions were 0.275 g N-S and 0.294 g E-W at 19.3 km distance from the epicentre. Two substitute two-component acceleration records of rock motion obtained at Vrancioia and Cascia station are used as the input base motion for the calculation of the correction coefficient of transversal wave velocity.

### 3.3.2.4 Summary of the Case Studies

Basic data for the case histories analyzed by Srbulov (2006a) are given in Tables 3.1 and 3.2.

The variations of shear modulus and damping ratio with shear strain were not known for any of the case histories, and they were assumed in the examples based on data by Vucetic and Dobry (1991). Soil plasticity index of 30 was assumed because the actual plasticity indices of sediments along depth were not known.

The least square regression between the best estimations of the modification factors  $F_m$  of sediments transversal wave velocities and the ratios  $R_b$  between the horizontal distances from the stations to the basin edges and the depth of sediments at the locations of the stations, shown in Fig. 3.13, indicates a good correlation, with the correlation coefficient of 0.93,

$$F_m = 17.45 \cdot 10^{-0.0682 \cdot R_b^2 + 0.165 \cdot R_b} \quad (3.14)$$

For the ratios  $R_b$  greater than about 5.5, the effect of basin edge is minimal, i.e.  $F_m \sim 1$ .

Stewart et al. (2005) reviewed information on ground motion amplification as a function of basin geometry. They recommend that the use of basin models is generally worthwhile for periods of ground motion greater than 0.75 s. All basin models involve adjusting the median of the log-normal distribution of spectral acceleration. The models considered require identification of basin depth at the site as well as identifying whether the seismic source location is coincident with the site basin location or distinct from the site basin location. Stewart et al. (2005) indicated that a number of studies found an average increase in ground motion amplification with the increase in the basin depth, although there is a significant scatter from the average values.

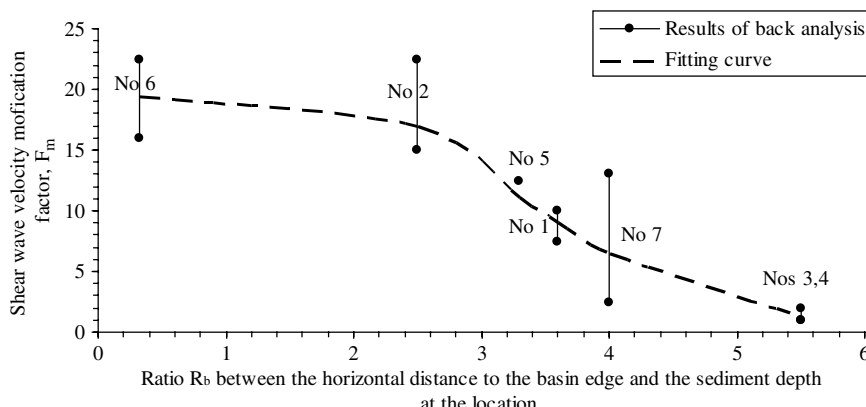


**Fig. 3.13** Dependence of transversal wave velocity modification factor  $F$  on the ratio  $R_b$  between the horizontal distance to the basin edge and the sediment depth at the location for 7 case histories considered

### 3.3.3 Local Soil Layers Effect

A famous case of the local layers effect is the collapse and extensive damage to buildings in the five to 20-story range in Mexico City from the 1985 Michoacan earthquake with  $M_s = 8.1$  at 350 km epicentral distance (e.g. Stone et al., 1987). The recorded peak horizontal acceleration on bedrock was only 0.03–0.04 g and on the surface of soft lake deposit 0.14 g. The site is underlain by about 40 m of soft clay with an average transversal wave velocity of 75 m/s, i.e. with the fundamental vibration period of 2 s. The elastic response spectral acceleration is more than 0.7 g at the period of 2 s. This “double-resonance” condition (amplification of bedrock motion by soil deposit and amplification of the soil motion by the structure) may not be a unique and isolated case.

Comparisons of peak acceleration attenuation relationships for sites that are underlain by different types of soil profiles show distinct trends in amplification behavior of ground motion (e.g. Seed et al., 1976). Although attenuation data are scattered, overall trends suggest that peak accelerations at the surfaces of soil deposits are greater than the peak accelerations of bedrock and soil at greater depths. The increase in amplitudes as waves propagate into media of lower density  $\rho_1$  and wave propagation velocity  $v_1$  (towards surface) can be explained by considering the principle of conservation of energy and the energy-flux density per unit of time in the direction of wave propagation (upwards).

$$\frac{1}{2} \cdot v_1 \cdot \rho_1 \cdot A_1^2 \cdot \omega^2 = \frac{1}{2} \cdot v_2 \cdot \rho_2 \cdot A_2^2 \cdot \omega^2 \quad \text{from which} \\ \frac{A_1}{A_2} = \sqrt{\frac{\rho_2 \cdot v_2}{\rho_1 \cdot v_1}}, \quad (3.15)$$

where  $\omega$  is circular frequency, the product  $\rho v$  is called soil impedance,  $(\rho_2 v_2)/(\rho_1 v_1)^{-1}$  is called the impedance contrast between two adjacent layers. At greater ground accelerations and shear strain, increased material damping causes the energy of propagating waves upwards to be partly transformed into heat. This energy loss causes a decrease in the difference between the amplitude  $A_1$  at the surface and the amplitude  $A_2$  at depth.

Based on data from Mexico City and San Francisco Bay area, and on additional ground response analyses, Idriss (1990) related peak accelerations on soft soil sites to those on rock sites. At low to moderate acceleration levels (less than about 0.4 g), peak accelerations at soft soil sites are likely to be greater than on bedrock and deep layers. In some cases, such as Mexico City in 1985 and the San Francisco Bay area in 1989, relatively small rock accelerations may cause (up to about 8.5 times) higher accelerations at the surface of soft soil deposits. The ranges of acceleration ratios by Idriss (1990) from the 1985 Michoacan and the 1989 Loma Prieta earthquakes together with the 66 case histories compiled by Srbulov (2003a) are shown in Fig. 3.14.

The simplest predictive model is based on a least square fit of the 66 recorded data. Such an approach leads to the following predictive equation of the averaged

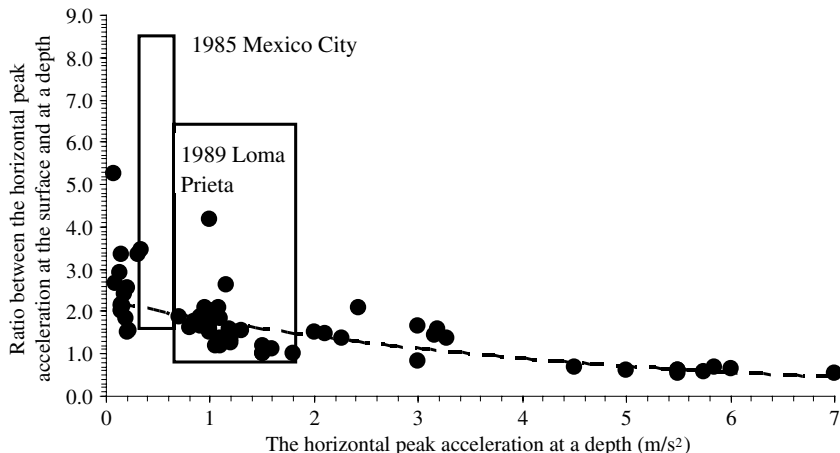


**Fig. 3.14** Ratios between the recorded horizontal peak accelerations at the surface and at depths (soil or bedrock) versus the horizontal peak accelerations at depths

peak horizontal surface to depth acceleration ratio using an exponential function fit with the correlation coefficient of 0.82.

$$\frac{a_{\text{peak,surface}}}{a_{\text{peak,depth}}} = 2.26 \exp^{-0.23 \cdot \frac{a_{\text{peak,depth}}}{g}} \quad (3.16)$$

Sarma (1994) considered analytical solution to the seismic response of viscoelastic soil layers and obtained a transfer function of the similar shape. He stated that the transient part of the complete solution is missing in the SHAKE program. Free of charge MS Excel spreadsheet EERA (<http://gees.usc.edu/GEEs/>) is an implementation of the equivalent-linear concept of one-dimensional site response analysis to earthquake shaking. It should be noted that the results of SHAKE and EERA can be different. SHAKE is in more widespread use than EERA so far. Other commercial software exists based on the same method.

A single degree of freedom oscillator (SDOFO) subjected to a harmonic load can be used to explain the effect of near surface soil layers on the peak horizontal acceleration of the base motion. The ratio between the peak output acceleration  $a_o$  and the corresponding peak input acceleration  $a_i$  of a SDOFO is shown in Fig. 3.15.

The amplification factor for harmonic motion of a SDOFO (e.g. Clough and Penzien, 1993) is:

$$\frac{a_o}{a_i} = \sqrt{\frac{1 + (2\beta_t\xi)^2}{(1 - \beta_t^2)^2 + (2\beta_t\xi)^2}}, \quad (3.17)$$

where  $\beta_t = \omega_d\omega_o^{-1}$  is the tuning ratio,  $\omega_d$  is the circular frequency of an input motion,  $\omega_o$  is the circular frequency of the output motion,  $\xi$  is the damping ratio.

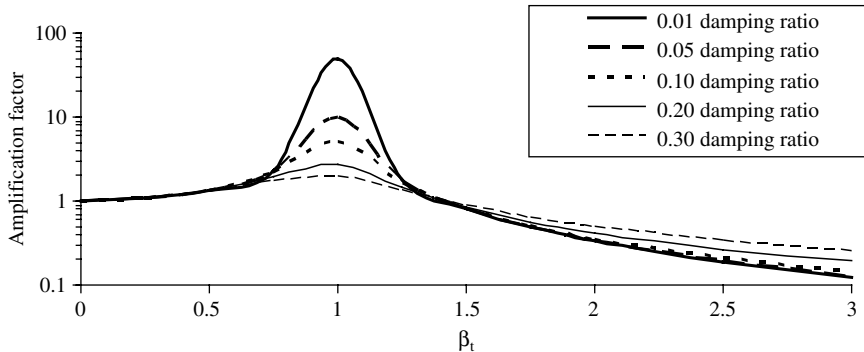


Fig. 3.15 Amplification factor between the output and input peak accelerations

When the peak acceleration of the input (base) motion increases, shear strain of soil increases and the shear modulus i.e. transversal wave velocity decrease (e.g. Section 2.2.1). With the decrease in transversal wave velocity, the fundamental period of soil layers increases and the circular frequency of soil layers decrease. With decrease in the circular frequency of soil layers (i.e. output motion), the tuning ratio increases and the amplification factor decreases when the circular frequency of the input motion (at depth) is greater than the circular frequency of the output motion (at the surface) as in the case of soil layers over bedrock

Both the peak horizontal acceleration surface to depth ratio and its scatter decrease with the increase in the base acceleration can be explained using the model of wave propagation through a single layer of soil with Kelvin-Voigt properties described in Section 3.3.2. For a uniform isotropic soil layer overlying rigid bedrock subjected to a harmonic horizontal motion, the amplification factor of the amplitudes of at depth acceleration  $a_{peak,depth}$  and at the surface  $a_{peak,surface}$  is (e.g. Kramer, 1996);

$$\frac{a_{peak,surface}}{a_{peak,depth}} = \frac{1}{\sqrt{\cos^2(\omega \cdot H/v_t) + [\xi \cdot (\omega \cdot H/v_t)]^2}}, \quad (3.18)$$

where  $\omega$  is the circular frequency of ground shaking,  $H$  is the layer thickness,  $v_t$  is the transversal wave velocity and  $\xi$  is damping ratio. The base acceleration amplification factor is shown in Fig. 3.16.

From Fig. 3.16 it follows that the amplification factor and its scatter are largest at smaller frequencies of ground shaking and soil damping ratio but also that they could reach large values even for significant damping ratio in linear elastic soil. The scatter of the ratios in Fig. 3.14 can be explained by different vibration modes (frequencies) of ground shaking, in addition to the influence of other factors.

Srbulov (2003a) used the formula for the frequency  $\omega_n$  and period  $T_n$  of the  $n_{th}$  mode of free vibration of an infinite layer, with constant soil properties over an

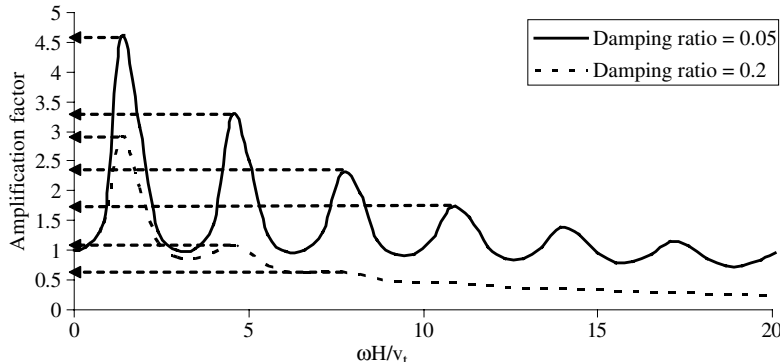


**Fig. 3.16** Influence of frequency on amplification factor of damped linear elastic layer

interval of shear strain, to back analyze the ratio between peak surface and at depth acceleration.

$$\omega_n = \frac{2 \cdot \pi \cdot (2 \cdot n_m - 1)}{4 \cdot H} \cdot \sqrt{\frac{G}{\rho}} \quad (3.19)$$

$$T_n = \frac{2 \cdot \pi}{\omega_n},$$

where  $H$  is soil layer thickness,  $G$  is shear modulus,  $\rho$  is unit soil density. The results indicated that the peak acceleration occurred in the first vibration mode in majority of the cases analyzed but that the peak ground acceleration could occur in other vibration modes up to the 6th mode.

The local soil layer effect is not independent from other factors affecting seismic hazard at a location because shear strain increases and shear stiffness decreases with increasing ground accelerations, which in turn affects the ground accelerations.

### 3.3.4 Topographic Effect

Ridges, canyons and ground slopes tend to oscillate differently from horizontal ground because their sides are not constrained by lateral earth pressures. Topographic effects were observed at a number of ridges such as adjacent to Pacoima Dam in California during the 1971 San Fernando ( $M_L = 6.4$ ) earthquake (e.g. Trifunac and Hudson, 1971), during five earthquakes in Matsuzaki in Japan (Jibson, 1987), during earthquakes in Italy and Chile (Finn, 1991), a small hill in Tarzana, California, during the 1994 Northridge earthquake (eg. Bouchon and Barker, 1996), etc.

Analysis of topographic effect is a complex problem, which depends on the geometry of the terrain and on the types, frequencies, and angles of incidence of the

incoming waves. Simplified analysis of topographic effects on slopes and ridges could be performed as indicated in Section 4.3.

### **3.3.5 Space and Time Clustering (and Seismic Gaps)**

Observations of space and time clustering of some earthquakes suggest that these earthquakes are not random events but follow a pattern. Space and time clustering on a smaller scale is connected with the sudden relief of tectonic stresses built up in the Earth's crust by tectonic fault rupture. A number of seismic gaps (i.e. parts of tectonic faults which have not ruptured for some time) have been identified around the world and large earthquakes have subsequently been observed on several of them.

The 1989 Loma Prieta earthquake occurred on a segment of the San Andreas Fault that had previously been identified as a seismic gap (e.g. Housner et al., 1990).

The global seismic hazard map (<http://www.seismo.ethz.ch/GSHAP/>) produced in 1999 shows a number of zones, which are potential seismic gaps. An example is the northern Pakistan-India border where the seismic hazard according to the map is moderate to high corresponding to the peak ground acceleration of about 1.6 to 2.4 m/s<sup>2</sup> with 10% probability of exceedance in 50 years for 475 years return period. The 2005 Kashmir earthquake ( $M_w = 7.6$ ) caused the peak horizontal acceleration of about 7 m/s<sup>2</sup> near its epicentre around Muzaffarabad (e.g. Durrani et al., 2005). Therefore, seismic gaps could be locations of future earthquakes.

The European-Mediterranean seismic hazard map (<http://wija.ija.csic.es/gt/earthquakes/>) indicates a few potential seismic gaps.

Ambraseys and Jackson (2000) noticed that “*Two regions of known late Quaternary faulting but with virtually no known significant earthquakes in the last 500 years stand out: the north-western Sea of Marmara and the southern branch of the North Anatolian Fault east of Bursa. Prior to 1500 the strike-slip fault system east of Bursa is known to have been active, but this earlier period has revealed no substantial earthquakes from the north-western Sea of Marmara. The seismicity of the last 500 years can account for most of the expected 22+3 mm per year right-lateral slip in the Marmara region. Whether 500 years is long enough to obtain a reliable seismic moment release rate is less clear.*”

#### **3.3.5.1 Case Study of the Seismicity at a Site in the Persian/Arabian Gulf**

Earthquake data until the end of 1979 are obtained from Ambraseys and Melville (1982), until June 1995 from Ambraseys et al. (2000) and the rest from USGS. The epicenters of the earthquakes within the area of about 500 × 450 km<sup>2</sup> are shown in Fig. 3.17. There were only a few earthquakes south from the site in the Persian/Arabian Gulf.

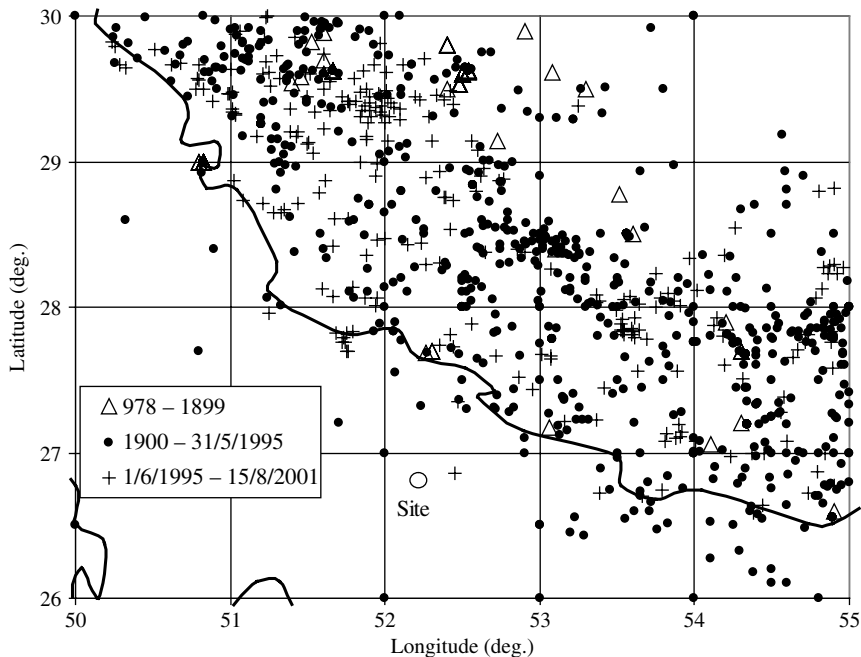


**Fig. 3.17** Epicenters of the earthquakes along a part of the west coast of Iran in the example

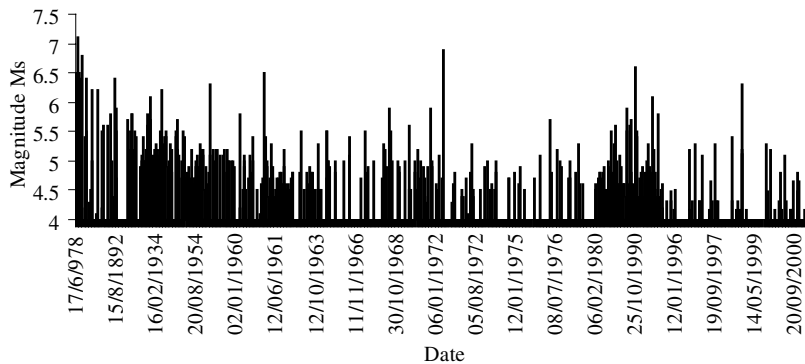


**Fig. 3.18** An example of the time clustering of earthquakes in the area shown in Fig. 3.17

An example of time clustering is shown in Fig. 3.18 for the earthquakes, which epicenters are shown in Fig. 3.17. The clustering of the earthquakes with magnitude greater than 4, which could cause structural damage, occurred at irregular time intervals.

## 3.4 Short Term Seismic Hazard Assessment

The earthquake return period of 475 years, considered in seismic codes and for peak rock accelerations shown on maps such as GSHAP, is only traditional. Recurrent periods of earthquakes within the period of the instrumental data (and historic data if they are not sparse) are considered in this monograph as short term. Instrumental data are available for period of about a hundred years only. Historic data availability varies between different regions. Ambraseys (2006a) showed that in most cases large earthquakes are less frequent when they are estimated from long-term data sets rather than from the instrumental period data sets making the notation of recurrence time and of hazard assessment questionable.

Because instrumental and historic earthquake data are sparse (incomplete) or not accurate, a seismic hazard assessment should also consider tectonic settings (geological features) and terrestrial or satellite observations of fault movements.

### 3.4.1 *Historic and Instrumental Seismic Data Based*

Prior to the development and deployment of modern seismic instruments, the sizes of earthquakes are based on their intensities, which are subjective and qualitative historic descriptions of the effects of earthquakes. Several scales of earthquake intensity exist such as Rossi-Forel (RF) now replaced by modified Mercalli intensity (MMI) scale, Medvedev-Spoonheuer-Karnik (MSK) scale and the Japanese Meteorological Agency (JMA) scale. A comparison between different earthquake intensity scales is provided by Richter (1958) and Murphy and O'Brien (1977). Several authors provide correlations between earthquake intensity and magnitude scales but the scatter in these relationships is usually very large because of unreliability of intensity data.

Gutenberg and Richter (1944) gathered data for the earthquakes in southern California over a period of many years and divided the number of exceedance of each magnitude by the length of the time period to define a mean annual rate of exceedance  $\lambda$  of an earthquake magnitude. The reciprocal value of the annual rate of exceedance for a particular magnitude is commonly referred to as the return period  $T_M$  of earthquakes exceeding magnitude  $M$ .

For engineering purposes, the effects of very small earthquakes are of little interest and it is common to disregard those that are not capable of causing significant damage, with the magnitudes less than about 4 to 5 (e.g. Kramer, 1996). Standard Gutenberg-Richter relationship predicts nonzero mean rates of exceedance for magnitudes up to infinity, which is not supported by available data. For these reasons, the bounded recurrence relationship is used (e.g. Kramer, 1996, who also listed other recurrence models).

Deterministic seismic hazard analysis (DSHA) has been used extensively in the past. Its goal is to determine worst-case ground motions. Reiter (1990) described four-step process for DSHA consisting of:

1. Identification and characterization of all earthquake sources capable of inducing ground motion of engineering significance at the site under consideration.
2. Selection of a source-to-site distance parameter for each source zone.
3. Selection of the controlling earthquake, which can produce the strongest shaking at the site.
4. Determination of the seismic hazard at the site in terms of peak values of ground motion or response spectrum ordinates.

The analysis is over conservative when the return period of the earthquake contributing to the worst-case ground motion is much longer than the useful life of a structure so that the probability of the earthquake occurrence is rather small.

In the past few decades the use of probabilistic concepts has allowed uncertainties in the size, location and rate of occurrence of earthquakes and in the variation of ground motion characteristics with earthquake size and location to be explicitly considered in the evaluation of seismic hazard. Probabilistic seismic hazard analysis (PSHA) provides a framework in which these uncertainties can be identified, quantified and combined in a rational manner to provide a more complete picture of the seismic hazard (e.g. Kramer, 1996). Reiter (1990) described four-step process for PSHA. Comments on these steps are as follow:

1. Identification and characterization of all earthquake sources capable of inducing ground motion of engineering significance at the site under consideration. In most cases, uniform probability distributions are used for each source zone under assumption that earthquakes are equally likely to occur at any point within the source zone. These distributions are then combined with the source geometry to obtain the corresponding probability distributions of source-to-site distance. Probability distributions of source-to-site distances are obtained assuming that the distances are independent of the source recurrence probabilities although they are related to them. For example, for only two point sources and two source-to-site distances each distance has 50% probability of occurrence if independent from the source recurrent period. If, for example, one source has a recurrence rate of  $10^{-2}$  per year and the other source  $10^{-3}$  then the weighted probabilities of source-to-site distances are 90.9% and 9.1% respectively, i.e.  $10^{-2} \times (10^{-2} + 10^{-3})^{-1} \times 100 = 90.9\%$  and  $10^{-3} \times (10^{-2} + 10^{-3})^{-1} \times 100 = 9.1\%$ .
2. The seismicity of each seismic zone is characterized by the recurrence relationship, which specifies the average rate at which an earthquake of some size will be exceeded. Such relationship can be established for very large regions involving many faults because each fault produces a rather limited range of less than  $\pm 1$  magnitude from the mean magnitude (e.g. Wells and Coppersmith, 1994). The use of recurrence relationship derived for a zone to a fault is very conservative and inappropriate. Also, considering zones instead of individual faults implies that large earthquakes could occur anywhere within that zone, which is very conservative.
3. Empirical attenuation relationships are selected for prediction of the effect of earthquake sizes at different distances. Such empirical attenuation relationships are defined for a fault with a single source-to-site distance and not for varying

distances along very large seismic zones. Equation (1.3) is applicable to a fault area.

4. The uncertainties in earthquake location, earthquake size, and ground motion parameter prediction are combined to obtain the probability that the ground motion parameter will be exceeded during a particular time period. A Poisson process of earthquake occurrence is assumed. Unless special measures are taken, this does not account for the time clustering of the events.

A PHSA is intended for evaluation of the hazard from independent events. For this reason dependent events, like foreshocks and aftershocks, are not considered and their effects must be accounted for in separate analyses. Similarly, time clustering of earthquake events is not considered by assuming Poisson's distribution of the events in time. When the most likely earthquake magnitude and the most likely source-to-site distance need to be defined, a technique of deaggregation is applied (e.g. McGuire, 1995; Kramer, 1996).

Instrumental and historic earthquake data (e.g. Ambraseys and Melville, 1982; Ambraseys et al., 1994; Ambraseys and Adams, 2001) are not always available in sufficient quantity and other data need to be used such as tectonic (e.g. Heaton and Kanamori, 1984), paleoseismic (e.g. McCalpin, 1996), archaeological (e.g. Ambraseys, 2005, 2006a; Galadini and Hinzen, 2006), observational (e.g. Jackson, 2001). Such considerations may not be conclusive and it is difficult to quantify their degree of uncertainty.

The use of logic trees (e.g. Kramer, 1996) may provide a convenient framework for an explicit treatment of model uncertainty. The assignment of weighted factors in the logic trees is subjective.

### **3.4.1.1 An Example of the Application of Gutenberg and Richter Type Relationship**

The example of Gutenberg – Richter relationship is based on data by Ambraseys and Sarma (1999) for the 1018 earthquakes from Iran ( $26^{\circ}$  to  $40^{\circ}$  North and  $44^{\circ}$  to  $64^{\circ}$  East) with the range of surface wave magnitudes from 4.5 to 7.4 over the period of 79 years (1900 to 1979). Figure 3.19 depicts a mean annual rate of exceedance versus the surface wave magnitudes obtained from these data.

The curve shown in Fig. 3.19 uses the following bi-linear expression for mean annual rate of exceedances depending on surface wave magnitudes:

$$\begin{aligned}\log_{10}(\lambda) &= 4.7 - 0.8 \cdot M_s \quad 4.5 \leq M_s \leq 7.1 \\ \log_{10}(\lambda) &= 11.27 - 1.72 \cdot M_s \quad 7.1 \leq M_s \leq 7.4\end{aligned}\tag{3.20}$$

### **3.4.2 Observational Method**

Measuring of fault movement and inference of fault activity based on the results of the measurements are gaining popularity. If it is assumed that all earthquake energy is released within a magnitude range from 5.5 to 9 (i.e. contribution of smaller

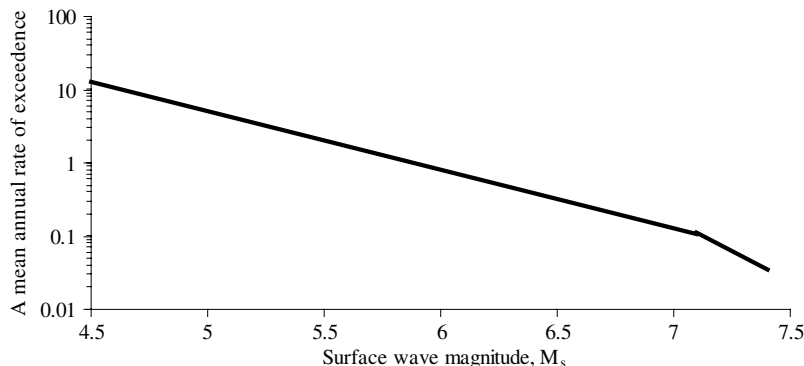


**Fig. 3.19** A mean annual rate of exceedance of Iranian earthquakes in the period 1900 to 1979

magnitudes is ignored and magnitudes greater than 9 are very rare) and that the average fault displacement is one-half of the maximum surface displacement then the rate of fault movement can be related to earthquake magnitude and earthquake recurrence period  $T_r$  as given by the following equations based on Slemmons (1982) data.

$$T_{r,lower\ bound} = 10^{(-3.614+0.657 \cdot M)} \cdot \frac{10}{fault\ slip\ rate} \quad (3.21)$$

$$T_{r,upper\ bound} = 10^{(-3.314+0.657 \cdot M)} \cdot \frac{10}{fault\ slip\ rate},$$

where  $M$  is earthquake magnitude (in the range from 5.5 to 9), and fault slip rate is in cm/year. The formulae are useful for fast moving faults. For a fault slip rate of less than 0.001 cm/year and the precision of measurement of up to 0.1 cm, the observation period should be in excess of 100 years.

It is difficult to infer stresses at fault surfaces because of great depths involved and non-linear stress-strain relationships exhibited by rocks (e.g. Srbulov, 2006b). Scholz (1968), for example, showed for marble that the relationship is highly non-linear and is not affected further with increase of confining pressures beyond 300 MPa ( $\sim 11$  km depth).

### 3.4.2.1 Radar and Satellite Techniques

The interferometric synthetic aperture radar (InSAR) technique is based on detecting the shift in phase of reflected radiation waves from the Earth's surface using the satellites orbiting around the Earth (e.g. Jackson, 2001). It enables vertical shifts in the landscape to be detected to accuracy of up to 0.1 mm. Processed satellite radar data allow ground movements to be mapped to 1 mm/year over wide areas (e.g. Ferretti et al., 2001). This technique is useful when a fault is not exposed at the surface. When a fault trace is exposed at the surface, traditional survey methods can

be used (such as leveling and electronic distance measurement) because only the change in relative displacements between two locations across a fault needs to be monitored.

An exponential increase of strain over time could indicate approach of a fault rupture. Strain can be inferred from recorded incremental displacements obtained by Global Positioning System (GPS) (e.g. Leick, 1995) or terrestrial surveying methods.

The relationships between incremental axial  $\Delta\varepsilon$  and shear  $\Delta\gamma$  strains and componential incremental displacements  $\Delta u$ ,  $\Delta v$ ,  $\Delta w$  in  $x$ ,  $y$ ,  $z$  directions at three observational points on the Earth's surface can be expressed as (e.g. Timoshenko and Goodier, 1951)

$$\begin{Bmatrix} \Delta\varepsilon_x \\ \Delta\varepsilon_y \\ \Delta\varepsilon_z \\ \Delta\gamma_{xy} \\ \Delta\gamma_{yz} \\ \Delta\gamma_{zx} \end{Bmatrix} = \begin{bmatrix} \frac{\partial}{\partial x} & 0 & 0 \\ 0 & \frac{\partial}{\partial y} & 0 \\ 0 & 0 & \frac{\partial}{\partial z} \\ \frac{\partial}{\partial y} & \frac{\partial}{\partial x} & 0 \\ 0 & \frac{\partial}{\partial z} & \frac{\partial}{\partial y} \\ \frac{\partial}{\partial z} & 0 & \frac{\partial}{\partial x} \end{bmatrix} \times \begin{Bmatrix} \Delta u \\ \Delta v \\ \Delta w \end{Bmatrix} \quad (3.22)$$

The incremental displacements at a place with coordinates  $x$ ,  $y$ ,  $z$  can be expressed as linear functions of the coordinates if a constant strain field is assumed (other functions are possible, e.g. Zienkiewicz and Morgan, 1983)

$$\begin{Bmatrix} \Delta u \\ \Delta v \\ \Delta w \end{Bmatrix} = \begin{bmatrix} a_1 & a_2 & a_3 \\ b_1 & b_2 & b_3 \\ c_1 & c_2 & c_3 \end{bmatrix} \times \begin{Bmatrix} x \\ y \\ z \end{Bmatrix} \quad (3.23)$$

The coefficients  $a_{1,2,3}$ ,  $b_{1,2,3}$ ,  $c_{1,2,3}$  are calculated from measured incremental displacements  $\Delta u_{1,2,3}$ ,  $\Delta v_{1,2,3}$ ,  $\Delta w_{1,2,3}$  at minimum three GPS survey locations with the coordinates  $x_{1,2,3}$ ,  $y_{1,2,3}$ ,  $z_{1,2,3}$

$$\begin{Bmatrix} a_1 \\ a_2 \\ a_3 \end{Bmatrix} = \begin{bmatrix} x_1 & y_1 & z_1 \\ x_2 & y_2 & z_2 \\ x_3 & y_3 & z_3 \end{bmatrix}^{-1} \times \begin{Bmatrix} \Delta u_1 \\ \Delta u_2 \\ \Delta u_3 \end{Bmatrix} \begin{Bmatrix} b_1 \\ b_2 \\ b_3 \end{Bmatrix} = \begin{bmatrix} x_1 & y_1 & z_1 \\ x_2 & y_2 & z_2 \\ x_3 & y_3 & z_3 \end{bmatrix}^{-1} \times \begin{Bmatrix} \Delta w_1 \\ \Delta w_2 \\ \Delta w_3 \end{Bmatrix}, \quad (3.24)$$

$$\begin{Bmatrix} c_1 \\ c_2 \\ c_3 \end{Bmatrix} = \begin{bmatrix} x_1 & y_1 & z_1 \\ x_2 & y_2 & z_2 \\ x_3 & y_3 & z_3 \end{bmatrix}^{-1} \times \begin{Bmatrix} \Delta v_1 \\ \Delta v_2 \\ \Delta v_3 \end{Bmatrix}$$

where the exponent  $-1$  denotes matrix inversion. Similar procedure applies for four or more GPS survey locations for which higher order interpolation functions are used. From Equations (3.23) and (3.24), Equation (3.22) becomes

$$\begin{Bmatrix} \Delta\epsilon_x \\ \Delta\epsilon_y \\ \Delta\epsilon_z \\ \Delta\gamma_{xy} \\ \Delta\gamma_{yz} \\ \Delta\gamma_{zx} \end{Bmatrix} = \begin{Bmatrix} a_1 \\ b_2 \\ c_3 \\ a_2 + b_1 \\ b_3 + c_2 \\ a_3 + c_1 \end{Bmatrix} \quad (3.25)$$

The locations of the observation points could be chosen so that two of them are on one side and parallel to a fault while the third one is across the fault and perpendicular to the direction of the first two observation points so that the calculated displacements are obtained in the directions parallel and perpendicular to the fault. For deep faults, which have not ruptured the Earth's surface, it can be assumed that the strains at depth are proportional to the strains at the surface although their increments in regular interval of time are considered and not the absolute values.

Ambraseys (2006b) compared knowledge relating to historical earthquakes with the understanding of present-day earthquake mechanisms and overall global positioning system (GPS) slip rates in the eastern Mediterranean region and demonstrated that the slip rates calculated from the historical data are in general comparable to those calculated from GPS measurements and field observations, while the size of historical earthquakes and their uncertainty can be quantified.

## 3.5 Long Term Seismic Hazard Assessment

Recurrent periods of earthquakes exceeding the period of instrumental data (and historic data if they are not sparse) are considered as long term in this monograph.

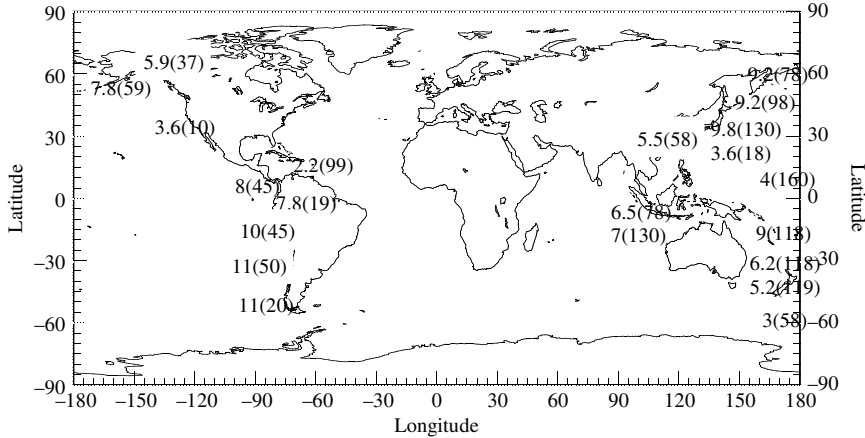
### 3.5.1 Tectonic Data Based

Plate tectonics (which evolved from the theory of continental drift, Taylor, 1910; Wegener, 1915) and elastic rebound theory (Reid, 1911) indicate that earthquakes occur to relieve the energy that accumulates as the plates move relative to each other.

For major subduction zones, Ruff and Kanamori (1980) related maximum magnitude to both the rate of convergence and the age of the subducted tectonic plate as:

$$M_w = -0.0089 \cdot T_p + 0.134 \cdot V_r + 7.96, \quad (3.26)$$

where  $T_p$  is the age in millions of years and  $V_r$  is the rate of tectonic plate subduction in cm/year. Heaton and Kanamori (1984) used a number of actual earthquake magnitudes to compare with the results from Equation (3.26). From this comparison, it is possible to determine the ages and rate of convergence along some of the subduction zones, Fig. 3.20.



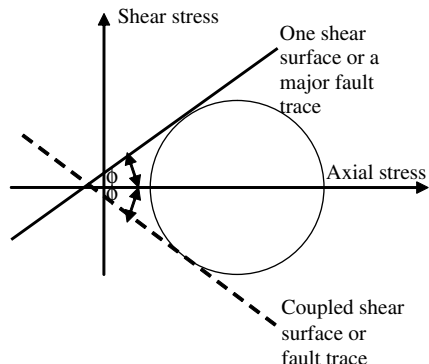
**Fig. 3.20** Rate of convergence in cm/year and age (in bracket) in millions of years before present of some of the subduction zones based on data by Heaton and Kanamori (1984)

Dependence of earthquake size on the causative fault area and the average slip of fault enabled establishment of empirical correlations between the fault parameters and earthquake magnitude. Wells and Coppersmith (1994) provided empirical relationships between the moment magnitude  $M_w$  (ranged 6–7), the surface rupture length  $L_r$  (km), the fault rupture area  $A_{fault}$  ( $\text{km}^2$ ), and the maximum surface displacement  $D_s$  (m) for different fault types. The ratio between fault area and its length gives an indication of its depth below the thickness of non-seismogenic zone (0–5 km).

$$\begin{aligned}
 M_w &= 5.16 + 1.12 \cdot \log L_{r,\text{strike-slip}} \pm 0.28 \cdot n_d \\
 M_w &= 5.00 + 1.22 \cdot \log L_{r,\text{reverse}} \pm 0.28 \cdot n_d \\
 M_w &= 4.86 + 1.32 \cdot \log L_{r,\text{normal}} \pm 0.34 \cdot n_d \\
 M_w &= 5.08 + 1.16 \cdot \log L_{r,\text{all}} \pm 0.28 \cdot n_d \\
 M_w &= 3.98 + 1.02 \cdot \log A_{\text{strike-slip}} \pm 0.23 \cdot n_d \\
 M_w &= 4.33 + 0.90 \cdot \log A_{\text{reverse}} \pm 0.25 \cdot n_d \\
 M_w &= 3.93 + 1.02 \cdot \log A_{\text{normal}} \pm 0.25 \cdot n_d \\
 M_w &= 4.07 + 0.98 \cdot \log A_{\text{all}} \pm 0.24 \cdot n_d \\
 M_w &= 6.81 + 0.78 \cdot \log D_{s,\text{strike-slip}} \pm 0.29 \cdot n_d \\
 M_w &= 6.52 + 0.44 \cdot \log D_{s,\text{reverse}} \pm 0.52 \cdot n_d \\
 M_w &= 6.61 + 0.71 \cdot \log D_{s,\text{normal}} \pm 0.34 \cdot n_d \\
 M_w &= 6.69 + 0.74 \cdot \log D_{s,\text{all}} \pm 0.40 \cdot n_d
 \end{aligned}, \quad (3.27)$$

where  $n_d$  is the number of standard deviations according to Wells and Coppersmith (1994). Field studies of fault rupture length and the maximum surface displacement

**Fig. 3.21** Orientations of shear surfaces and tectonic fault pair with respect to the direction of maximum axial stress



are important for inference of the sizes of past earthquakes. A number of other studies have been performed for different regions, e.g. for the Eastern Mediterranean region by Ambraseys and Jackson (1998).

It should be remembered that Mohr-Coulomb circle of stresses indicate that the shear surfaces and tectonic faults tend to appear in pairs inclined to each other at an angle equal to the double friction angle  $\phi$  of material, as shown in Fig. 3.21. Rock friction angles are described by Hoek (1983), for example.

### 3.5.2 Paleoseismic Data Based

Geomorphic changes arise due to seismogenic fault rupture of the Earth's surface, or by warping or folding of surfaces because of fault movement. McCalpin (1996) considers, for example, the amount of lateral offset of young stream channels, the thickness of colluvial wedges in fault exposures and the amount of uplift of former shorelines as the primary paleoseismic evidence caused by a particular fault. Geomorphic changes can also be caused by climate changes (glaciation for example), weathering and erosion/deposition processes, volcanism, tsunamis, slope failures etc.

The landforms are typically used to reconstruct paleoseismic offset histories: fluvial terraces, stream channels and alluvial fans. Geomorphic studies commonly yield the size of paleoearthquake and stratigraphic studies are most likely to yield the timing of paleoearthquakes to a maximum about 50,000 years before present. The uncertainty in measuring lateral displacement because of faulting has two components, the first arising from the preservation of the landform and its correlation across the fault (qualitative), the second from locating correlative points on the landform and then projecting them to the fault trace (quantitative) (Weldon et al., 1996).

The primary geomorphic indicator of paleoearthquakes on normal faults is a fault scarp. Normal fault scarps, according to strict definition, vary from mountain front thousands of meters high cut on bedrock, to decimeter scale scarples that

displace Quaternary alluvium and colluviums (Stewart and Hancock, 1990). Overlaps, step-overs and gaps are common in normal fault surface ruptures. Studies of large-scale range-front morphology are insufficiently precise to identify individual paleoearthquakes, so they belong to neotectonics. Also, range-front morphology can be controlled by factors other than uplift rate, such as climate, lithology and structure (McCalpin, 1996).

The primary geomorphic indicators of paleoearthquakes on reverse (thrust) faults are surface displacements around the faults (frequently bifurcated towards the surface), growth of surface folds and changes in the elevation of the land surface. Convergent tectonic plate margins are the largest and most widespread compressional tectonic environments. Local compressional tectonic environments are found at restraining bends or stopovers along transform and strike-slip faults, along transpressive strike-slip faults, in fold and thrust belts in some backarc regions and some in continental interiors. Paleoearthquake characteristics often become apparent only after observations at many sites are integrated into a composite view of coseismic deformation across a large region. Two types of secondary faults are associated with thrust faults. The crest of active surface anticlines are commonly cut by normal faults and grabens that trend along the fold crest parallel to the fold axis. Sudden bending of thick-bedded sequences of sediments is often accompanied by slip along bedding planes in the fold limbs. This slip generates slip faults that are rooted in the axis of folds and extend through the fold limbs (e.g. Carver and McCalpin, 1996).

Strike-slip faults produce characteristic landforms including linear valleys, offset of deflected streams, shutter ridges, sag ponds, pressure ridges, benches, scarps and small horsts and grabens (Keller, 1986). In many cases the fault trace is composed of a wide zone of alternating tension gashes (extensional) and moletracks (compressional) that trend obliquely with respect to overall fault strike.

Sieh and Jahns (1984), for example, used the offset of 380 m and 475 m of Wallace Creek, an ephemeral stream that flows southwest from the Temblor Range and crosses the San Andreas Fault, to recognize the past offsets which happened 10000 years and 3700 years before present, while the current offset is 120 m. From this they deduced a long-term slip rate for the fault of  $32 \pm 3$  mm/year. The site was last ruptured in the earthquake of 1957, when the slip was 9.5 m. From the offset of the gullies they were able to recognize four earlier earthquakes at the site with similar slips, although they did not determine their dates. Although few other methods are as accurate as radiocarbon dating, the disturbing degree of inter laboratory analytical variability is documented in some recent studies (e.g. McCalpin, 1996). The offsets of the gullies may not only be caused by past earthquakes but also past floods carrying large amounts of materials, which were deposited and formed natural barriers when the flow gradient decreased in the valley.

Matsuda et al. (1978), in another example, made a study of uplifted terraces in Kanto district. It seems that more earthquakes occurred on this plate boundary than are indicated by individual terraces. One possibility is that coseismic uplifts interfere with eustatic rises and falls in sea level so that only a few of them get preserved. Another possibility is that slip on imbricate strands accentuates just a few of the terraces (Scholz, 1990).

Secondary paleoseismic evidence, termed “forensic geotechnical earthquake engineering evidence” by Srbulov (2007d), is caused by seismic wave effects away from fault zone. It usually involves slope failures and sand liquefaction. Slope failures are dealt with in Chapter 4 and sand liquefaction in Chapter 5.

Earthquakes can trigger all sorts of slope failures, from disrupted slides and falls to coherent slides and lateral spreads. Slope failures are identified by anomalous topography, including arcuate or linear scarps, backward-rotated masses, benched or hummocky topography, bulging toes, and pounded or deranged drainage. Abnormal vegetation type or age also is common. Submarine failures can be identified with the aid of marine remote-sensing techniques (e.g. Field et al., 1982). However, slope failures can also be caused by other factors such as rainfall, erosion at the toe, loading at the crest, weathering, tectonics, ground water level change and artesian pressures.

Keefer (1984) studied the effects of 40 historical earthquakes on slope failures and the results of his finding are shown in Table 3.3. He also provided the graphs between an area affected by slope failures and the earthquake magnitude and the maximum epicentral distances of different types of slope failures and earthquake magnitudes. These graphs provide only limited values and their use will cause an underestimate of earthquake magnitudes and an overestimate of the source to site distances (e.g. Srbulov. 2007d).

Jibson (1996) reviews several methods for dating slope failures including historical, dendrochronology, radiocarbon, lichenometry, weathering rinds, pollen analysis, and geomorphic analysis.

Earthquakes can cause liquefaction of granular soil, but other causes of liquefaction exist too. Obermeier (1996) noted that, among other factors causing liquefaction are rapid sedimentation and loading, artesian conditions, slumping, chemical weathering and periglacial environment. He also describes the effect of soil liquefaction observed when a low permeability layer exists over liquefied soil. If the ground surface of the cap layer is slightly inclined then the top layer exhibits cracks, uneven

**Table 3.3** Types, frequency and minimum triggering magnitudes of earthquakes to cause slope failures

Type of slope failure	Frequency of occurrence during earthquakes	Minimum triggering earthquake magnitude M <sub>L</sub>
rock falls, disrupted soil	very frequently	4.0
slides, rock slides		4.0
soil lateral spreads, soil slumps, soil block slides,	frequently	5.0
soil avalanches		4.5
soil falls, rapid soil flows, rock slumps	moderately frequently	6.5
sub aqueous landslides, slow earth flows, rock block slides, rock avalanches	uncommon	4.0
		5.0
		5.0
		5.0
		6.0

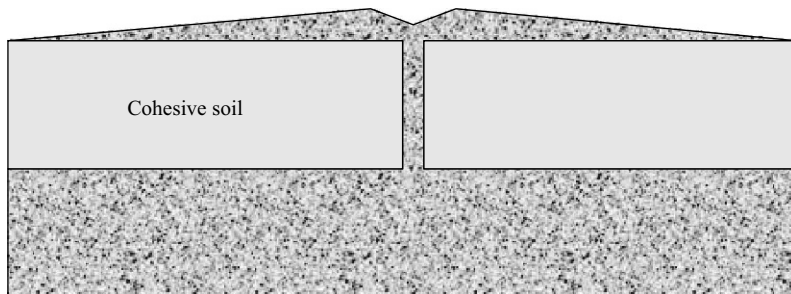


**Fig. 3.22** Cross section of a sand volcano

surface due to differential settlement and some lateral movement. If the ground surface of the cap layer is nearly horizontal and the thickness of the top layer is less than 10 m then so called sand volcanoes, Fig. 3.22, can be formed through previous desiccation cracks, rotten tree roots and channels burrowed by animals. The expelled sandy soil spreads around and forms a layer. When such layers are buried by new deposits, they leave a permanent record of the past event. If sand volcanoes are prevented by greater thickness of the overlaying layer or tree roots provide sufficient reinforcement to hold the top layer intact then sills are formed within upper sandy layers.

Besides earthquake magnitude, seismic hazard involves also determination of recurrence period of the magnitudes. Radiocarbon  $^{14}\text{C}$  dating of fossils can be used for estimation of the age of event. However, previous evidence can be destroyed by subsequent earthquakes, particularly if the subsequent earthquakes are of greater magnitudes than the previous earthquakes.

The importance of paleoseismology increases with decreased amount of other available data. Despite possible insufficient accuracy in the interpretation of prehistoric events, the existence of past events is important as evidence because the events tend to reoccur.

### 3.6 Summary

Assessment and selection of seismic data for the analyses is one of the most complex tasks in geotechnical and earthquake engineering. The simplified analyses require different seismic parameters as input data.

- Peak horizontal and vertical ground acceleration and velocity are frequently assessed using local or generalized empirical attenuation relationships based on earthquake magnitude, source to site distance, local soil and tectonic fault types. The attenuation relationships do not account for the effects of the rupture directivity, Moho bounce, sediment basin edge and topographic effects. The influence of such additional factors must be assessed individually and considered

by adding (a part of) standard deviations to the average values predicted by the attenuation relationships.

- Response spectral accelerations are usually obtained from local or international codes and standards or from a number of published attenuation relationships. The spectral accelerations are usually anchored to the ground peak acceleration at zero structural period. In any case, response spectral accelerations do not consider a number of additional factors listed above for the peak acceleration. The importance of such factors must be assessed individually and their effect taken into account for the response spectra.
- The choice of acceleration time histories is either based on earthquake magnitude, the site to source distance and local soil type if they are obtained from data bases or such that the acceleration response spectra of artificial time histories much predefined spectral values. A number of additional factors listed above for the peak acceleration must be considered separately and their effect taken into account in the selection of time histories.
- Earthquake magnitudes and the source to site distances used for the selection of the peak values, response spectral values of acceleration time histories are assessed by consideration of seismic hazard at a particular location. Seismic hazard consideration should take into account not only earthquake source size and type but also the effect of rupture propagation and space and time clustering, which are rarely considered in practice.
- Seismic hazard at a location should be based on consideration of not only all historic data on earthquake sources and instrumental data i.e. recording of recent earthquakes but also tectonic and paleoseismic data and observation of fault and ground surface movements using terrestrial or satellite methods.

The following chapters contain description which earthquake parameters are used as input data for the simplified models.

# **Chapter 4**

## **Slope Stability and Displacement**

### **4.1 Introduction**

Besides inducing inertia forces, earthquakes cause frequently ground failures and deformations. Different classifications of slope failures exist (e.g. Varnes, 1978). One such classification is given in the first column of Table 3.3. Besides the type of material involved (soil or rock) and the type of movement (rotational, translational or combined sliding, falling, spreading, flowing) other parameters may be considered such as speed of propagation (extremely rapid with more than 3 m/s to extremely slow with less than 10 cm/year), depth (shallow with extent smaller than the slope height and length, or deep with extent greater than the slope height and length) etc.

Ground movements caused by earthquakes can vary from a few centimeters to many kilometers. The objective of this chapters to describe different types of ground failures/displacements and simplified methods for their analyses.

### **4.2 Slope Stability**

Duncan (1996), for example, reviewed available methods for the analysis of stability and deformation of slopes in static condition. Essentially, one can use either a limit equilibrium method or a numerical method.

Limit equilibrium (LE) methods are very commonly used for slope stability analysis. Typically, a LE method fulfils only condition of equilibrium of forces and turning moments, while the other physical conditions may be violated. A safety factor is used in part to compensate for this incompleteness. A safety factor also caters for uncertainties in assumed slope geometry (with/without open cracks), soil properties, assumed loading, and boundary conditions (such as rainfall).

Numerical methods include finite elements, discrete elements, boundary elements, and finite difference methods. These allow analyses of slope deformability and slope-structure interactions. In principle, numerical methods can fulfill all equilibrium conditions of stresses, constitutive relations between the stresses and corresponding strains, and compatibility conditions between strains and displacements

gradients. However, there is considerable debate about the constitutive behavior of soil and how to model it. Numerical methods are often complex to use and verify.

### 4.2.1 Limit Equilibrium Method for Two-Dimensional Analysis by Prismatic Wedges

Many limit equilibrium methods are based on division of a potential sliding mass into vertical slices or wedges so that the equilibriums of forces and moments are considered for each slice or wedge. For the two-dimensional case, a potential sliding mass with slices, wedges and forces acting on a wedge are shown in Fig. 4.1. The inertial forces arising from ground motions are usually considered using pseudo static consideration, which is acceptable if ground properties and excess pore water pressure in cyclic condition are also considered.

In the above figure,  $N_i$  is force acting in the direction that is perpendicular to the surface of a wedge base or interface,  $T_i$  is force acting in the direction that is parallel to the surface of a wedge base or interface,  $W$  is wedge weight,  $GW$  is ground water force acting in the direction that is perpendicular to the surface of a wedge base or interface,  $c_{vm}$  and  $c_h$  are the ratios of the inertial forces acting on a wedge with respect to the wedge weight,  $b_i$  is breadth of wedge base or interface.

Conventional limit equilibrium methods use a constant factor of safety  $FS$  along a potential slip surface (and sometimes interfaces) under the assumption that soil shear strength is mobilized at all places at the same (or similar) shear strains. Srbulov (1987) developed a more sophisticated, though still simplified approach in which account was taken of the relation between shear stress and strain. The following description is based on the paper by Srbulov (2001) with permission from Elsevier.

Figure 4.2 shows a combined plot of soil shear strength dependence on compressive stress acting on considered surface and soil shear strength dependence on

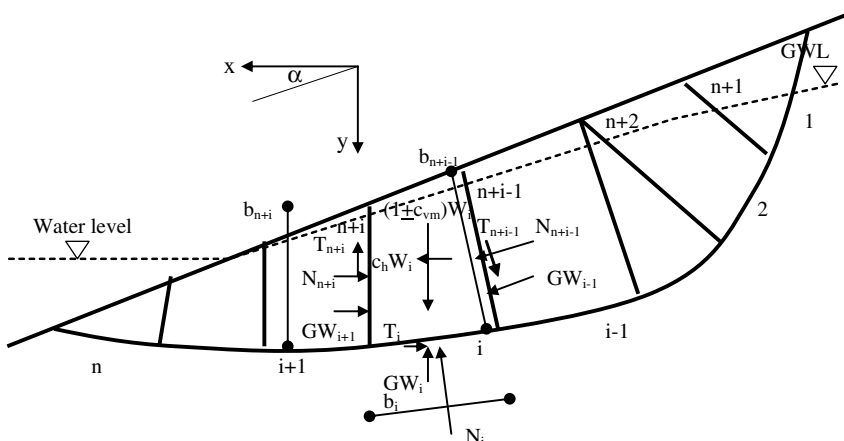
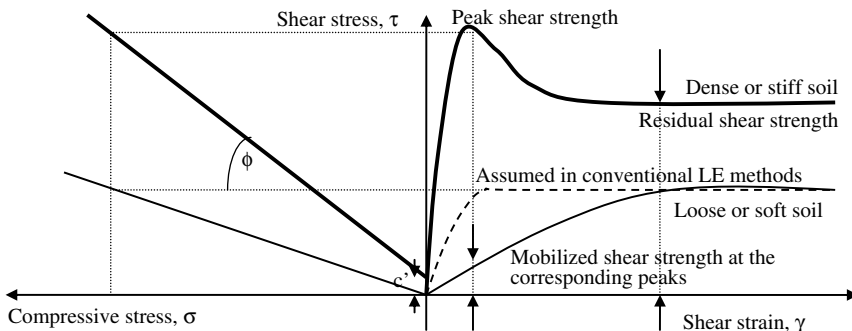


Fig. 4.1 Division of a potential sliding mass into  $n$  slices/wedges and forces acting on  $i$ th wedge



**Fig. 4.2** Stress and strain relationships for two different soil types within a slope

achieved shear strain. The left side shows soil friction angle  $\phi$  and shear strength (cohesion)  $c$  at zero compressive stress. These values are chosen as follows:

- In a drained analysis, during very slow shear rates (static condition without earthquake), the cohesion intercept  $c$  is the result of linearization of a non-linear relationship between soil shear strength and compressive stress.
- In an undrained condition, at fast shear rates during earthquake and in fine grained soil, the friction angle  $\phi$  is zero in fully saturated condition while the cohesion intercept  $c_u$  depends on many factors such as consolidation state (normally or over consolidated), soil plasticity index (Section 2.3), direction of shearing, shear rate etc.

The right side of Fig. 4.2 shows soil peak and residual strength of dense/stiff and loose/soft soil. Peak soil shear strength is the result of dense/stiff soil dilation on shearing, when soil grains/particles are tightly pack and must either roll over adjacent grains, which results in soil volume increase and decreases of excess pore water pressure, or to a lesser degree breaking of soil grains. Significant soil sample disturbance results in soil loosening/softening and an apparent loss of the peak shear strength. Dense/stiff soil is less deformable than loose/soft soil, which achieves its peak shear strength at larger deformations (strain). When dense/stiff and loose/soft soil coexists within a slope, the dense/stiff soil will achieve its peak shear strength sooner than loose/soft soil. The dense/stiff soil can then suffer loss of peak shear strength with further loading/straining, particularly if it alone cannot carry the applied load but also needs activation of the peak shear strength of adjacent loose/soft soil.

However, the use of peak shear strength of dense/stiff soil (which exhibits post peak shear strength decrease with increase in shear strain) when loose/soft soil is also present within a slope is unsafe in conventional limit equilibrium methods, which assume that both dense/stiff and loose/soft soils achieve their peak shear strength at the same shear strain, because shear strain is not considered by the method.

Brittle soil (which exhibits decrease of their shear strength and stiffness with increase in strain) tends to experience rapid slope failures leaving no time for eventual remediation. Because of the speed of development of brittle soil failures, the observational method is not useful in this case. Such soil behavior can also be a source of instability of numerical procedures if tangent soil modulus (Fig. 2.1) becomes negative in the post peak region and secant soil modulus is not considered.

The use of residual shear strength of dense/stiff soil when loose/soft soil is also present within a slope in order to be on a safe side is very conservative unless the slope failed before and exhibited large shear strain so that the actual soil shear strength is close to the residual strength.

Factor of safety  $FS$  is usually defined as the ratio between available shear strength  $\tau_a$  and the shear stress  $\tau_e$  necessary to maintain limit equilibrium

$$FS = \frac{\tau_a}{\tau_e}, \quad (4.1)$$

where  $\tau_a$  is equal to the peak shear strength  $\tau_p$  when  $FS > 1$  or to the post-peak strength if yielding occurs. Using a linear Mohr-Coulomb failure criterion, which relates shear  $\tau_a$  and compressive stresses  $\sigma$ ,  $FS$  can be expressed in terms of these stresses

$$FS = \frac{c' + (1 - r_u) \cdot \sigma' \cdot \tan \phi'_1}{\tau_e}, \quad (4.2)$$

where  $c'$  is soil cohesion,  $r_u$  is the excess pore water pressure ratio and  $\phi'_1$  angle of soil internal friction. Several proposals for non-linear shear strength criterion exist. For example, for  $c' = 0$  the change of soil friction angle  $\phi'_1$  with effective (total less excess pore water pressure) compressive stress level  $\sigma'$  can be expressed as:

$$\phi'_1 = \phi_b + \frac{\Delta\phi}{1 + \frac{\sigma'}{p_n}}, \quad (4.3)$$

where the parameters  $\phi_b$ ,  $\Delta\phi$  and  $p_n$  for different soil types and rock joints are given by Maksimovic (1989a to 1996b).

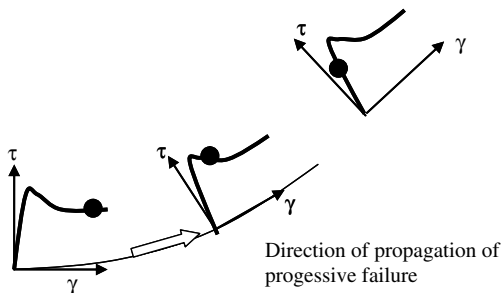
Equation (4.2) can be written in terms of normal  $N_i$  and shear  $T_i$  forces acting on a particular surface  $i$  as

$$FS = \frac{c' \cdot b_i + (1 - r_u) \cdot N'_i \cdot \tan \phi'_1}{T_i}, \quad (4.4)$$

where  $b_i$  is breath of the base or interface  $i$  of a wedge.

Knowing one of the components of the resultant forces acting along a slip surface and a constant  $FS$ , it is possible to calculate the other components, so that the number of unknown forces to be determined from available force and moment equilibrium equations is decreased.

**Fig. 4.3** Sketch of a shear zone with activated soil shear strength in the case of progressive failure



Shear strains are seldom uniform even within homogeneous soil and at relatively small stress levels. When shear strength of soil at large shear strain is smaller than its peak value then localized and propagating (progressive) failure may occur if induced shear strains are large enough, Fig. 4.3.

Similarly, if soil is heterogeneous and some parts mobilize and loose their peak shear strengths while the other parts are still on the way to mobilize the peak strength then again localized and progressive failures may occur. The problem of analyzing progressive failure may be avoided if only soil residual strength is considered. Soil reinforced by geogrids and geotextiles also experiences a progressive failure. However, when soil reinforcement is loaded beyond its ultimate strength it tends to break and completely loose all the strength as its residual strength is zero. In the later case, the use of residual strength only is pointless because it would lead to consideration of non-reinforced soil.

Different methods have been proposed to solve the problem of propagating (progressive) failure using numerical methods based on finite, discrete/distinct elements and finite difference. This sub-section describes a procedure for consideration of the local and progressive failures within the framework of limit equilibrium method when applied to analysis of stability of slopes, according to Srbulov (1987). The method has been applied to slopes, foundations, geogrid/geotextile reinforced embankments and retaining walls (Srbulov, 1988 to 2001) subjected to progressive failures.

The activation of shear stresses  $\tau_a$ ,  $\tau_e$  is accompanied by development of shear strains (Fig. 4.2) and therefore shear stress/strength can be expressed as a function of both axial stress  $\sigma$  and shear strain  $\gamma$ . The function is determined by soil shear tests. In its simplest form, when only the shape but not the value of function  $\tau - \gamma$  is assumed independent of  $\sigma$  up to the peak shear strength (Fig. 4.4), the function becomes for  $FS \geq 1$

$$\tau = C_s \cdot \sigma \cdot \gamma^k, \quad (4.5)$$

where  $C_s$ ,  $k < 1$  are soil constants determined by curve fitting from laboratory test results. The test results indicate that this assumption can be considered accurate for a rather large  $\sigma$  stress range only for cohesive soil under undrained conditions and reinforced soil when reinforcement strength has a greater influence on the behavior

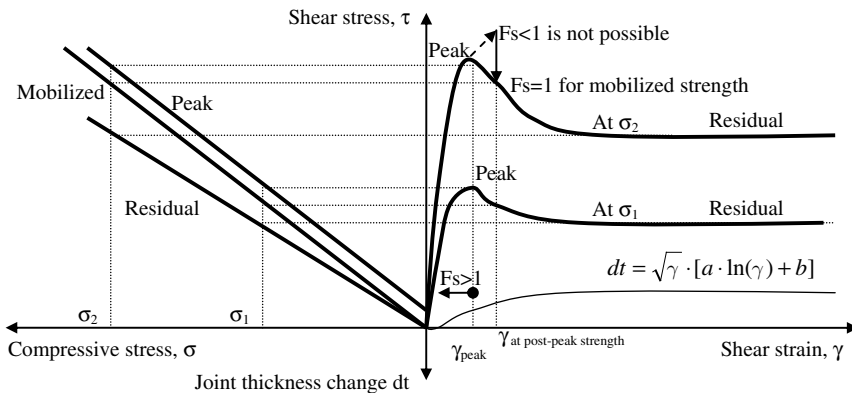


**Fig. 4.4** Stress and strain relationships for dense and stiff soil

of composite material. The  $\sigma$  stress dependent shapes of the function may be introduced but on account of the use of an additional iterative procedure that must be applied until the differences between initially assumed  $\sigma$  stress levels are close to the calculated  $\sigma$  stress levels within desired tolerance. An alternative approach would be division of a soil zone into sub-zones each corresponding to appropriate  $\sigma$  stress level as it has been done in the case when a nonlinear shear strength envelope is linearized within chosen  $\sigma$  stress intervals. While Fig. 4.2 shows stress/strain functions for dense/stiff and loose/soft soil, Fig. 4.4 shows such functions for dense/stiff soil only but for different compressive stresses  $\sigma_1$  and  $\sigma_2$ . In addition, Fig. 4.4 shows a functional relationship between the change in thickness  $dt$  of dense/stiff soil along a shear surface versus achieved shear strain  $\gamma$ .

Replacing Equations (4.5) into Equation (4.1), the factor of safety at the surface  $i$  can be written in the form

$$F_i = \frac{\gamma_{i,a}^k}{\gamma_{i,e}^k}, \quad (4.6)$$

where  $\gamma_{i,a}$  is the shear strain corresponding to available shear strength  $\tau_a$  at a joint  $i$  and  $\gamma_{i,e}$  is the shear strain corresponding to mobilized shear stress  $\tau_e$  at a joint  $i$ . Similarly at another surface  $j$ ,

$$F_j = \frac{\gamma_{j,a}^{k_1}}{\gamma_{j,e}^{k_1}}, \quad (4.7)$$

where the exponent  $k_1$  is different from  $k$  in the case when different soil types exist at the places  $i$  and  $j$ . From Equations (4.6) and (4.7) it follows

$$F_j = F_i \cdot \frac{\gamma_{j,a}^{k_1}}{\gamma_{i,a}^k} \cdot \frac{\gamma_{i,e}^k}{\gamma_{j,e}^{k_1}} \quad (4.8)$$

Unknown  $F_i$  can be determined from available equilibrium equations similarly to a constant  $FS$  in conventional methods. Mobilized shear strain can be determined from Equation (4.7)

$$\gamma_{j,e} = \frac{\gamma_{j,a}}{F_j^{\frac{1}{k_1}}} \quad (4.9)$$

The values of  $\gamma_{j,a}^{k_1}$  and  $\gamma_{i,a}^k$  are determined by soil stress-strain tests, such as simple shear. It should be noted that the ratio  $\gamma_{i,a}^k \gamma_{i,e}^{k-1}$  but not particular values of shear strains are necessary to calculate the local factor of safety at any surface  $j$ . This has a useful implication. If soil is tested in a direct shear apparatus then the ratio  $\gamma_{i,a}^k \gamma_{i,e}^{k-1}$  can be replaced by the ratio of measured horizontal displacements  $\delta_{i,a}^k \delta_{i,e}^{k-1}$ . If soil is tested in a triaxial apparatus then the ratio between measured axial strains is used  $\varepsilon_{i,a}^k \varepsilon_{i,e}^{k-1}$ . Load within geotextile/geogrid for soil reinforcement is usually described as a function of axial strain (eg. Jewel, 1990).

If a soil zone is divided into wedges (Fig. 4.1) and the wedges between their boundaries do not change their volumes (they are rigid) except that some local yielding is allowed at their tips then the ratio  $\gamma_{i,e}^k \gamma_{j,e}^{k_1-1}$  between the magnitudes of shear strains at two boundaries ( $i, j$ ) will be the same to the ratio  $\Delta_{i,e}^k \Delta_{j,e}^{k_1-1}$  of magnitudes of kinematically possible tangential displacements along these boundaries, because  $\gamma_{i,j}$  and  $\Delta_{i,j}$  will be directly proportional ( $\gamma_{i,j} = B_c \Delta_{i,j}$ , where  $B_c$  is an unknown constant). For rigid wedges, tangential displacements along a particular boundary will be constant. In undrained condition of saturated soil, there will be no volumetric changes along wedge boundaries and potential shear strain can be defined as the ratio between kinematically possible tangential displacements along the boundary and the boundary thickness. For a unit boundary thickness, the shear strains will be equal to the tangential displacements. Kinematically possible tangential displacements can be defined starting with a unit tangential displacement along the base of the first wedge. Proceeding along the external boundaries so that the known tangential displacement is the vector sum of the displacement in the directions of the interface and base of the following wedge it is possible to define all other kinematically possible displacements.

The assumption of no soil volume change along a boundary is not correct for drained conditions nor is correct to assume that the wedges are rigid. However, the volumetric changes due to normal stresses should be small for stiff soil and at relatively small  $\sigma$  stresses acting within most ground slopes. When they are likely to be significant such in soft clay and loose sand then the assumption of no volumetric strain due to normal stresses in drained condition is less acceptable.

Volumetric strain  $\varepsilon_v$  change along the boundaries (i.e. boundary thickness change  $dt$ ) with shear strain change is taken into account in the construction of kinematically possible displacements diagram as the inclinations of tangential displacement vectors with respect to the boundaries. From calculated  $F_j$  using Equation (4.8) it is possible to back calculate  $\gamma_{j,e}$  using Equation (4.9). The function of volumetric strain (specific thickness  $dt$ ) change versus shear strain  $\gamma$  (Fig. 4.4) is determined by

soil stress-strain tests. The angle of inclination  $\alpha_j$  of tangential displacement vector with respect to the boundary direction is simply

$$\alpha_j = \arctan \frac{dt_{j,e}}{\gamma_{j,e}} \quad (4.10)$$

Figure 4.5 depicts kinematically possible displacements for the first three wedges from Fig. 4.1 for simplicity.

If local over stressing occurs at face  $j$  (which means that  $F_j$  tends to become less than 1 and the mobilized strength greater than the peak value, which is impossible) then the yielding (Fig. 4.4), accompanied by an increase in shear strains  $\gamma_{j,e}$  can be simulated by the increase of  $\gamma_{j,a}$  in Equation (4.8) until  $F_j$  becomes equal to 1. Such simulation is necessary because fixed value  $\Delta_{j,e}$ , dependent on geometry only, is used instead of actual shear strain  $\gamma_{j,e}$ . With post peak increase (yielding) of shear strain  $\gamma_{j,e}$ , brittle soil will soften and therefore the corresponding decrease in the shear strength parameters  $c'$ ,  $\phi'$  with the increase in  $\gamma_{j,e}$  is taken into account in Equation (4.4). A change (an increase) in the factor of safety  $F_j$  will cause corresponding change in  $T_j$  force and consequently of all other forces because of the need to satisfy the equilibrium equations.

Using two wedges, Srbulov (1997) investigated the effect of rate of soil shear strength decrease below the peak value. He found that there will be an evident difference in the calculated factors of safety of the slope stability if soil decreases its peak strength towards the residual value more gradually then abruptly. In the former case the use of an instant jump from the peak to the residual strength is not appropriate. The calculated factors of safety by the extended method and by a classical method were also in a good agreement if soil exhibits an abrupt shear strength drop after the peak. However, classical method yields smaller factors of safety than the extended method for gradually decreasing post peak shear because the mobilized shear strength is somewhere between its peak and the residual value.

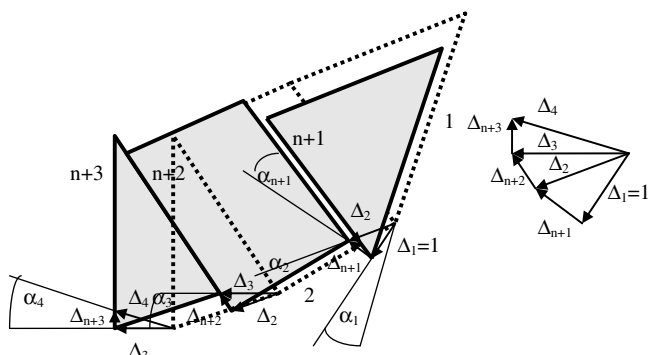


Fig. 4.5 Possible displacements  $\Delta_s$  of a moving mass

Two wedges were used by Srbulov (2001) for an investigation of the effect of change in volumetric strain (specific thickness) with shearing on calculated factor of safety. A function describing the specific thickness change  $dt$  with shear strain  $\gamma$  (Fig. 4.4) was adopted in the form which was deemed appropriate for both the contracting and dilating phases of soil volume (thickness) changes up to its constant value at the steady-state. Srbulov (2001) found that the effect of volumetric strain changes with shearing is not very important for the majority of slightly dilatant/contractant soil but could be very important for heavily over consolidated clay and very dense sand. Table 4.1 contains the list of unknown values, available equations and their numbers for  $n_w$  wedges.

It can be noted that the use of the local factors of safety  $F_j$  increased the number of unknown values and the number of available Equations (4.8) for  $n_w$  in comparison with the number of unknown values and available equations in conventional methods of limit equilibrium. It is also evident that the positions of normal forces  $N_i$  at the bases (except at the last base) are assumed to be in the middle of bases. Various assumptions have to be introduced in all procedures based on limit equilibrium method due to excessive number of unknown values in comparison with available limit equilibrium equations. Such assumptions cause that the solutions obtained by the methods are only approximate and not necessarily correct with regard to other stress-strain constitutive laws.

The system of  $3n_w$  equilibrium equations is nonlinear due to unknown  $F_i$  in the denominators of the coefficients of equations. It is possible to apply an iterative procedure by choosing an initial  $F_i (= 1)$ , solving  $3n_w - 1$  linear equations, checking

**Table 4.1** Unknown values, available equations, and their numbers for  $n_w$  wedges

Unknown values	Number	Available equations	Number
Normal forces $N$ at bases of wedges	$n_w$	Forces equilibrium in the horizontal direction	$n_w$
Location of $N$ at the last base (at other bases assumed in the middle of bases)	1	Forces equilibrium in the vertical direction	$n_w$
Normal forces $N$ at interfaces between wedges	$n_w - 1$	Moments equilibrium	$n_w$
Locations of $N$ at the interfaces	$n_w - 1$	$F_j = F_i \cdot \frac{\gamma_{j,a}^{k_1}}{\gamma_{i,a}^k} \cdot \frac{\gamma_{i,e}^k}{\gamma_{j,e}^{k_1}}$	$n_w - 1$
Shear forces $T$ at bases of wedges	$n_w$	at bases (except at $i$ ) at interfaces	$n_w - 1$ $n_w - 1$
Shear forces $T$ at interfaces between wedges	$n_w - 1$	$T_j = \frac{c'_j \cdot b_j + (1 - r_u, j) \cdot N'_j \cdot \tan \phi'_j}{F_j}$	
Factor of safety $F_i$	1	at bases	$n_w$
Local factors of safety $F_j$ at bases (except at $i$ ) at interfaces	$n_w - 1$	at interfaces	$n_w - 1$
Total	$7n_w - 3$	Total	$7n_w - 3$

the  $3n_w$ th equation and gradually changing (increasing)  $F_i$  in steps until all  $3n_w$  equilibrium equations are satisfied to a specified tolerance. Several iterations will be necessary for each step if local yielding occurs and therefore the coefficients of the equations must be readjusted. The results of the calculation are not applicable if the normal forces acting on the interfaces and the base of the last wedge are outside the limits of the interfaces and the base and also if calculated normal forces are negative (tensile) except in the case of reinforced soil when tensile stress must not exceed the reinforcement tensile strength. This indicates that assumed potential slip surface and the subdivision into wedges are not acceptable and need change. For an unstable wedge assembly, the equilibrium equations cannot be satisfied and the stepping procedure will continue to a predefined number of steps. For a stable wedge group, an average factor of safety of the group stability  $F_{avr}$  can be calculated from the formula for  $n_w$  wedges

$$F_{avr} = \frac{\sum_{i=1}^{2n_w-1} \tau_{a,i} \cdot b_i}{\sum_{i=1}^{2n_w-1} \frac{\tau_{a,i} \cdot b_i}{F_i}} \quad (4.11)$$

$F_{avr}$  is used for comparison with a constant  $FS$  from conventional methods and for the assessment of global stability of a group of wedges.

The expression relating acting forces and shear strains at a boundary  $j$  follows from Equations (4.4) and (4.8), when  $FS$  in Equation (4.4) is replaced by a local  $F_{s,j}$  from Equation (4.8), with addition of the cosine terms for the case when kinematically possible tangential displacements  $\Delta_{i,j}$  are inclined to the wedge surfaces because of change in the specific thickness  $dt$ .

$$T_j = \frac{c' j \cdot b_j + (1 - r_{u,j}) \cdot N'_j \cdot \tan \phi'_j}{F_i \cdot \frac{\gamma^{k_1}_{j,a}}{\gamma^{k_1}_{i,a}} \cdot \frac{\Delta^k_{i,e} \cdot \cos \alpha_i}{\Delta^{k_1}_{j,e} \cdot \cos \alpha_j}} \quad (4.12)$$

All local  $F_{s,j}$  will be the same if soil is homogeneous ( $\gamma^{k_1}_{j,a} \gamma^{k_1}_{i,a}^{-1} = 1$ ) and the ratios  $\Delta^k_{i,e} \Delta^{k_1}_{j,e}^{-1} = 1$  along a plane or the bases of wedges with same thicknesses of a circular cylinder with the interfaces passing through the centre of the cylinder. The extended limit equilibrium method described in this section can also be used for soil reinforced by one or more layers of geotextiles/geogrids.

When only one reinforcement zone exists, such as in reinforced embankments, then reinforcement can be treated as a soil layer (Srbulov, 1999). However, when many reinforced layers are present it is necessary to apply a composite material concept. Ingold (1982) referred to the work of Long et al. (1972) who observed that above a certain threshold value of applied confining pressure in triaxial apparatus there was a constant increase in applied vertical stress at failure in samples with reinforcement at a given tensile strength and spacing. Failure of the reinforced

samples was very brittle, with a drastic decrease in strength when the peak was passed. The brittleness was less severe at higher applied confining pressures or in less heavily reinforced samples. Post-failure inspection of dismantled samples consistently showed that the reinforcement had failed in tension. It was concluded that since, for tensile reinforcement failure, the failure envelopes of both the reinforced and non-reinforced sand are parallel, and therefore exhibit the same angle of internal shearing resistance, the additional strength imparted by the reinforcement could be represented by an apparent cohesion.

In addition, the orientation of reinforcement is likely to change with respect to a wedge boundary, from as-built position to an almost parallel orientation at the failure. Jewel (1990) proposed that the improvement in shearing resistance  $P_s$ , resulting from a reinforcement force,  $P_r$ , can be expressed by the equilibrium equation of forces

$$P_s = P_r \cdot (\sin \theta_r + \cos \theta_r \cdot \tan \phi'_1), \quad (4.13)$$

where  $\theta_r$  is the angle between the reinforcement direction and a normal to the boundary. Equation (4.13) also defines the degree of anisotropy of shearing resistance of reinforced soil with respect to the angle  $\theta_r$ . For  $\phi'_1$  close to  $30^\circ$  it follows from the above equation that almost a constant tensile force  $P_s$  greater or equal to  $P_r$  acts for the range of  $\theta_r$  between  $30^\circ$  and  $90^\circ$ , with the maximum  $P_s P_r^{-1}$  of 1.15 for  $\theta_r = 60^\circ$ . It can be assumed that an apparent cohesion is given by the expression

$$\bar{c} = \sum \frac{P_r}{b_j} \quad (4.14)$$

where  $\Sigma$  is applied to all reinforced layers crossing a particular considered wedge boundary if the distance to the end of reinforcement is sufficient for activation of reinforcement tensile strength. It also means that reinforced soil shear strength is considered isotropic, because it varies little with the angle  $\theta_r$  according to Equation (4.13).

The LE method for slopes can also be used for analysis of bearing capacity of footings similarly as the use of Sarma's method for bearing capacity of footings (Sarma and Chen, 1995, 1996).

#### 4.2.1.1 Case Study of the Stability of Cutting at Northolt in England

Appendix A.2 contains an Excel spreadsheet for the assessment of slope stability according to the method described in this section. The example in the spreadsheet is from Srbulov (1988, 1995). The near-failure slope stability problem was described by Skempton and Hutchinson (1969). They wrote that “*the cutting at Northolt was first excavated in 1903 with slope at 2.75:1. In 1936, widening of the cutting took place and the new slope was made at 2.5:1 with a small concrete wall. Movements became noticeable in January 1955; comprising slumping at the top and bulging just*

**Table 4.2** Local factors of safety and mobilized soil cohesion and friction angles in the example

Joint No	Local factor of safety	Mobilized soil cohesion (kPa)	Mobilized friction angle (degrees)
1	1	1	13
2	1	5.2	15
3	1	5.2	15
4	1	5.2	15
5	1	5.2	15
6	1	9.3	17
7	1	9.3	17
8	1.45	10.8	14.1
9	1.24	12.5	16.4
10	1.45	10.8	14.1
11	1.01	15.6	20

above the wall. Stability analyses using the method of Morgenstern & Price, with the slip surface and piezometric level, have recently been made by R.J. Chandler”.

For the peak soil shear strength Chandler calculated  $FS = 1.63$ , while for the residual shear strength  $FS = 0.54$ . It is interesting to notice that for the “fully softened or critical state condition” Chandler calculated  $FS = 0.77$ . Using the procedure described in this section and the soil parameters given in Appendix A.2, an average  $F_{avr} = 1.06$  is obtained. It should be mentioned that the  $F_{avr}$  slightly greater than one is the result of the local factors of safety larger than one along the interfaces of the slip zone as the local factors of safety along the slip surface are all equal to one, with the shear strength below the peak value, Table. 4.2.

While  $FS = 1.63$  corresponds to a stable slope,  $FS = 0.54$  or  $0.77$  to a failed slope,  $F_{avr} = 1.06$  indicates a slope near failure condition, which is usually accompanied by an increase in slope movements as they were observed in 1936. Therefore, the method described in this section is considered more appropriate for brittle soil than classical LE methods. The cross section of the cutting with its discretization into wedges is shown in Fig. 4.6.

#### 4.2.2 Single Tetrahedral Wedge for Three-Dimensional Analysis of Translational Stability

For narrow slope failures, the effects of forces acting on the sides of sliding mass are significant and cannot be ignored. This is frequently the case for slope failures in rock when sliding occurs along distinct joints. The analysis of translational stability of a tetrahedral wedge formed by slope plane, top plane, two potential sliding planes, and a tension crack plane (Fig. 4.7) is based on Hoek and Bray (1981).

The Lambert equal area projection is used by geographers to represent the spherical shape of the Earth’s on a flat surface (Hoek and Bray, 1981). The traces of planes on the surface of a reference sphere are used to define the dips and dip directions of the planes. Equal area projection is used to show the traces of the wedge bounding planes, Fig. 4.8.

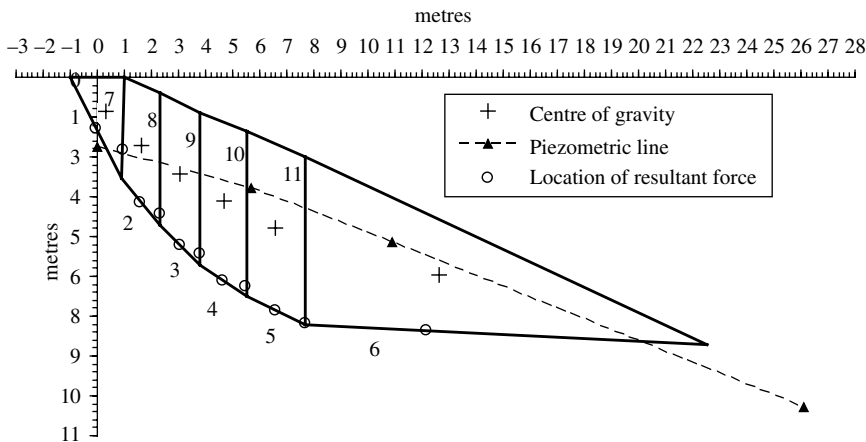


**Fig. 4.6** The cross section of the cutting at Northolt with the wedges used for the analysis of the stability

**Fig. 4.7** Geometry of a tetrahedral translational wedge with the bounding planes 1–5

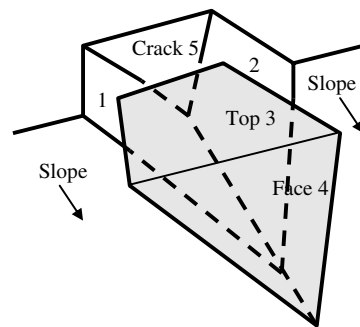
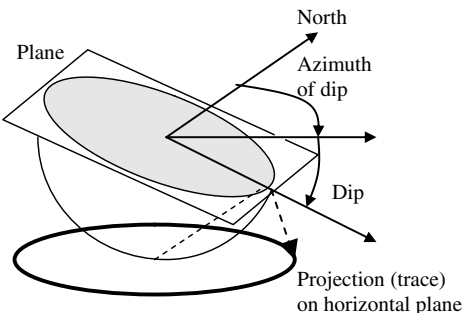
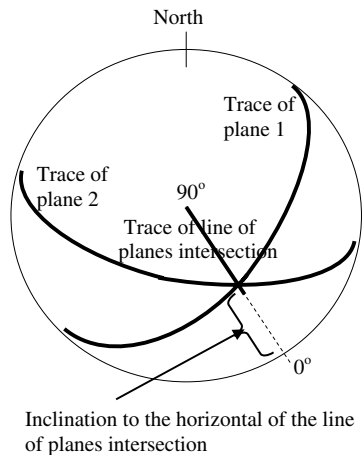


**Fig. 4.8** Method of construction of an equal area projection by intersection of a plane with a reference sphere



Only the intersection of a plane with the lower half of the reference sphere is sufficient to be projected on the horizontal plane, because the other half is symmetric. The inclination of the line of intersection of the planes 1 and 2 and of the sliding wedge (block) can be determined from the projection on horizontal plane, Fig. 4.9.

**Fig. 4.9** Projection on horizontal plane of the traces of the planes 1 and 2 and of the intersection line between them



The effect of inertial forces caused by an earthquake is considered as an additional external load in quasi-static approach. The calculation of the critical acceleration, which causes the factor of safety of wedge stability of one, is performed using trial and error procedure. If for assumed external load, the calculated factor of safety of wedge stability caused by the inertial forces is different from one then assumed additional external load is increased/decreased until calculated factor of safety becomes equal to one, in which case the critical acceleration is found.

#### 4.2.2.1 Example of Three Dimensional Slope Stability Analysis

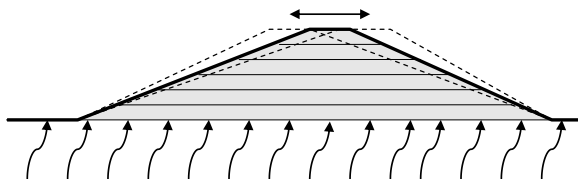
Appendix A.3 contains data for the example presented by Hoek and Bray (1981) in their Appendix 2 for dry slope. The critical acceleration of  $2.94 \text{ m/s}^2$  is calculated from the ratio between the additional external load and wedge weight when the factor of safety of slope stability is one.

### 4.3 Shear Beam Model for Reversible Displacement Analysis

#### 4.3.1 Two-Dimensional Analysis

Recognitions that seismic transversal waves arrive at a site in almost vertical direction, because of their refractions at the boundaries between stiffer and softer layers existing along the wave propagation from the source to ground surface, and that soil can behave as elastic material up to the peak acceleration of about  $3 \text{ m/s}^2$  enable the use of simplified models. Mononobe (1936) considered soil dynamic analysis in two-dimensions as shear beams, Fig. 4.10. The main assumptions of the shear beam model are:

**Fig. 4.10** Cross section of a shear beam with varying width along its height



- a cross section deforms in simple shear with only horizontal displacements present,
- either shear stresses or shear strain are uniform across horizontal planes

In reality, significant vertical displacements may exist in the near field of earthquake source although the horizontal displacements may predominate. Also, uniformity of shear stresses or strain requires uniformity of materials and loading across horizontal planes, which is frequently not the case. Nevertheless, the concept is useful as a first approximation of the problem because it allows that two-dimensional case is considered as one dimensional case.

Many authors considered shear beam model (e.g. Kramer, 1996). Ambraseys (1960) calculated the magnification factor for one cycle of synchronous damped oscillation of a triangular shape in its first mode of vibration as shown in Table. 4.3.

Large damping ratios are not realistic for an elastic material but rather for an equivalent linear elastic material, which properties are estimated based on Section 2.2.1. Consequently, care is needed in applying the Ambraseys' factors in practice.

Baldovin and Paoliani (1994) compiled data from 25 case histories concerning earth and rock fill dams, with heights varying from 8 m to over 200 m, affected by earthquakes, with the magnitudes range from 4.9 to 8.5. In many cases, the motions at the base and at the crest of the dams were recorded or sometimes estimated and computed. They observed that the crests to bases acceleration ratios were not significantly influenced by the geometries, heights and even upstream slope inclinations but mostly by the peak base acceleration. The upper and lower boundaries of the crest to base peak acceleration ratios based on their data are shown in Fig. 4.11.

The data indicate that the ratios between the peak accelerations at dam crests and the peak accelerations at dam bases are similar to the ratios between the peak accelerations at the ground surface and depths for level ground shown in Fig. 3.14.

For an equivalent harmonic motion, the amplitudes of horizontal displacements, if required, can be approximated by multiplying the acceleration amplitude by the factor  $T_d^2(4\pi^2)^{-1}$ , from Equation (2.15). The period of the first mode of dam free vibration,  $T_d = 2.61H_d v_t^{-1}$  (e.g. Dakoulas and Gazetas, 1985), where  $H_d$  is dam height and  $v_t$  is an average velocity of propagation of transversal waves through dam body.

**Table 4.3** The magnification factors at dam crest according to Ambraseys (1960)

Damping ratio (%)	0	5	10	15	20	25	30
Magnification factor	3.14	2.75	2.34	2.12	1.80	1.63	1.40

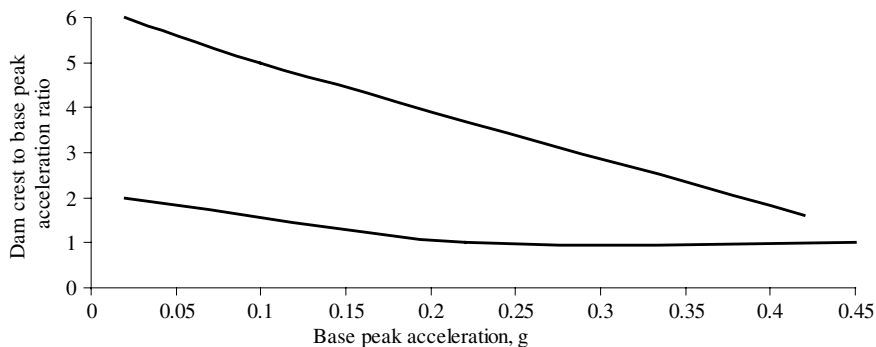


**Fig. 4.11** Recorded and estimated upper and lower bounds of the ratios between dam crest and the base peak accelerations

Chugh (1985) proposed a modified analysis of one-dimensional wave propagation through horizontally layered sites to account for the finite cross-sectional dimensions of an embankment dam overlying a foundation deposit. The comparisons of computed and observed responses of a dam support the use of the simple numerical procedure. Other simplified approaches have also been considered. Numerical analysis can be performed in two dimensions using computer codes, for example QUAD4M (<http://nisee.berkeley.edu/documents/SWSC/QUAD4M.zip>) based on the equivalent linear soil properties as used by SHAKE and time domain analysis.

### 4.3.2 Three-Dimensional Effect

Gazetas (1987) plotted the ratios between fundamental periods of dams in valleys of different shapes and infinitely long dams as function of the dam length  $L_d$  and height  $H_d$  (Fig. 4.12) and vibration mode.

The greatest differences exist for the first vibration mode and the dam length to height ratio  $L_d H_d^{-1}$  up to about 5.5. For  $L_d H_d^{-1} < 2.5$ , the ratios between the first fundamental period of dams in rectangular shaped canyons and dams of infinite lengths are approximately equal to  $0.5(L_d H_d^{-1})^{0.75}$ . For  $L_d H_d^{-1} < 5.5$ , the ratios

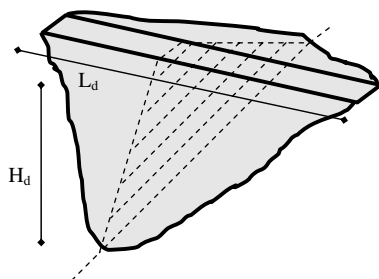


**Fig. 4.12** Three-dimensional dam with height  $H_d$  and length  $L_d$ . Two-dimensional cross section is shown by dashed lines

between the first fundamental period of dams in triangularly shaped canyons and dams of infinite lengths are approximately equal to  $0.35(L_d H_d^{-1})^{0.6}$ .

## 4.4 Sliding Block Models for Permanent Displacement Analysis

### 4.4.1 Co-Seismic Stage

This stage is analyzed using Newmark's sliding block method, which concept is introduced in Section 1.3. Any shape of potential sliding slope can be represented by its equivalent sliding block as indicated in Fig. 1.4. The equivalent sliding block parameters are:

- Angle of inclination to the horizontal  $\bar{\alpha}$  of the block is equal to inclination to the horizontal of the resultant of tangential forces  $\Sigma T$  shown in Fig. 1.4.
- For a linear relationship between shear strength and effective normal stress, an equivalent friction angle along the block base is

$$\bar{\phi} = \arctan \frac{FS \cdot \Sigma T}{\Sigma N} \quad (4.15)$$

where  $\Sigma T$  and  $\Sigma N$  are shown in Fig. 1.4 and  $FS$  ( $F_{avr}$ ) is the average factor of safety of slope stability.

- An average compressive stress on the block base is

$$\bar{\sigma} = \frac{\Sigma N}{A_s}, \quad (4.16)$$

where  $A_s$  is the area of slope sliding surface.

A sliding block with the forces acting on it in the case of horizontal ground motion only is shown in Fig. 4.13.

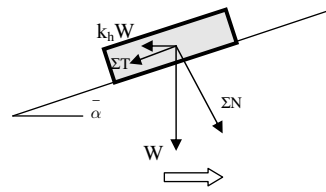


**Fig. 4.13** Sliding block with forces acting on it

where  $W$  is block weight,  $\Sigma N$  and  $\Sigma T$  are normal and tangential components of  $W$  force acting on the inclined plane with angle  $\bar{\alpha}$  to the horizontal,  $k_h$  is the ratio between the horizontal inertial and the gravitational acceleration. For a linear relationship between shear strength and effective normal stress, the factor of safety  $FS$  against block sliding is:

$$FS = \frac{\sum N \cdot \tan \bar{\phi}}{\sum T} = \frac{(W \cdot \cos \bar{\alpha} - k_h \cdot W \cdot \sin \bar{\alpha}) \cdot \tan \bar{\phi}}{W \cdot \sin \bar{\alpha} + k_h \cdot W \cdot \cos \bar{\alpha}} \quad (4.17)$$

The block will not move relative to the base as long as the base acceleration is less than a critical acceleration. The critical acceleration ratio for a horizontal ground motion can be obtained from Equation (4.17) when  $FS=1$ , i.e.

$$k_{h,cr} = \tan(\bar{\phi} - \bar{\alpha}) \quad (4.18)$$

The horizontal component of permanent co-seismic displacement of a sliding slope (block) relative to its base is calculated by double integration in time, Fig. 4.14, of the difference between the base acceleration and the critical acceleration. The permanent down slope displacement is calculated by dividing the results of the double integration by  $\cos \bar{\alpha}$ , where  $\bar{\alpha}$  is the inclination of the equivalent sliding block to the horizontal,  $\bar{\alpha} = \arctan [(\tan \bar{\phi} - FS \cdot K_R) \cdot (FS + K_R \cdot \tan \bar{\phi})]^{-1}$  from the Equation (4.17).

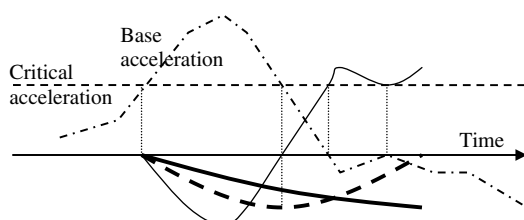
Calculation of the critical acceleration of a slope is performed directly for a slope (e.g. Sarma and Tan, 2006; Sarma, 1979) or by trial and error until calculated factor of safety of slope stability is equal to 1.0 using methods such as described in Sections 4.2.1 and 4.2.2. Hoek (1987) published a computer program for the analysis of slope stability and determination of the critical acceleration according to Sarma's (1979) method.

Ambraseys and Srbulov (1994, 1995), among others, provided the attenuation relationships of co-seismic permanent displacements depending on earthquake magnitude, earthquake source distance and the ratio between the critical acceleration for slope instability and the peak acceleration of ground. The attenuation relationships have been derived using least square regression performed on the permanent ground displacements, which are calculated using double integration in time of the difference between the base acceleration and the critical acceleration.

The following assumptions and limitations apply:

- Constant critical acceleration ratio is independent on the amount and rate of sliding.
- Earthquake magnitude  $M_s$  range 5 to 7.7.
- Earthquake source distances to 50 km.
- Acceleration records caused by thrust (46%), normal (26%) and strike slip (29%) faults with the mean depth of the events  $10 \pm 4$  km.

**Fig. 4.14** Integration in time of the block relative acceleration (thin continuous line) to velocity (thick dashed line) and to permanent displacement (thick continuous line)



- One-way horizontal component of displacement only for slopes. Down slope displacement is calculated by dividing the horizontal component with  $\cos \bar{\alpha}$ ,  $\bar{\alpha}$  is inclination to the horizontal of the equivalent block.
- Horizontal ground acceleration was considered only.

The attenuation relationship for one-way permanent horizontal component of displacements on sloping ground is according to Ambraseys and Srbulov (1994, 1995)

$$\log_{10}(u_1) = -2.47 + 0.47 \cdot M_s - 0.01 \cdot r_f + \log_{10} \left( \frac{\left[ 1 - \left( k_c / k_p \right) \right]^{2.64}}{\left( k_c / k_p \right)^{1.02}} \right) + 0.58 \cdot p, \quad (4.19)$$

and for two-way displacement on level ground is

$$\log_{10}(u_2) = -2.07 + 0.47 \cdot M_s - 0.012 \cdot r_f + \log_{10} \left( 1 - \frac{k_c}{k_p} \right)^{2.91} + 0.6 \cdot p, \quad (4.20)$$

where  $u_{1,2}$  are in cm,  $r_f = (h_f^2 + d_f^2)^{0.5}$ ,  $h_f$  is the hypocentral depth,  $d_f$  is the source distance,  $k_c$  is the ratio between the critical horizontal acceleration at which the factor of safety of slope stability is 1 and the gravitational acceleration,  $k_p$  is the ratio between the peak horizontal ground acceleration and the gravitational acceleration,  $p$  is the number of standard deviations.

The results of these relationships are shown in Fig. 4.15 for three earthquake magnitudes and three source-to-site distances.

From Fig. 4.15 it can be noticed that, although the variation of predicted permanent co-seismic displacements is relatively large, the absolute values of the displacements are large only for the strongest earthquakes in the near field and vulnerable slopes with the factor of safety close to 1. This is the result of relatively short duration of ground acceleration pulses and their alternating direction.

The effect of the vertical component of ground acceleration may not be important in many cases except for very steep natural and artificial slopes when the slip surface is nearly vertical i.e. parallel to the vertical acceleration component (e.g. Srbulov, 2003b). For very steep slopes (cliffs, nearly vertical reinforced soil and anchored slopes), neglecting of the vertical acceleration component could cause permanent displacements to be underestimated by hundreds of times.

#### 4.4.1.1 Comments of Shear Strain Rate Effects in Ring Shear

The results of tests on moist fine grained soil specimens at fast shear rates in ring shear apparatus (e.g. Parathiras, 1995) indicate an increase of the shear strength with shear rate in comparison with the strength at slow shear rate. This can cause ten-times or more decrease in co-seismic permanent displacements in comparison with the co-seismic permanent displacement caused by soil shear strength independent of shear rate (e.g. Srbulov and Parathiras, 1995).

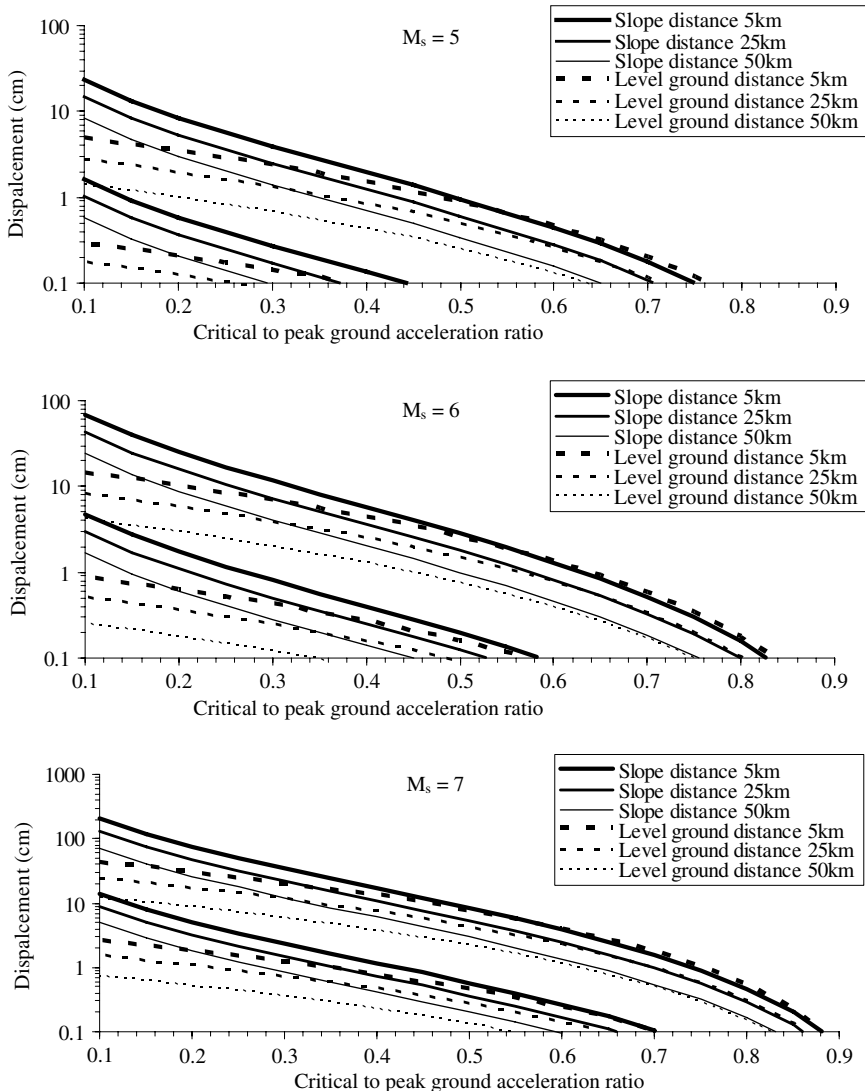


**Fig. 4.15** Average  $\pm$  one standard deviation of co-seismic displacements of slopes and level ground

Parathiras (1995), among others, reported on a decrease of the shear strength of submerged fine grained soil at fast shear rates when tested in ring shear apparatus and a periodic change in the height of the specimen with shearing even when the gap between two rings was fixed. One possible explanation follows. The period of change of the specimen height corresponds to the specimen circumference. Suppose that an inclined shear zone forms because of the application of torque to the top and bottom of the sample. A similar effect is observed in the hollow cylinder tests

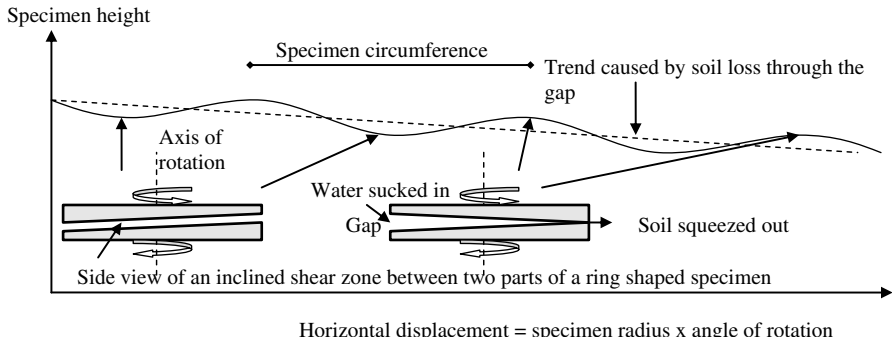


**Fig. 4.16** Observed change of specimen height with horizontal displacement in the ring-shear apparatus

(e.g. Saada et al., 1994). In the ring shear apparatus, the top and bottom parts of a specimen could have thicker and thinner portions along the perimeter. Where the top and bottom thicker portions coincide, the specimen height increases and where the top and bottom thinner portions coincide, a gap opens. When the gap opens, water is sucked into the specimen. Increased water content leads to softening of the sample and hence to its shear strength decrease. The concept is shown in Fig. 4.16.

Fearon et al. (2004) reported on tests on samples of London Clay sheared submerged at a rate of 100 and 1000 mm/min with measurement of excess pore water pressure at two opposite side of ring shear apparatus and showed both periodic changes of pore water pressure with the increase of displacement and also a change of sign of pore water pressure from positive (at the location of two thicker parts) to negative (at the location of two thinner parts) and back. This indicates that the inclined shear zone also rotates around the sample perimeter.

These considerations suggest that, because the test results are influenced by the apparatus, the results cannot be considered reliable despite popularity of ring shear device for testing of soil at fast shear rates and large shear displacements. A cylinder shear apparatus in which the shear zone is vertical should be able to provide more reliable results.

#### 4.4.1.2 An Example of Calculation of Permanent Slope Displacement

Appendix A.4 contains an example of calculation of permanent co-seismic displacement for a horizontal acceleration record shown in Fig. 6.11. When positive side of the record is considered for a down slope movement, the calculated permanent displacement of 37.1 cm corresponds to the critical acceleration  $1.02 \text{ m/s}^2$ . When the negative side of the record is considered the calculated permanent displacement is 39.5 cm for the same critical acceleration.

#### 4.4.2 Post-Seismic Stage

The co-seismic permanent displacements of slopes are relatively small because of short duration and alternating direction of earthquake pulses when the cyclic shear strength of soil or the excess pore water pressure does not cause the factor of safety of slope stability to decrease below 1. If it does fall below 1, then post-seismic very fast and large permanent displacement of slopes occurs driven by gravity. The moving mass gains momentum and comes at rest with the factor of safety greater than 1. This factor of safety may further increase in time with the excess pore water pressure dissipation and the increase of shear strength of soil.

Different theories exist to explain the increase of shear strength of soil in time when the movement ceased (e.g. Tika et al., 1996; Stark et al., 2005). The most likely reason seems to be that excess pore water pressure generated by shearing dissipates, the effective stress increases causing an increase in shear strength. The shear strength increase during the secondary consolidation stage may be caused by soil grain slippage and interlocking with rotation of principal stresses, which occurs when shearing stops.

When the inclination to the horizontal of the sliding block, an equivalent friction angle along the block base and an average compressive stress on the block base is determined according to Section 4.4.1 then it is not difficult to formulate two sliding blocks model (Ambraseys and Srbulov, 1995, with permission from Elsevier) for the analysis of post-seismic displacement, Fig. 4.17.

The block height  $h_b$  is

$$h_b = \frac{\bar{\sigma}}{\rho \cdot g \cdot \cos \bar{\theta}}, \quad (4.21)$$

where  $\rho$  is unit soil density,  $g$  is the gravitational acceleration. The initial block length  $L_o$  is

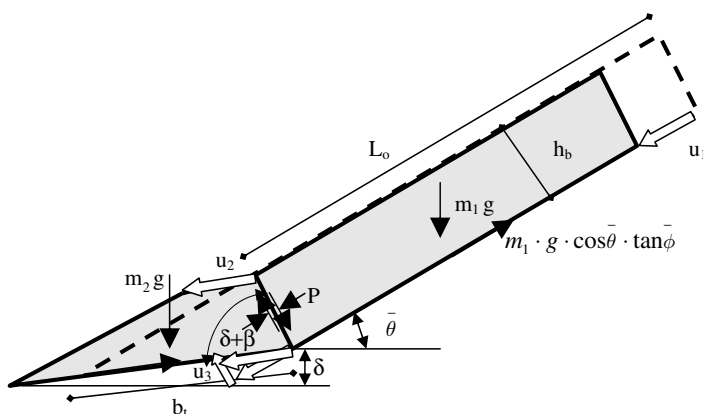


**Fig. 4.17** Two sliding block model for post-seismic stage (Ambraseys and Srbulov, 1995, by permission of Elsevier)

$$L_o = L' - b_t = L' - \frac{h_b}{\sin(\bar{\theta} - \delta)}, \quad (4.22)$$

where  $L'$  is the length of the actual slip surface of any shape,  $b_t$  is the initial width of the base of the toe,  $\delta$  is the angle of inclination to the horizontal of the base of the toe. The angle of inclination of the interface to the horizontal  $\beta$  is determined from the condition that the initial factor of safety for the two blocks is minimal. It is assumed that the value of  $\beta$  does not change when the blocks slide. The initial block mass  $m_1 = L_o h_b \rho$ , where  $\rho$  is unit soil density. The two sliding blocks model can represent an actual sliding slope if the interface axial force  $P$  is equal to the average of interface axial forces  $N_{n+i}$  shown in Fig. 4.1 and the interface shear displacement  $u_3$  is the sum of all interface displacements  $\Delta_{n+i}$  (three of them shown in Fig. 4.5).

From the equations of motion of the two blocks (Appendix A in Ambraseys and Srbulov, 1995), the equation of motion of the system is

$$\frac{d^2 u_1}{dt^2} = \frac{\bar{C} \cdot u_1 + \bar{D}}{\bar{B} \cdot u_1 + \bar{A}}, \quad (4.23)$$

where the constants  $\bar{A}$  to  $\bar{D}$  are functions of the geometry and properties of the slope and toe materials. Equation (4.23) can be solved numerically to obtain the acceleration, velocity and displacement of the block on the slope.

#### 4.4.2.1 Case Study of the Movement of the Slip at Maidipo in China

Appendix A.5a contains an example of the back analyses of a translational slide in China, which was not triggered by an earthquake, to test the model for purely frictional soil. The example is reproduced from the paper by Ambraseys and Srbulov (1995) with permission from Elsevier. The slide occurred in a natural slope of mudstone, siltstone and shale at Maidipo, a cross section of which is shown in Fig. 4.18.

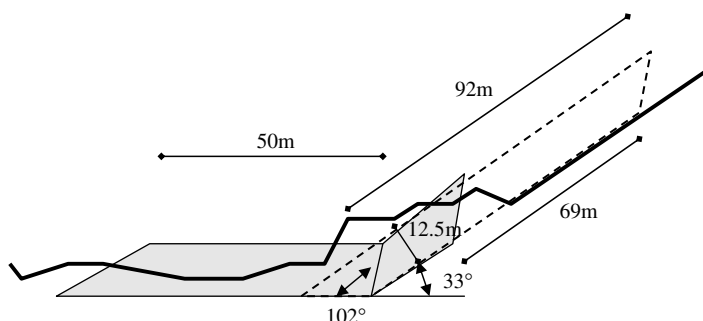


**Fig. 4.18** Sketch of the cross section of the translational landslide at Maidipo (Ambraseys and Srbulov, 1995, by permission of Elsevier)

There is no indication of pre-existing shear surfaces, except that the slide occurred along the joints in rock. The water level in the slope is not known, and from the brief description of the site it is assumed that the slope was dry. Zhongyou (1984) reconstructed the sequence of sliding, and suggested that the slip occurred in four stages, deduced from the fact that the slide material came to rest in four blocks. He estimated that the whole sliding sequence lasted 2 minutes and the peak velocity of the first block was about 28 m/s. The slide was probably triggered by the erosion or submergence of its toe and softening of the mudstones. This may led to a progressive loss of the toe support and the failure.

The geometry of the initial sliding block considered is shown in Fig. 4.18. Assuming that the strength properties of the toe and slope materials were the same ( $\alpha = 1$ ), that  $\delta = 0$ ,  $\gamma = 22 \text{ kN/m}^3$  and  $c = 0$ , the observed displacement of 69 m corresponds to  $\phi = 17.2^\circ$  and  $\beta = 102^\circ$  for the initial factor of safety  $F_o$  of 0.6, calculated using  $\phi = 17.2^\circ$ . The calculated duration  $T$  of the sliding according the sliding block model was 12.7 s. The calculated maximum velocity and acceleration of the motion are 8.55 m/s and 24% of the gravitational acceleration respectively, and the final factor of safety  $F_f$  is 2.4. For the mobilized angle of friction  $\phi = 17.2^\circ$  during the movement, the cohesion  $c$  required originally to maintain limit equilibrium was 48.5 kPa. These values are close to the lower bound shear strength parameters given by Zhongyou (1984) for the intact slope material as  $c = 50 \text{ kPa}$  and  $\phi = 20^\circ$ . In conclusion, the two sliding blocks model provided meaningful parameters of the slip at Maidipo.

Equation (4.23), with different constants  $\bar{A}$  to  $\bar{D}$ , is applicable to purely cohesive soil with undrained shear strength  $c_u$  or when an equivalent cohesion  $\bar{c} = \bar{\sigma} \cdot \tan \bar{\phi}$  is used in the place of an equivalent friction angle  $\bar{\phi}$ . For purely cohesive soil and when the constant  $\bar{B} = 0$  i.e. when  $\beta = 90^\circ - (\theta + \delta)/2$ , Equation (4.23) becomes a linear differential equation with constant coefficients with a closed form solution (Appendix A in Ambraseys and Srbulov (1995) with permission from Elsevier).

$$\text{Displacements } u_1 = u_2 = A_d \cdot B_d \cdot [1 - \cos(p_d \cdot t)]$$

where

$$A_d = (1 - F_o) \cdot \rho \cdot g \cdot h_b \cdot [L_o \cdot \sin \bar{\theta} + 0.5 \cdot b_t \cdot \sin \delta]$$

$$B_d = \frac{1}{\rho \cdot g \cdot h_b \cdot (\sin \bar{\theta} - \sin \delta) + \bar{c} \cdot (\alpha - 1)}$$

$$p_d = \sqrt{\frac{\rho \cdot g \cdot h_b \cdot (\sin \bar{\theta} - \sin \delta) + \bar{c} \cdot (\alpha - 1)}{\rho \cdot h_b \cdot (L_o + 0.5 \cdot b_t)}}$$

$$F_0 = \frac{\bar{c} \cdot \left[ L_o + \alpha \cdot b_t + 2R_b \tan \left( \frac{\bar{\theta} - \delta}{2} \right) \right]}{\rho \cdot g \cdot h_b \cdot (L_o \cdot \sin \bar{\theta} + 0.5 \cdot b_t \cdot \sin \delta)}$$

$$\text{Velocities } \frac{du_1}{dt} = \frac{du_2}{dt} = A_v \cdot B_v \cdot \sin(p_d \cdot t)$$

where

$$A_v = (1 - F_o) \cdot g \cdot \sqrt{\rho \cdot h_b} \cdot (L_o \cdot \sin \bar{\theta} + 0.5 \cdot b_t \cdot \sin \delta)$$

$$B_v = \frac{1}{\sqrt{[\rho \cdot g \cdot h_b \cdot (\sin \bar{\theta} - \sin \delta) + \bar{c} \cdot (\alpha - 1)] \cdot (L_o + 0.5 \cdot b_t)}}$$

$$\text{Accelerations } \frac{d^2 u_1}{dt^2} = \frac{d^2 u_2}{dt^2} = A_a \cdot B_a \cdot \cos(p_d \cdot t)$$

where

$$A_a = (1 - F_o) \cdot g \cdot (L_o \cdot \sin \bar{\theta} + 0.5 \cdot b_t \cdot \sin \delta)$$

$$B_a = \frac{1}{L_o + 0.5 \cdot b_t}, \quad (4.24)$$

where most of the symbols used are shown in Fig. 4.16,  $t$  is time,  $\rho$  is soil unit density,  $\alpha$  is a proportion of  $\bar{c}$  or the real undrained cohesion  $c_u$  of translational slides along the base of the toe. The duration  $T$  of sliding is

$$T = \pi \cdot \sqrt{\frac{\rho \cdot h_b \cdot (L_o + 0.5 \cdot b_t)}{\rho \cdot g \cdot h_b \cdot (\sin \bar{\theta} - \sin \delta) + \bar{c} \cdot (\alpha - 1)}} \quad (4.25)$$

The maximum slip  $u_{max}$  at the time  $T$  is

$$u_{max} = \frac{2 \cdot \rho \cdot g \cdot h_b \cdot (1 - F_o) \cdot (L_o \cdot \sin \bar{\theta} + 0.5 \cdot b_t \cdot \sin \delta)}{\rho \cdot g \cdot h_b \cdot (\sin \bar{\theta} - \sin \delta) + \bar{c} \cdot (\alpha - 1)} \quad (4.26)$$

The final factor of safety  $F_f$  at time  $T$  is

$$F_f = \frac{\bar{c} \cdot [L_o - u_{max} + \alpha \cdot (b_t + u_{max}) + 2 \cdot h_b \cdot \tan \frac{\bar{\theta} - \delta}{2}]}{\rho \cdot g \cdot h_b \cdot [(L_o - u_{max}) \cdot \sin \bar{\theta} + (0.5 \cdot b_t + u_{max}) \cdot \sin \delta]} \quad (4.27)$$

The maximum velocity  $du_{max}/dt$  and acceleration  $d^2 u_{max}/dt^2$  are

$$\frac{du_{max}}{dt} = 0.5 \cdot \pi \cdot \frac{u_{max}}{T}$$

$$\frac{d^2 u_{max}}{dt^2} = 0.5 \cdot \pi^2 \cdot \frac{u_{max}}{T^2} \quad (4.28)$$

#### 4.4.2.2 Case Study of the Movement of the Slide at Catak in Turkey

Appendix A.5b contains an example of the analysis of motion of the Catak slide in Turkey. The example is reproduced from the paper by Ambraseys and Srkulov

(1995) with permission from Elsevier. Genc (1993) concluded that there were several factors that triggered the Catak landslide, including the presence of faults and joints in deeply weathered marls, shales, tuffites, limestone and basalts. Also, the natural slope was over steepened by the Macka river incision, and the removal of material at the toe by road works on the Trabzon-Erzurum highway along with prolonged heavy rainfall exacerbated by a spring may have acted as the triggering mechanism for the mass movement. The speed of the slide is not known, but it was such that it crushed a coffee house and vehicles parked alongside the highway at the base of the hill, burying at least 66 people, including the operator of a road grader who was trying to remove material that had fallen onto the road during earlier slip movements. Sketch of the cross section of the Catak slide is shown in Fig. 4.19.

Because of the saturation of the slope, total strength analysis and an undrained strength of the slope material are used. The computation can be performed using the closed form solution with  $\beta_o = 71^\circ$ ,  $\delta = 0$ ,  $\gamma = 20 \text{ kN/m}^3$ . Assuming  $\alpha = 1$ , Equations (4.24) to Equations (4.28) predict that during sliding  $c_u = 144 \text{ kPa}$  with a corresponding initial factor of safety  $F_o = 0.71$ , calculated using  $c_u = 144 \text{ kPa}$ . For  $u_{max} = 142 \text{ m}$ , the final factor of safety  $F_f = 1.7$ . The duration of sliding  $T = 21 \text{ s}$  and the maximum velocity  $du_{max}dt^{-1} = 11 \text{ m/s}$ , with a maximum acceleration  $d^2u_{max}dt^{-2} = 16\%g$ . For the initial stage of  $F_s = 1.0$ , the value of the cohesion required initially to maintain limit equilibrium is  $c_u = 203 \text{ kPa}$ .

If the nonlinear numerical solution is used, the critical interface angle  $\beta = 97.5^\circ$ , which is determined iteratively minimizing the initial factor of safety  $F_o$ . For the observed maximum displacement  $u_{max} = 142 \text{ m}$ , it is calculated that during sliding  $c_u = 162 \text{ kPa}$ , and that the initial factor of safety  $F_o = 0.8$ , calculated using  $c_u = 162 \text{ kPa}$ . The duration of sliding  $T = 23.2 \text{ s}$ , and the maximum velocity and acceleration of the mass are  $9.6 \text{ m/s}$  and  $15\%g$  respectively, while the final factor of safety  $F_f = 1.44$ . For an initial factor of safety  $F_s = 1$ , the corresponding initial  $c_u = 208 \text{ kPa}$ .

The differences between the results obtained using the closed form, Equations (4.24) to Equations (4.28), and the numerical solution, Equation (4.23), are not great.

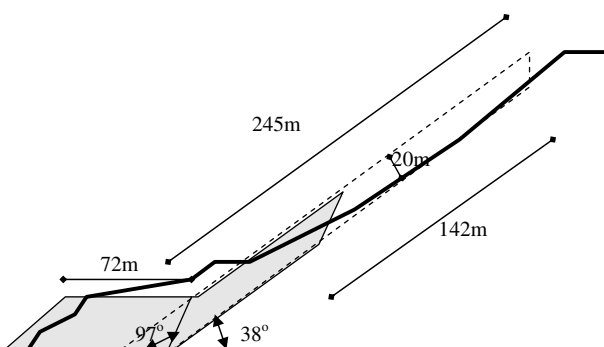


**Fig. 4.19** Sketch of the cross section of the Catak slide (Ambraseys and Srbulov, 1995, by permission of Elsevier)

## 4.5 Bouncing Ball Model of Rock Fall

Rodriguez et al. (1999) considered the effects of 36 earthquakes world-wide in the period 1980–1997 and found that rock falls and disrupted soil slides (with internal shear zones in addition to the main slip surface at the base) occurred in more than 80% of the cases considered. The rock mass involved was 3–5 m deep with depth to length ratio of 0.15; the threshold of minimum local magnitude of an earthquake that triggered rock falls was 5.5. However, the effects of rock falls are as important as the triggering mechanism, Srbulov (2007a).

Hoek (2006) described the mechanics of rock falls and the main factors influencing the falls. He mentions that the most important factor controlling the fall trajectory is the geometry of the slope. In particular, steep slopes impart a horizontal component to the path of a falling rock block and act as ‘ski-jumps’. Clean faces of hard unweathered rock are most dangerous because they do not retard the movement of the falling or rolling rock to any significant degree. The retarding capacity of the surface material is expressed mathematically by a coefficient of restitution. Clean surfaces of hard rock have high coefficients of restitution and low retarding capacity while soil, gravel and completely decomposed rock have low coefficients of restitution and higher retarding capacity. Other factors such as the size and shape of the rock boulders, the coefficients of friction of the rock surfaces and rock breaking into smaller pieces on impact are all of lesser significance than the slope geometry and the coefficients of restitution, according to Hoek (2006).

Hoek (1986), among others, provided a simple rock fall simulation model. Most of the rock fall models include a Monte Carlo simulation technique (Metropolis and Ulam, 1949) for variation of parameters included in the analysis. The models are based on an initial free fall of rock block. During earthquakes, rock blocks have an initial acceleration (and velocity), which increases the distance of blocks travel and their destructive capabilities. Such initial acceleration (and velocity) is considered with a bouncing ball model of rock fall in this section.

A rock block (ball) will start moving when the acceleration of its base exceeds the critical acceleration. Two basic triggering mechanisms are considered for calculation of the critical acceleration.

In sliding and rocking case (Fig. 4.20) and when only the horizontal acceleration component of the base is considered, the critical acceleration in the horizontal direction  $a_{ch}$  (positive down slope) is obtained from the equilibrium of forces acting on the block

$$a_{ch} = g \cdot \tan(\bar{\phi} - \bar{\theta}), \quad (4.29)$$

where  $g$  is the gravitational acceleration,  $\bar{\phi}$  is the friction angle in cyclic condition at the base of the block,  $\bar{\theta}$  is inclination to the horizontal of the block base. For the rocking case, the angle of inclination to the horizontal of the block base is assumed  $= \bar{\phi} - \bar{\theta}$  in order to be able to use the same equation for both modes of block movement.

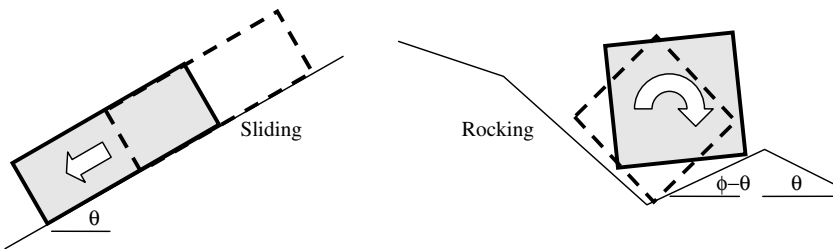


**Fig. 4.20** Sliding and rocking modes of block movement

When the critical horizontal acceleration is calculated for a rock block it is interesting to calculate the peak horizontal acceleration that could be caused by the earthquake source nearby. Rodriguez et al. (1999) plotted the graph of the combinations of moment magnitudes and fault distances at which disrupted landslides occurred. They suggested that such slides are as frequent as rock falls. The slides occurred from the combination of  $M_w = 5.85$  at the distance to fault projection on the surface of 108 km to the combination of  $M_w = 7.8$  at the distance to fault projection on the surface of 80 km. Using Equation (3.6), the peak horizontal acceleration on rock sites ( $S_S = S_A = 0$ ) and from odd fault types ( $F_N = F_T = 0$ ) could have been in the range from  $0.08 \text{ m/s}^2$  to  $0.93 \text{ m/s}^2$  on average.

Ignoring air resistance, the equations for the horizontal distance  $x$ , the vertical distance  $y$  (positive upwards) and the velocity  $v$  of an object movement through air in time  $t$  is (e.g. Gieck and Gieck, 1997)

$$\begin{aligned} x &= v_o \cdot t \cdot \cos \beta_{rf} \\ y &= v_o \cdot t \cdot \sin \beta_{rf} - g \cdot t^2 / 2 \\ v &= \sqrt{v_o^2 - 2 \cdot g \cdot y}, \end{aligned} \quad (4.30)$$

where  $v_o$  is the initial velocity of the object along the trajectory,  $\beta_{rf}$  is the angle (positive upwards) with the horizontal at the beginning of the movement,  $g$  is the gravitational acceleration. The angle  $\beta_{rf}$  can be estimated from the ratio between the vertical and horizontal component of the base acceleration. It is assumed that such ratio at any time corresponds to the ratio of the peak componential accelerations. The peak horizontal component is defined by Equation (3.6), or equivalent, while the peak vertical acceleration is defined, for example, by Equation (3.8).

The earthquake motion is complex and contains a range of frequencies. As already mentioned in Section 2.5, Seed et al. (1975) developed the concept of an equivalent number of significant stress cycles to represent an irregular time history of shear stress by a uniform series of harmonic stress cycles. For a harmonic load, the horizontal acceleration  $a_h$

$$a_h = a_{p,h} \cdot \sin \left( \frac{2 \cdot \pi}{T} \cdot t \right), \quad (4.31)$$

where  $a_{p,h}$  is the peak horizontal base acceleration from Equation (3.6) or equivalent,  $T$  is the period of the equivalent harmonic motion,  $t$  is time. For the critical horizontal acceleration in sliding or rocking  $a_{ch}$ , the corresponding time according to Equation (4.31) is

$$t_{a_{ch}} = \frac{T}{2 \cdot \pi} \cdot \arcsin \left( \frac{a_{ch}}{a_{p,h}} \right) \quad (4.32)$$

The horizontal base velocity  $v_h$  is obtained by integration in time of the horizontal base acceleration from Equation (4.31)

$$v_h = \frac{a_{p,h} \cdot T}{2 \cdot \pi} \cdot \left[ 1 - \cos \left( \frac{2\pi}{T} \cdot t \right) \right] \quad (4.33)$$

Combining Equations (4.31) and Equations (4.33) it follows

$$v_h = \frac{a_h \cdot T}{2 \cdot \pi} \cdot \frac{1 - \cos \left( \frac{2 \cdot \pi}{T} \cdot t \right)}{\sin \left( \frac{2 \cdot \pi}{T} \cdot t \right)} \quad (4.34)$$

When the critical horizontal acceleration in sliding or rocking  $a_{ch}$  from Equation (4.29) at the time  $t_{a_{ch}}$  from Equation (4.32) is used in Equation (4.34), the slant initial velocity  $v_o$  of block motion is

$$v_o = \frac{a_{ch} \cdot T}{2 \cdot \pi \cdot \cos \beta} \cdot \frac{1 - \cos \left( \frac{2 \cdot \pi}{T} \cdot t_{a_{ch}} \right)}{\sin \left( \frac{2 \cdot \pi}{T} \cdot t_{a_{ch}} \right)} \quad (4.35)$$

The predominant period  $T$  of base ground motion varies widely (Fig. 2.8) and therefore a range of its values needs to be considered in the calculation.

The calculation, based on Equation (4.30), is performed in small time increments using the spread sheet given in Appendix A.6. A constant check is performed if the block trajectory has crossed the terrain topography. If such crossing occurred then the angle of impact is calculated as a difference between  $\text{arc tan}(-\Delta y \Delta x^{-1})$  and  $\alpha_l$ , where  $\Delta y$  and  $\Delta x$  are the incremental vertical and horizontal distance along the block trajectory just before the impact and  $\alpha_l$  is the local angle of inclination to the horizontal at the impact place. It is assumed that the angle of bounced block from the place of impact is the same as the angle of the impact. However, the velocity of the bounced block will be different from the velocity before the impact due to energy loss at the impact.

It is possible that a falling block turns to rolling mode of motion over gently inclined surfaces. Rolling motion is usually slower and shorter than free fall and therefore usually of smaller significance than rock fall, analyzed in this section. It

is possible that a rock block crushes on impact with its base and continues as a rock avalanche (e.g. Wieczorek et al., 2000). The analysis of rock avalanches is considered in Section 4.6.

The velocity  $v_{out}$  of bounced block is determined from the equation of energy equilibrium

$$\frac{m \cdot v_{in}^2}{2} = \frac{m \cdot v_{out}^2}{2} + E_{loss}, \quad (4.36)$$

where  $m$  is the block mass,  $v_{in}$  is the incoming velocity of the block,  $E_{loss} = ma_r \cos[\arctan(-\Delta y \Delta x^{-1}) - \alpha_l] \delta_p$  is the energy loss due to plastic deformation  $\delta_p$  of the base in direction perpendicular to the impact surface,  $v_{out}$  is the outgoing velocity of the block,  $a_r$  is the block acceleration just before the impact,  $\Delta y$  and  $\Delta x$  are the incremental vertical and horizontal distance along the block trajectory just before the impact and  $\alpha_l$  is the local angle of inclination to the horizontal at the impact place. The block penetration  $\delta_p$  into the impact surface follows from the geometry of an equivalent ball shown in Fig. 4.21.

$$\delta_p = R - \sqrt{R^2 - B_b^2}/4. \quad (4.37)$$

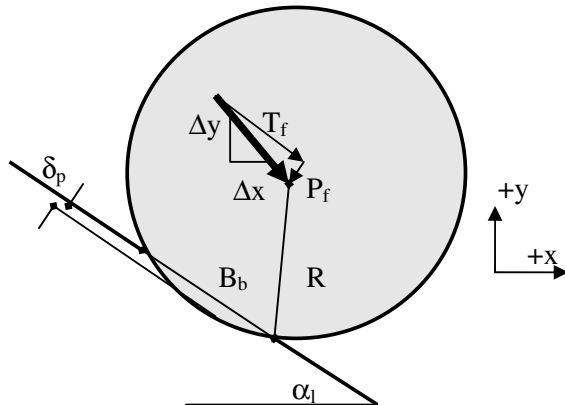
where  $R$  is the radius of an equivalent ball,  $B_b$  is the width of the equivalent ball penetration. The width  $B_b$  is determined by equalizing the axial component  $P_f$  of block impact force (Fig. 4.20) with ground resisting force  $F_g$  to such penetration. For fine cohesive soil (clay) and surface blocks, ground resisting force  $F_g$  is (e.g. Eurocode 7-1, Annex D, 2004)

$$\begin{aligned} F_g &= (\pi + 2) \cdot c_u \cdot 1.2 \cdot i_c \cdot \frac{B_b^2 \cdot \pi}{4} \\ i_c &= \frac{1}{2} \cdot \left( 1 + \sqrt{1 - \frac{T_f}{\frac{B_b^2 \cdot \pi}{4} \cdot c_u}} \right) \\ T_f &= m \cdot a_r \cdot \cos \left[ \arctan \left( \frac{-\Delta y}{\Delta x} \right) - \alpha_l \right] \\ P_f &= m \cdot a_r \cdot \sin \left[ \arctan \left( \frac{-\Delta y}{\Delta x} \right) - \alpha_l \right], \end{aligned} \quad (4.38)$$

where  $m$  is the block mass,  $a_r$  is the block acceleration just before the impact,  $c_u$  is soil cohesion in undrained condition adjusted for the rate effect,  $B_b$  is the width of equivalent ball penetration,  $\Delta y$  and  $\Delta x$  are the incremental vertical and horizontal distance along the block trajectory just before the impact,  $\alpha_l$  is the local angle of inclination to the horizontal at the impact place,  $T_f$  and  $P_f$  are the transversal and axial component of the impact force shown in Fig. 4.21.

For coarse frictional soil (sand and gravel) and surface blocks, ground resisting force  $F_g$  is (e.g. Eurocode 7-1, Annex D, 2004)

**Fig. 4.21** Basic parameters on equivalent ball impact upon a surface



$$\begin{aligned}
 F_g &= 0.5 \cdot \gamma_{soil} \cdot B_b \cdot N_\gamma \cdot 0.7 \cdot i_\gamma \cdot \frac{B_b^2 \cdot \pi}{4} \\
 N_\gamma &= 2(N_q - 1) \cdot \tan \phi \\
 N_q &= e^{\pi \cdot \tan \phi} \cdot \tan^2 (45^\circ + \phi/2) \\
 i_\gamma &= (1 - T_f/P_f)^{5/2} \\
 T_f &= m \cdot a_r \cdot \cos \left[ \arctan \left( \frac{-\Delta y}{\Delta x} \right) - \alpha_l \right] \\
 P_f &= m \cdot a_r \cdot \sin \left[ \arctan \left( \frac{-\Delta y}{\Delta x} \right) - \alpha_l \right], \tag{4.39}
 \end{aligned}$$

where  $m$  is the block mass,  $a_r$  is the block acceleration just before the impact,  $\gamma_{soil}$  is the unit weight of soil,  $\phi$  is the angle of soil internal friction,  $\Delta y$  and  $\Delta x$  are the incremental vertical and horizontal distance along the block trajectory just before the impact and  $\alpha_l$  is the local angle of inclination to the horizontal at the impact place,  $B_b$  is the width of equivalent ball penetration,  $T_f$  and  $P_f$  are the transversal and axial component of the impact force. For rock bases it is assumed that there will be no energy loss.

The calculations for following case histories are given in Appendix A.6.

#### 4.5.1 Case Study of Bedrina 1 Rock Fall in Switzerland

Bozzolo et al. (1988) used two mathematical models SASS and MASSI, which simulate the planar motion of an ellipsoidal rock down a mountain side, to back analyze the Bedrina-1 rock fall. SASS accounts for sliding, rolling, impact and free flight of an individual rock, while MASSI considers free flight and impact only. Bozzolo et al. (1988) concluded that SASS seemed to better predict maximum run-out distances while MASSI was advantageous for the estimation of the heights of free flight on rocky ground. They also used three cameras to record block

movements down the slope during the field tests. The observed block movements were different at each trial which may indicate a chaotic nature of the movement i.e. unrepeatable and unpredictable outcomes of the event.

In the Bedrina-1 area, a  $10 \text{ m}^3$  boulder (equivalent ball radius 1.3 m) had crashed through the highway path, which cross section is shown in Fig. 4.22.

In this case, the slope is considered made of rock while the highway path is considered made of gravel because of the presence of the road base and sub-base layers. Also, the two horizontal natural shelves at elevation -4 and -6.66 m are considered to have some talus deposit of gravel type. Assumed gravel properties are  $\phi = 35^\circ$  and  $\gamma_{soil} = 20 \text{ kN/m}^3$ . Assumed rock unit weight =  $25 \text{ kN/m}^3$ . Assumed initial velocity of 0.1 m/s and its inclination to the horizontal of  $-45^\circ$  were sufficient to trigger a rock fall. The results are shown in Fig. 4.22. Computed velocity of the impact with the highway = 50 m/s and the penetrations of the equivalent ball into gravel at el. -4 m and -133.3 m were 1.3 m. This is a rather large penetration and is not in agreement with the assumption used in Equation (4.39) about a surface block.

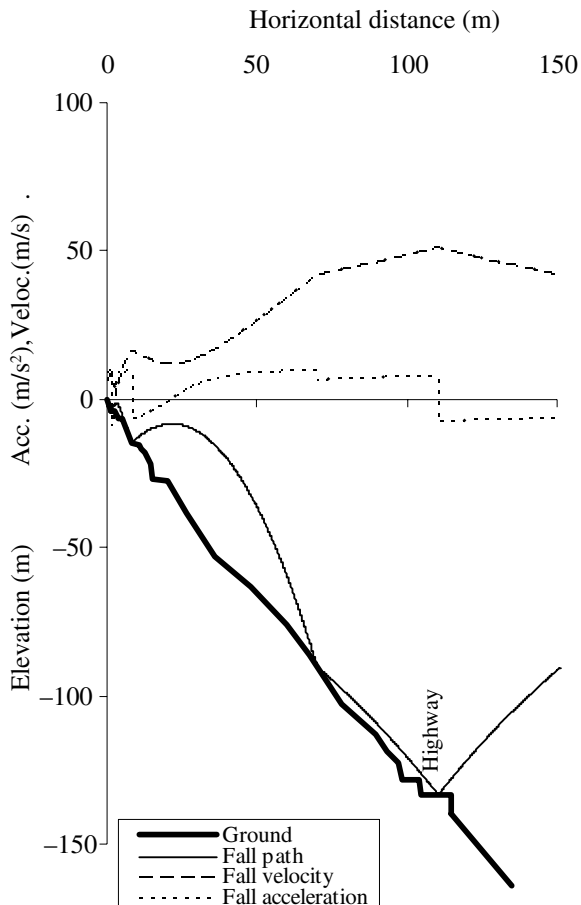


**Fig. 4.22** Bedrina 1 rock fall parameters (Srbulov, 2007a, by permission of Patron Editore)

However, practical formulae for spherical footings penetrating to different depths are not widely available.

It should be mentioned that the rock block acceleration does not exceed the gravitational acceleration and therefore the impact force does not exceed the rock block weight. However, the energy stored into a rock block on impact is proportional to the square of the impact velocity. It is the inability of rock block to compensate for such impact energy internally that can lead to rock crushing.

#### 4.5.2 Case Study of Shima Rock Fall in Japan

Ushiro et al. (1999) described a rock fall of approximately  $2.6 \text{ m} \times 1.3 \text{ m} \times 1.8 \text{ m}$  size (the equivalent radius of a ball of 1.1 m), which hit a car running on the Toyo-Yasuda road at 7:50 a.m. on 2 March 1996. The driver was injured and died later in hospital. The cross section of a possible path of rock fall is shown in Fig. 4.23.

The surface of the ground consists of sandstone and shale. There are many trees and boulders of 0.5 m to 0.8 m size along the slope. Many scars, splits and shearing were found on the trees along the path. The scars on the tree logs were located less than 1 m above the ground surface. Six depressions were found along the slope. Four

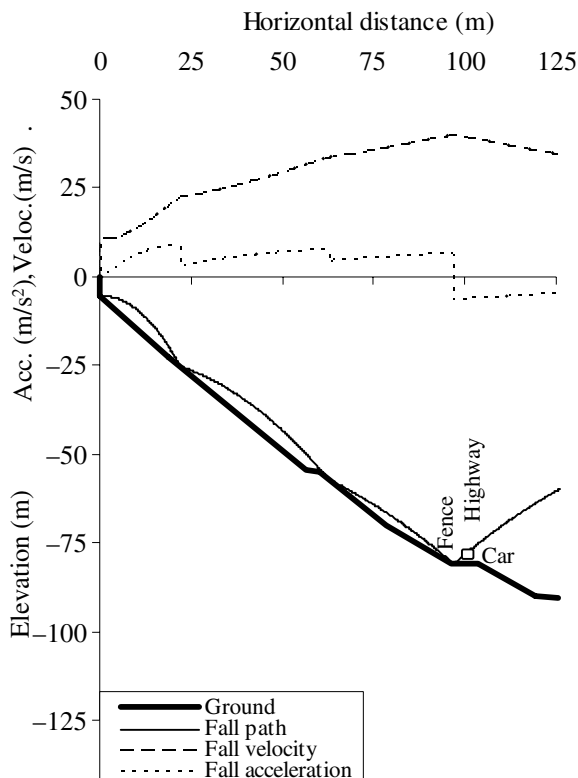


**Fig. 4.23** Shima rock fall parameters (Srbulov, 2007a, by permission of Patron Editore)

of them were above the highway level. The props of a guard fence installed along the side of the road were pushed into the ground 13 cm by the rock fall.

Assumed rock unit weight =  $25 \text{ kN/m}^3$ . Assumed initial velocity of 0.1 m/s and the velocity inclination to the horizontal of  $0^\circ$  were sufficient to trigger a rock fall. The results are shown in Fig. 4.23. Computed velocity of the impact with the car is 39 m/s, leaving no chance to the driver to avoid it.

Parametric analysis shows that the rock size is not of great importance for its travel path. If the rock fall started from a different place or the slope surface was covered by soil then the rock fall trajectory would have been different. Hoek (2006) stated that the slope geometry and the coefficients of restitution are the most important factors for rock falls.

#### 4.5.3 Case Study of Futamata Rock Fall in Japan

Ushiro et al. (1999) described a rock fall of approximate  $1 \text{ m} \times 0.7 \text{ m} \times 0.55 \text{ m}$  size (the equivalent radius of a ball of 0.45 m), which hit a pickup truck running

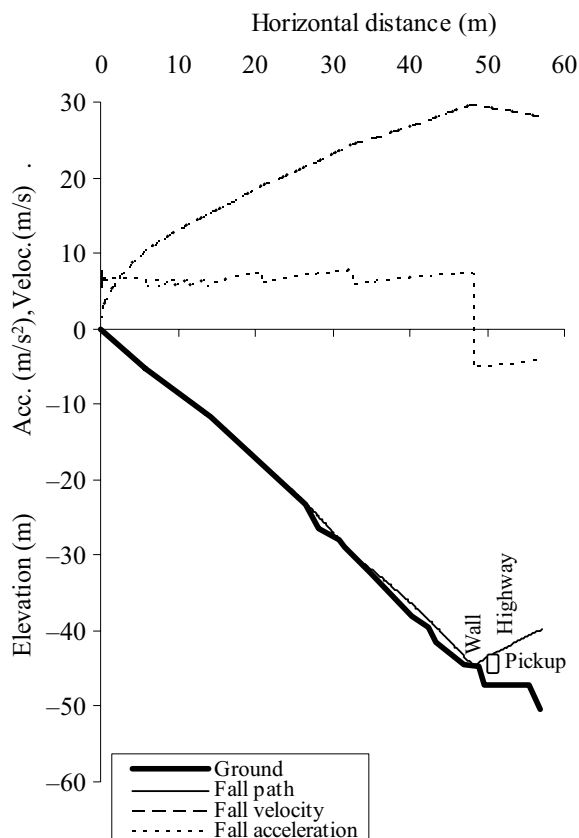


**Fig. 4.24** Futamata rock fall parameters (Srbulov, 2007a, by permission of Patron Editore)

on the Toyo-Yasuda road at 8:20 a.m on 11 August 1988. The boulder killed the driver's wife. The diver was seriously injured and hospitalized for 2 months. The cross section of a possible path of rock fall is shown in Fig. 4.24.

The slope consists of sandstone and shale and is covered with 1 m to 2 m thick talus. There were many 0.3 m to 0.5 m size boulders on the slope. Most scars on the trees were made within 1.1 m above the ground except the last tree next to the road which was hit at 2 m above the ground. Ushiro et al. (1999) estimated that the boulder initially rolled or slid on the slope, then jumped and bounced on the retaining wall adjacent to the road and finally hit the roof of the pickup.

Assumed rock unit weight =  $25 \text{ kN/m}^3$ . Assumed initial velocity of 0.1 m/s and its inclination to the horizontal of  $0^\circ$  were sufficient to trigger a rock fall. The results are shown in Fig. 4.24. Computed velocity of the impact with the pickup is 29 m/s, leaving no chance to the driver to avoid it.

The probability of collision between a falling rock and a car is rather small. Despite such a small probability, the fatal event happened. Therefore, a probabilistic approach is not appropriate for individuals but only for a larger number of events considered by insurance companies and authorities. There is also a question of reliability of estimated probability. If rock collision events are chaotic in nature then only the extreme values of the rock velocity, jump height and fall distance could be reliable but not particular results, which affect probability assessment if used to assess hazard of rock fall.

## 4.6 Simplified Model for Soil and Rock Avalanches, Debris Run-Out and Fast Spreads Analysis

Keefer (1984) found that rock avalanches are uncommon but soil avalanches abundant and that they are triggered by the earthquakes with large magnitudes, about 6.5. Because of very high speed of avalanche propagation and large volume of ground mass involved, the effect of their impact is devastating. For example, Villages of Yungay and Ranrahirca in Peru were buried by a giant avalanche in the 1970 Peruvian earthquake (e.g. Kramer, 1996). The ground movement involved 50 million cubic meters of material that covered an area of about 8000 square kilometers. About 25000 people were killed by the avalanche. Rodriguez et al. (1999) confirmed Keefer's (1984) findings concerning triggering of ground movements by earthquakes. However, the evaluation of the travel distance, moving mass acceleration and volume involved are also very important for the estimation of hazard caused by avalanches (Srbulov, 2007b).

A number of techniques exist for assessment of very fast ground movements involving avalanches, debris run outs and flow spreads.

- **Analytical and numerical methods.** Srbulov (2005a), for example, used a simple rolling cylinder model for calculation of distance of fast flow failures induced by sand liquefaction; McDougall and Hungr (2004, 2005) used a continuum model based on Lagrangian solution of the equations of motions and Hungr's

(1995) numerical model of unsteady flow; Havenith et al. (2003) used the discrete element method-UDEC; Srbulov (2003c) used a flow model for the analysis of possibility of the fast damage propagation through marine soil offshore Newfoundland; Chen and Lee (2000) used Lagrangian Galerkin finite element method; Sousa and Voight (1991) used an unsteady continuous flow model of an incompressible biviscous fluid; Hutchinson (1986) used a lumped mass model involving friction and pore water pressure dissipation).

- **Empirical and statistical methods.** McClung (2001), for example, used least square regression analysis and a Gumbel distribution based on data from Norway, the United States and Canada; Fannin and Wise (2001) applied an empirical-statistical method using forensic observations of post-logging landslide activity on the Queen Charlotte Islands, British Columbia; Finlay et al. (1999) used multiple regressions based on slope geometries in Hong Kong; Ambraseys (1988) compiled worldwide data from shallow earthquakes to estimate a limiting epicentral distance beyond which liquefaction has not been observed in earthquakes of different magnitudes.
- **Laboratory testing of small scale models.** McDougall and Hungr (2004), for example, used two-plains model for coarse granular material, Davies and McSaveney (2002) used silica sand dropped onto a 45° inclined slope, Modarressi et al. (1999) used centrifuge testing; Eckersley (1990) analyzed fast flow movements of coal fines.

While numerical methods tend to be general they require the use of proprietary software and a number of non-conventional ground parameters which must be assessed or assumed a priori by the user. Empirical and statistical methods are based on limited data sets and their use is often limited to specific cases. Laboratory methods can be limited by scaling laws, which sometimes cannot be all fulfilled simultaneously, and by available facilities for testing.

A simplified model described in this section for analysis of fast ground movements is based on the equations of motion, mass and energy balances and on conventional ground parameters. The model capability is checked for a number of case histories involving a rock avalanche, debris run-out and fast flow spread.

#### **4.6.1 Equation of Motion**

The equation of motion of a ground mass down slope between two vertical cross sections (Fig. 4.25) is:

$$m \cdot a = m \cdot g \cdot \sin \beta - \tau_b \cdot A_b + (\tau_u \cdot A_u - \tau_d \cdot A_d) \cdot \sin \beta + (\sigma_u \cdot A_u - \sigma_d \cdot A_d) \cdot \cos \beta, \quad (4.40)$$

where  $m$  is moving mass between two vertical cross sections,  $a$  is the mass acceleration,  $g$  is the gravitational acceleration,  $\beta$  is the base inclination to the horizontal between two cross sections,  $\tau_b$  is the average shear stress at the base and sides,  $A_b$  is the area of the mass contact with the base and sides,  $\tau_u$ ,  $\tau_d$  are the average vertical

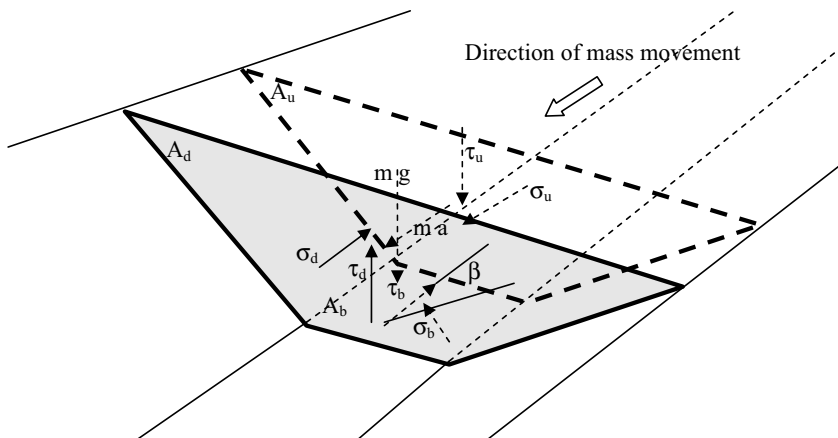


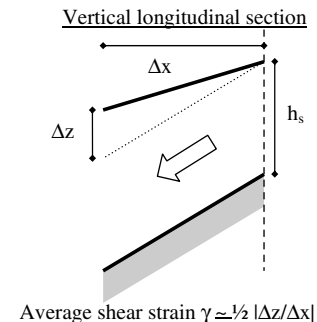
**Fig. 4.25** Two vertical cross sections (*shaded and with thick dotted line*) through a mass movement

shear stresses acting on the upstream and downstream vertical cross sections of the mass,  $A_u$ ,  $A_d$  are the upstream and downstream vertical cross section areas,  $\sigma_u$ ,  $\sigma_d$  are the average horizontal compressive stresses acting on the upstream and downstream vertical cross sections of the mass.

The initial triggering mass  $m_i$  and acceleration  $a_i$  can be estimated from limit equilibrium slope stability analyses, which are described in Section 4.2. The initial peak acceleration  $a_i$  can also be estimated from a number of attenuation relationships, such as given in Equations (3.6) and Equations (3.7). The effect of topography on the triggering peak ground acceleration can be significant as described in Section 3.3.4. The effect of acceleration amplification by ridges can be taken into account by adding a part or number of the standard deviations to the average values of accelerations.

The shear stress  $\tau$  in Equation (4.40) is calculated using the stress-strain relationship for a Kelvin-Voigt (K-V) solid in shear (i.e. material whose resistance to shearing deformation is the sum of an elastic part and a viscous part) instead of other possible stress-strain relationships such as frictional, plastic, Bingham etc. (e.g. McDougall and Hungr, 2004). The reason for choosing K-V model is that it represents a whole range of soil states from solid (small shear strain and its rate) to liquid (large shear strain and its rate) and that the model parameters can be defined based on soil index properties. The model is extensively used for the analysis of one dimensional propagation of shear waves in layered ground with the computer program SHAKE (Schnabel et al., 1972). The stress-strain relationship for K-V model is given in Equation (3.12). For mass movement, it is considered that shear stress reversal occurs at grabens and valleys across which mass moves so that the frequency of stress reversal is considered proportional to the ratio between the velocity of mass movement and distances of graben's peak and valley's trough. The relationships for shear modulus and damping ratio used in Equation (3.12) are given in Section 2.2.1.

**Fig. 4.26** Definition of average shear strain  $\gamma$  within moving mass (Srbulov, 2007b, by permission of Patron Editore)



Shear strain is very large at the contact of moving mass and its base and sides which implies that the corresponding shear modulus is very small according to Equation (2.3). In order to consider realistic values, the sum of  $G \cdot \gamma$  and  $\eta \cdot \partial \gamma \cdot \partial t^{-1}$  in Equation (3.12) is limited to the value of shear strength of moving coarse-grained material or the cohesion in undrained condition of fine grained material (with particles diameter less than about 0.005 mm). An average shear strain within moving mass is taken equal to a half of the ratio between the change of thickness  $\Delta z$  of moving mass and the horizontal length  $\Delta x$  over which it has been achieved as shown in Fig. 4.26.

The average shear strain rate in time  $\Delta \gamma \Delta t^{-1}$  is considered proportional to the average velocity  $v_m$  of moving mass over the distance  $\Delta x$ ,  $\Delta \gamma \Delta t^{-1} = (\gamma_d - \gamma_u) [\Delta x (v_m)^{-1}]^{-1} = (\gamma_d - \gamma_u) (v_m) (\Delta x)^{-1}$ . The initial mass velocity can be determined from a number of attenuation relationships, eg. Equation (3.9), taking into account the effect of topography. The effect of velocity amplification by ridges can be accounted for by adding a part or number of the standard deviations to the average values of velocities.

The average compressive stress on the vertical cross section of moving mass is calculated following Rankine (1857) as:

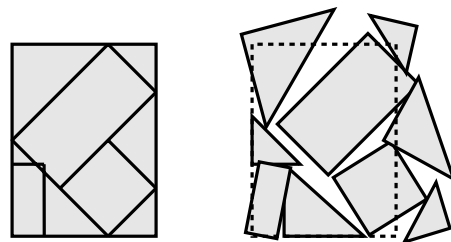
$$\sigma_{u,d} = \frac{1}{2} \rho \cdot g \cdot h_s \cdot \tan^2 \left( 45^\circ - \frac{\phi}{2} \right), \quad (4.41)$$

where  $\rho$  is the mass density,  $g$  is the gravitational acceleration,  $h_s$  is depth below surface,  $\phi$  is the friction angle in cyclic condition, Section 2.4.

#### 4.6.2 Mass Balance

The initial cross section area of moving mass is considered equal to the cross section area of the triggering slide at the beginning of movement. The cross section area of moving mass along the travel path is considered dependent on the base widths and the slopes of the terrain perpendicular to the travel path, which must be defined. During large movements soil and rock are loosened and sometimes broken down

**Fig. 4.27** Compact and bulked-up rock mass



leading to bulking-up, Fig. 4.27. According to Horner (1981), for example, the bulk-up of sand and gravel is 10–15%, clay 20–40%, loam/peat/topsoil 25–45% and rock 30–80%. The change of the initial volume is taken into account approximately in the simplified analysis.

Entrainment of material along travel path is an important feature of many rapid ground movements (e.g. McDougall and Hungr, 2005). It is assumed in the simplified model that the material entrainment occurs when shear stress acting on the ground present along travel path is greater than the shear strength of this material; deposition occurs when shear strength of base material is greater than acting shear stress. For this reason, the shear strength of base material together with the maximum depth of scour need to be estimated along expected avalanche path.

Hungr and Morgenstern (1984) found slight rate dependence of shear strength of sand. However, the shear strength of soil, rock fill and rock is strongly dependent on compressive stress (e.g. Maksimovic, 1989a to 1996b). Soil shear strength non-linearity should be taken into account when assessing the initial (in)-stability of a mass by limit equilibrium method. Hoek (1983) and Maksimovic (2005) showed that decrease in the calculated factors of safety of slope stability using limit equilibrium method and linear or non-linear shear strength criteria could be as high as 30%. Similar reduction of the calculated factor of safety of slope stability based on the peak soil shear strength can be expected in brittle soil that exhibit significantly smaller residual shear strength in comparison with its peak shear strength and progressive type of failure (e.g. Srbulov, 1997). Additional difficulty is estimation of excessive pore water pressure caused by earthquake shaking.

Davies and McSaveney (2002) considered that rock fragmentation lead to higher than normal internal pressures and the longer run out. However, rock fragmentation causes energy loss of a moving mass and therefore should cause shorter run distances. It is important that the material used for small scale laboratory tests has an appropriate frictional angle corresponding to the frictional angles of real material at high confining pressures.

#### 4.6.3 Energy Balance

The shear strain rate in Equation (3.12) is assumed proportional to the velocity of mass movement. The velocity of mass movement is estimated from the equation of

energy balance. The sum of potential and kinetic energy of a moving mass and the energy loss along travel path is constant

$$m \cdot g \cdot z_m + m \cdot \frac{v^2}{2} + 4 \cdot \pi \cdot \Sigma(W_s \cdot \xi) = const. \quad (4.42)$$

where  $m$  is the mass per unit length of travel path,  $g$  is the gravitational acceleration,  $z_m$  is the datum above the mass at rest position,  $v$  is the mass velocity,  $W_s$  is the strain energy,  $\xi$  is the damping ratio according to Equation (2.3), and  $\Sigma$  is the sum of energy loss over a travel path.

$$W_s = \frac{1}{2} \cdot G \cdot \gamma^2 \cdot V, \quad (4.43)$$

where  $G$  is the shear modulus,  $\gamma$  is the shear strain,  $V$  is the volume of the moving mass along travel path. The mass velocity is calculated at cross sections with known elevation above the datum.

The mass velocity is calculated independently from the mass acceleration according to Equation (4.40). Nevertheless, the first derivative in time of the mass velocity should correspond to the mass acceleration as close as possible. There will be some difference because the mass acceleration is calculated between sections and mass velocity at the sections.

The mass movements considered in Appendix A.7 were not triggered by earthquakes but are used because of lack of data about the cases triggered by earthquakes.

#### 4.6.3.1 Case Study of Pandemonium Creek Rock Avalanche in British Columbia

Evans et al. (1989) described and analyzed by Korner's (1976) dynamic model the Pandemonium Creek rock avalanche, which is located at 52°01'N, 125°46'W in the southern Coast Mountains of British Columbia, about 80 km southeast of Bella Coola. In 1959, a rock spur became detached from the headwall of a cirque near Pandemonium Creek due to an unknown reason. Approximately  $5 \times 10^6 \text{ m}^3$  of blocky, gneissic quartz diorite debris traveled about 9 km along a highly irregular path, descending a vertical distance of 2 km to the valley of South Atnarko River. The high mobility of the rock avalanche is manifested by super elevation range from 35 to 70 m in valley bends, a major run-up up to 335 m high, and two right-angle changes in flow direction, one down Pandemonium Creek and the other down South Atnarko River. The avalanche traveled over a glacier below the detachment zone from el. 2275 m to el. 1820 m, became constricted between two prominent lateral moraines along the path and most of it came to rest on the upper part of a fan at the mouth of Pandemonium Creek although one lobe traversed the fan and entered Knot Lakes, where it generated displacement waves that destroyed trees along the shore.

There are vertical aerial photographs of the site both before and after the event. A 1:5000 scale (contour interval 5 m) topographic map of the path, prepared from

aerial photographs flown in 1965, is used together with the field examination. An inspection of the air photos taken prior to the landslide and observations in the field indicate that the spur extended from el. 2625 m to el. 2275 m, it was approximately 175 m wide and 75 – 100 m thick. No earthquakes are known to have affected the area in 1959 and there were no major storms in July 1959. Unmodified debris on the Pandemonium Creek fan is poorly sorted and comprises angular to sub-rounded blocks (a few 10 – 15 m across and 30 – 500 m<sup>3</sup> in volume), boulders, and gravel, with only small amounts of sand and silt. No other properties of the material are provided in the paper by Evans et al. (1989) except the dynamic friction coefficient range 0.0025 – 0.186 and the turbulent resistance coefficient range 0 to 2000 m/s<sup>2</sup> used for parametric analyses by Korner's (1976) method. Discontinuous deposition took place on the glacier surface; some debris, including blocks up to 9 m size, remains in the upper travel path below the glacier; small amounts of debris are present in the run-up zone (one isolated block about 10 m size lies 50 m below the upper limit of the run-up zone). In its passage down Pandemonium Creek, the avalanche probably entrained some colluvial and glacial sediments; as well as probably some of the fan material in the run-out zone. Much of the debris was deposited on the fan in lobes with steep fronts up to 20 m high.

The longitudinal profile along the travel path is shown in Fig. 4.28 while the base widths along travel path together with an average inclination of ground surface perpendicular to the travel path are given in Appendix A.7.

The run-up along the slope above the junction with Pandemonium Creek is followed by run-down along the slope and down Pandemonium Creek and run-out over the fan and Knot Lakes shore. The friction angle of moving mass is assumed equal to 25°, which corresponds to the upper bound value in cyclic condition for medium dense sand according to Srbulov (2005a). The exceptions are the location of Pandemonium Creek fan and Knot Lake shore where the friction angle is assumed equal to 5°, due to likely presence of fine graded water saturated soil.

The constants  $\gamma_r$ ,  $a$ ,  $k$ ,  $\xi_{min}$  for moving mass are taken from Table 2.1 as for Tertiary and older deposits with  $PI = 0$  and for a mixture of the moving mass and the fan material as for Quaternary deposits with  $PI = 0$ . Moving mass unit density is assumed 2000 kg/m<sup>3</sup> and the shear wave velocity 205 m/s, with the exception of

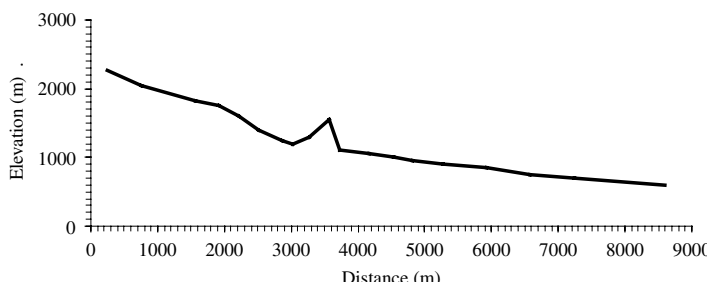


**Fig. 4.28** The vertical cross section considered along the path of the Pandemonium Creek avalanche (Srbulov, 2007b, by permission of Patron Editore)

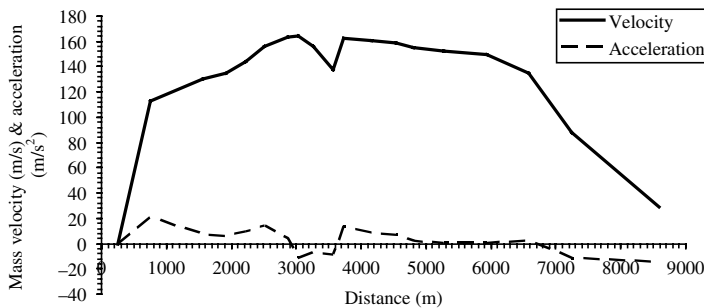


**Fig. 4.29** The mass velocity and acceleration along the path of the Pandemonium Creek avalanche from the elementary model (Srbulov, 2007b, by permission of Patron Editore)

the location of Pandemonium Creek fan and Knot Lake shore where the shear wave velocity is assumed to be 100 m/s.

The calculated velocity and acceleration of moving mass along the avalanche path are shown in Fig. 4.29. From this figure it follows that the maximum calculated velocity is 164 m/s. This peak velocity is in reasonable agreement with the upper bound peak velocity of about 130 m/s considered by Evans et al. (1989).

#### 4.6.3.2 Case Study of Shum Wan Road Debris Run-out in Hong Kong

Chen and Lee (2000) used Lagrangian Galerkin finite element method with a lumped mass matrix, a volume-weighted procedure and the method of least squares approximation for smoothing and enhancement of stability and efficiency of the numerical scheme to determine the nodal velocity and depth of a moving mass. They applied the method to Shum Wan Road debris run-out, which occurred during a heavy rainstorm, in Honk Kong on 13 August 1995. The debris was initiated as a landslide around the Nam Long Shan Road at elevation 75 mPD, crossed the Shum Wan Road at el. 5 mPD, damaged three shipyards and a factory near the seafront, and resulted in two fatalities and five injuries. The initial landslide involved about 26000 m<sup>3</sup> of soil and rock of which about a half remained on the hillside surface, and the other half was deposited on the reclaimed land at the bottom of the slope. The initial slide was up to 12 m deep and about 50 m wide while the debris run-out was about 90 m wide above Shum Wan Road. The released debris comprised mainly very soft or loose fluvial deposit of clay, silt, sand, gravel, and some cobles and boulders. Soil tests indicate that the clay seam along the initial landslide surface has an effective angle of friction of 22°. It has been concluded that the presence of clay seam and the ingress of water during prolonged heavy rainfall principally contributed to the failure.

The longitudinal section along a rather straight path of debris run-out is shown in Fig. 4.30 and the basic data in Appendix A.7.

Moving mass unit density is assumed 1800 kg/m<sup>3</sup> and that an average inclination to the horizontal of terrain perpendicular to the travel path is 45°. The constants  $\gamma_1$ ,

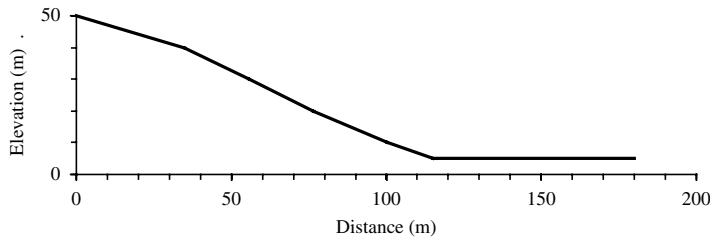


**Fig. 4.30** The vertical cross section considered along the path of the Shum Wan Road debris run-out (Srbulov, 2007b, by permission of Patron Editore)

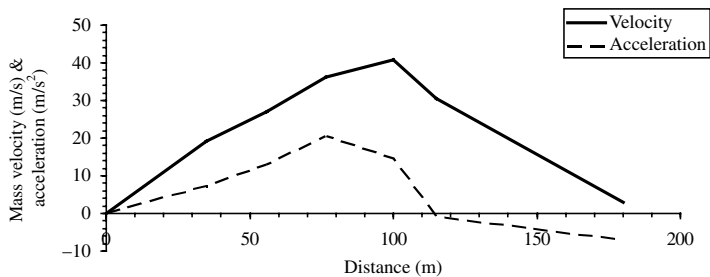


**Fig. 4.31** The mass velocity and acceleration along the path of the Shum Wan Road debris run-out from the elementary model (Srbulov, 2007b, by permission of Patron Editore)

$a$ ,  $k$ ,  $\xi_{min}$  for moving mass are taken from Table 2.1 as for Quaternary deposits with  $PI = 15$ . The friction angle within moving mass is assumed  $20^\circ$ .

The calculated velocity and acceleration of moving mass along the debris path are shown in Fig. 4.31. From this figure it follows that the maximum calculated velocity is 40 m/s. This peak velocity is greater than the maximum nodal velocity of about 14.4 m/s according to Chen and Lee's (2000) numerical model. The actual velocity is not known.

#### 4.6.3.3 Case Study of Coal Mine Waste Fast Spread at Aberfan in Wales

Hutchinson (1986) used a lumped mass sliding-consolidation model for an analysis of a fast spread of loose, cohesionless coal mine waste at Aberfan in 1966. The spread developed in a 67 m high tip of loose coal mine waste, consisting mainly of Carboniferous mudstones with some coal, deposited on a hillside of about  $12^\circ$  inclination. The foundation of the tip consisted of a layer of Late Pleistocene Head deposit, mainly silty clay solifluction debris several meters thick. The fast spread was preceded by a number of rotational slips and the removal of fines from its toe by seepage erosion, which was deposited as a sheet of slurry on the slopes below the tip toe.

The spread traveled quickly in several "black waves" down slope about 275 m before division into a north and south lobe. The northern lobe was smaller and came

to rest after a further travel of approximately 125 m, when its toe reached the low embankment of the old Glamorgan canal. The larger southern lobe reached this embankment after a further travel of about 150 m and had sufficient speed to override both this and the embankment of the dismantled railway, which were contiguous at that place, and to continue into the village of Aberfan for an additional 175 m, causing 144 deaths. The initial width of the spread run-out was 90 m and of the southern lobe about 130 m. The average thickness of the northern lobe was about 1.2 m and of the southern lobe about 2.0 m. Estimated the average speed of the spread , based on the account of eye-witnesses, was probably between 4.5 and 9.0 m/s and its maximum speed when it reached about 1 m high embankment between 11.2 and 13.5 m/s. The average bulk unit weight of the eastern part of the tip remaining after the failure was about 17.3 kN/m<sup>3</sup> and the Standard Penetration Test blow count corrected for effective overburden pressure ranged from 4 to 15 down to a depth of 10 m. The wide grading of the material involved, with the uniformity coefficient of about 18, can be classified as silty sandy gravel. This can explain the average friction angles of 39.5° in drained condition and 41.5° in undrained conditions obtained by triaxial compression tests on samples from the remaining part of the tip. A value of drained residual shear strength measured in the laboratory on a smear of fine material from the slip surface was as low as 17.5°.

The longitudinal section along a rather straight path of fast spread is shown in Fig. 4.32 and the basic data in Appendix A.7.

Moving mass unit density is assumed 1700 kg/m<sup>3</sup> and that an average inclination to the horizontal of terrain perpendicular to the travel path is vertical. The constants  $\gamma_r 1$ ,  $a$ ,  $k$ ,  $\xi_{min}$  for moving mass are taken from Table 2.1 as for Quaternary deposits with  $PI = 0$ . The friction angle in cyclic condition within moving mass is assumed 15° and shear wave velocity 100 m/s. The “black waves” are modeled as change in the spread thickness along the travel path. The effect of obstruction by buildings in Aberfan is modeled as soil entrainment.

The calculated velocity and acceleration of moving mass along the debris path are shown in Fig. 4.33. From this figure it follows that the maximum calculated velocity is 41 m/s. This peak velocity is greater than the maximum nodal velocity of about 13.5 m/s according to the eye witnesses in Aberfan. This comparison suggests that the simplified model may provide an upper bound value of the mass velocity.

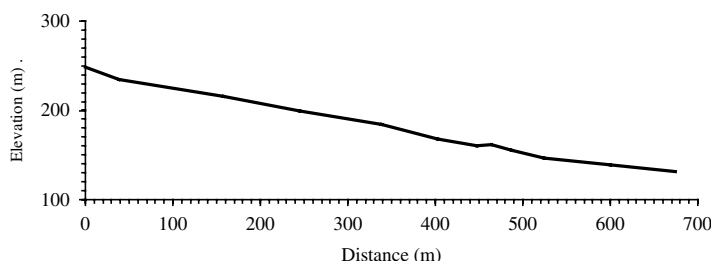


**Fig. 4.32** The vertical cross section considered along the path of the fast spread at Aberfan (Srbulov, 2007b, by permission of Patron Editore)

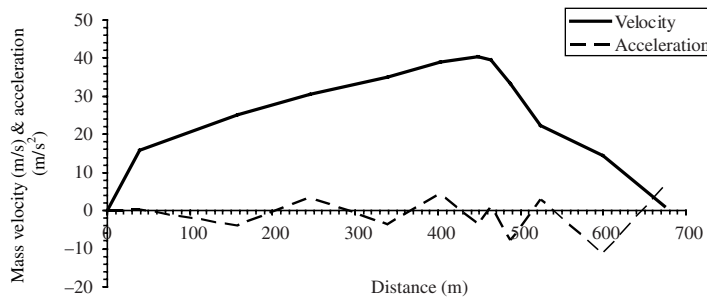


**Fig. 4.33** The mass velocity and acceleration along the path of the fast spread at Aberfan from the elementary model (Srbulov, 2007b, by permission of Patron Editore)

## 4.7 Summary

Several types of slope failures and ground displacements are considered in this section:

- Among sliding type slope failures, brittle failures are most problematical because they are fast and leave no time for remediation measures and in some cases for people to escape. Simplified analysis of stability of slopes in brittle soil and rock is possible using an extended limit equilibrium method described in Section 4.2.1.
- Reversible ground slope displacement, considered in Section 4.3, occurs when the inertial forces induced by ground motion do not cause exceedance of ground shear strength, triggering of slope failure, or irreversible slope movement.
- Permanent co-seismic displacement of failed slopes can be estimated using sliding block method and charts shown in Section 4.4.1. The charts are applicable to rigid ground with distinct slip surfaces and soil shear strength independent on slip rate and displacement.
- Post-seismic sliding may follow co-seismic stage if the ground shear strength necessary to maintain slope stability in static condition is decreased during earthquake by excess pore water pressure build-up or because of decrease of soil shear strength to its residual value. Two-sliding blocks method for analysis of post-seismic slope slip is described in Section 4.4.2.
- Rock falls are among most frequent and the fastest ground movements. Because of relatively small size of falling rock blocks, the effect of rock falls is important mainly for the individuals involved. Deterministic model of rock falls described in Section 4.5 can easily be used for parametric analyses of rock falls.
- Avalanches are relatively rare but have devastating consequences to the communities located on their path. Simplified model of avalanches, debris run-out and fast spreads, described in Section 4.6, can be used for estimation of the impact forces on barriers and of the height of such barriers to prevent jump-over of extremely rapid and massive ground movements.

# Chapter 5

## Sand Liquefaction and Flow

### 5.1 Introduction

Soil liquefaction frequently occurs when water saturated loose sandy soil is strongly loaded with prevented water drainage so that induced excess water pressure equals earth pressures. Strength of sandy soil is proportional to the difference between earth pressure and excess water pressure. When excess water pressure becomes equal to the acting earth pressure, soil shear strength decrease to zero and it behaves like a fluid i.e. liquefies.

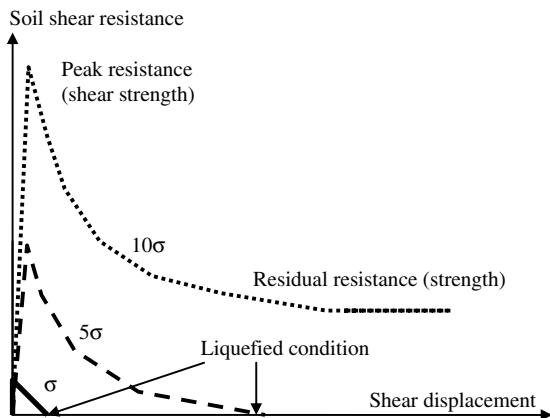
Various definitions of liquefaction have been proposed over the years (eg. Castro, 1969; Vaid and Chern, 1985).

Obermeier (1996) listed cases of soil liquefaction, which have not been caused by earthquakes. Among other factors causing liquefaction are rapid sedimentation and loading, artesian conditions, slumping, chemical weathering and periglacial environment.

Under high confining pressure, soil does not liquefy but loses a great portion of its shear strength due to excess pore water pressure built-up as shown in Fig. 5.1. Mobilized shear resistance of sand is mainly dependent on the magnitude of axial effective stress and shear displacement. Increased axial effective stress (by drainage for example) and decreased shear displacement (by confinement for example) improve soil resistance in general and to liquefaction in particular.

Seed and Harder (1990) presented graph of residual undrained shear strength of liquefied soil versus normalized blow count from the standard penetration tests. Olson and Stark (2002) proposed relationships between residual undrained shear strength  $c_{ur}$  to effective overburden pressure  $\sigma'_v$ , ratio of liquefied soil versus normalized blow count from the standard penetration tests, normalized tip resistance from the cone penetration tests and based on liquefaction flow failure case histories. Olson and Stark (2002) suggested that the  $c_{ur}/\sigma'_v$  from the liquefaction case histories varies in the range from 0.05 to 0.12, with an average value of 0.09. These ratios correspond to an equivalent friction angle range from  $2.9^\circ$  to  $6.8^\circ$  with an average value of  $5.1^\circ$ . Soil penetration resistance can be determined either before or after its liquefaction, generally giving different results. Assessment based on back analysis of liquefaction case histories is considered reliable.

**Fig. 5.1** Schematic of soil shear resistance versus horizontal displacement in loose sand at different axial effective stress  $\sigma$  magnitudes (modified from Yamamuro and Lade, 1997; Srbulov, 2005a, by permission of Patron Editore)



Sand liquefaction caused by ground motion usually involves only a limited depth range because of zero shear stress at the ground surface and high confining stress at greater depths. The seismic energy trapped in the soil crust overlaying a liquefied sand layer can cause an amplification of ground motion during the transition stage in comparison with the ground motion prior to liquefaction. This is possible when undamaged soil deposit has a higher resonant frequency than the dominant frequency of the earthquake. Soil softening will move the deposit towards resonance thus causing an increase in the amplification factors. For example, an accelerogram from site near an apartment building resting on liquefiable sand in 1964 Niigata earthquake (Aki, 1988) shows almost doubling of the peak acceleration of the top crust during the earthquake. This was attributed to the effects of resonance caused by softening during a transition from solid to liquid phase of underlying strata. The peak accelerations of the crust in the solid and liquid phase of underlying strata were similar.

The crust movement on sloping ground is a frequent cause of damage to piles (e.g. Berrill et al., 2001; Finn and Fujita, 2002).

The objectives of this chapter are to briefly summarize the conventional empirical methods for liquefaction assessment of horizontal ground, to describe simple rotating and rolling cylinder models for analyses of sand liquefaction potential and flow distance on sloping ground, and to show how these models are consistent with empirical methods.

## 5.2 Conventional Empirical Methods

### 5.2.1 Liquefaction Potential Assessment

Empirical procedures for analysis of potential of liquefaction mainly follow the work of Seed et al. (1985). The procedures are based on:

- a cyclic stress ratio,
- normalized blow count ( $N_1$ )<sub>60</sub> from the standard penetration tests (SPT),
- an empirical chart obtained from the past case histories.

According to Seed and Idriss (1971), the cyclic stress ratio, for magnitude  $M = 7.5$  earthquakes, is calculated according to the following formula

$$\frac{\tau}{\sigma'_v} = 0.65 \cdot \frac{a_{p,h}}{g} \cdot \frac{\sigma_v}{\sigma'_v} \cdot r_d, \quad (5.1)$$

where  $\tau$  is the shear stress caused by an earthquake,  $a_{p,h}$  is the peak horizontal ground acceleration (e.g. Equation 3.6 and 3.7),  $g$  is the gravitational acceleration,  $\sigma_v$  and  $\sigma'_v$  are the total and effective overburden pressure,  $r_d$  is a stress factor with depth.

A measured SPT blow count  $N$  can be normalized to an overburden pressure of 100 kPa according to Liao and Whitman (1986), and can be corrected to an energy ratio of 60% (the average ratio of the actual energy  $E_m$  delivered by hammer to the theoretical free-fall energy  $E_{ff}$ )

$$(N_1)_{60} = N \cdot \sqrt{\frac{100}{\sigma'_v}} \cdot \frac{E_m}{0.6 \cdot E_{ff}}, \quad \sigma'_v \text{ is in kPa}$$

$$0.5 < \sqrt{\frac{100}{\sigma'_v}} < 2, \quad (\text{Eurocode 8-5})$$

$$N = 0.75 \cdot N \quad \text{at depths} \leq 3m, \quad (\text{Eurocode 8-5}),$$
(5.2)

where  $\sigma'_v$  is the effective overburden pressure at the depth where  $N$  is recorded from SPT's blow count. Other corrections to  $N$  are applied, such as for the borehole diameter, rod length and sampler type (e.g. Skempton, 1986; Cetin et al., 2004).

Boundaries between liquefiable and non-liquefiable (silty) sand are published by NCEER and are periodically updated in the light of experience (Youd and Idriss, 2001). The boundaries are shown in Fig. 5.2 for earthquake magnitude  $M = 7.5$ ,

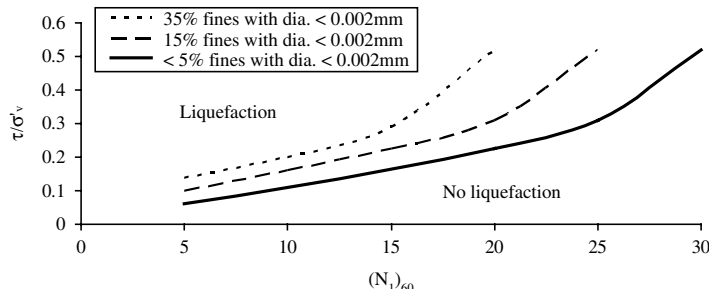


**Fig. 5.2** Boundaries for earthquake magnitude  $M = 7.5$ , effective overburden pressure 100 kPa, nearly horizontal ground surface and a depth of about 20 m below the ground surface (based on Eurocode 8-5)

**Table 5.1** Magnitude correction factors (dividers of the right hand side of Equation (5.1) according to Ambraseys (1988) and Eurocode 8-5

Magnitude M <sub>s</sub>	5.5	6.0	6.5	7.0	8.0
The correction factor	2.86	2.20	1.69	1.30	0.67

effective overburden pressure of 100 kPa, nearly horizontal ground surface and depths to about 20 m below the ground surface.

Different magnitude scaling factors are used (e.g. Cetin et al., 2004). Eurocode 8-5 uses the magnitude correction, i.e. divider of the right hand side of Equation 5.1, suggested by Ambraseys (1988) as shown in Table 5.1.

Different proposals exist for the stress factor with depth  $r_d$  because of its large scatter (e.g. Cetin et al., 2004). Eurocode 8, Part 5 adopts  $r_d = 1$ .

Similar procedures to the procedure based on SPT test results exist for the cone penetration test (CPT) results and transversal wave velocity measurements (e.g. Moss et al., 2006; Seed et al. 2003).

The empirical charts mentioned above are for nearly horizontal (level) ground only. Soil slopes are subjected to shear stress caused by gravity forces. Harder and Boulanger (1997), for example, provided graphs for correction of the cyclic stress ratio for sand and Boulanger and Idriss (2007) for silt and clay. The scatter of the correction factors in the graphs is large. Possible effect of slope inclination on liquefaction potential of sand with fines is investigated in more details in Section 5.3 using a simplified model.

### 5.2.2 Flow Consideration

Hamada et al. (1986) considered the effects of geotechnical and topographic conditions on permanent ground displacements observed in uniform sand of medium grain size in the 1964 Niigata ( $M = 7.5$ ), 1971 San Fernando ( $M = 7.1$ ) and 1983 Nihonkai-Chubu ( $M = 7.7$ ) earthquakes. Flow distances were found to be most strongly influenced by the thickness of the liquefied layer and the slopes of the ground surface and lower boundary of the liquefied zone. Flow distance  $u_f$  (m) was obtained from the equation

$$u_f = 0.75 \cdot L_l^{1/2} \cdot \beta_l^{1/3}, \quad (5.3)$$

where  $L_l$  is the thickness of the liquefied layer in meters and  $\beta_l$  is the larger inclination of the ground surface slope or the slope of the lower boundary of the liquefied zone in percent.

Youd et al. (2002), among others, used a large data base of lateral spreading case histories to develop empirical expressions relating lateral ground displacement to a number of source and site parameters. Empirical relationships are applicable to the data sets based on which they are derived and may not be extrapolated to other

cases. A simplified model described in Section 5.4 is based on both geometrical and physical properties of liquefied soil.

### 5.3 Rotating Cylinder Model for Liquefaction Potential Analysis of Slopes

#### 5.3.1 Model for Clean Sand

When structure of loose sandy soil deforms because of ground shaking, soil grains tend to move into pores between grains. As a result of such movement, soil tends to decrease its volume, which causes build-up of excess pore water pressure in submerged condition, decrease of effective stresses and of soil shear strength. If soil shear strength is decreased to zero then soil exhibits liquefaction. Soil grains movement into adjacent pores should be considered by a model. However, such a model will require also consideration of very complex water pressures variation in time; otherwise the model would indicate an increase in soil strength during ground shaking instead of its decrease.

In the simplified model considered in this section, submerged sand grains are represented as cylinders in two-dimensions, as shown in Fig. 5.3. No interaction between soil and water is considered because dynamically (highly) pervious condition is assumed to exist around a grain. When subjected to sufficient horizontal ground acceleration, the cylinders rotate about the edge of a groove created by adjacent sand grain i.e. cylinder, Fig. 5.3. If ground acceleration exceeds a critical value then the cylinders will not return back into the groove when ground motion decreases or reverses. Over the edge, the cylinders roll out for a considerable distance due to gained momentum and a relatively small residual resistance. It is sufficient to consider a single grain i.e. a cylinder in two-dimensions because adjacent sand grains (cylinders) move in phase in the horizontal direction and do not experience any lateral interaction.

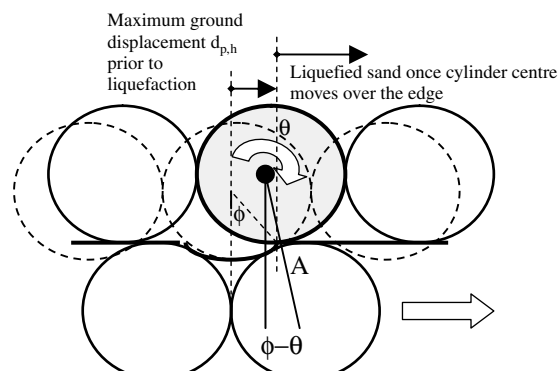


**Fig. 5.3** Simplified model of sand liquefaction for horizontal (level) ground

This is not the first time that a simplified model is used for consideration of ground shaking. The ancient Chinese seismometer used throwing of a little ball into mouth of a frog sculpture to indicate direction of ground shaking (<http://www.chcp.org/seismo.html>).

The angle of inclination of the groove at the edge (point A in Fig. 5.3) is equal to the frictional angle  $\phi$  of sand in cyclic conditions, Section 2.4. The half width of the groove is assumed to be proportional to the maximum horizontal ground displacement  $d_{p,h}$  during earthquake shaking before liquefaction, e.g. Equation 3.10. This is to assure model physical connection to actual ground motion. From the geometry in Fig. 5.3, the cylinder radius  $r = d_{p,h} [\sin(\phi - \beta)]^{-1}$ , where  $\beta$  is the angle of slope inclination, if any.

Only the submerged cylinder weight  $W = (\rho - \rho_w)g r^2 \pi$  and horizontal inertia force  $\rho_{ah} r^2 \pi$  act on the cylinder with radius  $r$  prior to its rotation;  $\rho$  and  $\rho_w$  are unit densities of sand and water,  $a_h$  is the horizontal ground acceleration and  $g$  is the gravitational acceleration. Moment equilibrium around point A (Fig. 5.3) of acting forces provides expression for the critical acceleration ratio  $a_{cr} g^{-1}$  in the horizontal direction prior the cylinder rotation

$$\frac{a_{cr}}{g} = \frac{\rho - \rho_w}{\rho} \cdot \tan(\phi - \beta), \quad (5.4)$$

where  $\phi$  is sand friction angle in cyclic conditions,  $\beta$  is slope inclination angle, if any. The critical acceleration for a submerged sliding block on a planar surface is equal to the critical acceleration for the rotating cylinder model.

When the ground acceleration exceeds this critical acceleration the cylinder is set in rotation. The equation of rotation of a rocking block is (e.g. Yim et al., 1980)

$$I_o \ddot{\theta} + W \cdot r \cdot \sin(\phi - \beta - \theta) = -r^2 \cdot \pi \cdot \rho \cdot a_h \cdot r \cdot \cos(\phi - \beta - \theta), \quad (5.5)$$

when only the horizontal component of ground acceleration  $a_h$  is considered in order to be able to compare the results of the model with the empirical method based on Equation (5.1) and Fig. 5.2, which consider horizontal ground motion only. The polar moment of mass inertia of a cylinder with radius  $r$  around a point is  $I_o = 2r^2 \pi \rho r^2$ ,  $\ddot{\theta}$  and  $\theta$  are rotational acceleration and rotation angle respectively of the block around a point,  $W$  is the block weight,  $\rho$  is unit density of block. Equation (5.5) is non-linear because of the presence of trigonometric functions of  $\theta$ . Another source of non-linearity is the instantaneous switching of equations as the block rocks alternately around its two edges.

Yim et al. (1980) solved the equation of motion using a fourth-order Runge-Kutta numerical integration scheme with a typical time step of 1/400 s. The accuracy of the computer program was checked by comparing its results with analytical results for single-pulse excitation (Housner, 1963) and with experimental results from shaking table experiments using earthquake-type excitations. Yim et al. (1980) found that small variations in the system parameters and ground motion lead to large changes in the response. In contrast to the conclusions for single-pulse excitations, the stability

of a block (cylinder) does not necessarily increase monotonically with increasing its size, or with the angle  $\phi$  nor does it necessarily decrease with increasing intensity of ground motion. Similarly, an increase in energy dissipation through the impact on the base, does not necessarily lead to smaller response of the block. Also, the influence of vertical ground motion is apparently non-conclusive. The sensitivity of the rocking response of a rigid block is present even in the case of single-pulse excitation. Hogan (1990) analyzed the chaotic nature of the steady state responses of a rocking rigid block under harmonic forcing.

Ground acceleration ( $a_h$  in Equation 5.5) can be expressed using a simple harmonic motion with an averaged period according to Section 2.5. The equation of a harmonic motion is

$$a_h = 0.65 \cdot a_{p,h} \sin(\omega_o \cdot t), \quad (5.6)$$

where  $a_{p,h}$  is the horizontal peak acceleration amplitude (e.g. Equations 3.6 and 3.7),  $t$  is time and the circular frequency  $\omega_o = 2\pi T_{eqv}^{-1}$ ,  $T_{eqv}$  is the period of equivalent harmonic motion. For the present model, the period is assumed equal to the ratio between the peak velocity and acceleration (eg. Fig. 3.6).

The rotating cylinder model will be considered to exhibit liquefaction if the cylinder rotation angle  $\theta$  becomes greater than  $\phi - \beta$ , i.e. when the cylinder centre passes over the edge of the groove (Point A in Fig. 5.3). For a range of angle  $\theta$  of up to about  $10^\circ$ ,  $= 0.174$  radians, sine of  $\theta = 10^\circ$  is 0.174 and cosine of  $\theta = 10^\circ$  is 0.985, which are close to the value of angle  $\theta$  in radians and 1 respectively. When sine and cosine functions of angle  $\theta$  are replaced by the first members of their Taylor series and the ground acceleration is replaced by its equivalent harmonic motion (Equation 5.6) then Equation (5.5) becomes

$$I_o \ddot{\theta} - W \cdot r \cdot \theta = -W \cdot r \cdot (\phi - \beta) - 0.65 \cdot r^3 \pi \cdot \rho \cdot a_{p,h} \sin(\omega_o \cdot t) \quad (5.7)$$

This is a non-homogeneous linear ordinary second order differential equation with constant coefficients. It can be expressed in more compact form as:

$$\ddot{\theta} - \omega^2 \theta = L_1 + K_1 \cdot \sin(\omega_o t) \quad (5.8)$$

where:

$$\begin{aligned} \omega^2 &= \frac{W \cdot r}{I_o} \\ L_1 &= -(\phi - \beta) \cdot \omega^2 \\ K_1 &= \frac{-0.65 \cdot r^3 \cdot \pi \cdot \rho \cdot a_{p,h}}{I_o} \end{aligned} \quad (5.9)$$

From Equation (5.6) follows that the cylinder will start rotation when  $a_h = a_{cr}$  at time  $t_1 = \omega_o^{-1} \arcsin[a_{cr} (0.65 a_{ph})^{-1}]$

The solution of Equation (5.8) is:

$$\theta = C_1 e^{\omega \cdot t} + C_2 e^{-\omega \cdot t} - \frac{L_1}{\omega^2} - \frac{K_1}{(\omega^2 + \omega_o^2)} \sin(\omega_o t) \quad (5.10)$$

The constants  $C_{1,2}$  for the condition that the initial cylinder rotation is zero and that the initial rotational velocity is  $[0.65 a_{p,h} \omega_o \cos(\omega_o t_1)][r \cos(\phi - \beta)]^{-1}$  at time  $t_1$  are:

$$\begin{aligned} C_1 &= \frac{e^{-\omega \cdot t_1}}{2\omega} \left\{ \frac{0.65 \cdot a_{p,h} \omega_o \cos(\omega_o t_1)}{r \cdot \cos(\phi - \beta)} + \frac{K_1}{(\omega^2 + \omega_o^2)} \left[ \omega \cdot \sin(\omega_o t_1) + \omega_o \cos(\omega_o t_1) \right] \right\} \\ C_2 &= \frac{e^{\omega \cdot t_1}}{2\omega} \left\{ \frac{-0.65 \cdot a_{p,h} \omega_o \cos(\omega_o t_1)}{r \cdot \cos(\phi - \beta)} + \frac{K_1}{(\omega^2 + \omega_o^2)} \left[ \omega \cdot \sin(\omega_o t_1) - \omega_o \cos(\omega_o t_1) \right] \right\} \end{aligned} \quad (5.11)$$

Only a half of a cycle (i.e. the rotation around point A) according to Equation (5.10) is considered with equivalent harmonic base motion so that the problem of chaotic rocking is not relevant.

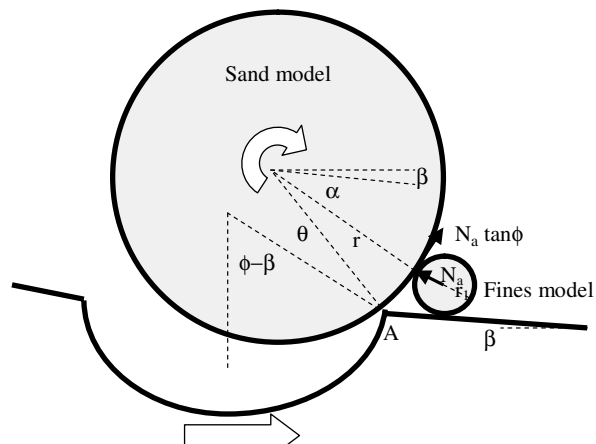
### 5.3.2 Model for Sand with Fines

Figure 5.4 shows rotating cylinder model of sand with fines.

The weight  $W_1$  of the fines model is assumed to be

$$W_1 = \frac{\% \text{fines}}{\% \text{fines} + \% \text{sand}} \cdot W, \quad (5.12)$$

where  $W$  is the weight of the basic model defined before. The radius of the fines model  $r_1 = \{W_1[\pi(\rho - \rho_w)g]^{-1}\}^{0.5}$ ,  $\rho$  and  $\rho_w$  are unit densities of soil and water



**Fig. 5.4** Rotating cylinder model of sand with fines (Srbulov, 2005a, by permission of Patron Editore)

and  $g$  is the gravitational acceleration. The angle  $\alpha$  in Fig. 5.4 is

$$\alpha = \arcsin \frac{r \cdot \cos(\phi - \theta) - r_1}{r + r_1} \quad (5.13)$$

The axial force  $N_a$  between a sand grain model and a fines model in the static condition, in the absence of earthquake accelerations, is

$$N_a = \frac{W_1 [\cos \beta \tan \phi - \sin \beta]}{\cos \alpha}, \quad (5.14)$$

where  $\beta$  is the angle of slope inclination, if any, and  $\phi$  is the angle of soil friction in cyclic conditions. The shortest distance  $x$  between the force  $N_a$  and point A in Fig. 5.4 is

$$x = r \cdot \sin \left( \frac{\pi}{2} - \phi + \theta - \alpha \right) \quad (5.15)$$

The shortest distance (level arm)  $y$  between the force  $N_a \tan \phi$  and point A in Fig. 5.4 is

$$y = r \cdot \left[ 1 - \cos \left( \frac{\pi}{2} - \phi + \theta - \alpha \right) \right] \quad (5.16)$$

When the sine and cosine functions are replaced by the first members of their Taylor series, the additional moments around point A of the forces  $N_a$  and  $N_a \tan \phi$  are

$$N_a \cdot r \cdot \left( \frac{\pi}{2} - \phi + \theta - \alpha \right) \quad (5.17)$$

The revised critical acceleration ratio is

$$\frac{a_{cr}}{g} = \frac{\rho - \rho_w}{\rho} \cdot \tan(\phi - \beta) \cdot \left[ 1 + \frac{\%fines}{\%fines + \%sand} \frac{\cos(\phi + \alpha)}{\cos \alpha} \right] \quad (5.18)$$

Revised coefficients in Equation (5.9) become

$$\begin{aligned} \omega^2 &= \frac{(W - N_a) \cdot r}{I_o} \\ L_1 &= \frac{-W \cdot r \cdot (\phi - \beta) + N_a \cdot r \cdot (\phi + \alpha - \frac{\pi}{2})}{I_o} \end{aligned} \quad (5.19)$$

Calculation of friction angles of liquefied soil according to the rotating cylinder model is performed for the horizontal (level) ground, earthquake magnitude 7.5 and

**Table 5.2** The source-to-site distances used in Equations (3.6), (3.9), (3.10) for the back analysis

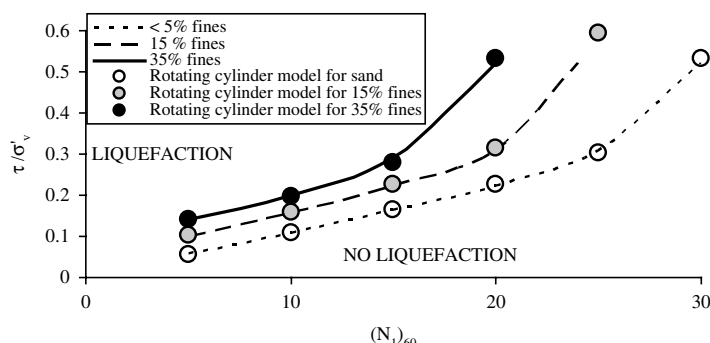
$(N_1)_{60}$	Distance (km) for maximum 5% fines	Distance (km) for 15% fines	Distance (km) for 35% fines
5	180.0	85.0	41.0
10	80.0	50.0	28.0
15	48.0	32.0	18.5
20	32.0	21.0	8.0
25	22.0	7.0	
30	9.0		

effective overburden pressure of 100 kPa. The standard penetration test blow count  $N$  is obtained from corrected  $(N_1)_{60}$  according to Equation (5.2). The average peak horizontal ground acceleration, velocity and displacements, which are necessary for definition of harmonic load amplitude and period and for the cylinder radius, are calculated using Equations (3.6), (3.9), (3.10) respectively for the source-to-site distances shown in Table 5.2.

The friction angles of liquefied soil in cyclic condition according to the rotating cylinder model as well as the ratios between the cyclic and static friction angles (Equation 2.7) are obtained by trial and error in order to achieve the model prediction of soil liquefaction following the border lines between liquefied and non-liquefied condition shown in Fig. 5.5.

The calculated angles and the ratios according to the rotating cylinder model are shown in Figs. 5.6–5.8.

The tangents of calculated range of friction angle from  $3.1^\circ$  to  $6.1^\circ$  at  $(N_1)_{60} = 5$  are in excellent agreement with the range from 0.05 to 0.12 of the  $s_{ur}\sigma_v^{-1}$  ratio suggested by Olson and Stark (2002). The model is less accurate for the rotation angle of the cylinder exceeding about  $10^\circ$ , for which the assumption that  $\sin \theta = \theta$  is less applicable.

**Fig. 5.5** Matching of the results of rotating cylinder model with the border lines from Fig. 5.2

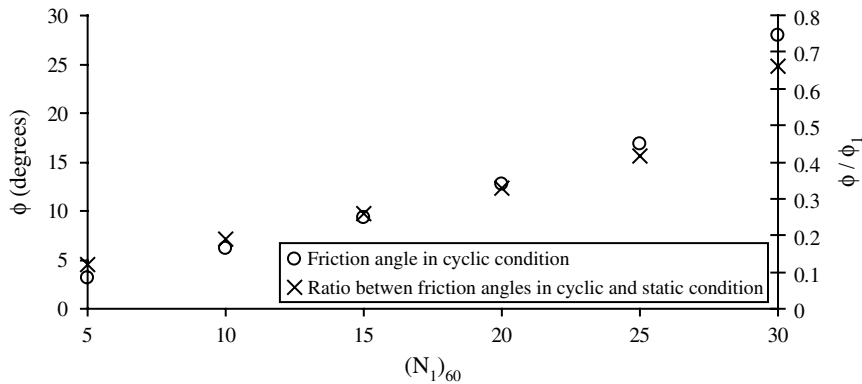


**Fig. 5.6** Friction angles of sand with less than 5% fines and the ratios between the friction angles in cyclic and static condition corresponding to the border line in Fig. 5.2 between liquefied and non-liquefied condition when analyzed by the rotating cylinder model

### 5.3.2.1 Case Studies of Liquefied Ground Slopes

The case histories of liquefaction of sloping sandy soil are obtained from Olson (2001). An abbreviated description of the case histories is given below.

1. **Sheffield Dam in California, USA.** The earth dam had a maximum height of about 7.6 m. The reservoir level was about 4.6 to 5.5 m at the time of failure, according to Seed et al (1969). The upstream and downstream slopes were inclined approximately 1 vertical to 2.5 horizontal. The upstream slope was covered by a 1.2 m thick clay blanket that extended 3 m into the foundation to act as a cut-off wall. Seed et al. (1969) estimated that the free field peak surface acceleration at the dam site was about 0.15 g from the 1925 Santa Barbara

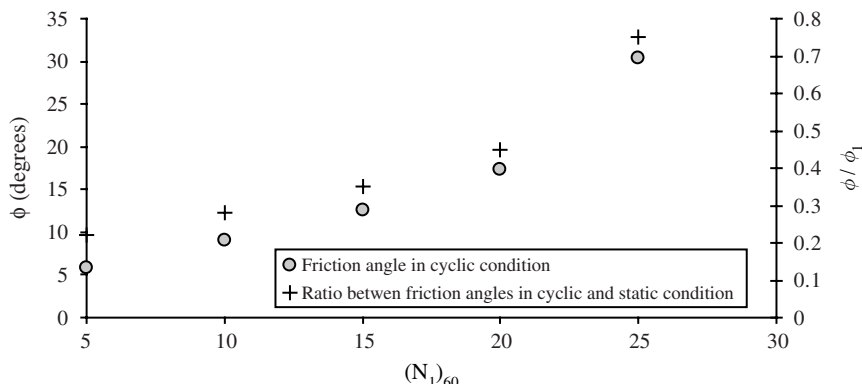


**Fig. 5.7** Friction angles of sand with 15% fines and the ratios between the friction angles in cyclic and static condition corresponding to the border line in Fig. 5.2 between liquefied and non-liquefied condition when analyzed by the rotating cylinder model

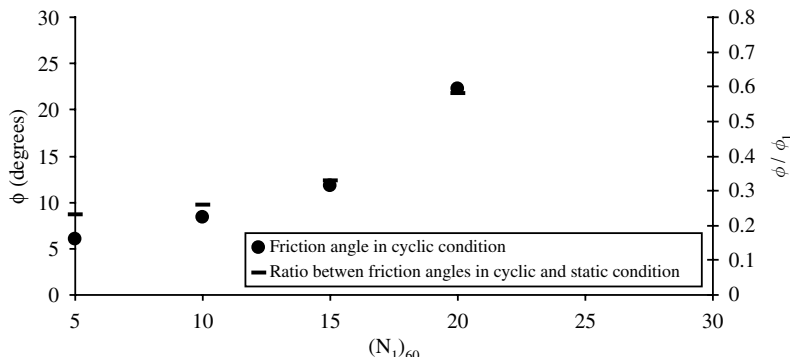


**Fig. 5.8** Friction angles of sand with 35% fines and the ratios between the friction angles in cyclic and static condition corresponding to the border line in Fig. 5.2 between liquefied and non-liquefied condition when analyzed by the rotating cylinder model

earthquake with  $M_L \sim 6.3$  at the epicentral distance of about 11 km. The failure caused a 130 m wide section of the downstream slope of the dam to flow for a distance of over 60 m downstream. Seed et al. (1969) concluded that the failure occurred due to liquefaction and strength loss of the soil along the base of the dam. The dam had been constructed of material consisting of silt, sand and sandstone with cobbles. Compaction was achieved only by the routing of light construction equipment over the fill. No penetration test results are available. The estimation of the blow counts was based on an appraisal of relative density and vertical effective stress.

2. **Solfatara Canal Dike in Mexico.** The Solfatara Canal dikes were destroyed over a 19 km stretch, from a point corresponding to the 1940 Imperial Valley earthquake fault trace. The earthquake magnitude was  $M_L = 7.1$ . Ross (1968) reported that the dikes were badly fissured along their length and settled over 2 m into the foundation soil. Ross (1968) investigated a 300 m stretch of dike that was reported to flow down slope a distance of approximately 23 m. From Ross's (1968) reconstruction of the pre and post failure geometry of the dike it appears that the dike was about 3 m high with the slope of about  $19^\circ$  to the horizontal. No strong motion instrument was located near the site. The instruments located in the city of El Centro measured a peak ground surface acceleration of 0.33 g. The stretch of the dike that failed is located closer to the fault trace than El Centro city and hence the ground shaking at the location of the dike was likely larger than 0.3 g. The dike fill consists of loose clean fine grained sand according to Ross (1968). Approximately 1 m thick layer of organic soil was encountered below the ground surface in another borehole. Fine sand with silty lenses was encountered below the organic rich soil layer (Ross, 1968). The natural soil has fines content of 6 to 8%. No penetration test results are available and the estimation of the blow counts was based on an appraisal of relative density and vertical effective stress.

3. **Lake Merced Bank in California, USA.** Ross (1968) investigated the slide along the bank of Lake Merced. The failure occurred at a distance of 4 to 6 km from the centre of the fault zone during the 1957 San Francisco earthquake with magnitude  $M_L = 5.3$ . Mainly the filled soil moved about 18 m into the lake, judging according to the final position of several slabs of the pavement. The fill soil was placed by end dumping into the lake. The slope of the fill was about 1 V to 1.5 H, while the slope of the natural ground was between 1 V to 3 H and 1 V to 4 H. No strong motion instruments were located at the site. The instruments located on a bedrock outcrop in Golden Gate Park in San Francisco (approximately 11.2 km from the earthquake epicentre) measured a peak ground acceleration of 0.12 g. At the fault distance of 4 to 6 km, the peak ground acceleration most likely was greater than 0.12 g. The near surface sediments around the lake are primarily fluvial and eolian sand, with some fluvial and lacustrine silt, clay and gravel. Ross (1968) indicated that the fill used for the roadway embankment consisted of very uniform fine eolian sand, with partings of silty sand from the adjacent cut areas. Unfortunately, the borings were conducted primarily through natural soil, while the flow failure appears to be primarily through fill soil. No penetration test results are available and the estimation of the blow counts was based on an appraisal of relative density and vertical effective stress.
4. **Uetsu Line Railway Embankment in Japan.** Yamada (1966) described a number of embankment failures during the 1964 Niigata earthquake with  $M_w \sim 7.5$ , which may induced a peak ground surface acceleration of 0.2 g at the Uetsu Line railway embankment. The 8 m high embankment had settled into the underlying peat nearly 1.5 m prior to the earthquake, allowing the lower portion of the embankment to become saturated. During the earthquake, it appears that the saturated portion of the fill liquefied along a length of about 150 m and flowed for a distance of more than 110 m over the slope of the natural ground at 1° to 2° to the horizontal. The water table was at the ground surface in the surrounding rice field. The embankment with an average slope inclination of about 21° was constructed of sand with high degree of uniformity. The embankment fill was not compacted based on a description of construction techniques for embankments and dikes available. No penetration tests were conducted at this site. The blow counts were estimated based on numerous SPT results through sand fill dikes with similar grain size distribution and constructed by similar techniques.
5. **Hachiro-Gata Road Embankment at Akita in Japan.** Ohya et al. (1985) described flow slide, as a result of liquefaction of sandy sediments, of the Hachiro-Gata road embankment leading to the Gomyoko Bridge during the 1983 Nihonkai-Chubu earthquake with magnitude 7.7. A peak ground acceleration of 0.168 g was measured in the town of Akita. Ohya et al. (1985) noted that sand boils formed at the toe of the slope following the earthquake. Differential settlements were on the order of 0.5 to 1.0 m. The embankment of loose fine sand was underlain by medium dense fine sand layer about 5 m thick. The embankment was about 4 m high with the slope inclined at 20° to the horizontal.

6. **La Marquesa Dam in Chile.** De Alba et al. (1987, 1988), among others, described the failure of La Marquesa dam located approximately 80 km from the epicentre of the 1985 central Chile earthquake with magnitude  $M_s = 7.8$ . The estimated peak ground acceleration at the dam site was approximately 0.6 g. The dam had a height of 10 m and the upstream slope inclined at about  $28^\circ$  to the horizontal. The largest displacements of 2 m vertically and 11 m horizontally (at the toe) occurred in the upstream direction. Extensive longitudinal cracking occurred, with crack widths up to 0.8 m and crack depths up to 2 m. Borings at the dam location indicated that a layer of loose silty sand, which is about 0.8 to 1.7 m thick, underlies the dam. The fines content of the silty sand was approximately 30% under the upstream slope and 20% under the downstream slope. Olson (2001) estimated an average diameter of soil particles based on the uniformity and fines content of the silty sand.
7. **La Palma Dam in Chile.** De Alba et al. (1987, 1988), among others, described the failure of La Palma dam located approximately 80 km from the epicentre of the 1985 central Chile earthquake with magnitude  $M_s = 7.8$ . Estimated the peak ground acceleration at the dam site was approximately 0.46 g. The dam had a height of 10 m and the upstream slope inclined at about  $28^\circ$  to the horizontal. The largest displacements of 1.5 m vertically and 5 m horizontally occurred in the upstream direction. Extensive longitudinal cracking occurred, with crack widths up to 1.2 m, crack lengths up to 80 m, and slumping of up to 1.5 m at the cracks. Borings at the dam location indicated that a layer of loose silty sand underlies the dam. The thickness of the layer was less than 1.0 m and the fines content was approximately 15%. Olson (2001) estimated an average diameter of soil particles based on the uniformity and fines content of the silty sand.
8. **Chonan Middle School at China in Japan.** Ishihara et al. (1990) and Ishihara (1993) documented the liquefaction failure of the playground embankment fill of the Chonan Middle School during the 1987 Chibaken-Toho-Oki earthquake with magnitude  $M = 6.7$ , which induced the peak ground acceleration of  $\sim 0.12$  g at the site. The liquefaction induced slump was up to 3 m. Numerous sand boils occurred in the playground area. Ishihara (1993) concluded that a relatively hard crust of surface soil at the toe, which heaved approximately 1 m, prevented large scale flow. The embankment fill was about 5 m high with a toe berm and the slope inclined at about  $30^\circ$  to the horizontal. The embankment and landscape fill consists primarily of loose very fine sand to silty sand, with thin interbeds of clayey sand and sandy silt, to a depth of approximately 8 m. The fines content of the fill soil is approximately 18%. Olson (2001) estimated an average diameter of soil particles base on the soil description (very fine gradation) and the fines content. It was assumed that typical Japanese SPT equipment with an energy ratio of 68% was used (Seed et al., 1985).
9. **Nalband Railway Embankment in Armenia.** Yegian et al. (1994b) documented the failure of a railway embankment near the town of Nalband during the 1988 Armenia earthquake with magnitude  $M_s = 6.8$ . The estimated peak ground acceleration at the site was between 0.5 and 1.0 g. The embankment was displaced

about 2 m laterally and 3 m vertically. The embankment was constructed by placing without compaction a layer and berm of gravelly sand fill on the naturally sloping deposit of volcanic tuff. The berm was overlain by about 0.5 m of low permeability soil that impeded drainage over most of the failure surface. The grain size distribution of samples of the gravelly sand was obtained from borings conducted after the earthquake. The embankment height was about 4 m with the slope inclined at about  $34^\circ$  to the horizontal. It consists of compacted silty sand, which appeared to have broken into intact blocks. It was assumed that the SPT equipment used at the site had the energy ratio of about 60%.

10. **Shibecha-Cho Embankment in Japan.** Miura et al. (1995, 1998) described flow failure of an embankment in the Kyanuma district, Shibecha-cho, during the 1993 Kushiro-oki earthquake with magnitude  $M = 7.8$ . Miura et al. (1995, 1998) estimated a peak ground acceleration of 0.38 g, which is measured at a nearby rock outcrop. The embankment suffered severe cracking, slumping up to 5 m and flow of approximately 23.5 m. The embankment was about 10 m high with the slope inclination of about  $31^\circ$  to the horizontal. The embankment fill consists primarily of loose volcanic silty sand and was compacted by construction traffic only. The grain size distribution was obtained from the borrow area and a sand boil. Only Swedish cone penetration tests were conducted following the earthquake and SPT blow counts were estimated from the Swedish cone results.
11. **Route 272 Embankment at Higashiarekinai in Japan.** Sasaki et al. (1994) described the failure of the embankment on the route 272 at Higashiarekinai in Japan during the 1993 Kushiro-oki earthquake with magnitude  $M = 7.8$ . Sasaki et al. (1994) estimated that the peak ground acceleration at the site was greater than 0.3 g based on acceleration attenuation relationships developed for this earthquake (Sasaki et al., 1994) and its proximity to Shibecha-cho where the peak acceleration was 0.38 g. The embankment was about 8 m high with the slope inclined at about  $34^\circ$  to the horizontal. The embankment crest slumped about 2.4 m and the toe moved horizontally about 25.3 m from the original position. The embankment is underlain by pumice bearing volcanic sand (Sasaki et al., 1994). Olson (2001) assumed that the foundation and fill conditions were similar to the Shibecha-cho embankment. SPT blow counts were measured in the failed fill but it was assumed that the Japanese SPT equipment had an energy ratio of 72% (Seed et al., 1985; Ishihara, 1993).

### 5.3.2.2 Summary of the Case Studies

Data in Table 5.3 for the case histories of liquefaction of sloping sandy soil are obtained from Olson (2001), except the correction factor for slope and values of  $\phi$  and  $\phi - \beta$ .

The differences between the friction angles in cyclic condition and averaged slope angles are all negative and therefore the slopes must be unstable during the earthquake shaking and further consideration by the rotating cylinder model is not necessary for these cases because the failure criterion according to the model is fulfilled.

**Table 5.3** Data for the case histories of liquefaction of sloping sandy soil

N <sub>o</sub>	Slope	Fines (%)	(N <sub>1</sub> ) <sub>60</sub>	Magnitude M	Distance (km) or (peak acc.)	Equivalent slope angle β (deg.)	$\tau/\sigma'_v$ and $(\sigma'_v)$ (kPa)	Correction factor for slope*	$\phi$ (deg) from Fig. 5.6 to 5.8	$\phi - \beta$ (deg.)
1	Sheffield dam, California, USA	40	6	6.5	11 (0.15 g)	13	0.23 (67)	0.4 to 0.7	7	-6°
2	Solfatara Canal dyke, Mexico	0	5	7	(0.3 g)	13	0.23 (86)	0.4 to 0.7	3	-10°
3	Lake Merced bank, California, USA	3	7	5.5	4 to 6	17.7	0.32 (55)	0.2 to 0.7	5	-12.2°
4	Uetsu-line railway embankment, Japan	1	3	7.5	(0.23 g)	11.8	0.21 (52)	0.45 to 0.75	3	-8.8°
5	Hachiro-Gata road embankment, Akita, Japan	15	4.4	7.7	(0.17 g)	9.1	0.16 (30)	0.6 to 0.8	5	-4.1°
6	La Marquesa dam, Chile	30	4.5	7.8	(0.6 g)	11.3	0.20 (65)	0.5 to 0.75	6	-5.3°
7	La Palma dam, Chile	15	3.5	7.8	(0.46 g)	14.6	0.26 (39)	0.3 to 0.7	5	-9.6°
8	Chonan middle school, Chiba, Japan	18	5.2	6.7	(0.12 g)	11.8	0.21 (58)	0.5 to 0.75	5	-6.8°
9	Nalband railway embankment, Armenia	20	9.2	6.8	(0.5 to 1.0 g)	10.2	0.18 (49)	0.85 to 0.95	9	-1.2°
10	Shibecha-Cho embankment, Japan	20	5.6	7.8	(0.38 g)	13.5	0.24 (66)	0.4 to 0.7	6	-7.5°
11	Route 272 embankment, Higashirekina, Japan	20	6.3	7.8	(0.38 g)	14.0	0.25 (52)	0.35 to 0.7	7	-7°

\* From Harder and Boulanger (1997).

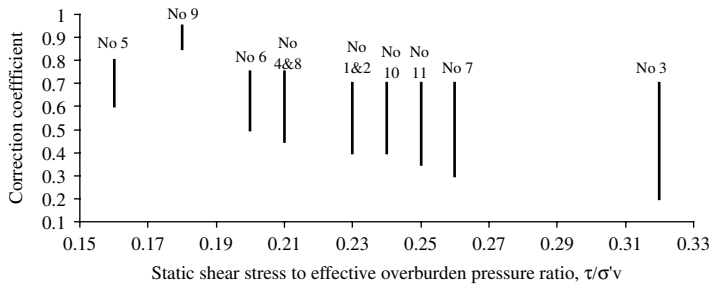


**Fig. 5.9** Correction coefficients for use in Equation 5.1 for slopes from Table 5.3

Large variations, mentioned at the beginning of Section 5.3, of the correction factors according to Harder and Boulanger (1997) to be used in Equation (5.1) for sloping ground are shown in Fig. 5.9 for the case histories considered.

## 5.4 Rolling Cylinder Model for Analysis of Flow Failures

### 5.4.1 Model for Clean Sand

Following the previous rotating cylinder model, the rolling cylinder model for flow analysis of slopes is shown in Fig. 5.10.

The equation of motion is

$$r^2\pi \cdot \rho \cdot \ddot{u} = r^2\pi \cdot g \cdot (\rho - \rho_w) \cdot (\sin \beta - \cos \beta \cdot \tan \delta_r), \quad (5.20)$$

where  $r$  is the cylinder radius,  $\rho$  is sand unit density,  $\ddot{u}$  is the acceleration of the cylinder,  $g$  is the gravitational acceleration,  $\rho_w$  is water unit density,  $\beta$  is slope angle to the horizontal,  $\delta_r$  is the residual angle of soil friction.

Some of actual sand grain friction along the path is converted to heat during flow failures. Tika et al. (1996) reported less than 1°C of temperature increase during fast shearing of clayey siltstone and claystone in ring shear apparatus. Frictional damping is likely to be small and is neglected in Equation (5.20). Also, damping caused by water viscosity is likely to be small and is neglected in Equation (5.20).

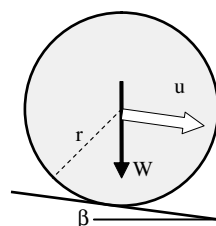


**Fig. 5.10** Rolling cylinder model (Srbulov, 2005, by permission of Patron Editore)

The solution of Equation (5.20) is

$$u = \frac{\rho - \rho_w}{\rho} \cdot g \cdot (\sin \beta - \cos \beta \cdot \tan \delta_r) \frac{t^2}{2} + v_o t, \quad (5.21)$$

where  $v_o$  is the initial velocity, which is assumed equal to the ground  $v_{p,h}$  from Equation (3.9). The limited time  $t$  of sand flow can be estimated from the principle of sedimentation of soil grains. For simplicity, it is assumed that all sand particles are spheres, and the velocity  $V_p$  of a particle can be given by Stokes law (e.g. Das, 1985) as

$$V_p = \frac{\gamma_s - \gamma_w}{18\eta_{aw}} D_{50}^2, \quad (5.22)$$

where  $\gamma_s$ ,  $\gamma_w$  are unit weight of soil particle and water respectively,  $\eta_{aw}$  is absolute viscosity of water and  $D_{50}$  is an average diameter of soil particles. The sedimentation time  $t = L_p V_p^{-1}$ , where  $L_p$  is the length of sedimentation path, which is assumed equal to the thickness of liquefied layer. This assumption is made because flow will not stop until the particles from the top of flow settle down. Absolute viscosity of water depends on temperature. At  $20^\circ\text{C}$ ,  $\eta_{aw} = 981 \times 10^{-5} \text{ g}/(\text{cm s})$  or  $\text{mPa s}$ . At  $10^\circ\text{C}$ , the viscosity is 29.8% greater and at  $30^\circ\text{C}$  20.3% smaller than the viscosity at  $20^\circ\text{C}$ .

#### 5.4.2 Model for Sand with Fines

Figure 5.11 shows the rolling cylinder model with fines.

The weight  $W_1$  of the fines model is given in Equation (5.12). The radius of the fines model is as before  $r_1 = \{W_1[\pi(\rho - \rho_w)g]^{-1}\}^{0.5}$ ,  $\rho$  and  $\rho_w$  are unit densities of soil and water and  $g$  is the gravitational acceleration. The angle  $\alpha$  in Fig. 5.11 is

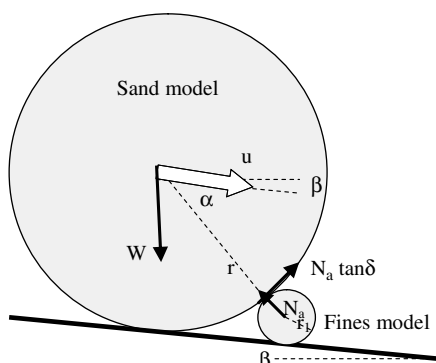


**Fig. 5.11** Rolling cylinder model with fines (Srbulov, 2005, by permission of Patron Editore)

$$\alpha = \arcsin \frac{r - r_1}{r + r_1} \quad (5.23)$$

The normal force  $N_a$  between a sand grain model and a fines model is

$$N_a = \frac{W_1[\cos \beta \tan \delta_r - \sin \beta]}{\cos \alpha}, \quad (5.24)$$

where  $\beta$  is the angle of slope inclination and  $\delta$  is the angle of residual soil friction in cyclic conditions. Revised Equation (5.21) is

$$u = \left[ \frac{\rho - \rho_w}{\rho} \cdot g \cdot (\sin \beta - \cos \beta \cdot \tan \delta_r) - N_a \cdot (\cos \alpha - \sin \alpha \cdot \tan \delta_r) \right] \frac{t^2}{2} + v_o t \quad (5.25)$$

#### 5.4.2.1 Summary of the Case Studies of Sand Flows Analyzed by Rolling Cylinder Model

The case histories from Olson (2001), considered for the analysis of potential of liquefaction of sloping sandy soil which data are given in Table 5.3, are used for back analyses by the rolling cylinder model, which data are given in Table 5.4. From the case histories analyzed, it has been found that the model provides adequate results when  $\delta_r = \beta$  and  $\beta < \phi$ . This means that the flow distance,  $u_f = v_{ph} t$ , is the product of the peak ground velocity  $v_{ph}$  and the sedimentation time  $t$  of soil particles.

Calculated flow distances are shown versus recorded flow distances in Fig. 5.12. The agreement between the predicted and actual flow distance is rather good despite numerous assumptions made by Olson (2001) about soil properties.

In Case No 4, the average diameter of soil particles  $D_{50}$  vary in a narrow range and the SPT blow counts varies in the range from 2 to 5. Therefore, either the estimated ground velocity caused by the earthquake or the residual angle of friction  $\delta_r$  had a significant effect in this case. The explanation of the inaccuracy is unlikely to be due to inaccurate estimation of peak ground velocity because even a doubling of the peak ground velocity would only double the calculated flow distance. To explain this actual distance of 110 m would require the residual angle of friction  $\delta_r$  to be  $1.412^\circ$  when natural ground angle was  $1.5^\circ$ . The model would then predict the observed flow distance. Such high model sensitivity indicates the lack of the model robustness. However, soil flow is chaotic in nature (term turbulent is used for fluids) and the results are very sensitive to small differences in the parameters. An example of sensitivity of calculated flow distance on residual angle of friction  $\delta_r$  for Case No 4 is shown in Fig. 5.13.

**Table 5.4** Data for the case histories of flow of liquefied sandy soil

N <sub>o</sub>	Slope	v <sub>o</sub> (m/s)	D <sub>50</sub> (mm)	L <sub>p</sub> (m)	Ground angle β (deg.)	Calculated displacement (m)	Recorded displacement (m)
1	Sheffield dam, California, USA	0.30	0.1	2	0	65.0	60
2	Solfatara Canal dyke, Mexico	0.40	0.2	2.3	2	24.6	23
3	Lake Merced bank, California, USA	0.21	0.21	10	17	$\beta > \phi$	18
4	Uetsu-line railway embankment, Japan	0.33	0.3–0.4	1.5	1–2	4.4	110
5	Hachiro-Gata road embankment, Akita, Japan	0.27	0.2	2	0	14.3	10
6	La Marquesa dam, Chile	0.22	0.15	1.4	0	14.9	11
7	La Palma dam, Chile	0.59	0.2	1	9	$\beta > \phi$	5
8	Chonan middle school, Chiba, Japan	0.15	0.2	2	0	8.3	3
9	Nalband railway embankment, Armenia	0.68	1.5	4	6	1.3	2
10	Shibecha-Cho embankment, Japan	0.51	0.2	5	7	$\beta > \phi$	23.5
11	Roue 272 embankment, Higashiaiarekinai, Japan	0.51	0.2	3	2	41.1	25.3

Adopted  $\gamma_s = 26.5 \text{ kN/m}^3$ ,  $\eta = 0.01 \text{ mPa s}$  at  $20^\circ\text{C}$ .

**Fig. 5.12** Calculated and recorded flow distances from the case histories, which data are given in Table 5.4

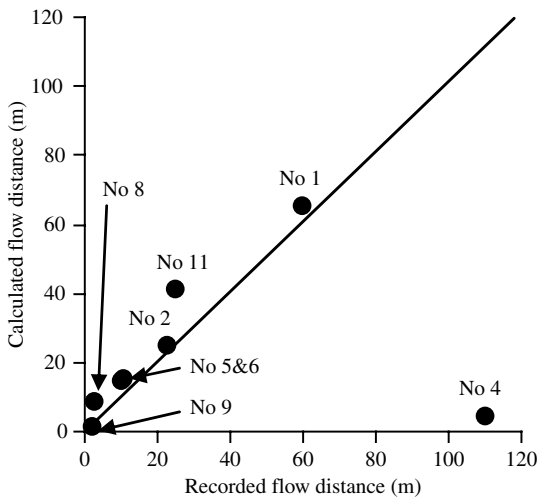
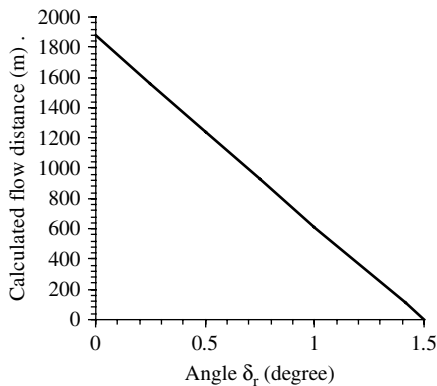


**Fig. 5.13** An example of sensitivity of calculated flow distance on residual angle of friction  $\delta_r$  in Case No 4



## 5.5 Summary

Liquefaction of horizontal ground during strong earthquakes is considered in practice using semi-empirical method based on case studies of liquefied and non-liquefied soil and soil penetration resistance in situ. This method requires the use of a correction coefficient for sloping ground. The available values of the coefficient vary widely and therefore their refinement is necessary.

- Rotating cylinder model, which is described in Section 5.3, is used to analyze liquefaction potential of sloping ground. A number of case studies of liquefied slopes, which are considered in Section 5.3, indicate clearly slope susceptibility to liquefaction. The same case studies are used for consideration of flow distances of liquefied sand.
- An alternative to the rotating cylinder model is to use Fig. 5.2 for level ground but with the cyclic stress ratio defined based on Fig. 1.4 as

$$\frac{\tau}{\sigma'_n} = \frac{C_h W}{\cos \bar{\alpha} \sum N(1 - r_u)} \quad (5.26)$$

where  $\bar{\alpha}$  is the angle of inclination of the equivalent sliding block to the horizontal,  $r_u$  is excess pore water pressure ratio. As  $W = \sum T \sin \bar{\alpha} + \sum N \cos \bar{\alpha}$ ,  $\sum T = \sum N'(1 - r_u) \tan \phi_1 FS^{-1}$  and  $FS = (\gamma' \gamma^{-1} - C_h \tan \bar{\alpha})(1 - r_u) \tan \phi_1 (\gamma' \gamma^{-1} \tan \bar{\alpha} + C_h)^{-1}$  for an equivalent sliding block, it follows that the cyclic stress ratio for a slope is

$$\frac{\tau}{\sigma'_n} = C_h \left[ \frac{1}{1 - r_u} + \frac{\gamma'/\gamma(1 - r_u) \tan \phi_1 - FS \cdot C_h}{FS\gamma'/\gamma + C_h(1 - r_u) \tan \phi_1} \cdot \frac{\tan \phi_1}{FS} \right] \quad (5.27)$$

where  $\gamma'$  and  $\gamma$  are submerged and total soil unit weights respectively for soil under water level. For soil above ground water level,  $\gamma^1 \gamma^{-1} = 1$ . FS is factor of safety of slope stability,  $\phi_1$  is soil friction angle in static condition.

- Rolling cylinder model, which is described in Section 5.4, is used for analysis of flow distance of liquefied sand. Based on the case histories analyzed, the model provides best results if the friction angle of liquefied soil is equal to angle of inclination to the horizontal of natural ground under slope and if slope angle is less or equal to soil friction angle in cyclic condition. In this case, flow distance is the product of the peak ground velocity caused by ground shaking and the sedimentation time of soil particles in liquefied condition. Rolling cylinder model is very sensitive to the changes in the input parameters such as the average particle diameter and frictional angle of liquefied soil. Such sensitivity is considered to be inherited because soil flow is chaotic in nature (term turbulent is used for fluids).

# **Chapter 6**

## **Dynamic Soil – Foundation Interaction**

### **6.1 Introduction**

Eurocode 8, Part 5 (2004) specifies that the effects of dynamic soil-structure interaction (DSSI) shall be taken into account where P- $\delta$  (2nd order) effects are significant, for structures with massive or deep-seated foundations (such as bridge abutments and gravity walls, piles, diaphragms and caissons), for slender tall structures and for structures supported on very soft soil, with average shear wave velocity less than 100 m/s. The code does not specify details how DSSI is analyzed.

Two types of DSSI are commonly referred to in the literature.

1. “Kinematic” interaction is caused by inability of a foundation to follow ground motion due to greater foundation stiffness in comparison with ground stiffness. In effect, stiff foundation filters high frequency ground motion to an averaged translational and rotational foundation motion. Average values are smaller than the maximum values and therefore “kinematic” interaction is beneficial except if averaged motion results in significant rotation and rocking of a foundation.
2. “Inertial” interaction is caused by the existence of structural and foundation masses. Seismic energy transferred into a structure is dissipated by material damping and radiated back into ground causing superposition of incoming and outgoing ground waves. As a result, the ground motion around a foundation can be attenuated or amplified, depending on a variety of factors.

The most important factor in determining the response is the ratio between the fundamental period of a foundation and the fundamental period of adjacent ground in the free field. The ratio of unity indicates resonance condition between foundation and its adjacent ground, which is to be avoided.

Considerable research, involving analytical, numerical and experimental modeling, has produced a variety of techniques for the evaluation of the interaction. The objective of this chapter is to present several simplified methods for analysis of foundations and retaining walls.

## 6.2 Advanced and Empirical Methods

### 6.2.1 Numerical Methods, Centrifuge and Shaking Table Testing

Numerical methods are well developed and numerous. A list of available computer programs can be found at [www.ggsd.com](http://www.ggsd.com). Advanced numerical methods use soil properties, whose determination is not a simple and routine task. Nonlinear numerical methods belong to the field of applied mathematics and evaluation of the results requires special expertise and experience.

Centrifuge tests are gaining in popularity and application, among researchers at least. The tests are performed on small scale models in laboratory using acceleration many times greater than the gravity acceleration. The enhanced gravity produced on the centrifuge is such that stresses at homologous points in model and full-scale prototype can be arranged to be identical. This ensures that the soil in the model behaves in the same way as in the prototype (Taylor, 1994; Kutter and Balakrishnan, 2000). Although some technical difficulties exist (e.g. Wilson, 1998), they are being resolved. In the coming decade or so, the facilities and expertise required for the testing is expected to become more accessible to practicing engineers.

Shaking table scale model tests are conducted under earth's gravity. These scale models have the major disadvantage that stresses are not correctly reproduced in the soil of the model, which can lead to major differences between the behaviors of the model and the full-size object it is intended to simulate. These model tests have been demonstrated to be sensitive to container boundary effects, scale modeling techniques, and adherence to similitude laws (e.g. Meymand, 1998). Both equivalent sinusoidal and earthquake type motions are used for model excitation.

### 6.2.2 System Identification Procedure

The fundamental objective of any system identification analysis is to evaluate the properties of an unknown system given a known input into and output from that system. The system is generally associated with structural flexibility alone, or the structural flexibility coupled with foundation flexibility in rocking and/or translation. The inputs and outputs are various combinations of free-field, foundation, and roof-level recordings. Expected results from the system identification procedure are:

- Modal frequencies and damping ratios of the structures for rigid and flexible base cases.
- Transfer functions describing the frequency dependent variations between input and output motions.

Important assumptions usually made in the system identification analyses are:

- The dynamic response of soil-structure systems can be described by linear dynamic models with proportional damping. This assumption is not valid when structures are damaged or yielded and when soil degradation occurs.

- Input and output motions used for system identification were representative, i.e. that lateral and rocking motions at the same elevation are uniform, which is true for rigid footings.
- Roof motions are not influenced by torsional deformations in the structure.
- Free field acceleration records are assumed to be representative of wider zones, which is seldom correct because of spatial heterogeneity of ground.

Stewart et al. (1998) analyzed 58 case histories and found that inertial interaction effects could cause vibration period lengthening ratios of 4 and 30% foundation damping and be negligible in some cases. However, they found that the analytical predictions were generally reasonably accurate, with some limitations for deep foundations and long-period structures.

## 6.3 Discrete Element Models

### 6.3.1 Lumped Mass Model Formula

Wolf (1994), among others, considered motion of a rigid structure caused by a horizontal ground acceleration  $a_{g,t}$  as shown in Fig. 6.1.

The coupled rotational and horizontal dynamic equilibrium equations at the centre of gravity of a rigid structure are based on the second Newton's law of motion.

$$I_o \frac{d^2\theta}{dt^2} + M_r - h_c P_b = 0 \quad (6.1)$$

$$m_s a_{g,t} + m_s h_c \frac{d^2\theta}{dt^2} + P_b = 0, \quad (6.2)$$

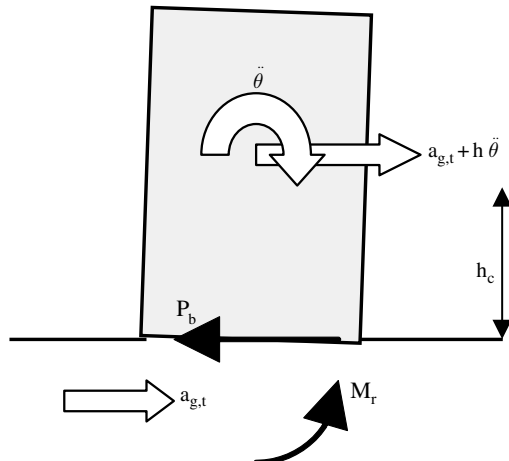


**Fig. 6.1** Model of a rigid structure

where  $I_o$  is the polar moment of mass inertia around the centroid,  $\theta$  is the structure rotation angle,  $t$  is time,  $M_r$  is the base reaction moment,  $h_c$  is the smallest distance between the centre of gravity and the base,  $P_b$  is soil resisting force acting at the base, and  $m_s$  is the structure mass. The resulting differential equation of the second order with constant coefficients is

$$\frac{d^2\theta}{dt^2} + \frac{M_r}{I} = -\frac{m_s h_c}{I} a_{g,t}, \quad (6.3)$$

where

$$I = I_o + m_s \cdot h_c^2 \quad (6.4)$$

Wolf (1994) solved Equation (6.3) in time domain based on an explicit algorithm with a predictor-corrector scheme, described in Section 6.3.3. He stated that: “*This rather simple discrete-element model with causal frictional elements may well yield a better approximation of reality than a complicated ‘rigorous’ analysis by the boundary-element method with non-causal linear-hysteretic damping or with some other sophisticated description of material damping*”.

In a simplified approach, Srbulov (2002), assumed that

$$M_r = m_s \cdot g \cdot h_c \cdot \theta \quad (6.5)$$

Equation (6.3) becomes

$$\frac{d^2\theta}{dt^2} + \omega^2 \theta = -\omega^2 \frac{a_{g,t}}{g}, \quad (6.6)$$

where  $\omega^2 = m_s g h_c I^{-1}$ . The solution of Equation (6.6) is

$$\theta = a \cos(\omega t) + b \sin(\omega t) + c \frac{d_{g,t}}{h_c} \quad (6.7)$$

The first and second derivatives are

$$\frac{d\theta}{dt} = -a\omega \sin(\omega t) + b\omega \cos(\omega t) + \frac{c}{h_c} \frac{d(d_{g,t})}{dt} \quad (6.8)$$

$$\frac{d^2\theta}{dt^2} = -a\omega^2 \cos(\omega t) - b\omega^2 \sin(\omega t) + \frac{c}{h_c} \frac{d^2(d_{g,t})}{dt^2}, \quad (6.9)$$

where  $a, b, c$  are constant and  $d_{g,t}$  is the horizontal ground displacement in time. For an equivalent harmonic motion with ground circular frequency  $\omega_g$ , the amplitudes of horizontal ground displacement and velocity are proportional to the amplitude of horizontal ground acceleration  $a_{g,t} = d^2(d_{g,t})dt^{-2}$ ,

$$\begin{aligned} d_{g,t} &= \frac{a_{g,t}}{\omega_g^2} \\ \frac{d(d_{g,t})}{dt} &= \frac{a_{g,t}}{\omega_g} \end{aligned} \quad (6.10)$$

When the initial  $d_{g,o}$ ,  $\theta_o$  and  $d\theta_o dt^{-1}$  are zero as well as the initial ground acceleration at time zero is a small value in comparison with other accelerations and can be ignored, Equations (6.7) and (6.9) become

$$\theta = \frac{-\left(\frac{\omega}{\omega_g}\right)^2 \frac{a_{g,t}}{g}}{1 + \left(\frac{\omega}{\omega_g}\right)^2} \quad (6.11)$$

$$\frac{d^2\theta}{dt^2} = \frac{-\omega^2 \frac{a_{g,t}}{g}}{1 + \left(\frac{\omega}{\omega_g}\right)^2} \quad (6.12)$$

When the ratio  $(\omega/\omega_g)^2$  is a small value and can be ignored then the horizontal peak foundation acceleration  $a_{f,p}$ , at a distance  $e$  from the centroid, follows from Equation (6.13)

$$a_{f,p} = -a_{p,h} \frac{m_s \cdot h_c \cdot e}{I}, \quad (6.13)$$

where  $a_{p,h}$  is the peak horizontal ground acceleration, e.g. Equations (3.6) and (3.7).

In Equation (6.13), it has been assumed that both foundation and ground peak accelerations appear at the same time, which is not true.

For multi-storey building, the total mass  $m_s$  is estimated as

$$m_s = m_i(S_t + 1 + B_s), \quad (6.14)$$

where  $S_t$  is the number of storeys above ground level and  $B_s$  the number of (sub) basements in a building,  $m_i$  is storey mass. The distance of the centre of gravity  $h_o$  above ground level, and  $h_c$  above foundation level, are estimated from

$$h_o = \frac{m_i H_s}{m_s} \left( \sum_{i=1}^{S_t} i - \sum_{j=1}^{B_s} j \right) \quad (6.15)$$

$$h_o = H_s \frac{\frac{S_t(S_t + 1)}{2} - \frac{B_s(B_s + 1)}{2}}{(S_t + 1 + B_s)} \quad (6.16)$$

$$h_c = h_o + H_s \cdot B_s, \quad (6.17)$$

where  $H_s$  is the distance between storeys, which is assumed to be the same for all floors. The polar moments of inertia  $I_o$  and  $I$  are calculated from

$$I_o = m_i \left[ h_o^2 + \sum_{i=1}^{S_t} (h_o - H_s \cdot i)^2 + \sum_{j=1}^{B_s} (h_o + H_s \cdot j)^2 \right] \quad (6.18)$$

$$I_o = m_i \left[ h_o^2(1 + S_t) - H_s \cdot h_o S_t (S_t + 1) + H_s^2 \frac{S_t(S_t + 1)(2S_t + 1)}{6} + h_o^2 B_s + H_s \cdot h_o B_s (B_s + 1) + H_s^2 \frac{B_s(B_s + 1)(2B_s + 1)}{6} \right] \quad (6.19)$$

$$I = I_o + m_s \cdot h_c^2 \quad (6.20)$$

### 6.3.1.1 Case Studies of Peak Accelerations of Piled Foundation Analyzed Using Lamp Mass Model

The first nine of the following case histories are summarized by Srbulov (2006c). All of them are also described in Section 6.4.2 of the book. The comparisons of the simplified model predictions with the recorded data are given in Table 6.1 and shown in Fig. 6.2.

The agreement between the recorded and calculated peak foundation accelerations is good even when using a number of simplifying assumptions and not considering soil-foundation interaction and soil properties, which results in the scatter between the recorded and calculated peak foundation accelerations. The ratios

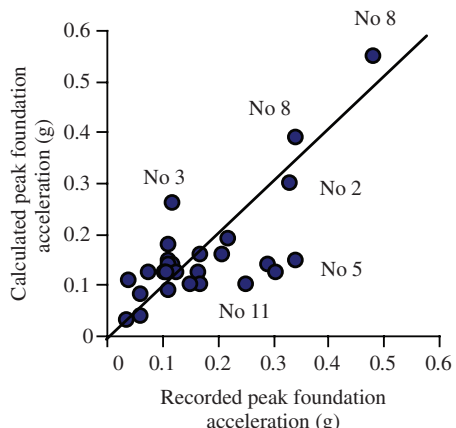


**Fig. 6.2** Recorded and calculated peak foundation accelerations according to the lump mass model

**Table 6.1** Recorded and calculated peak horizontal foundation accelerations  $a_{f,p}$ 

N <sub>o</sub>	Case	Estimated mass (kg)	Estimated h & e (m)	Estimated I ( $\text{kgm}^2$ )	$a_{p,h}(g)$	Calculated $a_{f,p}(g)$	Recorded $a_{f,p}(g)$
1	Oba-Ohashi road bridge in Japan (Ohira et al., 1984)	$3 \times 10^6$	10	$3 \times 10^8$	0.115	0.115	0.037
2	Meloland road overpass in California (Werner et al., 1987)	$1.1 \times 10^6$	7	$5.4 \times 10^6$	0.296	0.3	0.33
3	Chiba warehouse in Japan (Tominaga et al., 1989)	$4 \times 10^5$	14	$7.8 \times 10^7$	0.26 & 0.18	0.26 & 0.18	0.12 & 0.11
4	Hollywood storage building in California (Fenves and Serino, 1990)	$2.7 \times 10^7$	23	$2.0 \times 10^{10}$	0.17 & 0.21 0.20 & 0.11 in T & L	0.12 & 0.14 0.14 & 0.08	0.11 & 0.15 0.11 & 0.06 in T & L direction
5	Imperial Valley county service building in California (Hadjian et al., 1990)	$3 \times 10^7$	9	$3.5 \times 10^9$	0.20 & 0.22 in N & E	0.14 & 0.15	0.29 & 0.34 in N & E direction
6	Pacific Park Plaza building in California (Celebi and Safak, 1992)	$6 \times 10^7$	47.5	$1.8 \times 10^{11}$	0.22 & 0.26	0.16 & 0.19	0.17 & 0.22

**Table 6.1** (continued)

N <sub>o</sub>	Case	Estimated mass (kg)	Estimated h & e (m)	Estimated I (kgm <sup>2</sup> )	a <sub>p,h</sub> (g)	Calculated a <sub>t,p</sub> (g)	Recorded a <sub>t,p</sub> (g)
7	Norwalk buildings in California (Celebi, 1993)	2×10 <sup>7</sup> (A) & 4.7×10 <sup>7</sup> (B)	16.7	8.5×10 <sup>9</sup> & 1.9×10 <sup>10</sup>	0.25 & 0.13 in N & E	0.16 & 0.09	0.21 & 0.11 in N & E direction
8	Painter street bridge in California (Makris et al., 1994)	1.4×10 <sup>6</sup>	6	5.0×10 <sup>7</sup>	0.55 & 0.39 in T & L	0.056 & 0.041	0.48 & 0.34 in T & L direction
9	11 storey apartment house in Japan (Ohta et al., 1980)	2.1×10 <sup>6</sup>	15.5	7.0×10 <sup>8</sup>	0.056 & 0.041	0.04 & 0.03	0.061 & 0.035 in T & L direction
10	Dumbarton bridge in California (Fenves et al., 1992)	5.5×10 <sup>5</sup> in L 2.7×10 <sup>6</sup> 2.2×10 <sup>6</sup>	7.5-19 7.5-10 15	3.1×10 <sup>7</sup> -2.0×10 <sup>8</sup> 1.5×10 <sup>8</sup> -2.7×10 <sup>8</sup> 5.0×10 <sup>8</sup>	0.128	0.126	0.167-0.307 0.077-0.103
11	The Northwest connector in California (Fenves and Destroches, 1994)	1.0×10 <sup>6</sup> 4.5×10 <sup>4</sup> in L 8×10 <sup>3</sup> in T	19 18.5 2.7×10 <sup>6</sup> in T	3.6×10 <sup>8</sup> 1.5×10 <sup>7</sup> in L 0.09 0.11	0.126 0.126 0.126 0.11	0.126 0.126 0.126 0.1	0.126 0.126 0.126 0.17 0.1 0.1 0.15-0.25

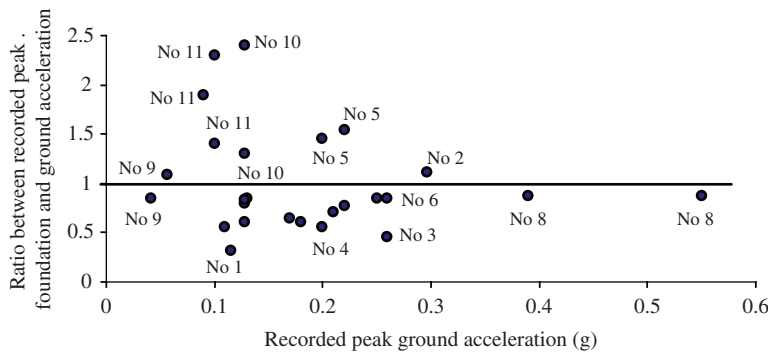


Fig. 6.3 Ratios between recorded peak accelerations of foundations and adjacent ground

between recorded peak accelerations of foundations and adjacent ground are shown in Fig. 6.3.

The following comments apply:

- In Case No 5 (**Imperial Valley County services building in El Centro, California**), the peak foundation acceleration is up to about 50% greater than the peak ground acceleration. Imperial Valley County services building is six storey reinforcement concrete building with the fundamental period of approximately 0.6 s. The building is underlain by silty sandy clay (USGS, 1984). The transversal wave velocity in the first five meters is 137 m/s, 194 m/s in the depth range five to 22.5 m and 267 m/s in the depth range 22.5–34 m. The averaged transversal wave velocity to a depth of 22.5 m is 177 m/s and the fundamental period is 0.5 s. The averaged transversal wave velocity to a depth of 34 m is 200 m/s and the fundamental period is 0.68 s. It is quite possible that the structure motion was in (near) resonance with the soil layer motion, resulting in high foundation accelerations. Resonance condition is not considered by the simplified method.
- In Case No 10 (**Dumbarton Bridge in San Francisco, California**), the peak foundation acceleration in the longitudinal direction is from 30% to 140% greater than the peak ground acceleration. The Dumbarton Bridge has the fundamental vibration period in the longitudinal direction of 1.9 s. The free field ground motion had the predominant vibration period of 2 s in both directions according to the Fourier spectra. The bridge vibration in the longitudinal direction was in (near) resonance with the ground vibration. Therefore, the avoidance of resonance condition is the most important feature of the soil-foundation interaction. Resonance condition is not considered by the simplified method.
- In Case No 11 (**the Northwest connector in California**), the peak foundation acceleration in the longitudinal direction is from 90% to 130% and in the transversal direction from 40% to 90% greater than the peak ground acceleration. Based on available data, it seems that the peak foundation acceleration occurred due to the fourth structural vibration mode with the period of about 0.6 s, which

corresponds to the predominant ground motion period. Consequently, higher structural vibration modes are also important for the peak foundation acceleration. Higher vibration modes are not considered by the simplified method. Therefore, its application should be limited to the structures with predominant single vibration mode.

### **6.3.2 Closed Form Solution in Time**

The lumped mass model, described in Section 6.3.1, provides good results without consideration of soil-foundation interaction except in the cases of soil-foundation resonance. Possible effect of soil-retaining wall interaction is considered in this section for gravity walls when wall slip over its base is prevented, Srbulov (2005b). Gravity walls involve stone, concrete, brick, reinforced concrete counterforts, caissons, cellular cofferdams, cribs, gabions and reinforced soil. Gravity walls use their own weight to transfer imposed loads to their foundations. They are rigid in comparison with surrounding soil, which displacements are averaged by the wall to a translational and rotational component.

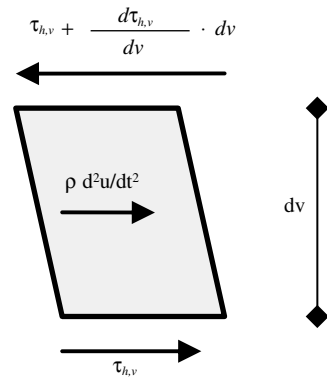
Kramer (1996) summarized the state of knowledge concerning dynamic response of retaining walls. Wall movements and pressures depend on the response of the soil underlying the wall, the response of the backfill, the inertial and flexural response of the wall itself, and the nature of the input motions. Because of these complexities, interacting phenomena and the inherent variability and uncertainty of soil properties, it is difficult to analyze all aspects of the seismic response of retaining walls accurately. Simplified models that make various assumptions about soil, structure and input motion are most commonly used for seismic design. Several simplified methods are mentioned here:

Okabe (1926) and Mononobe and Matsuo (1929) developed a pseudo-static analysis of seismic lateral earth forces on retaining structures, so-called Mononobe-Okabe (M-O) method. The M-O method is an extension of the static Coulomb (1776) theory of lateral earth pressures on retaining structures. It applies horizontal and vertical equivalent seismic forces to an active or passive rigid wedge in a dry cohesionless soil. No soil-structure interaction is considered, and soil strength degradation under cyclic loading must be assessed independently as soil input parameters. A variant of M-O approach is made normative in Eurocode 8: Part 5, Annex E (2004).

Richards et al. (1999) used a simple kinematic method to predict the seismic earth pressure of cohesionless soil against retaining structures due to uniform horizontal ground acceleration. They used superposition of nonlinear horizontal soil displacement in the free field and linear wall displacement. They found that the seismic active thrust on the wall equals the total horizontal force from the free-field stress solution.

Wolf (1994) described the use of discrete element models (DEM) for vibration analyses of rigid footings. A simple DEM is extended by Srbulov (2005b) for

**Fig. 6.4** Dynamic forces acting on a soil element behind wall



analysis of gravity walls by addition of a lateral earth force, comprising a transient part  $\Delta E$  and an average part  $E_s$ . The transient force  $\Delta E$  is determined from dynamic forces acting on a ground element in the horizontal direction behind a wall as shown in Fig. 6.4.

For simplified analysis in this section, it is assumed that the value of  $\Delta E$  per meter length of wall is proportional to the sum of inertial forces acting on the ground behind a wall because walls prevent free ground movement and are subjected to the ground forces.

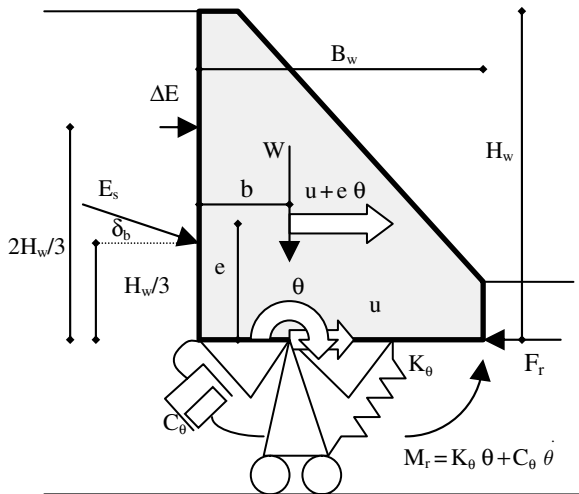
$$\begin{aligned}\Delta E &= \int_0^{H_w} \rho \cdot \frac{d^2u}{dt^2} \cdot (H_w - v) \cdot \tan\left(45^\circ - \frac{\phi}{2}\right) dv \\ &= \int_0^{H_w} \frac{\partial \tau_{hv}}{dv} \cdot (H_w - v) \cdot \tan\left(45^\circ - \frac{\phi}{2}\right) dv \\ \tau_{hv} &= 0.65 \cdot \frac{a_{top}}{g} \cdot \sigma_v\end{aligned}\quad (6.21)$$

where  $H_w$  is the wall height,  $d^2udt^{-2}$  is the horizontal acceleration,  $\sigma_v$  is the total vertical stress in soil behind wall at depth  $v$  below wall top,  $\tau_{hv}$  is the average shear stress on a horizontal plane through soil behind wall at depth  $v$ ,  $\phi$  is soil friction angle in cyclic condition. The equation for  $\tau_{hv}$  is similar to Equation (5.1).

The volume of ground mass involved in wall loading changes with direction of ground acceleration, towards or away from wall. Equation (6.21) considers an average active ground volume when ground acceleration changes sign and is equal to zero as in static condition. For layered and cohesive soil, an estimate of shear stress distribution along wall height can be obtained using SHAKE computer program.

Figure 6.5 depicts the model geometry, displacement  $u$  and rotation  $\theta$ , the forces ( $\Delta E$ ,  $E_s$ ,  $F_r$ , and  $W$ ) and soil reaction moment  $M_r$ . Soil reaction to rocking is

**Fig. 6.5** Model of a gravity wall (Srbulov, 2005b, by permission of Patron Editore)



considered in the form of an elastic spring and viscous dash point. The two triangles under the wall represent trapped soil beneath wall for Poisson's ratio greater than 1/3. The force  $F_r$  prevents completely any horizontal displacement of the wall, which is assumed to rest on two roller bearings with no resistance in the horizontal direction.

The additional lateral soil force per meter length of wall is

$$\Delta E = 0.65 \cdot a_{top} \cdot \rho \cdot \tan \left( 45^\circ - \frac{\phi}{2} \right) \cdot \frac{H_w^2}{2} \quad (6.22)$$

The force  $\Delta E$  acts at  $2H_w/3$  above wall base. The force  $E_s$  can be calculated from conventional theory of earth pressure in static condition but using cyclic soil shear strength.

Wolf (1994) formulated equations of motion for a rigid cylindrical structure on soil for a prescribed horizontal ground and wall acceleration, assuming that structural rotation  $\theta$  was the only degree of freedom. The rotational and horizontal equilibrium equations in the centre of gravity of the model (Fig. 6.5) are based on the second Newton's law of motion.

$$\begin{aligned} & (I + \Delta M_\theta) \cdot \ddot{\theta} + C_\theta \cdot \dot{\theta} + K_\theta \cdot \theta - e \cdot F_r + E_s \cdot \left[ \cos \delta_b \cdot \left( e - \frac{H_w}{3} \right) + \sin \delta_b \cdot b \right] \\ & - \Delta E \cdot \left( \frac{2 \cdot H_w}{3} - e \right) = 0 \\ & m \cdot (\ddot{u} + e \cdot \ddot{\theta}) + F_r - E_s \cdot \cos \delta_b - \Delta E = 0, \end{aligned} \quad (6.23)$$

where  $I$  is wall mass moment of inertia around the centre of gravity,  $\Delta M_\theta$  is the mass moment of inertia of the trapped soil beneath wall for Poisson's ratio greater

than  $1/3$ ,  $K_\theta$  and  $C_\theta$  are the rotational soil stiffness and dashpot coefficients respectively,  $m$  is wall mass,  $\theta$ ,  $e$ ,  $F_r$ ,  $H_w$ ,  $E_s$ ,  $\delta_b$ ,  $b$ ,  $\Delta E$ ,  $u$  are shown in Fig. 6.5.

The so called dynamic spring coefficient (real part of the dynamic soil stiffness) of the exact solution of the equation of motion exhibits a downward parabolic tendency (Wolf, 1994), i.e. decreases relatively quickly at smaller frequencies of vibrations but remains fairly constant at larger vibration frequencies. This behavior corresponds to trapped soil beneath the wall, which moves as a rigid body in phase with the wall (Wolf, 1994). A closed match is achieved by defining the trapped mass in rocking motion to be (Wolf, 1994)

$$\Delta M_\theta = 0.3 \cdot \pi \cdot \left( v - \frac{1}{3} \right) \cdot \rho \cdot \left( \frac{B_w^3}{3 \cdot \pi} \right)^{\frac{5}{4}}, \quad (6.24)$$

where  $\rho$  is soil unit density,  $v$  is Poisson's ratio  $> 1/3$ ,  $B_w$  is wall breadth at its base. The coefficients  $K_\theta$  and  $C_\theta$  for surface foundation on homogeneous half space in rocking motion (e.g. Wolf, 1994) per 1 m length

$$K_\theta = \frac{G}{8 \cdot (1-v)} \cdot \left[ 3.73 \cdot \left( \frac{B_w}{1} \right)^{2.4} + 0.27 \right] \quad (6.25)$$

$$C_\theta = \rho \cdot c_s \cdot \frac{1 \cdot B_w^3}{12},$$

where  $G$  is soil shear modulus,  $v$  is Poisson's ratio,  $\rho$  is soil unit density,  $c_s$  is soil characteristic wave velocity, for  $v < 1/3$   $c_s = c_t [0.5(1-2v)(1-v)^{-1}]^{-0.5}$ , and for  $v > 1/3$   $c_s = 2c_t$ , where  $c_t$  is soil transversal wave velocity,  $B_w$  is wall breadth at its base. The reason for using the velocity  $c_s$  for rocking motion is explained by Wolf (1994) as follows.

For the rocking motion producing compression and extension, axial waves dominate for small and intermediate values of  $v$ , resulting in the use of  $c_p$ , which is the longitudinal wave velocity. But  $c_p$  tends to infinity for  $v$  approaching 0.5. This causes apparently anomalous behavior. Use of  $c_p$  for the higher values of  $v$  would overestimate the radiation damping characterized by  $C_\theta$ . In view of the fact that  $c_s = 2c_t$  yields the correct high frequency asymptote of damping for both  $v = 1/3$  and  $1/2$  and in addition provides a best fit for small frequencies, this value is used throughout the range of nearly incompressible soil (Wolf, 1994).

From Equations (6.23) and (6.24) it follows

$$\begin{aligned} & \left[ I + \Delta M_\theta + e^2 \cdot m - 0.65 \cdot \rho \cdot \tan \left( 45^\circ - \frac{\phi}{2} \right) \cdot \frac{H_w^3}{3} \right] \cdot \ddot{\theta} + C_\theta \cdot \dot{\theta} + K_\theta \cdot \theta = \\ & = \left[ 0.65 \cdot \rho \cdot \tan \left( 45^\circ - \frac{\phi}{2} \right) \cdot \frac{H_w^3}{3} - e \cdot m \right] \cdot \ddot{u} + E_s \cdot \left( \cos \delta_b \cdot \frac{H_w}{3} - b \cdot \sin \delta_b \right) \end{aligned} \quad (6.26)$$

Soil shear modulus  $G$  is dependent on shear strain amplitude, which in turn is dependent on the peak ground acceleration and therefore the shear modulus  $G$  dependence directly on the peak ground acceleration is given in Table 2.2. In this case, Equation (6.26) is an inhomogeneous linear second order ordinary differential equation with constant coefficients within a time interval. Its closed form solution depends on the values of the constants. A more compact form of Equation (6.26) is

$$\theta + 2 \cdot \alpha \cdot \theta + \beta^2 \cdot \theta = \chi + \lambda \cdot t$$

where

$$\begin{aligned} I_o &= I + \Delta M_\theta + m \cdot e^2 - 0.65 \cdot \rho \cdot \tan\left(45^\circ - \frac{\phi}{2}\right) \cdot \frac{H_w^3}{3} \\ \alpha &= \frac{C_\theta}{2 \cdot I_o} \\ \beta^2 &= \frac{K_\theta}{I_o} \\ \ddot{u} &= a_o + a_1 \cdot t \\ \zeta &= 0.65 \cdot \rho \cdot \tan\left(45^\circ - \frac{\phi}{2}\right) \cdot \frac{H_w^3}{3} - e \cdot m \\ \chi &= \frac{\zeta \cdot a_o + E_s \cdot \left(\frac{H_w \cdot \cos \delta_b}{3} - \sin \delta_b \cdot b\right)}{I_o} \\ \lambda &= \frac{\zeta \cdot a_1}{I_o} \end{aligned} \quad (6.27)$$

For the under damped case  $k^2 = \alpha^2 - \beta^2 < 0$ , the solution for a time interval  $\Delta t$  for which  $a_o$  and  $a_1$  in Equation (6.27) are constants is (e.g. Gieck and Gieck, 1997)

$$\begin{aligned} \omega &= \sqrt{\beta^2 - \alpha^2} \\ \theta &= e^{-\alpha \cdot t} \cdot [C_1 \cdot \sin(\omega \cdot t) + C_2 \cdot \cos(\omega \cdot t)] + \frac{\chi + \lambda \cdot t}{\alpha^2 + \omega^2} - \frac{2 \cdot \alpha \cdot \lambda}{(\alpha^2 + \omega^2)^2} \\ \dot{\theta} &= e^{-\alpha \cdot t} \cdot \{C_1 \cdot [\omega \cdot \cos(\omega \cdot t) - \alpha \cdot \sin(\omega \cdot t)] - C_2 \cdot [\alpha \cdot \cos(\omega \cdot t) \\ &\quad + \omega \cdot \sin(\omega \cdot t)]\} + \frac{\lambda}{\alpha^2 + \omega^2} \end{aligned} \quad (6.28)$$

where the constants  $C_1$  and  $C_2$  are determined at the beginning of each time interval (with constant  $a_o$  and  $a_1$ ) from the values of  $\theta_o$  and  $\dot{\theta}_o$  at the end of the previous time interval.

$$\begin{aligned} C_1 &= \frac{1}{\omega} \cdot \left\{ \left[ \theta_o - \frac{\chi}{\alpha^2 + \omega^2} + \frac{2 \cdot \alpha \cdot \lambda}{(\alpha^2 + \omega^2)^2} \right] \cdot \alpha + \dot{\theta}_o - \frac{\lambda}{\alpha^2 + \omega^2} \right\} \\ C_2 &= \theta_o - \frac{\chi}{\alpha^2 + \omega^2} + \frac{2 \cdot \alpha \cdot \omega}{(\alpha^2 + \omega^2)^2} \end{aligned} \quad (6.29)$$

### 6.3.2.1 An Example of Comparison with the Results of Mononobe-Okabe Method

There are no available results of field measurements of earth forces acting on the back of gravity walls during earthquakes. For this reason, a comparison between the results of calculations of earth forces acting on the back of a wall according to the Mononobe-Okabe method (using 0.65 of the peak acceleration) and the closed form solution in time is performed. The spreadsheet in Appendix A.8 is used for the calculation of maximum lateral force acting on the back of a gravity wall for selected ground acceleration time histories.

A simple triangular shape of model cross section is considered. The model height  $H_w$  is 5 m and  $B_w = H_w$  with corresponding  $e$  and  $b$  of  $H_w/3$ . For  $B_w = H_w$  and wall density of  $2400 \text{ kg/m}^3$ , the wall mass moment of inertia is  $100 B_w^4 = 62500 \text{ kgm}^2$ . Assumed unit weight of soil  $\gamma = 20 \text{ kN/m}^3$ , soil friction angle in cyclic condition  $\phi = 0.83(N_1)_{60}$  (Srbulov, 2005a), soil-wall interface angle  $\delta_b = \phi$ . Based on MIL-HDBK (1997) curves, the transversal wave velocity  $c_t$  (m/s) of sand under the wall is approximately

$$c_t = 90 \cdot N_1^{0.333}, \quad (6.30)$$

where  $N_1$  is normalized number of blow counts from the standard penetration test. The corresponding sand longitudinal wave velocity  $c_p = c_t[0.5(1 - 2\nu)(1 - \nu)^{-1}]^{-0.5}$ , where  $\nu = 0.25$  is assumed.

The lateral soil force on retaining wall is calculated according to Mononobe-Okabe method for the vertical back of wall,  $o = 0$ , and horizontal soil backfill,  $\eta_w = 0$ .

$$E = \frac{1}{2} \cdot K_{AE} \cdot \gamma \cdot h_w^2 \cdot \cos \delta_b$$

$$K_{AE} = \frac{\cos^2(\phi - o - \psi)}{\cos \psi \cdot \cos^2 o \cdot \cos(\delta_b + o + \psi) \cdot \left[ 1 + \sqrt{\frac{\sin(\delta_b + \phi) \cdot \sin(\phi - \eta_w - \psi)}{\cos(\delta_b + o + \psi) \cdot \cos(\eta_w - o)}} \right]^2}$$

$$\psi = \arctan\left(\frac{a_h}{g}\right), \quad (6.31)$$

where  $a_h$  is the horizontal ground acceleration (0.65 of the peak value for the equivalent harmonic motion).

The average component of the lateral soil force on retaining wall  $E_s$  is calculated according to Coulomb (1776) for the vertical back of wall,  $o = 0$ , and horizontal backfill,  $\eta_w = 0$ .

$$E_s = \frac{1}{2} \cdot K_a \cdot \gamma \cdot h_w^2 \cdot \cos \delta_b$$

$$K_a = \frac{\cos^2(\phi - o)}{\cos^2 o \cdot \cos(\delta_b + o) \cdot \left[ 1 + \sqrt{\frac{\sin(\delta_b + \phi) \cdot \sin(\phi - \eta_w)}{\cos(\delta_b + o) \cdot \cos(\eta_w - o)}} \right]^2} \quad (6.32)$$

**Table 6.2** Basic data for the acceleration records from European Earthquake Data Base (Srbulov, 2005b, by permission of Patron Editore)

N <sub>o</sub>	Earthquake	Date	Time	Depth (km)	Magnitude M <sub>L</sub> /M <sub>s</sub>	Station/ component	Epicentral/ fault distance (km)	Peak accel- eration (m/s <sup>2</sup> )
A1	Campano Lucano	23/11/1980	18:34:52	16	6.6/6.87	Sturno/N-S	32/14	2.12
A2	Alkion	24/02/1981	20:53:37	10	6.8/6.69	Xilokastro OTE/Long.	19/4	2.84
A3	Athens	07/09/1999	11:56:50	9	-/5.6	Athens 3 (Kallithea)/ N46	23/-	2.60
B1	Montenegro	15/04/1979	06:19:41	12	-/7.0	Ulcinj Hotel Olimpic/ N-S	24/9	2.88
B2	Alkion	24/02/1981	20:53:37	10	6.8/6.69	Korinthos OTE/ E-W	20/13	3.04
B3	Kocaeli (Izmit)	17/08/1999	00:01:40	17	-/7.8	Yarimca- Petkim/ EW	17/25	2.40

The basic data of input acceleration records obtained in the free field on stiff and medium soil and used in the comparison are shown in Table 6.2.

The results of the comparison are shown in Fig. 6.6.

Small differences in the calculated values are because the Mononobe-Okabe results are obtained for 0.65 of the peak ground accelerations of 2.5 m/s<sup>2</sup> while the actual range of the peak accelerations of the records is 2.12–3.04 m/s<sup>2</sup>.

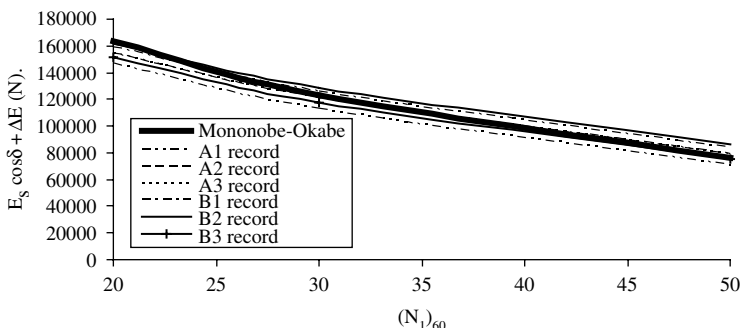


**Fig. 6.6** Results of comparison of dynamic earth forces acting on the gravity wall in the example

### 6.3.3 Time Stepping Procedure

Permanent displacements of gravity walls caused by earthquakes have been recorded on a number of occasions, e.g. Pitilakis and Moutsakis (1989), Inagaki et al. (1996).

Kramer (1996) mentioned a few rigorous two-dimensional finite element analyses that predict permanent deformations. A rigorous analysis should be capable of accounting for nonlinear, inelastic, behavior of soil and of the interfaces between soil and wall elements. Complex numerical methods require validation of their results, which is not an easy task, great expertise and are rather expensive and time consuming. There is clearly a need for simplified rational methods.

Whitman and Liao (1985) identified shortcomings of the Richards and Elms (1979) method as: neglect of the dynamic response of the backfill, neglect of kinematic factors, neglect of tilting mechanism, neglect of vertical acceleration. Whitman and Liao (1985) combined different sources of uncertainty and defined permanent displacement of a rigid wall.

Zeng and Steedman (2000) considered rocking and sliding of rigid block model on a rigid foundation. They assumed that the soil behind the model behaves as a rigid plastic material, following the wall as it moves outward. The procedure was validated by data from centrifuge tests.

Kim et al. (2004) computed the dynamic force on the back of the wall by using the force components calculated from existing equations. They verified the proposed model by comparing its results with those from series of shaking table tests. Their model uses the excess pore water pressure ratio ( $r_u$  = excess pore pressure in the back-fill over initial effective vertical stress), which is not easy to define for dynamic conditions.

Wolf (1994) described a discrete element model for coupled rocking and horizontal displacement of foundation of a three-cylinder compressor. This model is extended by Srbulov (2006d) by incorporation of slip possibility and addition of lateral dynamic earth force for analyses of gravity walls response to earthquakes. The 2D discrete element model according to Wolf (1994), with addition of possibility of wall slip and earth lateral force acting on the back of wall, is shown in Fig. 6.7. Soil reaction to wall movement is considered in the horizontal direction and in rotation

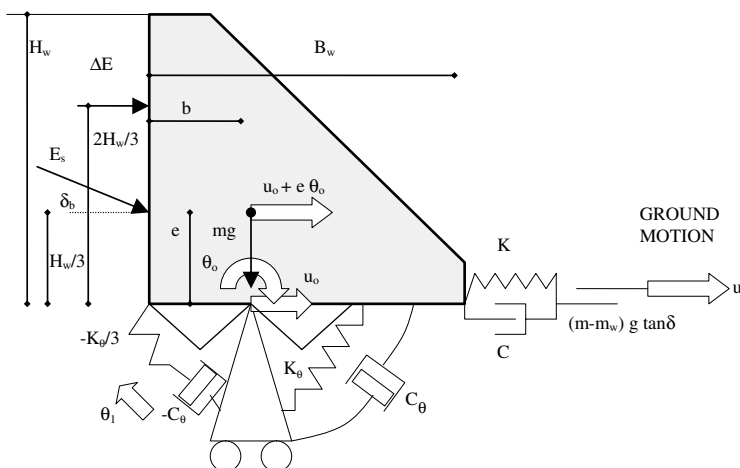


**Fig. 6.7** Discrete element model of a gravity wall (Srbulov, 2006d, by permission of Patron Editore)

by elastic springs and dashpots. In the horizontal direction, a sliding element limits the horizontal force that soil can sustain before wall sliding occurs. The elastic spring and dashpot with negative coefficients are artificial and are introduced by Wolf (1994). The two triangles under the wall represent trapped soil beneath wall for Poisson's ratio greater than 1/3 (Wolf, 1994).

The relationship for soil reaction moment contains a convolution integral in time. As an alternative to the recursive evaluation of the convolution integral, a physical discrete element model, which incorporates rigorously the convolution implicitly, is used according to Wolf (1994). The equation of the model rotational motion is:

$$(\Delta M_\theta + I) \cdot \ddot{\theta}_o + K_\theta \cdot \theta_o - \frac{K_\theta}{3} \cdot (\theta_o - \theta_1) + C_\theta \cdot \dot{\theta}_o - S \cdot e = M_{E+\Delta E} \quad (6.33)$$

An additional internal rotational degree of freedom located within the foundation soil and connected by a rotational spring with a coefficient  $-K_\theta/3$  to the base and by a rotational dashpot with a coefficient  $-C_\theta$  to the rigid support, is introduced by Wolf (1994). Both  $\theta_1$  and the negative coefficients are artificial and are introduced by Wolf (1994) for mathematical reason.

$$-\frac{K_\theta}{3} \cdot (\theta_1 - \theta_o) - C_\theta \cdot \dot{\theta}_1 = 0 \quad (6.34)$$

The equation of the model translational motion is:

$$m \cdot (\ddot{u}_o + e \cdot \ddot{\theta}_o) + S = E \cdot \cos \delta_b + \Delta E \quad (6.35)$$

The  $S$  force in Equations (6.33) and (6.35) is

$$S = \min \left| \frac{K \cdot (u_o - u) + C \cdot (\dot{u}_o - \dot{u})}{(m - m_w) \cdot g \cdot \tan \delta_b} \right| \quad (6.36)$$

The relative acceleration between a rigid wall and its base is:

$$\ddot{u}_{relative} = \ddot{u}_o - \ddot{u} \quad when \quad K \cdot (u_o - u) + C \cdot (\dot{u}_o - \dot{u}) > (m - m_w) \cdot g \cdot \tan \delta_b \quad (6.37)$$

The symbols used in Equations (6.33)–(6.37) are:  $\Delta M_\theta$  is the trapped soil mass moment of inertia when soil Poisson's ratio is greater than 1/3 (Equation 6.24),  $I$  is the wall mass moment of inertia around the wall center of gravity,  $\theta_o$  is the angle of wall rotation,  $K_\theta$  is the rotational static stiffness coefficient (Equation 6.25),  $\theta_1$  is an additional internal rotational degree of freedom,  $C_\theta$  is the rotational dashpot coefficient (Equation 6.25),  $C$  is the translational dashpot coefficient,  $e$  is the distance between wall centroid and its base,  $u_o$  is the horizontal wall displacement,  $K$  is the translational static stiffness coefficient,  $M_{E+\Delta E}$  is the rotational moment around the wall center of gravity from the average seismic earth force  $E_s$  (Equation 6.32) and the transient part  $\Delta E$  (Equation 6.22),  $m$  is the wall mass,  $m_w$  is the mass of

water corresponding to submerged part of wall volume,  $u$  is the horizontal ground displacement,  $\delta_b$  is the angle of friction between ground and wall,  $g$  is the gravitational acceleration; dot and double dot above a variable represent the first and second derivative in time.

For assumed surface foundation on homogeneous half space and 1 m wall length in plane strain condition  $K$  and  $C$  are according to Wolf (1994)

$$K = \frac{G}{2 \cdot (1 - \nu)} \cdot \left[ 6.8 \cdot \left( \frac{B_w}{1} \right)^{0.65} + 0.8 \cdot \frac{B_w}{1} + 1.6 \right] \quad (6.38)$$

$$C = \rho \cdot c_t \cdot 1 \cdot B_w$$

where  $G$  is the shear modulus of soil beneath wall (Subsection 2.2.1),  $B_w$  is the wall base width,  $\nu$  is the Poisson's ratio,  $\rho$  is the unit density of soil beneath wall,  $c_t$  is soil transversal wave velocity.

It is assumed for this discrete element model that the rate of change of the horizontal displacement of soil with depth is opposite to the rate of change of soil vertical displacement along the horizontal direction as shown in Fig. 6.8.

Because shear strain is the sum of rates of changes of horizontal displacement along vertical and vertical displacements along horizontal and because these rates are of similar value but with opposite signs it follows that the shear strain beneath a wall is small until slip occurs. Soil stiffness is constant and maximum at small strain levels so that an elastic – ideal plastic soil model is considered. Soil mass damping is neglected for small shear strain levels.

For use in an explicit algorithm Equations (6.33)–(6.35) are reformulated according to Wolf (1994) as:

$$\dot{\theta}_1 = \frac{K_\theta}{3 \cdot C_\theta} \cdot (\theta_o - \theta_1) \quad (6.39)$$

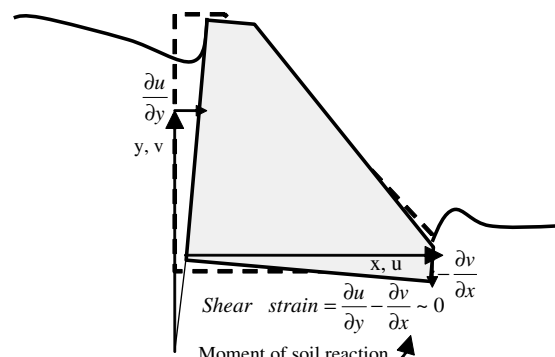


**Fig. 6.8** Shear strain components beneath a gravity wall (Srbulov, 2006d, by permission of Patron Editore)

$$\ddot{\theta}_o = \frac{M_{E+\Delta E} - \frac{2}{3} \cdot K_\theta \cdot \theta_o - C_\theta \cdot \dot{\theta}_o - \frac{K_\theta}{3} \cdot \theta_1 + S \cdot e}{I + \Delta M_\theta} \quad (6.40)$$

$$\ddot{u}_o = \frac{E_s \cdot \cos \delta_b + \Delta E - S}{m} - e \cdot \ddot{\theta}_o \quad (6.41)$$

For the parameter  $\theta_1$  no prediction or correction are formulated. Starting from the known motion at time  $(n-1)\Delta t$ , that is

$\theta_{on-1}$ ,  $\dot{\theta}_{on-1}$ ,  $\ddot{\theta}_{on-1}$ ,  $\theta_{1n-1}$ ,  $\dot{\theta}_{1n-1}$ ,  $u_{on-1}$ ,  $\dot{u}_{on-1}$ ,  $\ddot{u}_{on-1}$ , the final rotations and displacement and the predicted velocities at time  $n\Delta t$  are calculated by the following equations:

$$\theta_{on} = \theta_{on-1} + \Delta t \cdot \dot{\theta}_{on-1} + \frac{\Delta t^2}{2} \cdot \ddot{\theta}_{on-1} \quad (6.42)$$

$$\theta_{1n} = \theta_{1n-1} + \Delta t \cdot \dot{\theta}_{1n-1} \quad (6.43)$$

$$u_{on} = u_{on-1} + \Delta t \cdot \dot{u}_{on-1} + \frac{\Delta t^2}{2} \cdot \ddot{u}_{on-1} \quad (6.44)$$

$$\langle \dot{\theta} \rangle_{on} = \dot{\theta}_{on-1} + \frac{\Delta t}{2} \cdot \ddot{\theta}_{on-1} \quad (6.45)$$

$$\langle \dot{u} \rangle_{on} = \dot{u}_{on-1} + \frac{\Delta t}{2} \cdot \ddot{u}_{on-1} \quad (6.46)$$

The symbol  $\langle \cdot \rangle$  denotes a predicted value. Based on these values in place of  $\dot{\theta}_{on}$ ,  $\dot{u}_{on}$ , the rotational velocity  $\dot{\theta}_{1n}$  and the accelerations  $\ddot{\theta}_{on}$ ,  $\ddot{u}_{on}$  follow from Equation (6.39)–(6.41) formulated at time  $n\Delta t$ . The two predicted velocities are corrected as

$$\dot{\theta}_{on} = \langle \dot{\theta} \rangle_{on} + \frac{\Delta t}{2} \cdot \ddot{\theta}_{on} \quad (6.47)$$

$$\dot{u}_{on} = \langle \dot{u} \rangle_{on} + \frac{\Delta t}{2} \cdot \ddot{u}_{on} \quad (6.48)$$

For stability of the explicit algorithm the time step  $\Delta t$  must be smaller than the (smallest) natural period divided by  $\pi$  that is  $2\omega^{-1}$ . The rocking natural frequency can be computed according to Wolf (1994):

$$\omega_r = \sqrt{\frac{K_\theta \cdot k_\theta(b_o)}{I + \Delta M_\theta + e^2 \cdot m}} \quad (6.49)$$

$$k_\theta(b_o) = 1 - \frac{1/3 \cdot b_o^2}{1 + b_o^2} \quad (6.50)$$

$$b_o = \omega_r \cdot z_o / c_p \quad (6.51)$$

$$z_o = \frac{9 \cdot \pi \cdot r_o}{32} \cdot (1 - \nu) \cdot \left(\frac{c}{c_t}\right)^2 \quad (6.52)$$

$$r_o = \sqrt[4]{\frac{B_w^3}{3 \cdot \pi}} \quad (6.53)$$

Equation (6.49) is solved iteratively starting with  $\omega_r = 0$ . The parameters  $I$ ,  $\Delta M_\theta$ ,  $K_\theta$ ,  $e$ ,  $m$  are as in Equations (6.33)–(6.35),  $c_p$  is the velocity of longitudinal waves through soil beneath wall;  $c_t$  is the velocity of transversal waves through soil beneath the wall;  $c = c_p$  for Poisson's ratio  $\nu < 1/3$  and  $c = 2c_t$  for  $\nu > 1/3$ ,  $B_w$  is the wall base width. The circular frequency of horizontal motion is

$$\omega_h = \sqrt{\frac{K}{m}} \quad (6.54)$$

The fundamental frequency  $\omega$  of the coupled system can be approximated using the uncoupled natural frequencies according to Wolf (1994)

$$\frac{1}{\omega^2} = \frac{1}{\omega_h^2} + \frac{1}{\omega_r^2} \quad (6.55)$$

### 6.3.3.1 Case Study of the Caisson Type Quay Walls at Kobe Port

Inagaki et al. (1996) described seaward displacements of the caisson walls (Fig. 6.9) of about 5 m maximum and 3 m average and investigated the mechanism of deformation of the caisson walls by shaking table tests. The shaking table tests indicated that the excess pore water pressure in the replacement sand beneath the caisson did not reach 50% of the initial confining pressure. Both the shaking table tests and the in-situ investigation by diving suggested that the mechanism of the deformation of the caisson is not the sliding of the caisson during earthquake shaking but an overall deformation of the foundation soil beneath the caisson.

On 16 January 1995, Hyogoken-Nanbu earthquake of surface wave magnitude  $M_s = 6.9$  occurred in Hanshin area. In Kobe port, Inagaki et al. (1996) recorded the earthquake motion at the ground surface by a SMAC-B2 accelerometer. The corrected peak accelerations are  $5.25 \text{ m/s}^2$  in N43W direction and  $2.30 \text{ m/s}^2$  in E43N direction. The SPT N values at the recording station, as shown in Fig. 6.10, are obtained about two weeks after the earthquake.

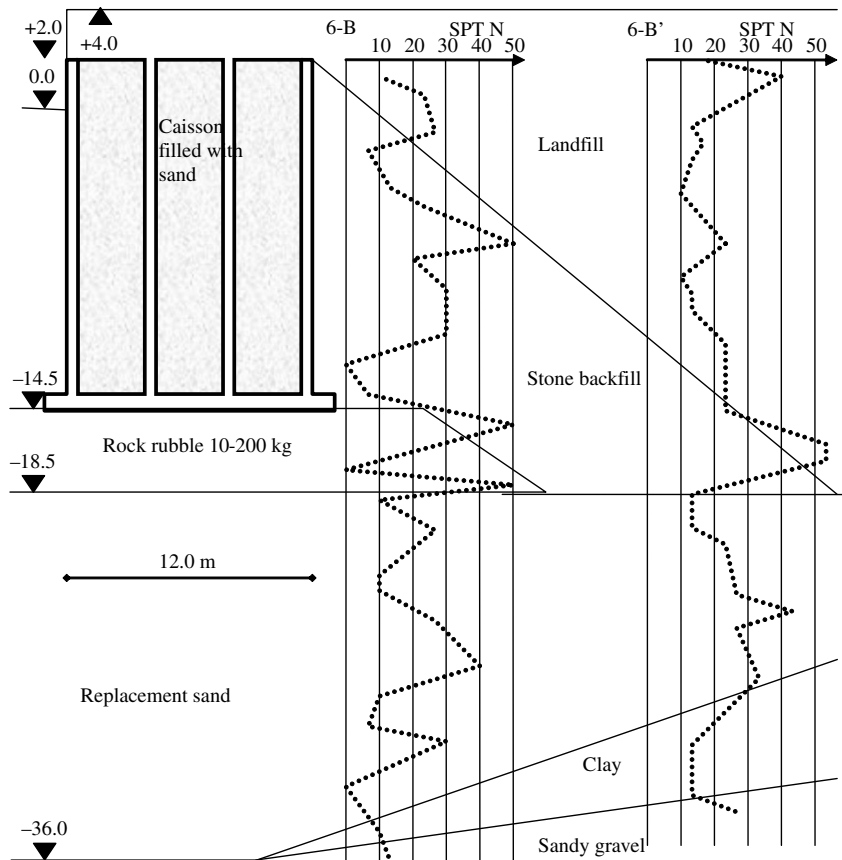


**Fig. 6.9** Cross section through a caisson in Kobe port (Srbulov, 2006d, by permission of Patron Editore)

Liquefaction occurred around the recording station. The wave forms of the acceleration time histories in the horizontal direction indicate that the liquefaction occurred after 1.8 s from the beginning of the record.

The recorded acceleration time histories were not available for this example. Inagaki et al. (1996) derived a relationship between transversal wave velocity  $v_t$

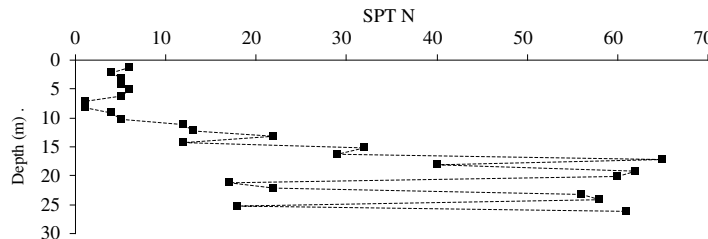


**Fig. 6.10** Standard penetration tests (SPT) blow count N in Kobe port

and SPT  $N$  value at Port and Rokko Island in Kobe port. For the average values of  $v_t$  and  $N$

$$v_t = 91.0 \cdot N^{0.337} \quad (6.56)$$

Calculated transversal wave velocity at the location of the recording station  $v_t = 156$  m/s for adopted  $N = 5$  down to 10 m depth. The transversal wave velocity increases to 286 m/s ( $N = 30$ ) at 16.0 m depth and remains approximately at 315 m/s ( $N = 40$ ) to the depth of 26 m at the location of the recording station. Substitute acceleration records obtained at Nishi-Akashi station during the same earthquake over soil with average transversal wave velocity less than 180 m/s (PEER) were used by Srbulov (2006d). The peak horizontal accelerations of the substitute records are 4.58 m/s<sup>2</sup> and 3.20 m/s<sup>2</sup>.

The quay wall shown in Fig. 6.9 is founded on 4 m thick 10–200 kg stone rubble over about 17.5 m thick layer of filled sand. Stone backfill was placed next to the wall and decomposed granite (Masado) was used for landfill. For the calculations in this paper, standard penetration resistance  $N = 10$  is used for the landfill in the upper half of the wall height,  $N = 30$  is used for the stone backfill in the lower half of the wall height,  $N = 50$  for the rock rubble and  $N = 10$  for the replacement sand beneath the rock rubble. Calculated transversal wave velocity for the replacement sand, according to Equation (6.56), is 198 m/s. The results of cyclic triaxial tests performed on samples of the landfill soil and replacement sand (Inagaki et al., 1996) indicate these friction angles in cyclic condition equal to about 10.2° and 11.3° respectively, which are about a half of the corresponding angles in one loading cycle, i.e. static condition.

The caisson wall shown in Fig. 6.9 was displaced towards the sea about 4 to 5 m, settled about 2 m and tilted about 4 to 5 degrees. If the wall deformation was caused by the excessive back pressures, which developed as a result of liquefied backfill soil, then the wall would not have settled 2 m as observed. The acceleration time history of the ground beneath the wall is assumed to be the same as for the Nishi-Akashi station with the amplitudes multiplied by a factor of 1.14 to obtain the peak acceleration of 5.25 m/s<sup>2</sup>. The spatial distribution of the ground acceleration within the port area is considered greater than the variation of ground motion along depth and therefore deconvolution of the surface motion is not performed. For the wall height of 16.5 m and the width of 12 m, the calculated wall and soil above the wall mass is  $4 \times 10^5$  kg. The wall and soil above mass moment of inertia around the centre of gravity is  $1.4 \times 10^7$  kgm<sup>2</sup>/m. Other values in the calculation that are assumed are the unit density of soil beneath the wall 1800 kg/m<sup>3</sup>, the longitudinal wave velocity beneath the wall 400 m/s, the unit weight of soil behind the wall 16 kN/m<sup>3</sup>, the friction angle between wall and stone rubble/backfill 20°. The maximum time step for the algorithm stability is calculated as 0.1 s while the actual used is 0.01 s.

The results of calculations are given in Appendix A.9 and shown in Fig. 6.11 for the horizontal component with the peak acceleration of 5.25 m/s<sup>2</sup>.

From Fig. 6.11 it is evident that the calculated wall co-seismic slip is about one tenth of the observed average wall horizontal displacement, which is in accordance with the conclusion of Inagaki et al. (1996) that the deformation mechanism was not

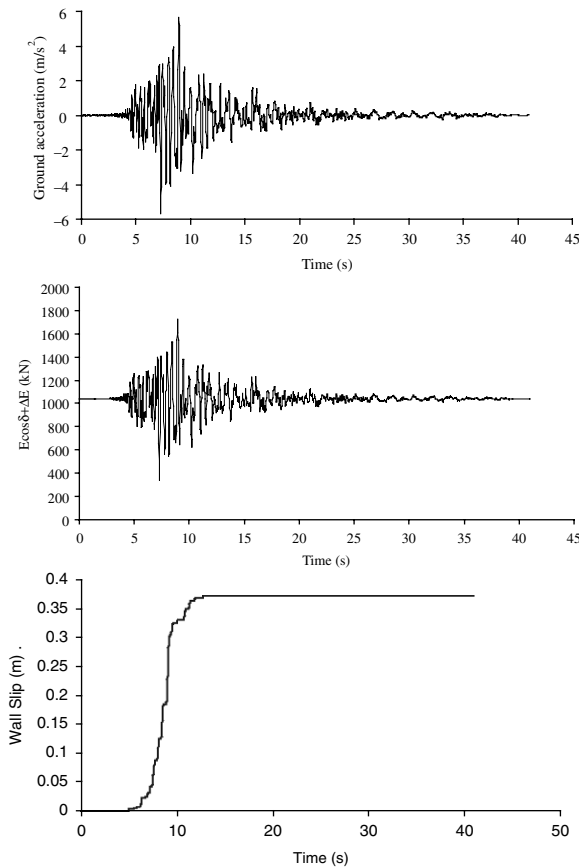


**Fig. 6.11** The time histories of ground acceleration, lateral earth force on wall and coseismic wall slip for the caisson at Kobe port during the 1995 Hyogoken-Nanbu earthquake (Srbulov, 2006d, by permission of Patron Editore)

due to the sliding alone of the caisson during earthquake shaking. The calculated peak lateral force on the wall of about 1670 kN/m is about 60% of the horizontal component of the force calculated according to the Mononobe-Okabe method using the friction angle of soil  $\phi = 15^\circ = \Psi$ ,  $\delta = 20^\circ$ . Likely reason for such a difference is the wall slip, which prevented build up of greater load.

It is possible that the large wall displacement occurred when the friction angles of landfill soil and replacement sand were decreased by cyclic loading to about  $10^\circ$ . The factor of safety of slope stability in post-seismic condition is calculated using the method of Bishop (1955) and a grid of centers of potential slip surfaces. The minimum factor of safety of 0.82 is obtained for the slip surface shown in Fig. 6.12a.

By finding the resultant forces of axial and tangential components of forces acting on the slip surface it is possible to define a sliding block equivalent to a slip

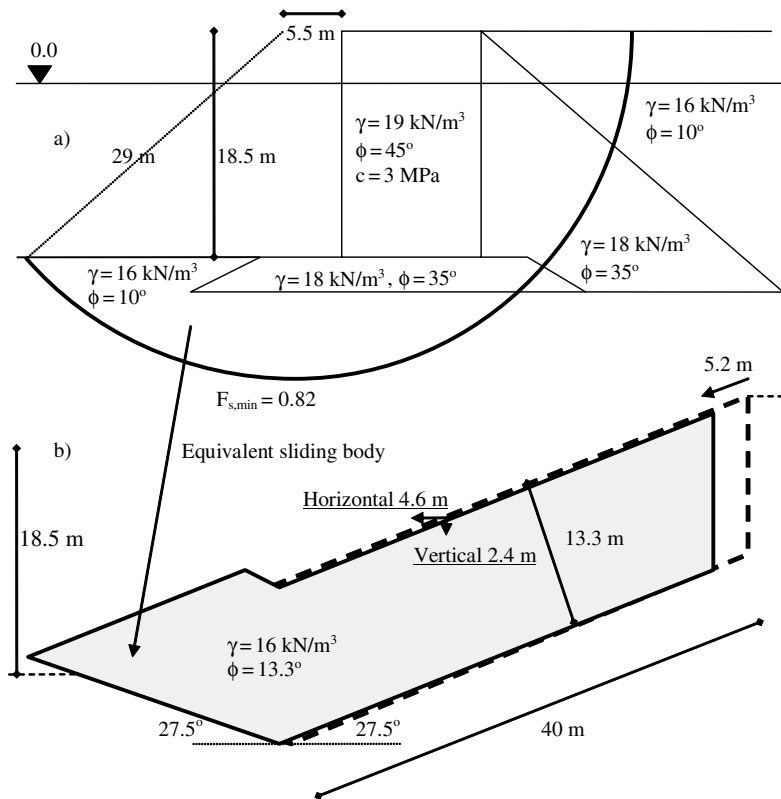


**Fig. 6.12** (a) Post-seismic stability and (b) displacement of a caisson in Kobe port during the 1995 Hyogoken-Nanbu earthquake (Srbulov, 2006d, by permission of Patron Editore)

surface of any shape (e.g. Sarma, 1979). The calculation is performed automatically using computer software (Maksimovic, 1988). The angle of inclination to the horizontal of the equivalent block is  $27.5^\circ$ , the equivalent friction angle on the sliding surface of a single block is  $17.4^\circ$  and the equivalent axial stress is  $189 \text{ kPa}$ . The block length is calculated as  $18.5[\sin(27.5^\circ)]^{-1} = 40 \text{ m}$ , where  $18.5 \text{ m}$  is the slope height. The block thickness is calculated as  $189[16 \times \cos(27.5^\circ)]^{-1} = 13.3 \text{ m}$ , where the equivalent unit weight is assumed  $16 \text{ kN/m}^3$ . The angle of block inclination at the toe is assumed  $27.5^\circ$  for symmetry.

The motion of a block on a surface that is approximated by two plane basal surfaces with assumed vertical interface (Fig. 6.12b) is analyzed according to Ambraseys and Srbulov (1995) and Section 4.4.2. The friction angle of  $13.3^\circ$  corresponds to the initial factor of safety of 0.82 of the two-block model. The calculated slip of  $5.2 \text{ m}$  along the slip surface, i.e.  $4.6 \text{ m}$  in the horizontal and  $2.4 \text{ m}$  in the vertical direction, is in good agreement with the recorded maximum horizontal displacements and the wall settlement of about  $2 \text{ m}$ . The post-seismic slip could have happened within a time interval of  $8 \text{ s}$ .

Dakoulas and Gazetas (2008) back calculated earth and water pressures acting against the caisson quay walls using Pastor-Zienkiewich elasto-plastic constitutive model applied within FLAC software. Calculated excess pore water pressure ratio range between 0.6 and 0.9 towards the end of ground shaking is greater than the maximum of 0.5 measured by Inagaki et al. (1996) during shaking table test. For SPT blow count range between 10 and 20 in borehole 6-B' (Fig. 6.9), excess pore water pressure ratio varies between 0.5 and 0.8 in Figs. 2.6 and 9.3.

### 6.3.3.2 Case Study of the Kalamata Harbor Quay Wall

Not all quay walls exhibit extra large displacements during strong earthquakes. Pitilakis and Moutsakis (1989) described and analyzed by two dimensional finite elements the overall wall (Fig. 6.13) behavior during the 1986 Kalamata earthquake. They found that the calculated acceleration at the top of the wall was almost 30% larger than at its base, the behavior of the wall was not governed by a rigid plastic movement, the wall and the neighboring backfill acted in a very similar way during the seismic excitation and the vertical component of the ground motion had very little effect on the magnitude of the seismic pressure.

On 13 September 1986, an earthquake of surface wave magnitude  $M_s = 6.2$  occurred in the southern part of Peloponnesus. The epicentre of the main shock was located 12 km north of the port of Kalamata. The depth of the main shock was 8 km. The main shock was recorded by two SMA-1 accelerometers located at the basement of the 7 storey Prefecture Hall and the 2 storey Old P.T.T. Office. The peak horizontal accelerations recorded at the basement of the Prefecture Hall were 2.11 and  $2.91 \text{ m/s}^2$  and at the basement of the P.T.T. Office 2.35 and  $2.67 \text{ m/s}^2$ . The

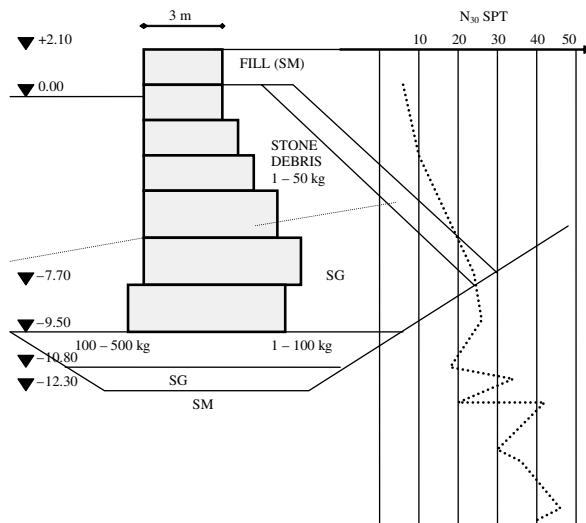


**Fig. 6.13** The cross section of the Kalamata harbor quay wall (Srbulov, 2007c, by permission of Patron Editore)

acceleration records used in this paper are from the P.T.T. Office (Ambraseys et al., 2004).

A typical soil profile of the coastal area is shown in Fig. 6.13 from Pitilakis and Moutsakis (1989). The quay wall is founded through a 2.5–3.0 m thick layer of silty sand (SM) and gravelly sand (SG) on the silty sand formation (SM-ML). This formation covers a great part of the east costal area to a depth of 20 m. The mean standard penetration test (SPT) blow count ( $N_{30}$ ) is about 20 and the shear wave velocity of about 200 m/s (Pitilakis and Moutsakis, 1989). The upper formation is underlain by a gravelly sand formation (GS) which in turn lies on a marl formation at a depth of 60–70 m. The results ( $N_{30}$ ) of SPT in the backfill material behind the wall are shown in Fig. 6.13. An average  $N_{30} = 10$  through silty sand (SM) fill is adopted in the upper half height of the wall and an average  $N_{30} = 25$  through gravelly sand and stone debris is adopted in the lower half height of the wall and below the wall base for the calculations in this example.

During the 1986 Kalamata earthquake, the quay wall was displaced horizontally about 15±5 cm and slightly rotated 4°–5° seaward (Pitilakis and Moutsakis, 1989). The acceleration time history of the ground beneath the wall is assumed the same as for the P.T.T. Office. Although deconvolution of a linear elastic system should theoretically produce a unique solution, practical difficulties often arise, e.g. Kramer (1996). Also, the spatial variability of the ground accelerations in the area is more likely to be greater than the assumed variation of ground acceleration with depth. For the wall height of 11.6 m and the base width of 6.0 m, the calculated wall and soil above wall mass is about  $1.4 \times 10^5$  kg/m. The wall and soil above wall mass moment of inertia around the center of gravity is  $2.0 \times 10^6$  kgm<sup>2</sup>/m. Other values in the calculation assumed based on experience are the unit density of soil beneath the wall 1800 kg/m<sup>3</sup>, the longitudinal wave velocity beneath the wall 600 m/s, the unit weight of soil behind the wall 16 kN/m<sup>3</sup>, the friction angle between wall and rock fill 30°. The maximum time step for the algorithm stability is calculated to be 0.06 s while 0.01 s has been used.

The results of calculations are shown in Fig. 6.14 for the horizontal component of ground motion with the peak acceleration of 2.67 m/s<sup>2</sup>.

From Fig. 6.14 it is evident that the calculated wall slip of 12 cm is within the observed range of 15±5 cm. The calculated peak lateral force on the wall of about 600 kN/m is about a half of the horizontal component of the force calculated according to the Mononobe-Okabe method using the friction angle of soil  $\phi = 15^\circ = \psi, \delta = 30^\circ$ . Likely reason for such a difference is the wall slip, which prevented build up of greater load.

The average lateral force on the wall in the discrete element model was calculated for the backfill friction angle equal to a half of the friction angle in static condition throughout the time history. For this reason the calculated lateral forces on the wall at the beginning of shaking are greater than they should be, because soil friction angle does not decrease instantaneously on the onset of shaking but reduces gradually with increasing number of pulses.

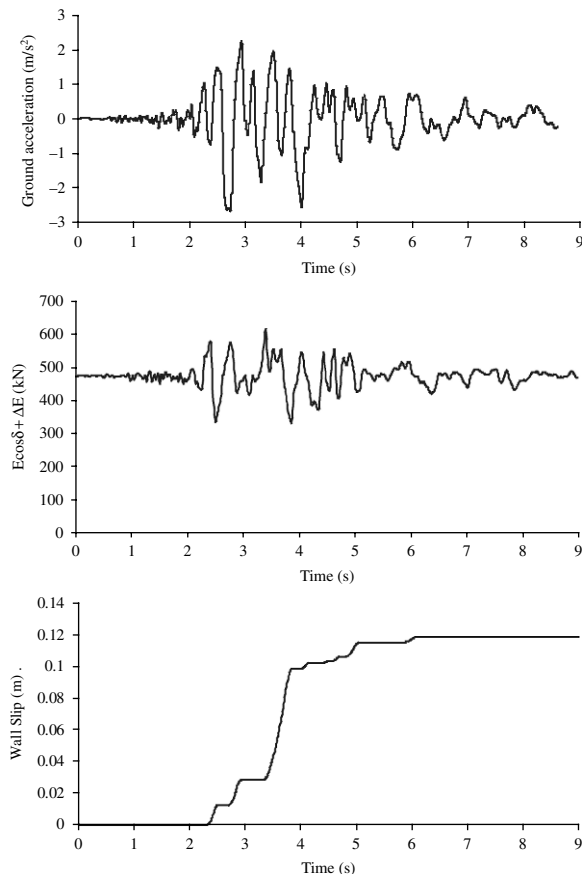


**Fig. 6.14** The time histories of ground acceleration, lateral earth force on wall and coseismic wall slip for the Kalamata harbor quay wall during the 1986 Kalamata earthquake (Srbulov, 2007c, by permission of Patron Editore)

### 6.3.3.3 The Effect of Assumed Soil Properties on Calculated Lateral Forces

A number of soil properties have been assumed for the calculation of lateral soil forces on the walls. The effect of variation of soil properties on the calculated forces is illustrated in Fig. 6.15. From Fig. 6.15, it follows that the effects can be significant and that all relevant soil properties should be determined rather than assumed.

## 6.4 Single Degree of Freedom Oscillator on Flexible Base for Piled Foundations and Flexural Retaining Walls

This section describes the use of a simplified method for consideration of dynamic soil structure interaction (DSSI) effect on the peak horizontal acceleration of piled

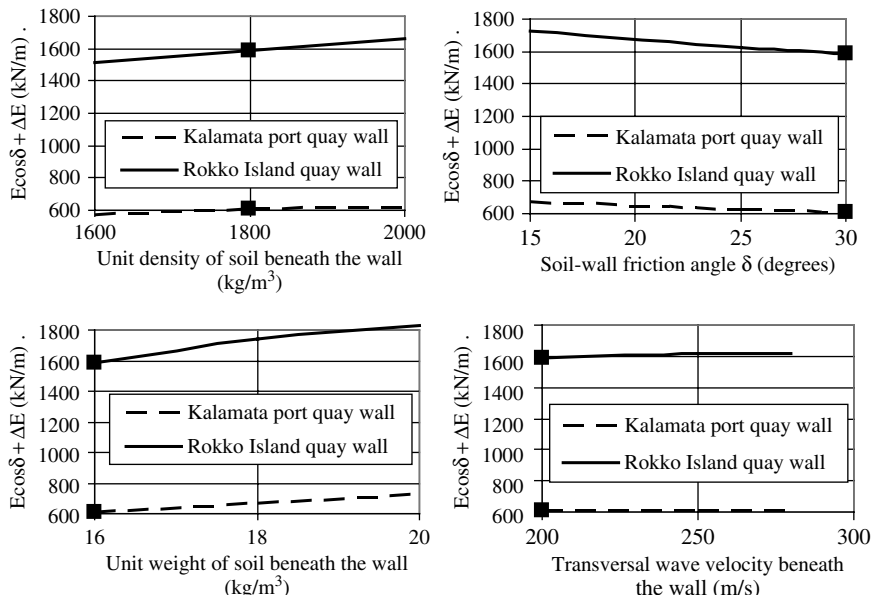


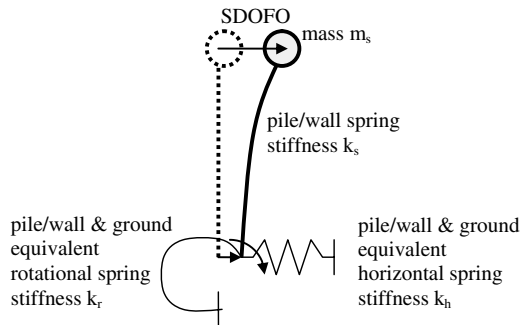
**Fig. 6.15** The effect of soil properties on the lateral forces on the walls (Srbulov, 2007c, by permission of Patron Editore)

foundations and flexural retaining walls. Piles and flexural retaining walls use their strength and stiffness to transfer imposed loads to surrounding ground and to limit local deformation.

Design of structures for earthquake resistance is frequently performed using response spectra, which examples are shown in Fig. 1.6 and 2.9. The response spectrum describes the maximum response of a single degree of freedom oscillator (SDOFO) to a particular input motion as a function of the fundamental frequency (or the fundamental period) and damping of the SDOFO, which model is shown in Fig. 1.5. Many design codes contain design acceleration spectra represented by the spectral shape dependent on ground types and the design ground acceleration. The spectra are defined for SDOFO with rigid base condition (Fig. 1.5) without taking into account soil-foundation interaction effects.

Several authors used SDOFO for consideration of DSSI effects (e.g. Stewart et al., 1998, Wolf, 1985, 1994). Wolf (1985), among others, showed that DSSI increases the fundamental period of a coupled system considering structure-foundation-ground joint response and increases the damping ratio of the coupled system in comparison with the fundamental period and damping of the structure in rigid base condition, Fig. 1.5. The spectral acceleration decreases with the increase in damping ratio and for the periods greater than the fundamental period of ground vibration. Due to the increase in the fundamental period and damping ratio of the coupled system, it is considered that DSSI is often beneficial and frequently ignored.

**Fig. 6.16** Undamped coupled linear elastic SDOFO



The DSSI effect is considered approximately using an equivalent SDOFO (Fig. 6.16), with frequency and damping depend on the frequencies and dampings of the representative structure with its foundation and the surrounding ground. The peak pile/wall accelerations are obtained as the spectral accelerations of the equivalent SDOFO and compared with the recorded peak foundation accelerations for the case histories with available seismological, geotechnical and structural data and with the lateral earth force according to the Mononobe-Okabe method. The spectral accelerations of an equivalent SDOFO are usually defined with respect to the free field peak horizontal ground accelerations. Eurocode 8 – Part 1 defines the response spectra with respect to design ground acceleration on type A ground, i.e. rock.

#### 6.4.1 *Ground Motion Averaging for Kinematic Interaction Effect Consideration*

Earthquakes produce complex ground motion with the frequencies that span a broad range. The frequencies are often concentrated around a predominant frequency indicated in the response spectra. Due to differences in ground and pile/wall stiffnesses, averaging of ground motion over pile/wall length is termed kinematic soil-foundation interaction. Newmark et al. (1977) proposed a simple procedure for averaging of free-field ground motion. Sarma and Srbulov (1996) used this approach for analysis of a number of case histories including piled and shallow foundations. Although the inclination of incoming seismic waves is frequently near vertical at shallow depths because of the wave refractions at the boundaries between stiffer and softer ground along the wave path from the source to ground surface, the spatial wave incoherence occurs as a result of ground heterogeneity. It is not easy to estimate such spatial incoherence for shallow foundations because of large ground volumes and depths involved.

The expression for the average horizontal acceleration  $a_{h,t}$  over a length along pile/wall at time  $t$  (e.g. Sarma and Srbulov, 1996) when piles follow the ground motion

$$\begin{aligned}
 a_{h,t} &= \frac{1}{L_s} \int_{L-L_s}^L a_l dl \\
 &= \frac{c_t}{L_s} \int_{t-T_s}^t a_t dt \\
 &= \frac{1}{T_s} (v_{tp} - v_{t-T_s}),
 \end{aligned} \tag{6.57}$$

where  $L_s = c_t 2\pi \omega_e^{-1}$  is a length along pile/wall over which ground motion is averaged,  $L$  is the distance from pile/wall top to a referent point under the pile/wall,  $a_l$  is ground acceleration at depth  $l$  along the pile/wall at time  $t$ ,  $c_t$  is soil transversal waves velocity and is assumed equal to the velocity of transversal waves passing through ground along the pile/wall,  $T_s = 2\pi \omega_e^{-1}$  is the time (in seconds) necessary for a seismic wave to pass along  $L_s$  and must be less or equal to the ratio between the pile/wall length and  $c_t$ ,  $v_{tp}$  and  $v_{t-T_s}$  are the ground velocities below the pile/wall tip at times  $t$  and  $t - T_s$ . The ground velocities can be obtained from corresponding acceleration time history by numerical integration in time.

#### 6.4.1.1 An Example of the Kinematic Soil-Foundation Interaction Effect

The response spectral acceleration ratios in Appendix A.10 are given for a SDOFO with respect to the surface accelerations in the free field. Fig. 6.17 depicts the response spectral acceleration ratios for 5% of the critical damping and  $T_s$  of 0.02 s (the digitization time interval of the record from Fig. 2.10) and  $T_s$  of 0.1 s (for example over 7.5 m long and stiff pile/wall in very soft ground with the transversal wave velocity  $c_t$  of 75 m/s). The averaging of high frequency (small period) ground motion by the stiff structure caused a 25% decrease in the maximum elastic response spectral acceleration.

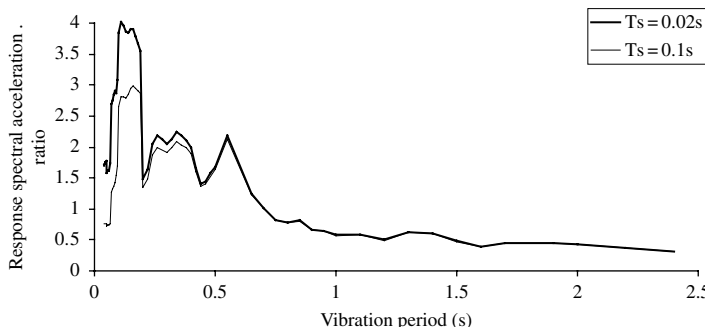


Fig. 6.17 Response spectral acceleration ratios for 5% of the critical damping and two values of  $T_s$

### 6.4.2 Acceleration Response Spectra Ratios for Inertial Interaction Effect Consideration

The fundamental circular frequency  $\omega_e = 2\pi T_e^{-1}$  of undamped coupled linear elastic SDOFO (Fig. 6.16) is calculated from the following formula (e.g. Wolf, 1994):

$$\frac{1}{\omega_e^2} = \frac{1}{\omega_s^2} + \frac{1}{\omega_h^2} + \frac{1}{\omega_r^2} \quad (6.58)$$

where  $\omega_s$  is the natural circular frequency of pile(s)/wall in fixed base condition,  $\omega_h$  is equal to the natural frequency of the dynamic model in the horizontal direction, assuming that pile/wall is rigid (infinitely stiff) and that the foundation cannot rock (the rocking stiffness is infinite),  $\omega_r$  equals the natural frequency corresponding to the rocking motion for pile groups (infinitely stiff) and with no horizontal motion of the foundation (the horizontal stiffness is infinite). Rocking motion is negligible for relatively thin flexural retaining walls. In reality, the horizontal and rocking motions of foundations are coupled and not independent. The natural circular frequency  $\omega_s$  of pile(s)/wall for rigid base condition is:

$$\omega_s = \sqrt{\frac{k_s}{m_s}}, \quad (6.59)$$

where  $k_s$  are the coefficient of lateral stiffness of pile(s)/wall and  $m_s$  is their mass.

Determination of the natural circular frequencies of pile group in horizontal  $\omega_h$  and rocking  $\omega_r$  motion can be rather complex. Novak and Grigg (1976), Poulos (1979), Wolf (1994), among others, used the concept of dynamic interaction factors between only two piles within a pile group. The presence of other piles is disregarded; the corresponding reflections and refractions are not taken into account. In the simplified method used in this section, piles/wall is represented by an equivalent deep foundation. A deep foundation is modeled by a stack of embedded disks over the foundation depth in the strength-of-material approach by Wolf and Deeks (2004).

The circular frequencies  $\omega_h$  and  $\omega_r$  are determined from the peaks of ratios between the amplitudes of the horizontal and rocking motion of embedded disks and the amplitudes of free-field ground motion. The free-field ground motion for vertically propagating shear waves with circular frequency  $\omega$  is described by Wolf and Deeks (2004) as

$$u^f(z, \omega) = u^f(\omega) \cdot \cos \frac{\omega}{c_t} \cdot z, \quad (6.60)$$

where the depth  $z$  is measured downwards from the free surface,  $u^f(\omega)$  is the surface amplitude of the free field ground motion,  $\omega$  is the ground circular frequency,  $c_t$  is ground transversal wave velocity. Computer program CONAN (by Wolf and Deeks, 2004, <http://www.civil.uwa.edu.au/~deeks/conan/>) is used for the

calculations. Layered soil sites and half space or rock bases can be considered. Soil properties required for the calculations are unit density  $\rho$ , Poisson's ratio  $\nu$ , shear modulus  $G$  and damping ratio  $\xi_g$ , from Subsection 2.2.1. The radii of the equivalent disks for the vertical motion  $r_v$  are calculated as:

$$\begin{aligned} r_v &= \sqrt{N_{piles} \cdot r_{pile}^2} \\ r_v &= \sqrt{\frac{b_c \cdot l_c}{\pi}} \end{aligned} \quad (6.61)$$

The radii  $r_h$  of the disks for the horizontal motion are

$$\begin{aligned} r_h &= \sqrt[4]{N_{piles} \cdot r_{pile}^4} \\ r_h &= \sqrt[4]{\frac{b_c \cdot l_c^3}{3 \cdot \pi}} \end{aligned} \quad (6.62)$$

The radii  $r_r$  of the disks for the rotational motion are

$$\begin{aligned} r_r &= \sqrt[4]{\frac{4 \cdot I_r}{\pi}} \\ I_r &= \sum_1^{N_{piles}} \left( \frac{r_{pile}^4 \cdot \pi}{4} + r_{pile}^2 \cdot \pi \cdot y_{pile}^2 \right) \\ I_r &= \frac{b_c \cdot l_c^3}{12}, \end{aligned} \quad (6.63)$$

where  $r_{pile}$  is a half of pile diameter,  $y_{pile}$  is the shortest distance between pile centroid and the neutral axis of rotation,  $b_c$  and  $l_c$  are the breadth and length of a rectangular pile cap. The rocking motion is negligible for relatively thin flexural retaining walls.

The effects of material damping and of radiation damping are separated (Wolf, 1994) to derive simple expressions that lead to physical insight. This is achieved by considering the effect of material damping on the damping coefficients only. The equivalent hysteretic damping ratio  $\xi_e$  determined at resonance is used over the whole range of frequency of a coupled SDOFO (Wolf, 1994)

$$\xi_e = \frac{\omega_e^2}{\omega_s^2} \cdot \xi_s + \left(1 - \frac{\omega_e^2}{\omega_s^2}\right) \cdot \xi_g + \frac{\omega_e^2}{\omega_h^2} \cdot \xi_h + \frac{\omega_e^2}{\omega_r^2} \cdot \xi_r, \quad (6.64)$$

where  $\xi_s$  is structural hysteretic damping ratio,  $\xi_g$  is soil hysteretic damping ratio, radiation damping ratio in horizontal direction is  $\xi_h$  and in rotational motion of a pile group is  $\xi_r$ . The values of  $\omega_e$  and  $\omega_s$  are given in Equations (6.58) and (6.59) respectively. The circular frequencies  $\omega_h$  and  $\omega_r$  are determined from the peaks of

ratios between the amplitudes of the horizontal and rocking motion of embedded disks and the amplitudes of free-field ground motion using the computer program CONAN mentioned earlier.

Clough and Penzien (1993) described the procedure for determination of  $\xi_s$ ;  $\xi_g$  can be obtained from Table 2.2. The radiation damping ratio in the horizontal direction  $\xi_h$  of a pile/wall is according to Wolf (1994)

$$\begin{aligned}\xi_h &= \frac{a_h \cdot z_h}{2 \cdot r_h} \\ z_h &= \pi \cdot r_h \cdot (2 - \nu)/8 \\ a_h &= \frac{\omega_h \cdot r_h}{c_t},\end{aligned}\tag{6.65}$$

where  $r_h$  is according to Equation (6.62),  $\nu$  is soil Poisson's ratio,  $c_t$  is soil transversal wave velocity,  $\omega_h$  is the circular frequency of horizontal motion.

The radiation damping ratio in rotational motion  $\xi_r$  of a pile/wall cap is according to Wolf (1994)

$$\xi_r = \frac{a_r \cdot c_r}{2 \cdot k_r}\tag{6.66}$$

For  $\nu < 1/3$ ,

$$\begin{aligned}c_r &= \frac{z_r \cdot c_t}{r_r \cdot c_p} \\ z_r &= \frac{9}{8} \pi (1 - \nu) \cdot r_r \\ a_r &= \frac{\omega_r \cdot r_r}{c_p} \\ k_r &= 1\end{aligned}\tag{6.67}$$

and for  $1/3 < \nu < 1/2$

$$\begin{aligned}c_r &= \frac{z_r}{2 \cdot r_r} \\ z_r &= \frac{9}{8} \pi (1 - \nu) \cdot r_r \\ k_r &= 1 - 0.6 \cdot (\nu - \frac{1}{3}) \cdot \frac{z_r}{r_r} \cdot a_r^2 \\ a_r &= \frac{\omega_r \cdot r_r}{2 \cdot c_t}\end{aligned}\tag{6.68}$$

where  $r_r$  is according to Equation (6.63),  $\nu$  is soil Poisson's ratio,  $c_t$  is soil transversal wave velocity,  $c_p$  is soil longitudinal wave velocity,  $\omega_r$  is the circular frequency in rotational motion.

### 6.4.2.1 Case Studies of Peak Horizontal Accelerations of Pile Caps

The objective of the case studies is to indicate accuracy and precision of the use of elastic acceleration spectra of coupled SDOFO for prediction of the peak acceleration of piled foundations and flexural retaining walls.

1. **Ohba-Ohashi Road Bridge in Japan.** Ohira et al. (1984) presented the results of observations of the response of foundation piles of a road bridge in the city of Fujisawa in Kanagawa prefecture of Japan. The Kanagawa-ken Seibu earthquake with magnitude 6.0 occurred on the 8 August 1983. Its epicentral distance was at 20 km and the hypocentral depth at 42 km according to Ohira et al. (1984). The recorded peak horizontal acceleration of the foundation was  $36.7 \text{ cm/s}^2$  along the bridge axis and of the ground surface  $113.5 \text{ cm/s}^2$  at a distance of 70 m away from and parallel to the bridge axis. The bridge spans a valley about 400 m wide at the location of the bridge crossing. The sediments in the valley involve diluvial deposits of cohesive soil and fine sand, with the shear wave velocity of 400 m/s, upon which extremely soft alluvial strata of humus and silt, with the shear wave velocity between 40 and 65 m/s, exist. The depth of the top soil at the location of instrumented pier No. 6 is about 22 m. The instrumented pier No. 6 is supported by 64 steel pipe piles of diameter 600 mm and length 22 m; half are battered at 5 v:1 h. The pile cap size is  $12 \times 12 \text{ m}$ . An estimated coefficient of the lateral stiffness of the pile group is about  $7 \times 10^8 \text{ N/m}$ . The power spectra of recorded horizontal accelerations in direction of the bridge axis at the pile cap indicate the equivalent fundamental period of about 1.3 s, which corresponds to  $\omega_e$  of 4.8 rad/s. Estimated lumped mass is  $3 \times 10^6 \text{ kg}$  and the height of the lumped mass is 10 m above the foundation. The values of  $T_s = 0.44 \text{ s}$  and  $\xi_e = 0.125$  were used in the analyses by Srbulov (2006c).
2. **Meloland Road Overpass in California.** Werner et al. (1987) applied a system identification methodology to the array of strong-motion recordings, in order to assess the seismic response characteristics of the bridge, located east of El Centro in California, shaken strongly by the 1979 Imperial Valley earthquake. A two-span reinforced concrete box girder structure is located only 0.5 km away from the causative fault for the earthquake, with a local magnitude 6.6, which occurred on the 15th October 1979. The horizontal peak accelerations in the free field were 0.315 g (000 component) and 0.296 g (270 component). The recorded peak accelerations of the pile cap were 0.28 g (000 component) and 0.33 g (270 component). A single pier of the bridge is supported by 25 timber piles of 0.3 m diameter and 15 m length. The piles are driven into medium stiff sandy clay with an average SPT  $N$  value of 14 according to Meymand (1998). The transversal wave velocity of 219 m/s corresponds to the 14 NSPT, according to equation (6.56). The Fourier amplitude spectra (Werner et al. 1987) for the transverse (270 component) motion at the base of the pier indicate the predominant equivalent frequency of 0.375 Hz, which corresponds to  $\omega_e$  of 2.35 rad/s. Based on the bridge fundamental frequency in the transversal direction to the bridge axis of 2.47 Hz, the structural damping

ratio of 0.072 (Werner et al., 1987) and the coefficient of lateral stiffness of the structure  $k_s = 260 \text{ MN/m}$  (Zhang and Makris, 2001), an estimated lump mass is  $1.1 \times 10^6 \text{ kg}$  and the height of the lump mass is 7.0 m. The values of  $T_s = 0.068 \text{ s}$  and  $\xi_e = 0.086$  were used in the analyses by Srbulov (2006c).

3. **Chiba Warehouse in Japan.** Tominaga et al. (1989) provided data concerning a warehouse founded on steel tubular piles and improved reclaimed land by sand compaction piles in the Keiyo industrial area along the east side of Tokyo Bay. The Chibaken-Toho-Oki earthquake affected the area in December 1987. The earthquake occurred offshore (east) of Chiba prefecture about 50 km away from Chiba. The USGS NEIC database lists the surface wave magnitude of 6.4, the epicentre at  $35.36^\circ\text{N}$ ,  $140.21^\circ\text{E}$ , the depth of 62 km and the origin date on the 17th December 1987. The free field peak horizontal ground acceleration recorded was  $2.53 \text{ m/s}^2$  in E-W direction of  $1.77 \text{ m/s}^2$  in N-S direction. The peak acceleration recorded on the floor of the warehouse was  $1.18 \text{ m/s}^2$  in E-W direction and  $1.07 \text{ m/s}^2$  in N-S direction. Therefore a significant attenuation took place, possibly due to soil-structure interaction. The intense ground motion lasted about 20 s. The top 15 m below the ground surface was densified using compaction piles. The ground water level is about 5 m below the ground surface. The rack type warehouse is 127.75 m long in E-W direction, 33.3 m wide and 28.4 m high, constructed in 1984/85. Steel pipe piles about 25 m long support the rack. The natural period  $T$  of the fixed base structure is according to the Uniform Building Code (1997)  $0.0853 h_n^{0.75}$  where  $h_n$  is height in meters above the base to level that is uppermost in the main portion of the structure. In this case  $T$  is 1.0 s and  $\omega_s$  is  $6.28 \text{ rad/s}$ . Estimated lumped mass per two pile group is  $4 \times 10^5 \text{ kg}$  based on assumed their design capacity. Estimated height of the lumped mass is 14 m above the foundation. The values of  $T_s = 0.069 \text{ s}$ ,  $\omega_e = 4.0 \text{ rad/s}$  and  $\xi_e = 0.038$  were used in the analyses by Srbulov (2006c).
4. **Hollywood Storage Building in California.** Fenves and Serino (1990) provided data on the response of the building in Los Angeles shaken by a number of earthquakes in time. The 9th February 1971 San Fernando earthquake had a local magnitude of 6.4. It occurred at the epicentral distance of 35 km from the building. The earthquake induced the peak surface ground acceleration of  $0.17 \text{ g}$  in the transversal and  $0.21 \text{ g}$  in the longitudinal direction of the building at the parking lot some 42 m away, which may not be far enough for true free field condition. The peak accelerations recorded at the base of the building were  $0.11 \text{ g}$  in the transversal direction and  $0.15 \text{ g}$  in the longitudinal direction of the building. The 1st October 1987 Whittier earthquake had a local magnitude of 5.9. It occurred at the epicentral distance of 25 km from the building. The earthquake induced the peak surface ground acceleration of  $0.20 \text{ g}$  in the transversal and  $0.11 \text{ g}$  in the longitudinal direction of the building at the parking lot some 42 m away. The recorded peak accelerations at the base of the building were  $0.11 \text{ g}$  in the transversal direction and  $0.06 \text{ g}$  in the longitudinal direction of the building. Sandy clay layer exists to a depth of about 60 m below the ground surface. This layer is underlain by sedimentary formations, which rest on slate. The fourteen-storey reinforced concrete building is 66 m long, 15.5 m wide and

45.5 m high, constructed in 1925. The foundation consists of concrete piles that vary in length from 3.6 m at the edge of the building to 9 m near the centre and they are located at large spacing. Observed fundamental period of the building oscillation in the longitudinal direction is 0.6 s and in the transversal direction 1.9 s. An estimated lumped mass is  $2.7 \times 10^7$  kg based on live load of 5.3 kPa per storey area and the self-weight of the structure. An estimated height of the lumped mass is 23 m above the foundation. The values of  $T_s = 0.034$  s,  $\omega_e = 6.87$  radians/s in the longitudinal and 3.11 rad/s in the transversal direction and  $\xi_e = 0.182$  in the longitudinal and 0.034 in the transversal direction were used in the analyses by Srbulov (2006c).

5. **Imperial Valley County Services Building in California.** Hadjian et al. (1990) reported the case of the building severely damaged in the 1979 Imperial Valley earthquake with a local magnitude 6.6 on the 15th October 1979. Lee et al. (1982) reported the horizontal peak accelerations in the free field (104 m away from the building) as 0.20 g (N02E component) and 0.22 g (N92E component) and on the ground floor of 0.29 g (NS component) and 0.34 g (EW component). The recording instrument is located about 38 m from the centre of the building. Both torsion and/or soil/structure (near) resonance could have caused the increased peak accelerations. The ground profile consists of layers of mixed clay, silt and sand. The 6 storey reinforced concrete building has an area of  $60 \times 124$  m. It is supported on 204 Raymond step-taper piles driven 14 m trough soft to stiff sandy clay. The predominant period of the structure is 0.61 and 1.75 s in NS and EW direction respectively according to Hadjian et al. (1990). In this section, an estimated lump mass is  $3 \times 10^7$  kg based on assumed 1.5 MN design bearing capacity of Raymond piles. The estimated height of the lumped mass is 9 m. The values of  $T_s = 0.083$  s,  $\omega_e = 3.55$  rad/s in EW and 9.24 rad/s in NS direction and  $\xi_e = 0.027$  in EW and 0.25 in NS direction were used in the analyses by Srbulov (2006c).
6. **Pacific Park Plaza Building in California.** Celebi and Safak (1992) provided the preliminary analyses of the response of the building shaken by the 1989 Loma Prieta earthquake. The 17th October 1989 Loma Prieta earthquake had a surface wave magnitude of 7.1 and the epicentre at 97 km from the building. Two free-field stations (located about 33 and 126 m away from the building) recorded the horizontal peak accelerations of 0.22 and 0.26 g. The recorded horizontal peak accelerations on the ground floor of the structure were 0.17 and 0.22 g. The underlying soil consists of several layers of silty fine sand fill, soft black silty clay (Bay mud), and very stiff to hard silty clay (old Bay mud). The depth to hard soil (silty sandy clay) is 33–50 m. The thickness of the Bay mud is 12–15 m. The 30-storey (95 m high), three-winged  $17 \times 34$  m each at  $120^\circ$ , ductile moment-resistant reinforced concrete framed Pacific Park Plaza Building, located in Emeryville east of San Francisco California, was constructed in 1983. The building is founded on 1.5 m thick reinforced concrete mat over 828 35.5 cm square precast concrete piles driven 30 m beneath and along the column lines. The predominant frequencies at approximately 0.4 Hz and 1.0 Hz were identified visually by Celebi and Safak (1992) from

the acceleration response and also from the Fourier amplitude spectra of the processed records, which reveal significant torsional motion. Forced vibration tests performed earlier by others indicated the first vibration mode frequency of about 0.6 Hz. In this section, an estimated lump mass is  $6 \times 10^7$  kg and the height of the lumped mass is 47 m above the foundation. The values of  $T_s = 0.15$  s,  $\omega_e = 3.11\text{--}3.55$  rad/s and  $\xi_e = 0.19\text{--}0.23$  were used in the analyses by Srbulov (2006c).

7. **Norwalk Buildings in California.** Celebi (1993) considered responses of two adjacent buildings, offset by 16.3 m, in Norwalk during the 1987 Whittier earthquake. The earthquake with a surface wave magnitude of 5.6 occurred on the 1st October 1987. The recorded peak accelerations in the free field were 0.21–0.25 g (NS components) and 0.09–0.13 g (EW components). The recorded peak accelerations at the basement were 0.20–0.21 g (NS components) and 0.11 g (EW component). The upper medium dense (3–5 m depth) to dense (8–10 m depth) granular soil are underlain by older Pleistocene non-marine deposits. Building A is a 7 storey rigid steel frame structure with its basement supported on concrete piles, which length varies from 8.6 to 11.6 m. The plane dimensions are  $70 \times 43$  m and its height including the basement is 33.4 m. Building B is a 7 storey ductile moment resisting frame structure with its basement resting on 9.1 m deep caissons. The plan dimensions are  $141 \times 41.5$  m and its height including the basement is 34.4 m. Building A has identical first-mode frequencies of 0.65 Hz for both building axes. Building B has fundamental modes at 0.76 Hz and 0.83 Hz in the major and minor axis respectively. Low amplitude vibration tests conducted before the earthquake indicated the fundamental frequency of about 1 Hz for building A. In this example, the estimated lump masses of the buildings are  $2 \times 10^7$  kg for building A and  $4.7 \times 10^7$  kg for building B. The estimated heights of the lump masses are 17 m. The values of  $T_s = 0.038$  s,  $\omega_e = 4.02$  rad/s for the building A and 4.88 rad/s for the building B and  $\xi_e = 0.024$  for the building A and 0.036 for the building B were used in the analyses by Srbulov (2006c).
8. **Painter Street Bridge in California.** Makris et al. (1994) provided data on the response of a concrete bridge located near Rio Dell shaken by the Petrolia earthquake. The 25th April 1992 Petrolia earthquake had a local magnitude of 7.1. It occurred at a fault distance of 18 km. The earthquake induced the peak surface ground acceleration of 0.55 g in the transversal and 0.39 g in the longitudinal direction of the bridge in the nearby field some 20 m away. The recorded peak accelerations at the pile cap were 0.48 g in the transversal direction and 0.34 g in the longitudinal direction of the bridge. Medium dense clayey to gravelly sand and sandy silt exists to a depth of 10 m below the ground surface. This layer is underlain by very dense gravelly and silty sand. The upper 10 m of soil has a shear wave velocity of 250 m/s and density  $1600 \text{ kg/m}^3$ . The shear wave velocity of 350 m/s and density of  $2200 \text{ kg/m}^3$  are assumed to 40 m depth. The structure is a continuous two-span, cast-in-place, pre-stressed post-tensioned-concrete, box-girder bridge constructed in 1973. Two pile groups, each consisting of  $4 \times 5$  driven concrete piles of 0.36 m diameter and 7.62 m length, support

the bridge. The pile cap dimensions are  $3.66 \times 4.57$  m. An estimated lumped mass is  $1.13 \times 10^6$  kg and the fundamental frequency  $\omega_s = 21$  rad/s according to Makris et al. (1994). The estimated height of the lumped mass is 6 m above the foundation. The values of  $T_s = 0.03$  s,  $\omega_e = 10.2$  rad/s and  $\xi_e = 0.125$  were used in the analyses by Srbulov (2006c).

9. **Eleven Storey Apartment House in Japan.** Ohta et al. (1980) described recordings carried out to investigate the soil-structure interaction between a structure on piled foundation and soft alluvial subsoil. The records from seven earthquakes were obtained but only the seventh earthquake induced ground acceleration of some significance. The earthquake occurred off Miyagi in Japan on the 12th June 1978 at 17:14 local time. The earthquake magnitude was 7.4 (according to Japanese scale), its focal depth was 40 km and the epicentral distance 350 km. The earthquake caused peak horizontal ground acceleration of 0.041 and 0.056 g of the gravitational acceleration in the longitudinal and transversal direction of the building some 35 m away from the building. The peak horizontal accelerations recorded on the ground floor were 0.035 and 0.061 g in the longitudinal and transversal direction of the building. The eleven-storey apartment house is made of reinforced concrete and steel composite frame, with bearing walls in the transversal direction and frame system in the longitudinal direction. The structure is 8.35 m wide, 42 m long and 31 m high. The structure rests on cast-in place concrete piles, which are approximately 26 m long and 1.3–1.5 m in diameter. The structure is connected by an expansion joint to an adjacent building with a similar structure. The thickness of the top alluvial silt deposit at the site is about 25 m; diluvial sandy gravel, sand and clay deposits exist under the top layer. The fundamental period of vibration of the soil layers is 0.7 s according to the peak spectral acceleration based on recorded free field acceleration.
10. **The Dumbarton Bridge in California.** Fenves et al. (1992) described and analyzed by finite elements the response of 2226 m long and forty three span bridge to the 1989 Loma Prieta earthquake. The 1989 Loma Prieta earthquake had a magnitude  $M_L = 7.1$  and the epicenter at approximately 55 km from the bridge. The peak horizontal accelerations in two orthogonal directions were 0.127 g in the free field at a site approximately 1.2 km from the west approach to the bridge. The peak horizontal accelerations recorded in the longitudinal direction of the bridge were from 0.167 g to 0.307 g and in the transversal direction from 0.077 g to 0.126 g. The smallest peak accelerations were recorded at the pier 13, which is located near the middle of the approach structure, and the largest peak accelerations were recorded at the pier 17, which is located at the end of the main structure. The main channel structure between piers 16 and 31 consists of several 60 m spans, two 70 m spans and one 104 m span in the centre between piers 23 and 24. Two trapezoidal steel box girders with a composite 0.24 m thick lightweight concrete deck are continuous over the piers. The box sections have an average width of 7.6 m and a nearly constant height of 2.9 m. The two approach structures have 45.75 m spans consisting of five 1.37 m high hollow triangular girders constructed of prestressed lightweight

concrete, with composite 0.21 m thick lightweight concrete deck. The ends of the girders are supported on the transverse bent caps of the piers, and there are intermediate diaphragms between girders at the third points of each span. The approach structures are founded on 15 m to 18 m thick and the main structure on 3 m thick soft clay. The soft clay layer is underlain by stiffer silty clay, older bay clay, and the formation of very stiff clay. The depth of bedrock is believed to be at least 180 m. The piers of the approach structures have from 28 to 43 piles. These are either 0.5 diameter prestressed concrete piles or 0.56 m diameter steel piles. The pile lengths are from 18 m to 24 m. The pier foundations of the main structure have either 21 to 32 prestressed concrete piles with 1.37 m diameter, or 52 steel piles with 0.56 m diameter. The piles are embedded approximately 15 m and extended approximately 15 m from the mudline through the water to the pile cap at the mean water elevation. The fundamental vibration period of the instrumented spans is 1.92 s in the longitudinal direction. The fundamental vibration period in the transversal direction is 2.15 s for the piers 13–15, 1.2 s for the pier 17 and 1.6 s for the central pier 21. The structural masses are estimated from Equation (6.59). The stiffnesses  $k_s$  are obtained from the ratios between the calculated shear forces and the horizontal displacement obtained from processed acceleration records at the top of the piers.

11. **The Northwest Connector in California.** Fenves and Desroches (1994) described and analyzed by finite elements the response of 775 m long and sixteen spans connector to the 1992 Landers and Big Bear earthquakes. The Landers event, with a magnitude of  $M_s = 7.6$  and at an epicentral distance of 80 km, induced the free field peak horizontal ground acceleration of 0.09 g. The same day Big Bear event, with a magnitude of  $M_s = 6.6$  and at an epicentral distance of 45 km, induced the free field peak horizontal ground acceleration of 0.11 g. The recorded peak horizontal accelerations of the pile cap located about a quarter length of the connector were about 0.1 g during the Landers and Big Bear earthquake. However, the recorded peak horizontal accelerations of the pile cap located at the mid span of the connector were about 0.17 g in both directions during the Landers earthquake and 0.25 g (in the longitudinal direction) and 0.15 g (in the transversal direction) during the Big Bear earthquake. The connector is curved reinforced concrete 12 m wide and 2.4 m high box girder bridge over sixteen spans supported by single columns and diaphragm abutments. The structural system consists of six frames, connected at five intermediate hinges. The connector crosses the northern segment of the San Jacinto fault zone. The site consists of deep unconsolidated alluvial deposits about 300 m thick. The top soil layer generally involves medium to dense clean and silty sand with varying thickness from 6 m to 18 m. The 28–48 pile groups contain 0.3 m square precast prestressed piles. The pile lengths range from 6 m to 15 m. Thirty additional around the perimeter driven steel pipe piles are 0.4 m diameter and 18 m to 25 m long. The fundamental vibration mode of the structure has a period of 1.5 s, the second mode 1.2 s, the third mode 1 s and 0.8 s, 0.65 s and 0.55 s respectively at higher modes during the Landers earthquake. The fundamental vibration mode of the structure has a period of 1.8 s, the second mode 1.25 s, the

third mode 1.15 s and the fourth mode 0.95 s during the Big Bear earthquake. According to the response spectra, the free field predominant period was 0.6 s with a secondary period at about 1.9 s during the Landers earthquake and about 0.6 s with secondary periods at about 0.3 s and 1.8 s. The structural masses are estimated from Equation (6.59). The stiffnesses  $k_s$  are obtained from the ratios between the calculated shear forces and the horizontal displacement obtained from processed acceleration records at the top of the piers.

#### 6.4.2.2 Summary of the Case Studies

The relevant data of the case histories analyzed by Srbulov (2006c) are given in Table 6.3. The results of the calculations are shown in Fig. 6.18. The overall accuracy of the prediction method is good but its individual precision is poor when average spectral horizontal accelerations (e.g. Ambraseys et al., 2005a) are considered for piles groups. The scatter of the predictions based on the average spectral accelerations is about a half of the scatter of the predictions of peak horizontal ground accelerations in the free field based on empirical attenuation relationships, Equation (3.6). As the prediction of ground motion in the free-field is rather uncertain, greater accuracy should not be expected for the prediction of pile/wall motion.

#### 6.4.2.3 An Example of Calculation of Dynamic Lateral Ground Force on a Flexural Retaining Wall

The supporting height  $H_w = 5$  m is considered as in Sections 6.3.2. The coefficient of lateral stiffness  $k_s$  of a cantilever wall fixed at its toe and uniformly loaded is (e.g. Gieck and Gieck, 1997)  $k_s = 8E_w I_w l_w^{-3}$ , where  $E_w$  is wall Young modulus,  $I_w$  is second moment of wall cross section area,  $l_w = 15$  m is assumed wall height measured from its toe, Fig. 6.19. For a reinforced concrete wall  $E_w$  is about 21 GPa and  $I_w = t_w^3/12$  per meter length, where assumed wall thickness  $t_w = 1$  m. For wall mass per 1 m length  $m_s = 37500 \text{ kg/m}^3$ ,  $\omega_s = 10.5 \text{ rad/s}$  (Equation 6.59).

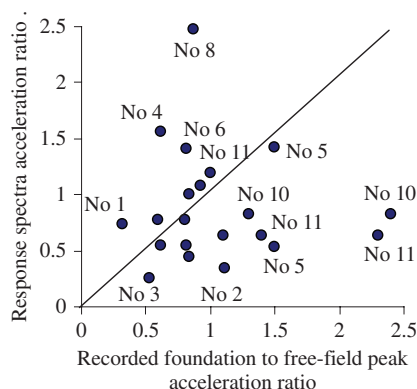


**Fig. 6.18** Recorded versus predicted foundation to free-field peak horizontal acceleration ratios

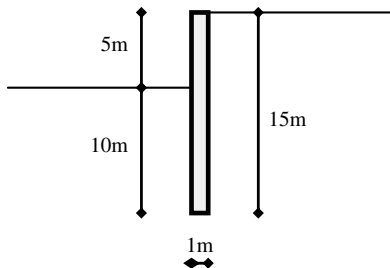
**Table 6.3** Recorded and calculated peak horizontal pile cap to free field acceleration ratios  $a_{e,p}/a_{hp}$ 

N <sub>e</sub>	Case	Earthquake magnitude	Source to site distance (km)	$\omega_e$ (radians/s)	$T_e = \frac{2\pi}{2\pi\omega_e}(s)$	$\xi_e$	Spectral acceleration ratio	Actual $a_{e,p}/a_{hp}$
1	Ohba-Ohashi road bridge in Japan (Ohira et al., 1984)	6	20	4.8	1.3	0.12	0.74	0.32
2	Meloland road overpass in California (Werner et al., 1987)	6.6	0.5	2.35	2.67	0.07	0.34	1.11
3	Chiba warehouse in Japan (Tomonaga et al., 1989)	6.4	50	$\frac{1}{\sqrt{\frac{1}{1^2} + \frac{1}{44^2} + \frac{1}{40^2}}} = 1.0$	6.28	0.06	0.26	0.46-0.61
4	Hollywood storage building in California (Fenves and Serino, 1990)	6.4 5.9	35 25	3.30 to 10.47	1.9-0.6	0.05	0.54-1.56	0.65-0.71 0.55-0.54
5	Imperial Valley county service building in California (Hadjian et al., 1990)	6.6	?	$\frac{1}{\sqrt{\frac{1}{(10.3 \times 3.6)^2} + \frac{1}{32^2} + \frac{1}{30^2}}} = 9.3 \text{ to } 3.4$	0.67-1.8	0.24-0.08	1.42-0.53	1.45-1.54

Table 6.3 (continued)

N <sub>o</sub>	Case	Earthquake magnitude	Source to site distance (km)	$\omega_e$ (radians/s)	$T_e = \frac{2\pi}{2\pi\omega_e^{-1}}(s)$	$\xi_e$	Spectral acceleration ratio $a_{c,p}a_p^{-1}$	Actual $a_{c,p}a_p^{-1}$
6	Pacific Park Plaza building in California (Celebi and Safak, 1992)	7.1	97	2.51–6.28	2.5–1.0	0.08–0.21	0.55–1.41	0.77–0.85
7	Norwalk buildings in California (Celebi, 1993)	5.6	?	4.5	1.4	0.08	0.45	0.84–0.85
8	Painter street bridge in California (Makris et al., 1994)	7.1	18	$\frac{1}{\sqrt{\frac{1}{21^2} + \frac{1}{73^2} + \frac{1}{65^2}}} = 19.1$	0.33	0.15	2.47	0.87–0.87
9	11 storey apartment house in Japan (Ohta et al, 1980)	7.4	350	3.8	1.65	0.07–0.09	1.08	1–0.85
10	Dumbarton bridge in California (Fenves et al., 1992)	7.1	55	3.27 2.92 5.24	1.92 2.15 1.2	0.05 0.05 0.05	0.83 0.77 1.19	1.3–2.4 0.6–0.8 1.0
11	The Northwest connector in California (Fenves and Desroches, 1994)	7.6 6.6	80 45	3.93 3.93 3.60	1.6 1.6 1.75	0.05 0.05 0.05	1.0 1 0.63	0.84 1.1 1.4–2.3

**Fig. 6.19** Cross section of the retaining wall in the example



The radii of the equivalent disks for the horizontal motion  $r_h = 0.56$  m per meter length of the wall (Equation 6.62). As expected, the calculations using CONAN confirm that the circular frequencies  $\omega_h$  of the flexural wall are close to the circular frequencies of ground motion. For a layer thickness equal to the wall height  $l_w = 15$  m, considered blow counts  $(N_1)_{60}$  of 20, 35 and 50, the corresponding transversal wave velocities  $c_t = 244, 294$  and  $327$  m/s respectively from Equation (6.30), the fundamental circular ground frequencies  $\omega_h = 2\pi c_t (4 \times l_w)^{-1} = 25.5, 30.8$  and  $37.1$  rad/s respectively. From Equation (6.58), the equivalent circular frequencies of the coupled wall-ground system  $\omega_e = 9.7, 9.9$  and  $10.1$  rad/s respectively.

In comparison, the predominant circular frequencies of ground accelerations for the records from Table 6.2 are  $15.7$  rad/s for the records A1 and A2,  $28.5$  &  $57.1$  rad/s for the record A3,  $25.1$  rad/s for the records B1 and B2 and  $12.5$  rad/s for the record B3

The structural hysteretic damping ratio is assumed  $\xi_s = 0.02$ . From Tables 6.2 and 2.2 it follows that  $\xi_g$  is about  $0.08$ . From Equation (6.65) and for assumed  $\nu = 0.25$ ,  $\xi_h = 0.020$ . From Equation (6.64),  $\xi_e = 0.02$  for  $\xi_r = 0$ .

For  $\omega_e$  of about  $10$  rad/s and  $\xi_e = 0.02$ , the spectral accelerations at the period of  $2\pi/10 = 0.63$  s for the records from Table 6.2 are  $7.5$  m/s $^2$  (record A1),  $5$  m/s $^2$  (records A2 and B2),  $4$  m/s $^2$  (records A3),  $7$  m/s $^2$  (record B1),  $8$  m/s $^2$  (record B3) according to data by Ambraseys et al. (2004). For assumed uniform distribution of ground acceleration along the wall height, the corresponding lateral dynamic ground

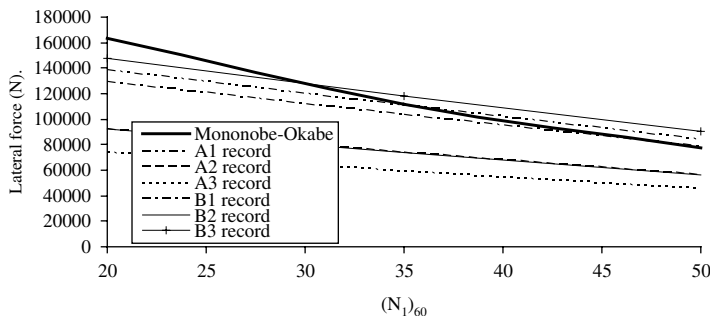


**Fig. 6.20** Results of comparison of dynamic lateral forces acting on the flexural wall in the example

forces on the wall for active wedges inclined at  $45^\circ + \phi/2$  to the horizontal (for assumed soil friction angle in cyclic condition  $\phi = 0.83(N_1)_{60}$  according to Srbulov (2005a) and unit density of soil  $\rho = 2000 \text{ kg/m}^3$ ) are shown in Fig. 6.20.

The procedure is applicable to anchored walls as well. The anchor stiffness is simply added to the wall stiffness  $k_s$ . Anchor stiffness is the ratio between applied force and resulting displacement at its head.

## 6.5 Summary

Several simplified methods for analyses of dynamic soil-foundation interaction are described in this section:

- Formula for the calculation of the peak horizontal acceleration of foundations of rigid structures with lumped mass can provide good results. It must be remembered that this model does not consider soil-foundation interaction and soil properties in addition that it is unable to account for higher modes of structural vibration and for resonance condition.
- Closed form solution in time for analysis of gravity walls in seismic condition does not consider wall sliding, which is assumed to be prevented by a fixed lateral support. The only mode of wall movement considered is rotation. The solution uses the assumption of the lateral dynamic force acting on wall comparable to the Mononobe-Okabe method.
- Time stepping procedure for gravity retaining walls and caissons used for the case of base sliding is suitable when the permanent displacement is co-seismic. For post-seismic permanent displacement, two sliding blocks method described in Sub-section 4.4.2 provides more realistic results.
- Single degree of freedom oscillator (SDOFO) on flexible base when applied to piled foundation indicates good accuracy of prediction of peak foundation acceleration on average but poor precision of prediction for individual cases. It may not be surprising when the prediction of peak ground acceleration in the free-field is rather uncertain. When SDOFO on flexible base is applied to flexural retaining walls, it predicts the values of lateral forces on the walls comparable to Mononobe-Okabe method.

# **Chapter 7**

## **Bearing Capacity And Additional Settlement of Shallow Foundation**

### **7.1 Introduction**

Ground shaking caused by earthquakes can affect shallow foundations in several ways:

- Cyclic degradation of soil strength, associated with plastification and the development of excess pore pressures, may allow a bearing capacity failure to take place, such as punching through or rotational type failures.
- Significant horizontal inertial forces induced by earthquakes can change the failure mechanism to one in which the bearing capacity of shallow foundations is mainly controlled by sliding resistance or overturning.
- Liquefaction or a significant loss of soil shear stiffness in cyclic condition of soil layers beneath and around a foundation can result in very large settlements of shallow foundations and therefore loss of serviceability of structures supported by such foundations.
- Re-distribution of excess pore pressures after an earthquake can lead to softening or failure in ground that was not so affected during the earthquake itself. The magnitude and timescales for this effect can be relatively short for granular soils. In cohesive soils, dissipation of excess pore pressures is a process of consolidation that can take many months or years.

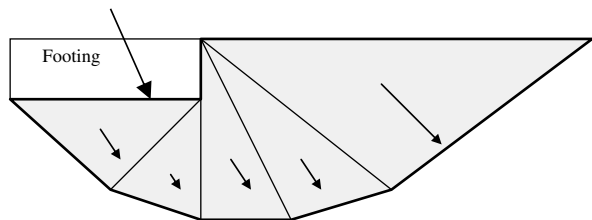
The objective of this chapter is to describe pseudo-static analyses of bearing capacity and additional settlements of shallow foundations.

### **7.2 Bearing Capacity: Pseudo-Static Approaches**

The bearing capacity of a shallow foundation can be assessed based on several methods such as described in Section 4.2 for soil slopes as shown in Fig. 7.1 or Annex F of Eurocode 8, Part 5 (2004).

In a simplified pseudo-static approach, the bearing capacity of shallow foundation in seismic condition can be calculated as the bearing capacity of shallow foundation in static condition but with an apparently increased ground surface

**Fig. 7.1** Trial slip surface for calculation of foundation bearing capacity in seismic condition



inclination. For horizontal acceleration due to the earthquake, the increased ground surface inclination is  $\arctan(0.65a_{p,h}g^{-1})$ , where  $a_{p,h}$  is the peak horizontal ground acceleration and  $g$  is the gravitational acceleration. A correction factor which accounts for inclination of ground surface is given by Hansen (1970).

The method used in Appendix A.11 for calculation of bearing capacity of shallow foundation in static condition based on Eurocode 7, Part 1, Annex D (2004) contains a correction factor for the inclination of the foundation base, instead of the ground surface. The angle of inclination of foundation base to the horizontal can be taken equal to  $\arctan(0.65a_{p,h}g^{-1})$ .

### 7.3 Bearing Capacity: Effects of Sub-Surface Liquefaction

If the thickness of top non-liquefied soil crust is small then punch through type failure can occur, Fig. 7.2.

In the case of punch through type failure, a shallow foundation can sink until the buoyancy force acting on the failed mass comes into equilibrium with the applied load. The vertical foundation capacity  $F_v$  in the case of punch-through failure is (eg. SNAME, 1997)

$$F_v = F_{v,b} - A_f \cdot H_l \cdot \gamma + 2 \frac{H_l}{B_f} (H_l \cdot \gamma + 2p_0') K_s \tan \phi \cdot A_f \quad (7.1)$$

where  $F_{v,b}$  is determined assuming the foundation bears on the surface of the lower liquefied layer,  $A_f$  is foundation area,  $H_l$  is distance from foundation level to the

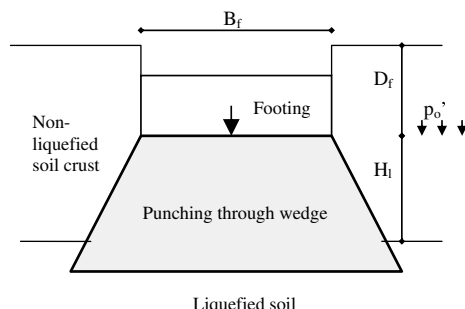


**Fig. 7.2** Punching through mode of failure in post-seismic condition

level of liquefied layer below,  $\gamma$  is unit weight of non-liquefied soil ( $\gamma'$  if submerged),  $p_0'$  is effective overburden stress at the foundation depth,  $K_s$  is the coefficient of punching shear that is calculated from the equation  $K_s \cdot \tan \phi = \frac{3c_u}{B_f \cdot \gamma}$ ,  $\phi$  is friction angle of non-liquefied layer,  $c_u$  is undrained shear strength of liquefied sand layer (= 0.05 to 0.12 of the effective overburden pressure acting on the top of liquefied layer, Section 5.1),  $B_f$  is diameter of an equivalent circular foundation, and:

$$F_{v,b} = (c_u \cdot N_c + p_0') \cdot A_f, \quad (7.2)$$

where  $c_u$  is again the undrained shear strength of liquefied sand layer (Section 5.1),  $N_c$  is bearing capacity factor taken as 5.14,  $p_0'$  is effective overburden pressure,  $A_f$  is foundation area.

## 7.4 Bearing Capacity: Effects of Structural Inertia and Eccentricity of Load

Rotational type failures can occur when the inertial force acting on structure causes an excessive eccentricity of loading on the foundation, Fig. 7.3.

Bearing capacity of soil is defined for an effective foundation area, i.e. the area which centroid coincides with the location of the resultant force on foundation. If the ultimate bearing capacity of soil beneath the effective foundation area is exceeded in seismic condition then soil failure is initiated. Footing displacement caused by such

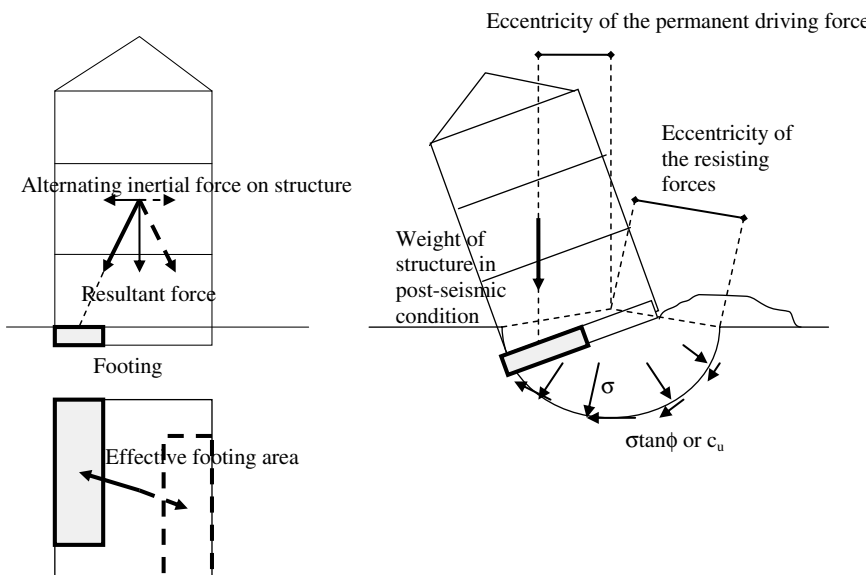


**Fig. 7.3** Rotational type failure of a shallow foundation initiated by the inertial forces acting on a structure and driven by self weight of structure in post-seismic condition

failure may be small during each seismic pulse because of its short duration and reversible direction. The number of strong earthquake pulses is usually small and does not cause global foundation failure unless the incremental displacements are accumulated in one direction because of asymmetric conditions (eg. heterogeneous soil beneath foundation, two closely adjacent buildings preventing free swaying of each of them) or soil liquefaction. Accumulated unidirectional displacement causes eccentricity of the permanent driving force (structural weight) and further increase in permanent displacements. One approach to the analysis of this type of failure is to use the same methods as are used for slope stability analyses, described in Subsection 4.2.

#### **7.4.1 An Example of Calculation of Bearing Capacity of Shallow Foundation in Seismic Condition**

A strip foundations with width of 1 m is considered resting on the surface of homogeneous frictional only soil with  $\phi = 35^\circ$  or cohesive only soil with  $c_u = 50 \text{ kPa}$ . Considered unit weight of soil is  $19 \text{ kN/m}^3$ . Considered ratio between the vertical and the horizontal component of ground acceleration is  $1/2$ . The results are compared with the results of the procedure given in Annex F of Eurocode 8, Part 5 (2004) for the foundation under a vertical centered load, as shown Fig. 7.4.

In the example, only the effect of horizontal ground acceleration on soil mass under the foundation is considered for the case that the load on the foundation is applied over a roller bearing, with the horizontal force and moment on the foundation equal to zero. In applied Eurocode procedure, it is assumed that the soil factor  $S = 1.15$  for cohesive soil is for C ground type, which is predominantly stiff clay. Significant difference in the results obtained by the use of these two methods is evident for cohesive soil only. Faster decrease of the ultimate load according to Annex F of Eurocode 8, Part 5 (2004) is caused by the dimensionless soil inertia force i.e. the expression  $1 - 0.21 \cdot F^{-1.22}$ .

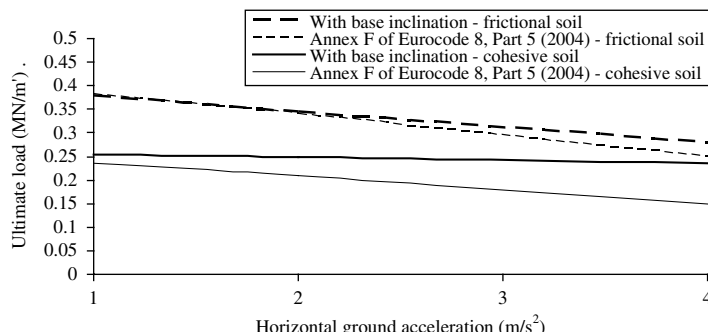


**Fig. 7.4** Ultimate loads on 1 m wide strip foundations

## 7.5 Additional Settlement in Granular soils

Significant additional settlement of a shallow foundation only occurs if the stiffness of coarse granular soil is decreased during ground shaking. If this occurs, the main additional foundation settlement is driven by gravity forces in post-seismic (soil consolidation) stage, similar to the slope displacement described in Subsection 4.4.2.

Ohsaki (1970) reported on settlements from 0.5 m to 0.7 m of a 5 m thick layer of very loose sand in Hachinohe, Japan, due to the 1968 Tokachioki earthquake of magnitude 7.9. Settlements from 0.5 m to 1 m were observed at Port and Rokko Island in Kobe, Japan, due to the 1995 Hyogoken Nanbu earthquake of magnitude 6.9.

Liu and Dobry (1997) described eight centrifuge model experiments conducted to investigate the mechanism of liquefaction induced settlement of a shallow foundation, as well as the effectiveness of sand densification by vibro compaction under the foundation. They found that as soil becomes more impervious, significant negative excess pore pressures can develop under the foundation during shaking, and the contribution of post-shaking foundation settlement increases, while the total foundation settlement does not change very much compared to more pervious soil. They provided summarized plots of normalized foundation settlements versus normalized widths of the two to four storey residential and commercial buildings in the 1964 Niigata earthquake of magnitude 7.5 in Japan and in the 1990 Luzon earthquakes of magnitude 7.8 in Philippines, which indicates that the widths of the buildings were a predominant factor for the settlements of the buildings.

The estimated liquefaction depth was 6 m to 10 m during the 1990 Luzon earthquake and 5 m to 18 m during the 1964 Niigata earthquake. The blow counts of the SPTs conducted in the areas after the events varied in the range from 0 to 20 in Dagupan city in Philippines and 0 to 30 in Niigata. The ratio between the building width and the thickness of liquefaction was mostly in the range from 0.5 to 2.0, i.e. the building widths were in the range from about 3 m to about 35 m. The ratio between averaged foundation settlement and thickness of liquefaction was in the range from about 0.08 to 0.18 for the building width to thickness of liquefaction ratio of 0.5 and in the range from 0 to 0.1 for the building width to thickness of liquefaction ratio of 1.5. The settlements were in the range from about 0.25 m to 0.5 m for the building width of 3 m and in the range from 0 to 2.5 m for the building width of about 20 m.

Foundation settlement is caused by the vertical load acting on foundation, i.e. by additional vertical effective stress within soil caused by such load. In a simplified approach, the additional vertical stress  $\Delta\sigma_v$  at a depth  $z > 0$  caused by point load  $F_p$  at the ground surface can be calculated according to Boussinesq (1885) formula.

$$\Delta\sigma_v = \frac{3 \cdot F_p \cdot z^3}{2 \cdot R^5} \quad (7.3)$$

$$R = \sqrt{z^2 + d_h^2} > 0,$$

where  $d_h$  is the horizontal distance between the location where the load  $F_p$  is acting and the location where the stress is calculated. The foundation settlement  $\Delta s$  caused by softening of a deep soil layer is calculated according to the following formula, provided that punching through type failure of the top non-liquefied soil crust does not occur.

$$\Delta s = \int_{D_l - t_l}^{D_l} \frac{\Delta\sigma_v}{M_d} dz, \quad (7.4)$$

where  $M_d$  is soil deformation modulus, which is inversely proportional to the coefficient of soil volumetric compressibility that is discussed in Section 2.6,  $D_l$  is the maximum depth of liquefied soil layer,  $t_l$  is the thickness of the layer.

### 7.5.1 Examples of Estimation of Additional Settlement Caused by Sand Liquefaction

Consider a square foundation of plan dimensions  $1 \times 1 \text{ m}^2$  and a rectangular foundation of dimensions  $1 \times 10 \text{ m}^2$ . If the foundation pressure in both cases is 100 kPa, the acting forces would be 100 kN to 1000 kN on the square and rectangular foundation respectively. For the square foundation and depth range from 6 m to 10 m within liquefied soil, the corresponding  $\Delta\sigma_v$  range based on Equation (7.3) is from 4.1 kPa to 1.5 kPa. For the rectangular foundation and depth range from 5 m to 18 m within liquefied soil, the corresponding  $\Delta\sigma_v$  range based on Equation (7.3) is from 60 kPa to 4.6 kPa.

Stroud (1988) used the ratio between actual and ultimate foundation load as an indirect measure of strain level. He compiled a large number of data for normally and over consolidated sand and clay and presented charts relating average secant modulus beneath the foundations and  $N_{60}$  from SPTs. For the ratio between ultimate and actual foundation load greater than 3 (i.e. the factor of safety greater than 3), soil deformation modulus is equal to  $N_{60}$  in MPa, according to Stroud (1988). If liquefied layer has  $N_{60}$  less than one then soil modulus is less than 1 MPa. Using this value of 1 MPa together with the changes of stress mentioned above, the calculated additional settlements based on Equation (7.4) are greater than 0.01 m for the square foundation and greater than 0.3 m for the rectangular foundation, which are still less than the settlements caused by punching through type failure.

Tokimatsu and Seed (1987) provided a chart for estimation of volumetric strain after liquefaction of saturated sand in a magnitude 7.5 earthquake from the cyclic stress ratio and normalized standard penetration resistance ( $N_1$ )<sub>60</sub>. Large volumetric strain variation of 10 times is shown for the variation of ( $N_1$ )<sub>60</sub> from zero to 10 and 100 times for the variation of ( $N_1$ )<sub>60</sub> from zero to 20.

Ishihara and Yoshimine (1992) provided a chart for estimating post liquefaction volumetric strain of sand without fines as a function of factor of safety against

liquefaction or maximum shear strain. Large variations of the volumetric strain between 20% and 55% are predicted for the factor of safety against liquefaction of just less than one and the relative density of 30% (i.e. SPT's  $N$  of 3). Consequently, the accuracy of predicted additional foundation settlement may not be great.

## 7.6 Summary

A shallow foundation with an adequate static factor of safety may be capable of sustaining the additional loads caused by inertial forces induced by ground motion. Even so, very strong ground motion can change the critical failure mode, such that the bearing capacity may become mainly controlled by sliding resistance of soil. Very strong ground motion can also cause decrease of soil shear strength and stiffness in cyclic condition and soil liquefaction. In such cases, the following events may happen:

- Punching through type failures occur if the thickness of the top non-liquefied soil crust under foundation is not sufficient to sustain foundation load. A simple formula can be used to analyze this type of failure.
- Global rotational type failures occur during and after earthquakes when the incremental displacements are accumulated in one direction because of symmetric conditions (eg. heterogeneous soil beneath foundation, two closely adjacent buildings preventing free swaying of each of them) or soil liquefaction. One approach to the analysis of this type of failure is to use the same methods that are used for slope stability analyses.
- Large foundation settlements are caused by significant decrease of soil stiffness/liquefaction in cyclic condition. If no punching through type failure occurs then simple formulae can be used for assessment of additional foundation settlement. If punching through type failure occurs then foundation settlement is dependent on value of buoyancy force necessary to achieve equilibrium with the punched through soil volume.

# **Chapter 8**

## **Seismic Wave Propagation Effect on Tunnels and Shafts**

### **8.1 Introduction**

It may seem that underground structures are not at great seismic risk unless they are located within active faults or within liquefied soil zones. One might argue that such structures are confined within surrounding ground and that they follow the deformation of the surrounding ground. However, experience in the 1995 Hyogoken Nanbu (Kobe) earthquake shows this to be incorrect. The earthquake caused the failure of parts of the underground Daikai Station that was located away from an active fault, and where the ground did not experience soil liquefaction.

Dowding and Rozen (1978) studied the response of 71 tunnels in rock to earthquake motions. The damage ranged from cracking to closure in 42 cases. Sharma and Judd (1991) compiled a database on the response of 192 tunnels during 85 earthquakes throughout the world; 94 of the tunnels suffered from small to heavy damage. More than half the damage reported was caused by events that exceeded magnitude 7 of the Richter scale, and nearly 75% of the damage reported occurred within 50 km of the earthquake epicentre. There was no damage in tunnels where the horizontal peak ground acceleration was up to 0.2 g. In most cases where damage was reported, the peak ground accelerations were larger than 0.4 g. The data show that shallow tunnels are at greater risk during earthquakes than deeper tunnels; roughly 60% of the total cases had overburden depths less than 50 m and suffered some damage. Ground type is also important; 79% of the openings excavated in soil were reported to have suffered some damage.

The objective of this chapter is to describe simplified methods for analysis of tunnel and shaft response to ground motion.

### **8.2 Wave Propagation Effect on Cut and Cover Tunnels and Shafts**

Gazetas et al. (2005) performed 2D numerical analyses of the behaviors of the cut and cover station of Sepolia, the under construction tunneled station at Monastiraki and the temporary prestressed anchor piled wall at abandoned Kerameikos station

affected by the surface wave magnitude 5.9 Mount Parnitha earthquake in 1999. The peak accelerations measured at Sepolia station of 0.17 g at the station base and 0.43 g at the station roof were almost equal to the design accelerations calculated under the assumption that the station responds as an above ground structure. The successful performances of the temporary structures at Monastiraki and Kerameikos, which experienced ground surface peak accelerations of the order of 0.50 g, were explained by Gazetas et al. (2005) as a result of inherent flexibility of the wall in stiff soil, with shear wave velocity range from 350 to 720 m/s.

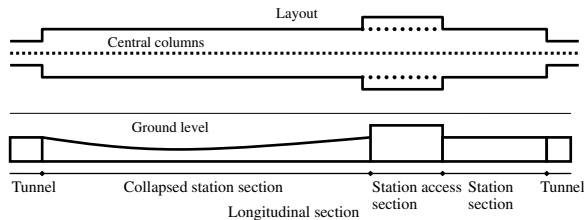
Huo et al. (2005) studied the collapse of the Daikai Station, a cut and cover structure in the subway system in Kobe, during the 1995 Hyogoken-Nanbu earthquake in Japan. The tunnel and access sections adjacent to the station, with similar structural characteristics and analogous soil conditions, did not collapse. Huo et al. (2005) conducted 2D dynamic finite element analyses by ABAQUS software package to investigate the load transfer mechanisms between the underground structure and the surrounding soil and to identify the causes for different behavior of similar sections subjected to the same seismic loading using a hysteretic nonlinear soil model. The model investigated two factors that influence the response of an underground structure: the relative stiffness between the structure and the degraded surrounding ground and the frictional characteristics of the interface. Huo et al. (2005) concluded that a stiff structure and a strong interface have beneficial effect on the structural behavior.

Srbulov (2007c) proposed a simplified analysis of wave amplitude effect on a cut and cover tunnel, and demonstrated the analysis for the case of the 1995 Daikai Station failure.

### ***8.2.1 Case Study of the Daikai Station Failure in 1995***

The station was built between 1962 and 1964 by cut and cover method in Kobe city in Japan. The station is located about 15 km from the epicentre of the Hyogoken-Nanbu earthquake with a moment magnitude of 6.9, which occurred at 5:46 a.m. on 17 January 1995 local time and date. The earthquake hypocentral depth was about 17.9 km, according to PEER database. According to this database, the two horizontal and vertical peak ground accelerations were  $2 \times 0.61$  g and 0.27 g respectively at Takatori station, which is located about 13 km from the epicentre of the Hyogoken-Nanbu earthquake. The peak horizontal displacements were in the range from 33 cm to 36 cm in the horizontal directions at Takatori station, with averaged ground shear wave velocity of 256 m/s in the upper 30 m below the ground surface according to PEER. During the earthquake, more than 30 columns of the central section of the Daikai station completely collapsed over a total length of about 110 m, which caused the failure of the overlying concrete roof slab and resulted in a 2.5 m subsidence on the road above the subway according to Huo et al. (2005).

**Fig. 8.1** Sketch of the layout and longitudinal section of the Daikai Station



The Daikai station contains three main parts: the main section of the station, which collapsed, the subway tunnels section and the station access section with two underground levels where no severe damage occurred, Fig. 8.1.

The collapse section consisted of a rectangular reinforced concrete box structure, which was 17 m wide and 7.17 m high, with central columns spaced at 3.5 m in the longitudinal direction. The columns were about 5.5 m high and had a rectangular reinforced concrete cross section of 0.4 m by 1.0 m. The columns in the failed section had 30 bars of 32 mm diameter in the axial direction and ties of 9 mm diameter spaced at 350 mm as transverse reinforcement. The compression tests on column's concrete specimen indicated strength values of about 39.7 MPa. The yield stress of the reinforcing steel was 235.2 MPa. The top of the concrete roof in this section was located about 4.8 m below the ground surface. The tunnel section consisted of a smaller rectangular reinforced concrete box structure 6.36 m high by 9.0 m wide, with a series of central columns with reinforced concrete cross section 0.4 m by 0.6 m spaced at 2.5 m. The top of the concrete roof in this section was located about 5.2 m below the ground surface. The station access section consisted of a reinforced concrete structure 10.12 m high and 26.0 m wide, with central columns identical to those in collapsed section. The top of the concrete roof in this section was located about 1.9 m below the ground surface according to Huo et al. (2005).

It is worth mentioning that the station section of the same cross section like the collapsed section but on the other side of the station access section did not collapse.

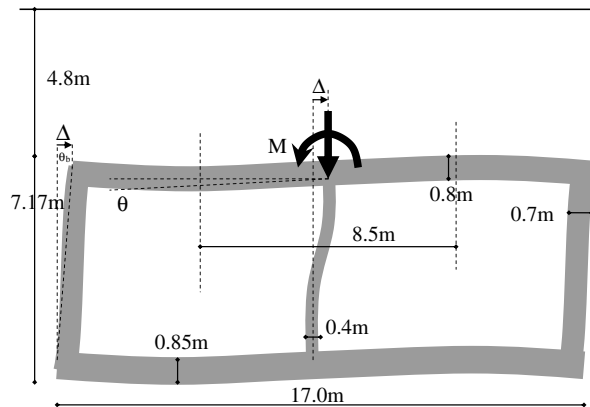
The site of the Daikai Station is composed of man made fill up to 2 m thick, soft Holocene alluvial deposits about 5–7 m thick and dense Pleistocene deposits down to the bedrock at several kilometers depth. The ground profile at the failed section was investigated by two boreholes. Transversal wave velocity is 120 m/s at 5 m depth, varies from 200 to 250 m/s at a depth range from 8 to 17 m, and linearly increases from 230 m/s at 17 m depth to 400 m/s at 30 m depth.

The station had a drainage system at the bottom slab. The ground water level was located at a depth of 6–8 m below the ground surface, which was 3–5 m lower than in 1959, prior to the construction of the station (e.g. Huo et al., 2005). Ground conditions have a significant influence on structural motion.

Deformed shape of the vertical section of Daikai station which failed is shown in Fig. 8.2.

Using CONAN software, Srbulov (2007c) obtained that the difference between the free field displacement and the structural displacement is minimal, i.e. a few

**Fig. 8.2** Envisaged displacements in cross section of the collapsed section of the Daikai Station magnified 10 times for clarity (Srbulov, 2007c, by permission of Patron Editor)



percent only. The horizontal displacement  $\Delta$  is estimated from the peak ground displacement of 0.36 m. A practical difficulty is the assessment of differential horizontal displacement along the station depth. For a shear wave velocity of about 200 m/s and the predominant period of  $2\pi/3 = 2.1$  s it follows that the wave length is  $200 \times 2.1 = 420$  m. The predominant circular frequency of 3 radians/s is inferred from the relative displacement spectrum at Takatori station (PEER). For the maximum wave amplitude of 0.36 m, it follows that the maximum differential displacement  $\Delta$  over the station height of 7.17 m could have been up to  $0.36 \times \sin[90^\circ \times 7.17 \times (0.25 \times 420)^{-1}] = 0.039$  m. An alternative would be to use SHAKE analyses to calculate differential horizontal displacements at the tunnel top and bottom.

From Fig. 8.2 and for  $\Delta = 0.039$  m it follows that the angle  $\theta_b = 0.039/7.17 = 0.0054$  radians. It is assumed that the rotation of the end of the central column was also 0.0054 radians. It is assumed that the vertical force on the central column is  $4.8 \times 8.5 \times 3.5 \times 19 \times (1 + 0.27) = 2713 + 732$  kN during seismic shaking. The maximum axial stress due to the vertical force is  $(2713 + 732) \times (0.4 \times 1.0)^{-1} \sim 8.6$  MPa, which is only 21.5% of the concrete yield strength of about 40 MPa. The bending moment  $M$  and transversal force  $T$  at the top of the column due to the horizontal displacement  $\Delta$  and rotation  $\theta_b$  are calculated according to Blake (1989) for a beam with fixed opposite end:

$$\begin{aligned} M_\Delta &= \frac{6 \cdot E \cdot I_a \cdot \Delta}{h_h^2}, & T_\Delta &= \frac{12 \cdot E \cdot I_a \cdot \Delta}{h_h^3} \\ M_\theta &= \frac{4 \cdot E \cdot I_a \cdot \theta_b}{h_h}, & T_\theta &= \frac{6 \cdot E \cdot I_a \cdot \theta_b}{h_h^2}, \end{aligned} \quad (8.1)$$

where  $E$  is Young modulus,  $I_a$  is the second moment of area, free column height  $h_h = 7.17 - 0.8 - 0.85 = 5.52$  m. For a homogenous cross section  $I_a = 1.0 \times 0.4^3 \times 12^{-1} = 0.0053$  m<sup>4</sup>. For Young modulus  $E = 2 \times 10^7$  kPa, it follows that  $M_\Delta =$

$793 \text{ kNm}$ ,  $T_\Delta = 287 \text{ kN}$ ,  $M_\theta = 415 \text{ kNm}$  and  $T_\theta = 113 \text{ kN}$ . For a homogeneous cross section it follows that the additional axial stress due to the bending moments is  $(793 + 415) \times 0.2 \times (0.0053)^{-1} = 45585 \text{ kPa}$ . The maximum summary axial stress is  $8.6 + 45.6 = 54.2 \text{ MPa}$ , which is about 135% of the concrete yield strength of 40 MPa.

For the subway running tunnel section, the same procedure results in  $\Delta = 0.034 \text{ m}$ ,  $\theta_b = 0.0054$  radians, the vertical force on the central column is  $5.2 \times 4.5 \times 2.5 \times 19 \times (1 + 0.27) = 1111.5 + 300 \text{ kN}$ , the maximum axial stress due to the vertical force is  $(1111.5 + 300)(0.4 \times 0.6)^{-1} \sim 5.9 \text{ MPa}$ ,  $M_\Delta = 428 \text{ kNm}$ ,  $T_\Delta = 155 \text{ kN}$ ,  $M_\theta = 250 \text{ kNm}$  and  $T_\theta = 68 \text{ kN}$  for  $h_h = 5.52 \text{ m}$ , the additional axial stress due to the bending moments is  $(428 + 250) \times 0.2 \times (0.0032)^{-1} = 42375 \text{ kPa}$  for a homogeneous cross section with  $I_a = 0.6 \times 0.4^3 \times 12^{-1} = 0.0032 \text{ m}^4$  and the maximum summary axial stress is  $5.9 + 42.4 = 48.3 \text{ MPa}$ , which is about 120% of the concrete yield strength of 40 MPa.

For the station access section, the same procedure results in  $\Delta = 0.054 \text{ m}$ ,  $\theta_b = 0.0054$  radians, the vertical force on the central column is  $1.9 \times 8.5 \times 3.5 \times 19 \times (1 + 0.27) = 1074 + 290 \text{ kN}$ , the maximum axial stress due to the vertical force is  $(1074 + 290)(0.4 \times 1.0)^{-1} \sim 3.4 \text{ MPa}$ ,  $M_\Delta = 473 \text{ kNm}$ ,  $T_\Delta = 111 \text{ kN}$ ,  $M_\theta = 269 \text{ kNm}$  and  $T_\theta = 47 \text{ kN}$  for  $h_h = 8.52 \text{ m}$ , the additional axial stress due to the bending moments is  $(473 + 269) \times 0.2 \times (0.0053)^{-1} = 28000 \text{ kPa}$  for a homogeneous cross section with  $I_a = 1.0 \times 0.4^3 \times 12^{-1} = 0.0053 \text{ m}^4$  and the maximum summary axial stress is  $3.4 + 28 = 31.4 \text{ MPa}$ , which is about 78% of the concrete yield strength of 40 MPa.

The calculated similar maximum axial stresses within the subway tunnel section, where no severe damage occurred, and within the main section of the station, which collapsed, does not necessarily mean that the simplified procedure used is incorrect. The same cross section like the collapsed section but on the other side of the station access section did not collapse. The localized damage to a part of the station could be the result of the fault directivity effect (Section 3.3.1), which may have caused an amplification of the ground motion within a limited area of the station.

Penzien (2000) presented an analytical procedure for evaluating the racking deformation of rectangular and circular tunnel linings caused by soil-structure interaction during a seismic event.

### 8.2.2 Case Study of a Ten Story Building in Mexico City

Case history for a shaft has not been found so far. Piled foundation is considered instead. Mendoza and Romo (1989) described the failure of a ten story building supported on piles through soft soil during the 1985 Michoacan earthquake with magnitude  $M_s = 8.1$  at an epicentral distance of 350 km from Mexico City. The peak acceleration of the record obtained at Ciudad Universitaria was only 0.035 g. However, Mexico City is situated partly on soft lake deposits, which likely amplified bedrock motion. Transversal wave velocities through the lake deposits vary in the

range from 30 m/s from 2.6 m below the ground surface to 75 m/s at 49 m depth, with exception of two stiffer layers at 28 to 29 m depth with transversal wave velocity of 150 m/s and 32 to 35 m depth with transversal wave velocity of 130 m/s according to Stephenson and Lomnitz (2005). They also indicated that the layer at 49 to 160 m depth has transversal wave velocity of 475 m/s. The top 2.6 m of soil above ground water level is hard crust with the transversal wave velocity likely comparable to the velocity of stiffer deep layers. The basement of the building was located at 2.6 m depth.

One-dimensional vertical wave propagation from the bedrock towards the ground surface in the free field is analyzed using SHAKE program. Change in the shear modulus and damping ratio of the soft deposits with shear strain is adopted according to Ovando-Shelley et al. (2003). SHAKE provided time histories of shear strain at specified depths. Horizontal displacements at these depths were calculated by the integration of the strain along depth.

According to engineering beam theory, bending moment  $M_b$  in beam and piles is

$$M_b = E \cdot I_a \cdot \frac{d^2 u}{dz^2}, \quad (8.2)$$

where  $E$  is Young modulus of pile material,  $I_a$  is the second moment of pile cross section area,  $d^2 u / dz^2$  is the second derivative of pile horizontal displacements. The second derivatives of the horizontal displacements are calculated along depth, as shown in Fig. 8.3. Larger  $M_b(EI_a)^{-1}$  ratios are evident at a depth of 2.6 m (where pile tops are located), at a depth of 6 m where the soil transversal wave velocity increases from 30 to 40 m/s and at a depth of 16 m where the soil transversal wave velocity increases from 40 to 50 m/s. These results are explained by seismic wave refraction at the boundaries of layers with different transversal wave velocities.

If it is assumed that the pile bending followed the ground bending then the maximum bending moment in the piles was about  $0.07 \times 2 \times 10^7 \times 0.5^4 \pi \times 64^{-1} = 1384 \text{ kNm}$ . The maximum compressive stress in the piles due to pile bending was

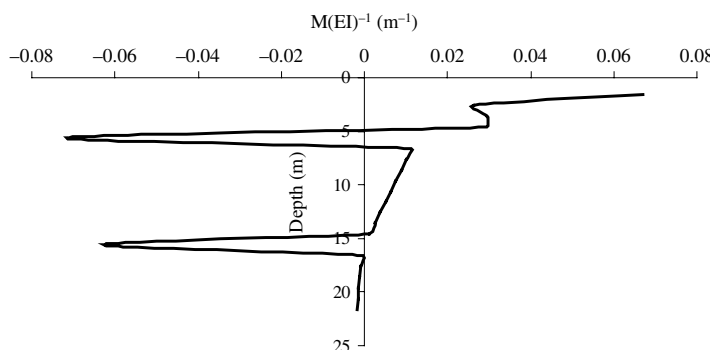


Fig. 8.3 The maximum values of the second derivatives of the horizontal displacements of soil

$1384 \times (0.5^3 \pi / 32)^{-1} = 1.1 \times 10^5$  kPa, which is extremely great. Therefore, it seems that the pile failures occurred in bending leading to a complete building toppling.

### 8.3 Wave Refraction Effect on Deep Tunnels and Shafts

The influence of wave refraction at the boundaries between two materials with significantly different transversal wave velocities is considered below for piled foundations. There is a lack of data for shafts and deep tunnels.

Mizuno (1987) documented a number of pile flexural failures at locations too deep to be caused by loading from pile top in soil that could not possibly have suffered a severe loss of strength due to liquefaction. Damage was associated with the presence of strong discontinuities in strength and stiffness of the soil profile, suggesting that relatively large local curvatures would be imposed on the piles by the surrounding soil as the soil deforms in association with the propagating seismic waves. Gazetas and Mylonakis (1998) concluded that the kinematic bending moment in piles depends on the following factors:

- The stiffness contrast between any two consecutive soil layers in the deposit, which can be represented by the ratio of the square of the respective shear wave velocities.
- The boundary conditions at the head of the pile cap, i.e. fixed or free head.
- The proximity of the excitation frequency to the fundamental (first) natural frequency of the soil deposit.
- The ratio between the depths measured from the top of the pile down to the interface of the layers with the sharpest stiffness contrast and the active length of the pile, beyond which a head-loaded pile behaves as an infinitely long beam. The approximate formula (eg. Poulos and Davis, 1980) for the active length  $L_a \sim 1.5(E_p E^{-1})^{1/4} d_p$ , where  $E_p$  and  $E$  are Young modulus of pile and soil respectively and  $d_p$  is pile diameter.

In fact, the bending of piles during earthquakes at the contact of two layers with different shear wave velocities can be explained considering wave refraction. Using Fermat's principle, Snell showed (e.g. Kramer, 1996) that the ratio between sinuses of the angle between the wave path and the normal to the interface between two layers and the velocity of longitudinal or transversal waves is constant. Snell's law indicates that waves traveling from higher velocity materials into lower velocity materials will be refracted closer to the normal of the interface (Fig. 8.4) and vice versa.

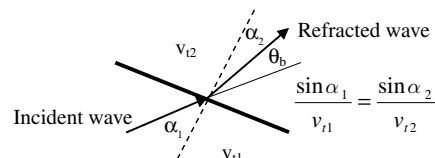


**Fig. 8.4** Constant ratios between the sinuses of angle to transversal wave velocities according to Snell's law

The angle  $\theta_b$ , which can be used in Equation (8.1) to calculate bending moment and transversal force in a pile, shaft or a deep tunnel, is simply a difference between the angles  $\alpha_1$  and  $\alpha_2$  of the wave paths on two sides of an interface. Practical difficulty is in determining the initial angle of wave propagation, which is dependent on the location of earthquake hypocentre and the shear wave velocity distribution along the hypocentral depth.

## 8.4 Summary

Tunnels and vertical shafts (as well as piles) are confined by surrounding ground and must experience similar displacements as the surrounding ground.

- Differential displacements and additional rotations, which are presumably caused by different ground wave amplitudes along wave propagation path at a time instant, of the columns of a cut-and-cover station section are calculated using simple formulae. Simple formulae are also used for calculation of additional stresses within the columns that failed at the Daikai station in 1995.
- The effect of different transversal wave velocities (shear stiffnesses) of horizontal layers on bending moments of piles is considered using the results of SHAKE computer program for the soil and piles that failed under a ten story building in Mexico city during the 1985 Michoacan earthquake.
- The change of angle of propagation of ground waves (wave refraction) when waves arrive inclined to the interface between materials with different transversal wave velocities is calculated using a simple formula.

# **Chapter 9**

## **Comments on Some Frequent Liquefaction Potential Mitigation Measures**

### **9.1 Introduction**

Potentially liquefiable sand can be treated to eliminate or decrease its liquefaction potential or the effects of sand liquefaction (such as flow failure, excess pressure on structures and additional structural displacements) can be accommodated because the triggering factor for sand liquefaction, i.e. earthquake, cannot be controlled. Many mitigation measures, which are aimed at increasing sand density i.e. its shear strength, increasing its permeability and/or decreasing its degree of saturation, exist (e.g. Kramer, 1996, Schaefer et al., 1997). Comments are made in this chapter on some of the more frequently used methods.

### **9.2 Stone Columns**

Stone columns, with 0.7 m to 1 m diameter and down to 20 m depth, performed satisfactorily during and after a number of strong earthquakes in western United States and Japan (e.g. Port and Harbor Research Institute, Ministry of Transport, Japan, 1997).

Stone columns are usually constructed by vibratory probes, which penetrate ground under self-weight, usually aided by water jetting. Horizontal vibrations of the probe are induced by rotating eccentric weights mounted on a shaft driven by a motor housed within the casing. The probe displaces and densifies sand along its penetration depth. Stone backfill is introduced in controlled batches, either from the surface down the annulus created by penetration of the probe or through feeder tubes directed to the tip of the probe. Re-penetration of each stone backfill batch forces the stone radially into the surrounding soil, forming a vibro-stone column that is tightly interlocked with the soil in a system which has lower compressibility, higher shear strength and permeability than natural soil (e.g. Schaefer et al., 1997).

Despite extensive research and development concerning stone columns, field trials are still the best and most reliable method for the column design. Because stones are frequently displaced within soil matrix, the standard and cone penetration tests are difficult to perform to the full depth of the columns. Measurement of transversal

wave velocity after the column installation is an efficient way for construction quality control and to check that liquefaction potential has been eliminated.

Correlations between transversal wave velocity and the soil resistance to liquefaction are still under development. Andrus and Stokoe (1997, 2000) compiled a chart similar to Fig. 5.2. The transition between liquefied and non-liquefied zone is rather steep at the transversal wave velocity of about 200 m/s. The chart shown in Fig. 5.2 may be used when  $(N_1)_{60}$  is calculated from Equation (6.56) or similar or taken from Table 3.1 of Eurocode 8, Part 1 (2004).

### 9.3 Soil Mixing

Stone columns in soil with over 20% fines are not as efficient as stone columns in sand. Soil-cement grid walls were effective in preventing ground liquefaction and accompanying lateral flow during major earthquakes (e.g. Schaefer et al., 1997).

Soil mixing with cementitious materials is achieved by mixing shafts consisting of auger cutting heads (usually 0.5 m to 4 m in diameter and down to 20 m depth), discontinuous auger flights and mixing paddles. As the mixing augers are advanced into soil, grout is pumped through their stems and injected into soil at their tips. The grout is thoroughly mixed with soil by the auger flights and mixing paddles. At desired depth, the augers are withdrawn with continuous mixing to achieve a continuous column of higher strength and stiffness than natural ground. A variant of mechanical soil mixing is jet grouting where soil is mixed with cement grout injected horizontally through rotated nozzle under high pressure in a previously drilled borehole (e.g. Kramer, 1996).

For whole soil mass mixtures that are not located under structures, the minimum uniaxial compressive strength  $S_u$  of the samples taken from mixed soil should be greater than twice the radius  $r_{MC}$  of the Mohr – Coulomb circle defined by Equation (9.1) based on Fig. 9.1 and multiplied by a factor of safety. For soil mixtures that are located under structures, the cyclic shear stress  $\tau$  induced by the structure should be used instead.

$$r_{MC} = \sqrt{\tau^2 + \frac{\sigma_v'^2}{4} \cdot (1 - K'_o)^2}, \quad (9.1)$$

where shear stress  $\tau$  is determined from Equation (5.1),  $\sigma_v'$  is effective overburden pressure at a depth,  $K'_o$  is coefficient of soil lateral pressure (typically approximated

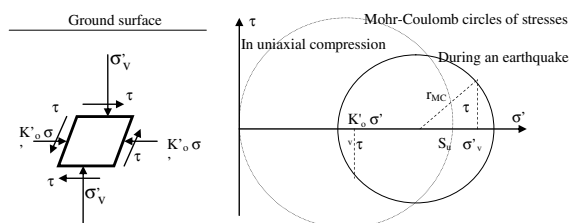


**Fig. 9.1** Stresses acting on an element of soil at depth during an earthquake and corresponding Mohr-Coulomb circles of stresses

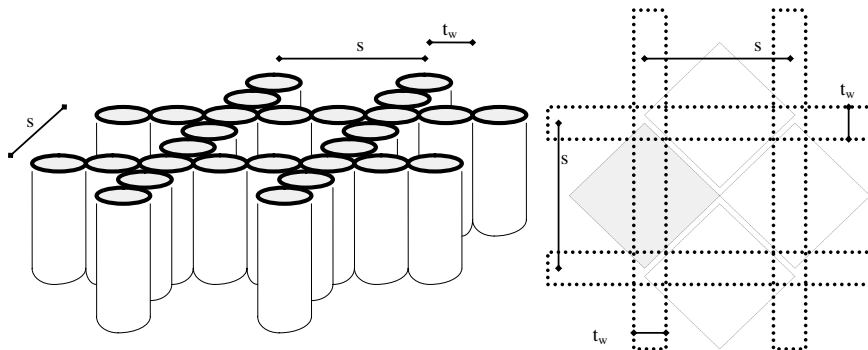


**Fig. 9.2** A slant view of soil-cement grid walls and the square areas of soil stabilized by each walls

as  $1 - \sin \phi'$  following simplified expression by Jaky (1944), for normally consolidated soils, where  $\phi'$  is soil friction angle.

When soil is stabilized by cement in ground that is rich in sulphate salts, or with water rich in these salts, then sulphate resistant cement must be used in place of ordinary Portland cement. This is to avoid shear strength loss due to sulphate attack (e.g. Rollings et al., 1999), and stiffness degradation including swelling (e.g. Puppala et al. 2004). Lime stabilized soil can also suffer from similar damage caused by chemical reactions in sulphates rich soil or water (e.g. Sivapullaiah et al., 2000).

For cost effectiveness, soil-cement grid walls are used instead of whole soil mass mixing, Fig. 9.2.

The minimal uniaxial compressive strength  $S_u$  of the samples taken from soil-cement walls must be greater than the strength of whole soil mass mixture for the ratio  $0.5 s t_w^{-1}$ . The contribution of shear strength of soil between the walls should not be considered because the peak shear strengths of soil between the walls is activated at much larger shear strains than the peak shear strength of soil-cement mixture as indicated in Fig. 4.2. If soil between the walls exhibits full shear stress  $\tau$  then it liquefies.

## 9.4 Excess Water Pressure Relief Wells

The relief wells should dissipate excess pore water pressure  $\Delta u$  as sand volcano does, Fig. 3.22. The excess pore water pressure build-up is caused by increase in confining stresses.

A pore pressure ratio  $r_u = \Delta u \sigma'^{-1}$  according to Equation 2.11, when the friction angles in cyclic conditions  $\phi$  are obtained from Fig. 5.6 to 5.8, is shown in Fig. 9.3.

The time of the excess pore water pressure build-up is assumed to be equal to the duration of the equivalent harmonic cycle described in Section 2.5. Dissipation of excess pore water pressure in time in the vertical direction is assumed to be according to Terzaghi's (1925) theory of primary consolidation. The theory involves the following assumptions:

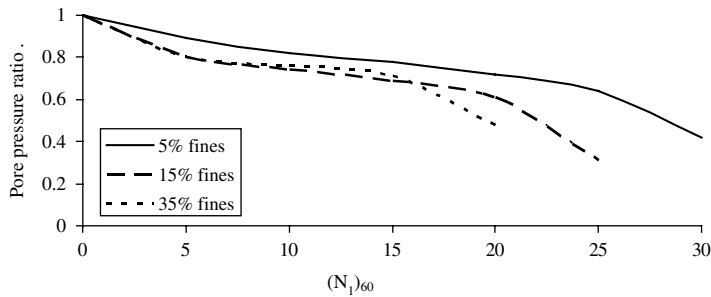


**Fig. 9.3** Excess pore water pressure ratios versus  $(N_1)_{60}$  from SPTs based on Figures 5.5 to 5.7

- Soil is homogeneous and saturated.
- Soil compression in the vertical direction only is caused by squeezing out of water from the voids.
- Ground water discharge velocity  $v$  is proportional to the product of the hydraulic gradient  $i$  and coefficient of permeability  $k$  (Darcy's law).
- The coefficient of consolidation  $c_v = k(\gamma_w m_v)^{-1}$  is constant, where  $k$  is coefficient of permeability of soil,  $\gamma_w$  is unit weight of water,  $m_v$  is coefficient of volume compressibility of soil.

The method is described in many text books. The governing equation is

$$\frac{\partial u_t}{\partial t} = \frac{k}{\gamma_w \cdot m_v} \cdot \frac{\partial^2 u_t}{\partial z^2}, \quad (9.2)$$

where  $u_t$  is excess pore water pressure at time  $t$  and depth  $z$ ,  $k$  is the coefficient of permeability of soil in Darcy's Law (units of velocity),  $\gamma_w$  is the unit weight of water (usually taken as  $9.81 \text{ kN/m}^3$  or  $10 \text{ kN/m}^3$  in earth's gravity), and  $m_v$  is coefficient of volume compressibility of soil (units of strain/stress). For the boundary conditions:

- $u_t = \Delta u$  at any depth and at time  $t = 0$ , where  $\Delta u$  is the excess pore water pressure caused by the earthquake.
- $u_t = 0$  at  $z = 0$ , at the top at time  $t > 0$ .
- $u_t = 0$  at  $z = 2H$  at time  $t > 0$  where  $2H$  is the thickness of liquefied layer when that layer is bounded above and below by freely drainable materials, within which the excess pore pressures are effectively zero and unaffected by the earthquake. In any other case,  $H$  is the length of the longest path of excess pore water pressure dissipation.

The excess pore water pressure at any depth  $z$  at any time  $t$  is (e.g. Simons and Menzies, 1977)

$$u_t = \frac{4 \cdot \Delta u}{\pi} \sum_{m=0}^{m=\infty} \frac{(-1)^m}{2 \cdot m + 1} \cdot e^{-(2 \cdot m + 1)^2 \cdot \pi^2 \cdot T_v / 4} \cdot \cos \left[ \frac{(2 \cdot m + 1) \cdot \pi \cdot (H - z)}{2 \cdot H} \right], \quad (9.3)$$

where the time factor  $T_v = c_v t H^{-2}$ . Degree of consolidation  $U_z$  at any depth  $z$  is defined as  $U_z = 1 - u_t(\Delta u)^{-1}$ .

For radial pore pressure dissipation due to presence of pressure relief wells, Equation (9.1) can be written as

$$\frac{\partial u_t}{\partial t} = c_{vr} \cdot \left( \frac{\partial^2 u_t}{\partial d_r^2} + \frac{1}{d_r} \cdot \frac{\partial u_t}{\partial d_r} \right), \quad (9.4)$$

where  $u_t$  is excess water pressure at time  $t$ ,  $d_r$  is radial distance measured from centre of the well,  $c_{vr} = k_h (m_v \gamma_w)^{-1}$ ,  $k_h$  is the coefficient of permeability of soil in the horizontal direction. For the solution of Equation (9.4), the following boundary conditions are used, Fig. 9.4:

- $u_t = \Delta u$  at any radial distance and at time  $t = 0$ .
- $u_t = 0$  at  $d_r = r_w$  ( $r_w$  is the radius of the well) at time  $t > 0$ .
- $\partial u_t / \partial r = 0$  at  $d_r = r_e$  ( $r_e$  is a half of the distance  $d_e$  between wells centre to centre).

Barron (1948) solved the problem of equal strain consolidation with no smear. The excess pore water pressure  $u_t$  at any time  $t$  and at radial distance  $r$  is

$$u_t = \frac{4 \cdot \Delta u \cdot \exp \left( -8 \cdot T_r / F_n \right)}{d_e^2 \cdot F_n} \left[ r_e^2 \cdot \ln \left( \frac{d_r}{r_w} \right) - \frac{d_r^2 - r_w^2}{2} \right]$$

$$T_r = \frac{c_{vr} \cdot t}{d_e^2}$$

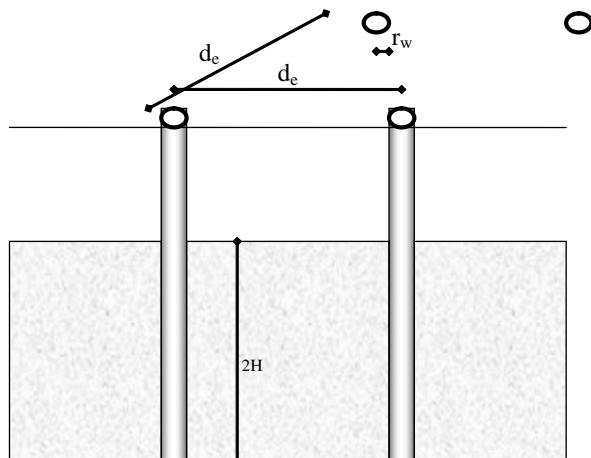


**Fig. 9.4** Cross section and layout of pressure relief wells

$$F_n = \frac{r_r^2}{r_r^2 - 1} \cdot \ln(n) - \frac{3 \cdot r_r^2 - 1}{4 \cdot r_r^2}$$

$$r_r = \frac{r_e}{r_w}, \quad (9.5)$$

where the symbols used in Equation (9.5) are defined above. The degree of consolidation  $U_r$  due to radial drainage  $U_r = 1 - u_t(\Delta t)^{-1}$ . Carrillo (1962) defined the overall degree of consolidation when dissipation of excess pore water pressure takes place in both the vertical and radial direction simultaneously  $U = 1 - (1 - U_z)(1 - U_r)$ . When liquefaction occurs then  $U = 0$ .

Absence of liquefaction does not mean absence of large deformations. Also, pressure relief wells can become clogged in time by bacteria and algae grow or by siltations from surrounding soil when ground water level oscillates in time.

#### 9.4.1 An Example for Pressure Relief Wells

In the example given in the Handbook on Liquefaction Remediation of Reclaimed Land by the Port and Harbor Research Institute, Ministry of Transport, Japan (A.A. Balkema, Rotterdam, 1997)  $r_u = 0.2$ , the equivalent time to attain liquefaction is 5 s, the coefficient of soil permeability is  $3 \times 10^{-4}$  m/s, the coefficient of soil compressibility  $m_v = 3 \times 10^{-5}$  m<sup>2</sup>/kN, i.e.  $c_v = k(\gamma_w m_v)^{-1} = 1$  m<sup>2</sup>/s, the coefficient of drain permeability is 0.1 m/s, the well radius  $r_w = 0.3$  m, the well depth  $H = 10$  m. From the design charts given in the handbook, the well spacing  $d_e = 1.5$  m.

The simplified procedure in Appendix A.12, based on Equations (9.3) and (9.5), indicates greater than 95% degree of consolidation at any time and consequently no liquefaction occurrence. For layered soil, the computer program FEQDrain (<http://nisee.berkeley.edu/elibrary/Software/FEQDRAIN.ZIP>) described by Pestana et al. (1997) could be used.

## 9.5 Summary

Some frequently used methods for elimination or minimization of liquefaction potential are commented on in this section.

- Stone columns are used when the amount of fines (particles with diameter less than about 0.005 mm) does not exceed about 20%. The method of installation of stone columns tends to increases the density of natural soil and therefore its resistance to liquefaction. Increased stiffness and water permeability of column-soil system contribute to increased safety.
- Soil mixing with cement is used when the amount of fines (particles with diameter less than about 0.005 mm) exceeds about 20%. Increased shear strength of mixed soil can sustain shear stresses induced by earthquakes. Sulphate resistant

cements must be used in soil and ground water containing soluble sulphate salts, which are aggressive to ordinary Portland cement.

- Excess pore water pressure relief wells are used when other methods are not appropriate. Well functionality is affected by a number of factors, such as soil coefficient of water permeability/ soil compressibility and drain clogging/ silting in time, which may not be well known or controlled.

# Appendices – Microsoft Excel Workbooks on Compact Disk

The MS Excel spreadsheet format is used for maximum portability. Microsoft provides MS Excel viewer free of charge at its Internet web site.

The spreadsheets are kept as simple as possible.

If MS Excel complains at the start about the security level of macros please click on Tools then Macro then Security button and adjust the security level to at least medium. The spreadsheet must be exited and re-entered for the change made to take place.

The spreadsheets are applicable to the case studies and examples considered in this monograph.

## A.1 Coordinates of Earthquake Hypocentre and Site-to-Epicentre Distance

The coordinates x, y, z are calculated by solution of three equations:

$$(x - x_i)^2 + (y - y_i)^2 + (z - z_i)^2 = d_i^2, \quad (\text{A.1.1})$$

where  $x_i$ ,  $y_i$ ,  $z_i$  are coordinates of seismograph stations,  $i = 1\dots3$ ,  $d_i$  is the source to station distance calculated from Equation (1.1). Depending on the orientation of the vertical  $z$  axis, the hypocentral depth could have positive or negative sign. A view of the spreadsheet results is shown below (Fig. A1.1).

The site to epicentre distance in km and azimuth (the angle measured clockwise from North direction) between them are calculated from the formulae

$$\begin{aligned} \text{Distance} &= 111 \cdot \frac{180}{\pi} \cdot \text{Atn} \left( \frac{\sqrt{1 - [\sin(EN)* \sin(SN) + \cos(EN)* \cos(SN)* \cos(SE-EE)]^2}}{\sin(EN)* \sin(SN) + \cos(EN)* \cos(SN)* \cos(SE-EE)} \right) \\ \text{Azimuth} &= \text{Arc sin} \frac{\cos(SN)* \sin(SE-EE)}{\sin \left( \frac{\text{Distance} \cdot \pi}{111 \cdot 180} \right)}, \end{aligned} \quad (\text{A.1.2})$$

where  $EN$  and  $EE$  are the northings and eastings (in degrees) of an earthquake epicentre,  $SN$  and  $SE$  are the northings and eastings (in degrees) of a seismic station. For

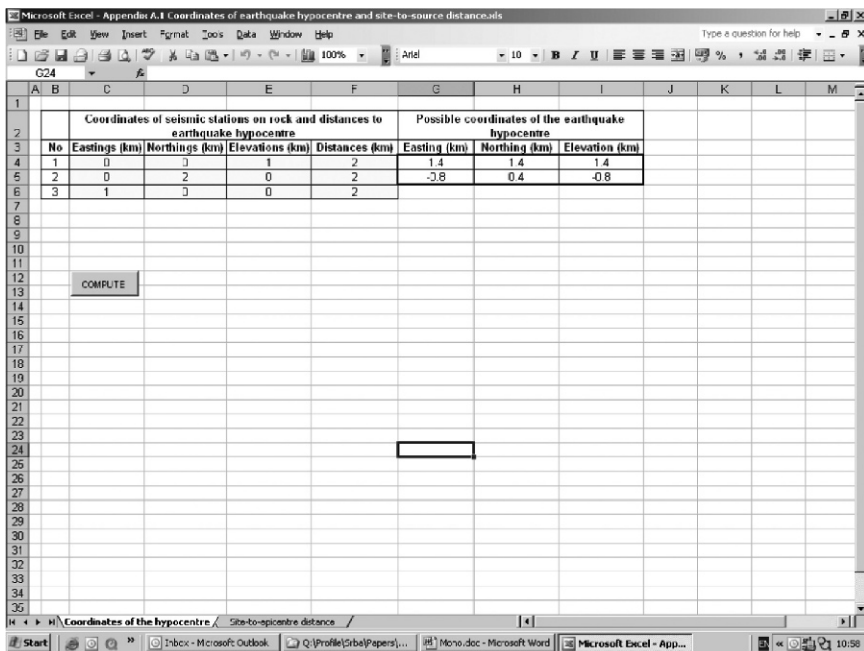


Fig. A1.1 Spreadsheet ‘Coordinates of the hypocentre’ in workbook Appendix A.1

distance and azimuth between two stations, it is simply necessary to input the station northings and eastings in place of those data for an earthquake. Equation (A.1.2) is valid when the differences between two locations on Earth’s surface (stations or epicentres) does not exceed geographical  $12^\circ$ , in which case Earth’s curvature has to be taken into account. A view of the spreadsheet results is shown below (Fig. A1.2).

## A.2 Limit Equilibrium Method for Northolt Slope Stability

The Excel macro solves  $2n_w - 1$  equations of equilibrium of forces in the horizontal and vertical direction and  $n_w$  equations of equilibrium of the rotating moments, where  $n_w$  is the number of wedges into which a potential sliding mass is subdivided. From Fig. 4.1 it follows for the horizontal  $x$  direction:

$$\sum_{i=1}^{n_w} N_i \sin \alpha_i - T_i \cos \alpha_i + N_{n+i-1} \cos \alpha_{n+i-1} - T_{n+i-1} \sin \alpha_{n+i-1} - N_{n+i} \cos \alpha_{n+i} + T_{n+i} \sin \alpha_{n+i} + c_h W_i + F_{xi} + GW_i \sin \alpha_i + GW_{i-1} \cos \alpha_{n+i-1} - GW_{i+1} \cos \alpha_{n+i} = 0 \quad (\text{A.2.1})$$

Microsoft Excel - Appendix A.1 Coordinates of earthquake hypocentre and site-to-source distance.xls												Type a question for help	X	X	X	X
	A	B	C	D	E	F	G	H	I	J	K	L	M	N	O	P
1																
2	Epicentral latitude				10	geographic degrees										
3	Epicentral longitude				25	geographic degrees										
4																
5	Seismic station latitude				11	geographic degrees										
6	Seismic station longitude				25	geographic degrees										
7																
8	Site-to-epicentre distance				155.7	kilometres										
9	Site-to-epicentre azimuth				44.43	degrees										
10																
11																
12																
13																
14																
15	COMPUTE															
16																
17																
18																
19																
20																
21																
22																
23																
24																
25																
26																
27																
28																
29																
30																
31																
32																
33																
34																
35																
36																

Fig. A1.2 Spreadsheet ‘Site-to-epicentre distance’ in workbook Appendix A.1

For the vertical  $y$  direction:

$$\sum_{i=1}^{n_w-1} -N_i \cos \alpha_i - T_i \sin \alpha_i + N_{n+i-1} \sin \alpha_{n+i-1} + T_{n+i-1} \cos \alpha_{n+i-1} \\ - N_{n+i} \sin \alpha_{n+i} - T_{n+i} \cos \alpha_{n+i} + (1 \pm c_{vm}) W_i + F_{yi} - GW_i \cos \alpha_i \\ + GW_{i-1} \sin \alpha_{n+i-1} - GW_{i+1} \sin \alpha_{n+i} = 0 \quad (\text{A.2.2})$$

For the moments around the centroids of wedges:

$$\sum_{i=1}^{n_w} N_i d_{n_i} + T_i d_{t_i} + N_{n+i-1} d_{n_{n+i-1}} + T_{n+i-1} d_{t_{n+i-1}} + N_{n+i} d_{n_{n+i}} + T_{n+i} d_{t_{n+i}} \\ + F_{xi} d_{fxi} + F_{yi} d_{fyi} + GW_i d_{wi} + GW_{i-1} d_{w_{n+i-1}} + GW_{i+1} d_{w_{n+i}} = 0, \quad (\text{A.2.3})$$

where  $d_{n,tf,w}$  are the shortest distances between the lines of actions of the forces and wedge centroids.

The procedure starts with a factor of safety of 1, calculates all axial and transversal forces along wedge boundaries and checks the  $n_w^{\text{th}}$  equation of equilibrium of

forces in the vertical direction. If the absolute value of the sum of all vertical forces acting on the  $n_w^{th}$  wedge is greater than 2% of the  $n_w^{th}$  wedge weight then the factor of safety is increased by 0.5 and the checking procedure continued. If after 15 checks the sign of the sum of all vertical forces acting on the  $n_w^{th}$  wedge has not been changed then the slope is considered unstable. If the sign of the sum of all vertical forces acting on the  $n_w^{th}$  wedge has been changed during stepping procedure then the last considered factor of safety is decreased by 0.05 until the absolute value of the sum of vertical forces acting on the  $n_w^{th}$  wedge is smaller than 2% of the  $n_w^{th}$  wedge weight.

The axial forces at the bases of wedges are assumed at the centers of the bases except at the base of the last wedge and therefore the turning moments of the axial forces with respect to the centers of the bases are zero (shown as blanks).

When a local factor of safety equals to 1.00 then shown number of steps of soil shear strength drops below the peak strength equals to the number of degrees below soil peak friction angle. Similarly, the peak cohesion value is decreased for the number of steps of strength drops times the difference between the peak and residual cohesion over the difference between the peak and residual friction angle.

A number of iterations to define local factors of safety are performed at each step because of a recursive dependence of the rate of joint thickness change ( $dt_{j,e}\gamma_{j,e}^{-1}$ ) on local factor of safety  $F_j$  (i.e. the number of steps of strength drop below the peak value) and the local factor of safety  $F_j$  on the rate of joint thickness change (i.e. on  $\gamma_{j(i),e}$  in Equation 4.8, where  $\gamma_{j(i),e} = dt_{j(i),e}(\tan\alpha_{j(i)})^{-1}$ ). A view of the spreadsheet results is shown below (Fig. A2).

### A.3 Single Wedge for Three-Dimensional Slope Stability

The spreadsheet provides:

- Factor of safety against sliding of the wedge with/ without external resultant load and anchor (cable) resultant force
- Factor of safety and most unfavorable azimuth and dip angle for given resultant external load
- Minimal resultant anchor (cable) force and most favorable azimuth and dip angle for required factor of safety

Critical acceleration acting on the wedge is determined by trial and error until the factor of safety against sliding of the wedge equals to 1.0 under applied resultant external load. A view of the spreadsheet results is shown below (Fig. A3).

Joint No	Axial force, N (kN)	Transversal force, T (kNm)	Torsion moment, M (Nm)	M/N (m)	Local factor of safety	Number of steps of strength drops	COMPUTE	Step No	Number of iterations	Imbalanced force Y (kN)	Average factor of safety
2	1	370	1013		0.32	1.00		1	7	-1304.5	1.06
2	2	8913	2211		0.32	1.00		2	36	33.3	
4	3	8214	2050		0.25	1.00		3	36	8.4	
5	4	1226	256		0.27	1.00					
5	5	1179	2191		0.20	1.00					
7	6	71922	203.04	2119.66	2.35	0.49	1.00				
8	7	2372	3145	1673	0.71	1.33	1.00				
9	8	6098	2305	10372	1.73	0.38	1.48				
10	9	10541	3232	21647	2.07	0.31	1.24				
11	10	15556	3567	36935	2.29	0.23	1.49				
12	11	20559	6373	61877	2.59	0.27	1.01				
13											
14											
15											
16											
17											
18											
19											
20											
21											
22											
23											
24											
25											
26											
27											
28											
29											
30											
31											
32											
33											
34											
35											
36											
37											
38											
39											
40											
41											
42											
43											
44											
45											
46											

Fig. A2 Spreadsheet ‘Results’ in workbook Appendix A.2

## A.4 Co-Seismic Sliding Block

The spreadsheets performs double integration in time of the difference between the base and critical acceleration of a sliding block in order to calculate permanent block sliding at time intervals (whenever the base acceleration exceeds the critical acceleration) and to calculate cumulative permanent block sliding. Down slope and level ground sliding can be considered. A view of the spreadsheet results is shown below (Fig. A4).

## A.5a Post-Seismic Sliding Blocks for Maidipo Slip in Frictional Soil

The formulae used for the calculation are given in Appendix B of the paper by Ambraseys and Srbulov (1995). A view of the spreadsheet results is shown below (Fig. A5a).

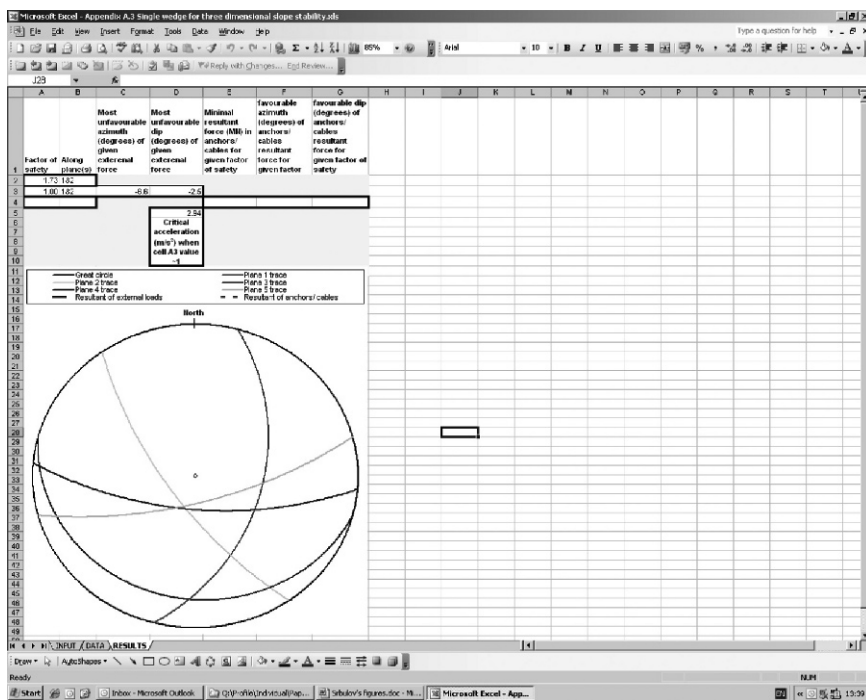


**Fig. A3** Spreadsheet ‘Results’ in workbook Appendix A.3

### A.5b Post-Seismic Sliding Blocks for Catak Slip in Cohesive Soil

The formulae used for the calculation are given in Appendix A of the paper by Ambraseys and Srbulov (1995). A view of the spreadsheet results is shown below (Fig. A5b).

### A.6 Bouncing Block Model of Rock Falls

A view of the spreadsheet results is shown below (Fig. A6).

### A.7 Simplified Model for Soil and Rock Avalanches, Debris Run-Out and Fast Spreads

A view of the spreadsheet results is shown below. No macros are used for the calculations (Fig. A7).

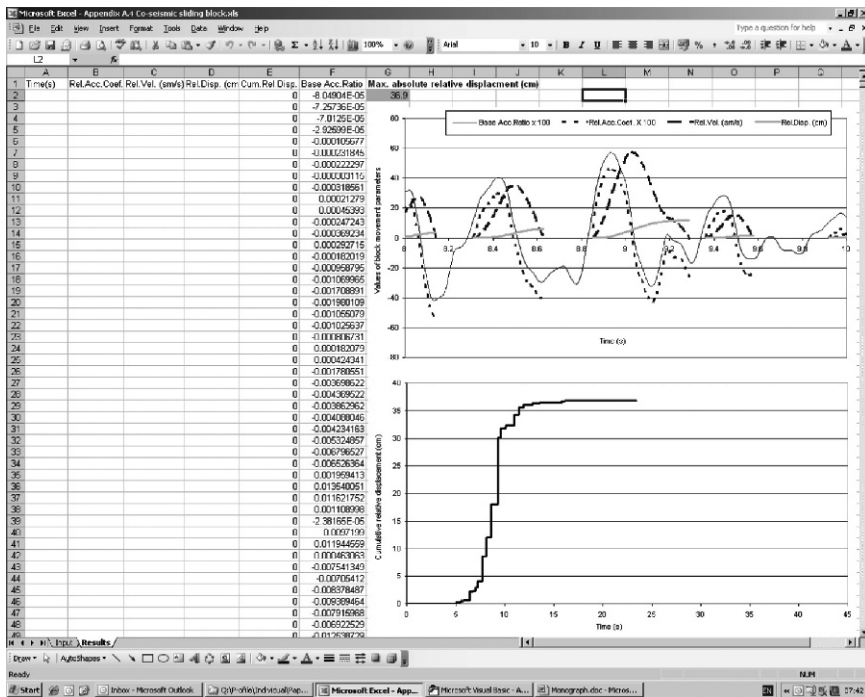


Fig. A4 Spreadsheet 'Results' in workbook Appendix A.4

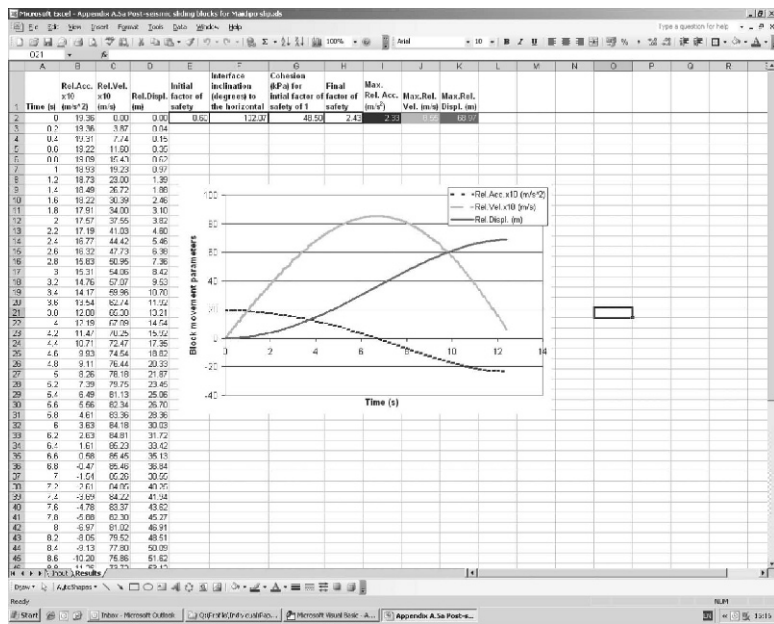


Fig. A5a Spreadsheet 'Results' in workbook Appendix A.5a

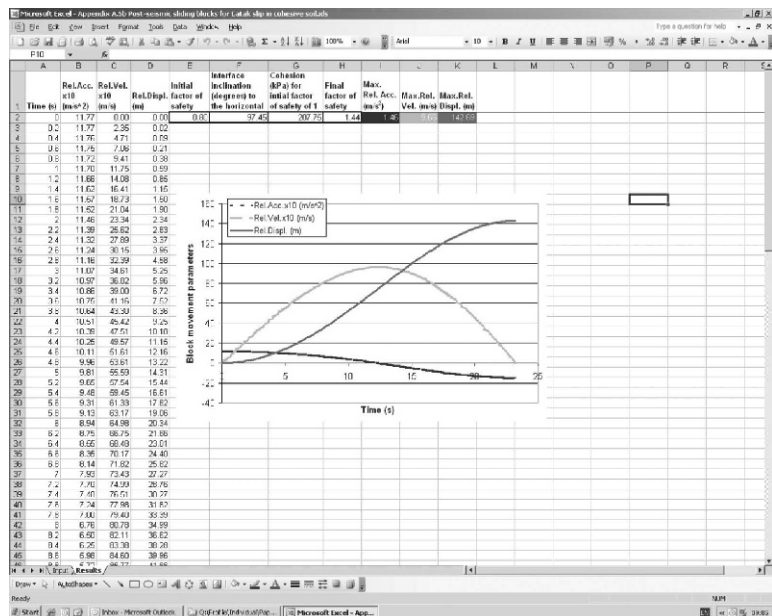


Fig. A5b Spreadsheet 'Results' in workbook Appendix A.5b

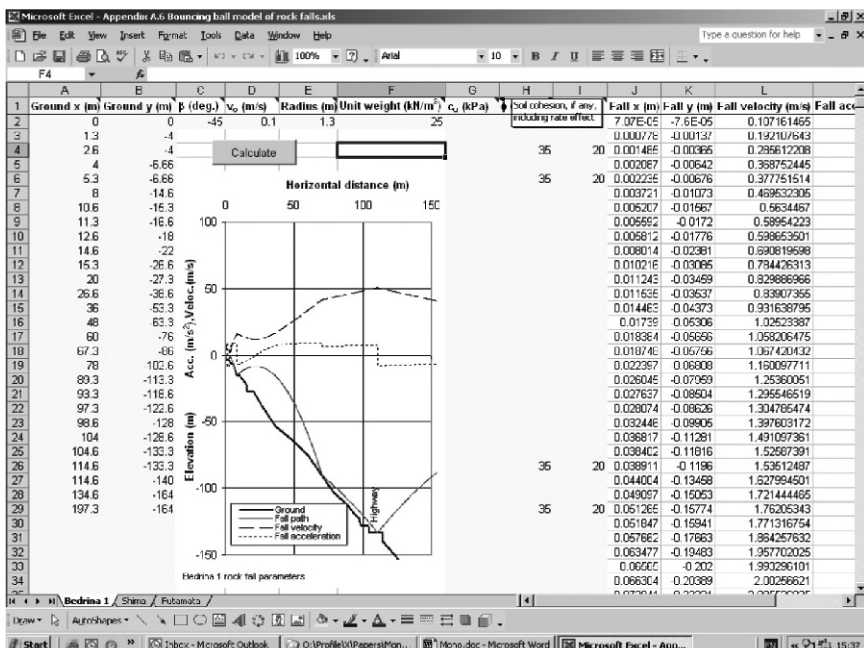
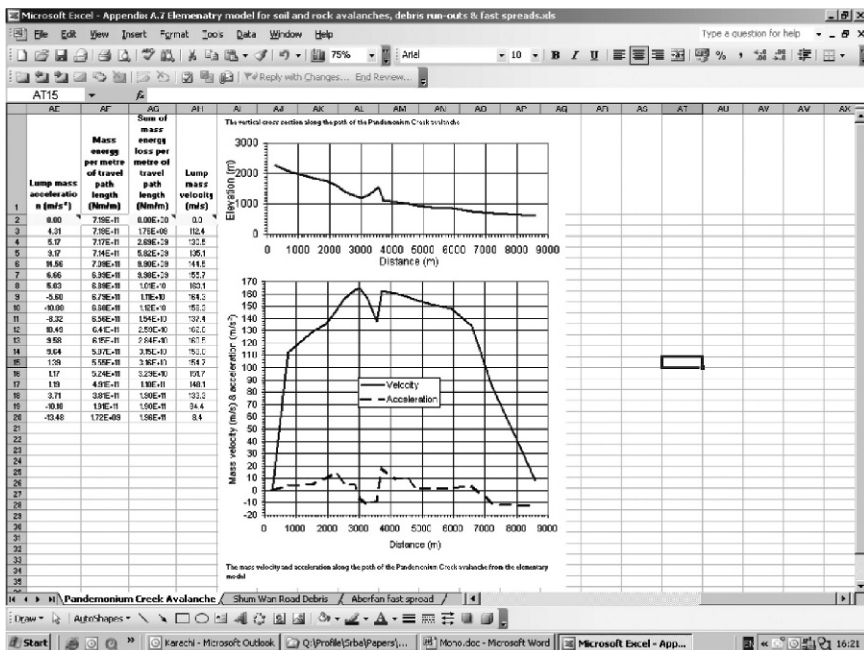


Fig. A6 Spreadsheet 'Bedrina 1' in workbook Appendix A.6

@Seismicisolation



**Fig. A7** Spreadsheet ‘Pandemonium Creek Avalanches’ in workbook Appendix A.7

## A.8 Closed-Form Solution for Gravity Walls

A view of the spreadsheet results is shown below (Fig. A8).

### A.9a Time Stepping Procedure for Kobe Wall

A view of the spreadsheet results is shown below (Fig. A9a).

### A.9b Time Stepping Procedure for Kalamata Wall

A view of the spreadsheet results is shown below (Fig. A9b).

## A.10 Accelerogram Averaging and Acceleration Response Spectra

The averaging is performed according to Equation (6.57). A view of the spreadsheet results is shown below (Fig. A10.1).

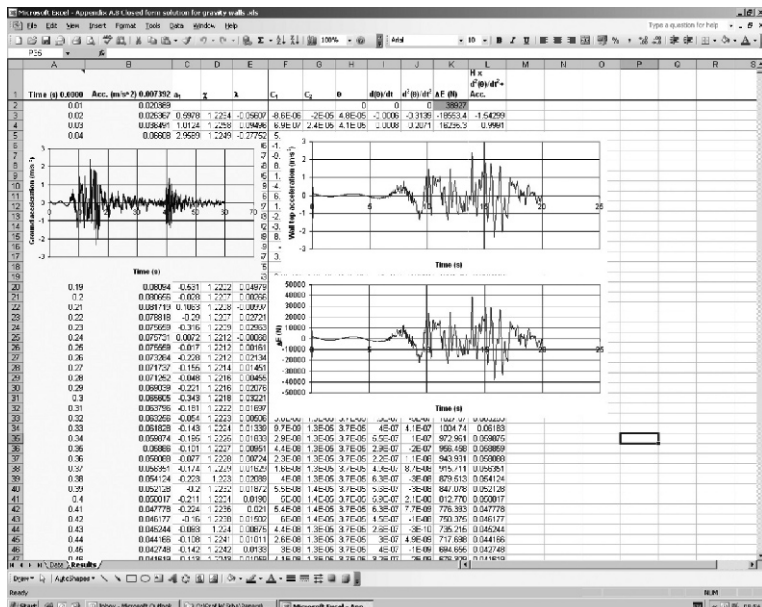


Fig. A8 Spreadsheet ‘Results’ in workbook Appendix A.8

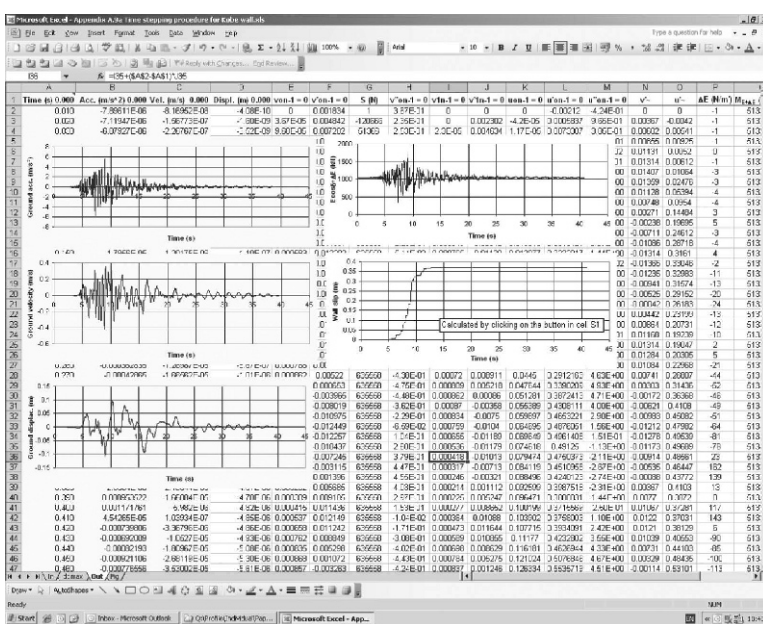


Fig. A9a Spreadsheet ‘Out’ in workbook Appendix A.9a

## Appendices

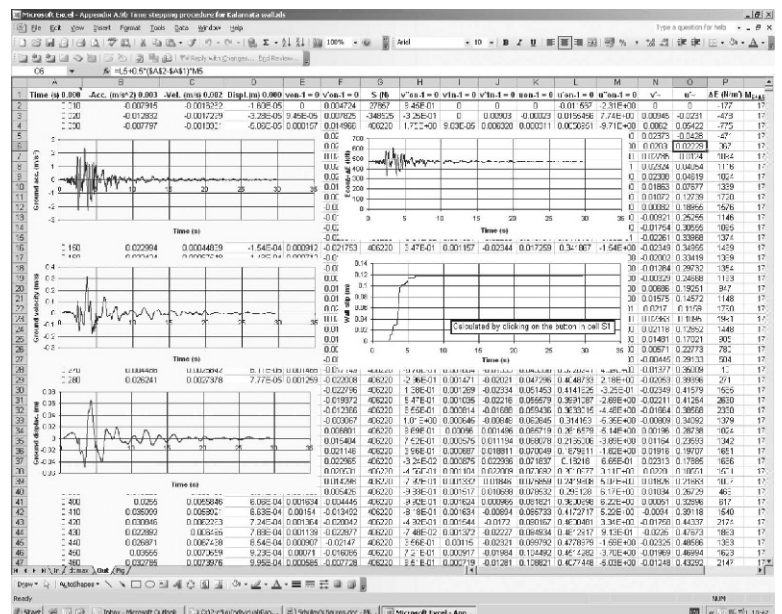


Fig. A9b Spreadsheet ‘Out’ in workbook Appendix A.9b

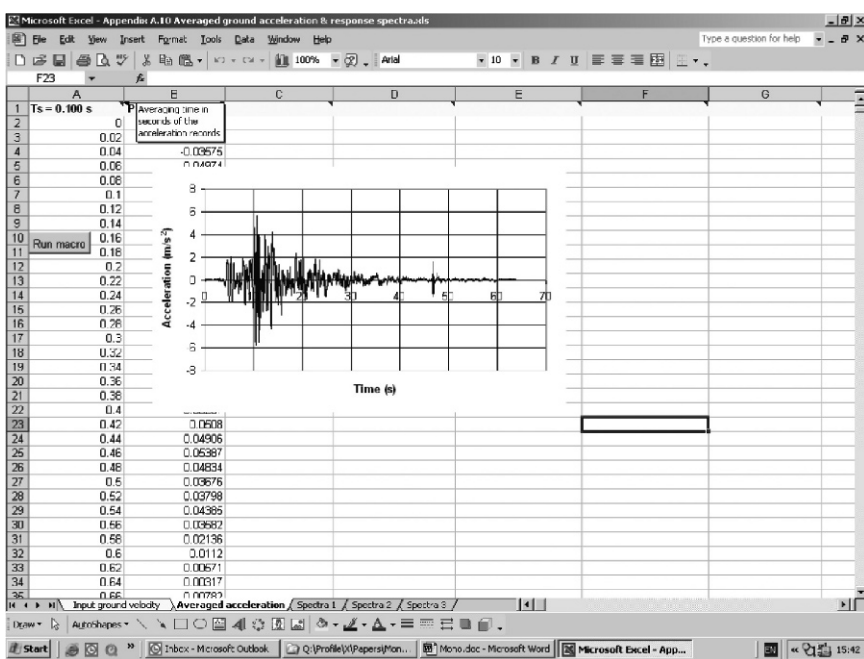


Fig. A10.1 Spreadsheet ‘Averaged acceleration’ in workbook Appendix A.10

Acceleration response spectra represent the peak values of the absolute accelerations of single degree of freedom oscillators (SDOFO) with different periods (frequencies) of vibrations. The absolute accelerations are obtained from the formula

$$\begin{aligned}
 \text{Abs.acc.}(t) = \omega_s \cdot \frac{1 - 2 \cdot \zeta^2}{\sqrt{1 - \zeta^2}} \cdot \int_0^t \text{Ground acc.}(\tau) \cdot e^{-\zeta \cdot \omega_s \cdot (t - \tau)} \cdot \\
 \sin \omega_s \cdot \sqrt{1 - \zeta^2} \cdot (t - \tau) \cdot d\tau + \\
 2 \cdot \omega_s \cdot \zeta \cdot \int_0^t \text{Ground acc.}(\tau) \cdot e^{-\zeta \cdot \omega_s \cdot (t - \tau)} \cdot \\
 \cos \omega_s \cdot \sqrt{1 - \zeta^2} \cdot (t - \tau) \cdot d\tau
 \end{aligned} \quad (\text{A.10.1})$$

where the circular frequency of a SDOFO  $\omega_s$  is according to Equation (6.59),  $\zeta$  is a part of the critical damping,  $t$  is time. The equation describing the response

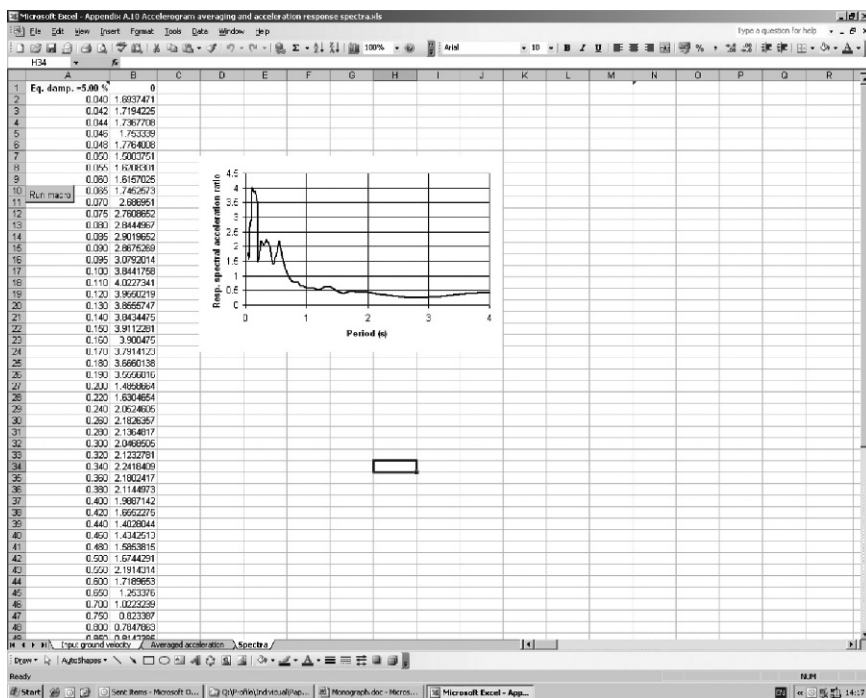


Fig. A10.2 Spreadsheet ‘Spectra’ in workbook Appendix A.10

of a linear system to arbitrary pulse of duration  $d\tau$  occurring at  $t = \tau$  is called Duhamel's integral. A view of the spreadsheet results is shown in Fig. A10.2. The response spectral acceleration ratio is shown with respect to the spectral acceleration at zero structural period i.e. with respect to the peak ground acceleration (Fig. A10.2).

## A.11 Bearing Capacity of Shallow Foundation

The analysis is performed according to Annex D of Eurocode 7, Part 1 (2004) with addition of the overburden pressure at the foundation depth. A view of the spreadsheet results is shown below. Lower part of the graph is controlled by soil to foundation sliding resistance in the case of coarse grained soil (Fig. A11).

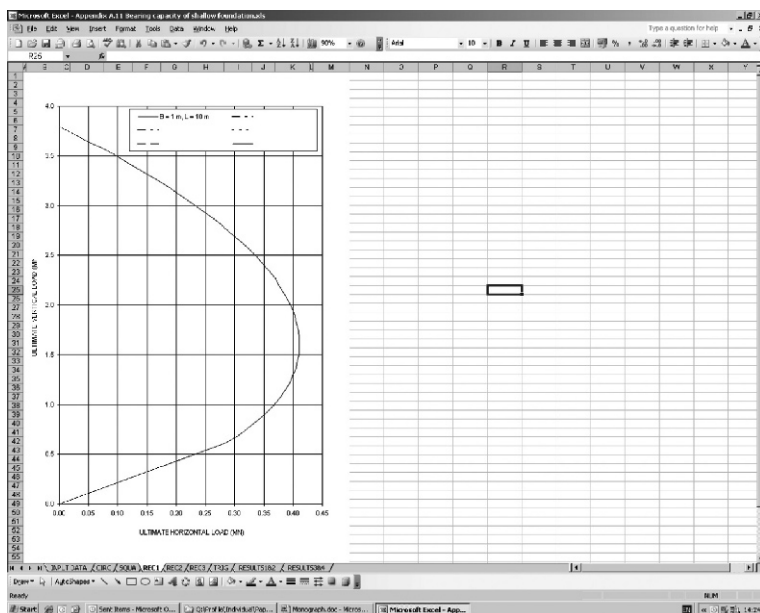


Fig. A11 Spreadsheet 'Rec 1' in workbook Appendix A.11

## A.12 Excess Pore Water Pressure Dissipation

A view of the spreadsheet results is shown below (Fig. A12).

	A	B	C	D	E	F	G	H	J	K	L	M	N	O	
1	H (m)	$c_s$ ( $m^{-2}s$ )	$c_d$ ( $m^{-2}s$ )	At (s)	$d_s$ (m)	$r_s$ (m)	Top layer	Presence of the top impermeable layer (0=not present/1=present)							
2	10	1.00E+00	1.00E+00	0.357	1.5	0.3									
3							Degree of scaling								
4	Time (s)	0.357	0.714	1.071	1.428	1.785	2.142	2.498	2.856	3.213	3.57	3.927	4.284	4.641	4.998
5	Depth (m)	100	100	100	100	100	100	100	100	100	100	100	100	100	100
6	0.4	95.36003	99.83408	99.94008	99.99779	99.99999	100	100	100	100	100	100	100	100	100
7	0.8	95.36003	99.83409	99.94009	99.99779	99.99999	100	100	100	100	100	100	100	100	100
8	1.2	95.36003	99.83409	99.94009	99.99779	99.99999	100	100	100	100	100	100	100	100	100
9	1.6	95.36003	99.83409	99.94009	99.99779	99.99999	100	100	100	100	100	100	100	100	100
10	2	95.36003	99.83409	99.94009	99.99779	99.99999	100	100	100	100	100	100	100	100	100
11	2.4	95.36003	99.83409	99.94009	99.99779	99.99999	100	100	100	100	100	100	100	100	100
12	2.8	95.36003	99.83409	99.94009	99.99779	99.99999	100	100	100	100	100	100	100	100	100
13	3.2	95.36003	99.83409	99.94009	99.99779	99.99999	100	100	100	100	100	100	100	100	100
14	3.6	95.36003	99.83409	99.94009	99.99779	99.99999	100	100	100	100	100	100	100	100	100
15	4	95.36003	99.83409	99.94009	99.99779	99.99999	100	100	100	100	100	100	100	100	100
16	4.4	95.36003	99.83409	99.94009	99.99779	99.99999	100	100	100	100	100	100	100	100	100
17	4.8	95.36003	99.83409	99.94009	99.99779	99.99999	100	100	100	100	100	100	100	100	100
18	5.2	95.36003	99.83409	99.94009	99.99779	99.99999	100	100	100	100	100	100	100	100	100
19	5.6	95.36003	99.83409	99.94009	99.99779	99.99999	100	100	100	100	100	100	100	100	100
20	6	95.36003	99.83409	99.94009	99.99779	99.99999	100	100	100	100	100	100	100	100	100
21	6.4	95.36003	99.83409	99.94009	99.99779	99.99999	100	100	100	100	100	100	100	100	100
22	6.8	95.36003	99.83409	99.94009	99.99779	99.99999	100	100	100	100	100	100	100	100	100
23	7.2	95.36003	99.83409	99.94009	99.99779	99.99999	100	100	100	100	100	100	100	100	100
24	7.6	95.36003	99.83409	99.94009	99.99779	99.99999	100	100	100	100	100	100	100	100	100
25	8	95.36003	99.83409	99.94009	99.99779	99.99999	100	100	100	100	100	100	100	100	100
26	8.4	95.36003	99.83409	99.94009	99.99779	99.99999	100	100	100	100	100	100	100	100	100
27	8.8	95.36003	99.83409	99.94009	99.99779	99.99999	100	100	100	100	100	100	100	100	100
28	9.2	95.36003	99.83409	99.94009	99.99779	99.99999	100	100	100	100	100	100	100	100	100
29	9.6	95.36003	99.83409	99.94009	99.99779	99.99999	100	100	100	100	100	100	100	100	100
30	10	95.36003	99.83409	99.94009	99.99779	99.99999	100	100	100	100	100	100	100	100	100
31															
32															
33															

Fig. A12 Spreadsheet ‘Data’ in workbook Appendix A.12

# References

- Abramson LW, Lee TS, Sharma S, Boyce GM (1996) Slope stability and stabilization methods. John Wiley and Sons, Inc., New-York, New-York
- Aki K (1988) Local site effects on strong ground motion. In: Earthquake engineering and soil dynamics II – recent advances in ground motion evaluation. ASCE Geotechnical Special Publication 20:103–155
- Akkar S, Bommer JJ (2007) Empirical prediction for peak ground velocity derive from strong-motion records from Europe and the Middle East. Bulletin of Seismological Society of America 97:511–530
- Ambraseys NN (1960) The seismic stability of earth dams. In: The 2nd conference on earthquake engineering, Tokyo 2:1345–1362
- Ambraseys NN (1988) Engineering seismology. Earthquake Engineering and Structural Dynamics 17:1–105
- Ambraseys NN (1990) Uniform magnitude re-evaluation of European earthquakes associated with strong motion records. Earthquake Engineering and Structural Dynamics 19:1020
- Ambraseys NN (2005) Archaeoseismology and neocatastrophism. Seismological Research Letters 76:560–564
- Ambraseys NN (2006a) Earthquakes and archaeoseismology. Journal of Archaeological Science 33:1008–1016
- Ambraseys NN (2006b) Comparison of frequency of occurrence of earthquakes with slip rates from long-term seismicity data: The cases of Gulf of Corinth, Sea of Marmara and Dead Sea Fault Zone. Geophysical Journal International 165:516–526
- Ambraseys NN, Melville CP (1982) A history of Persian earthquakes. Cambridge University Press, Cambridge
- Ambraseys NN, Srbulov M (1994) Attenuation of earthquake induced ground displacements. Earthquake Engineering and Structural Dynamics 23:467–487
- Ambraseys NN, Melville CP, Adams RD (1994) The seismicity of Egypt, Arabians and the Red Sea – a historical review. Cambridge University Press, Cambridge
- Ambraseys NN, Srbulov M (1995) Earthquake induced displacements of slopes. Soil Dynamics and Earthquake Engineering 14:59–71
- Ambraseys NN, Jackson JA (1998) Faulting associated with historical and recent earthquakes in the Eastern Mediterranean region. Geophysical Journal International 133:390–406
- Ambraseys NN, Srbulov M (1998) A note on the point source approximation in ground motion attenuation relations. Journal of Earthquake Engineering 2:1–24
- Ambraseys NN, Sarma SK (1999) The assessment of total seismic moment. Journal of Earthquake Engineering 3:439–462
- Ambraseys NN, Jackson JA (2000) Seismicity of the Sea of Marmara (Turkey) since 1500. Geophysical Journal International 141:F1–F6
- Ambraseys N, Smith P, Berardi R, Rinaldis SD, Cotton F and Berge-Thierry C (2000) Dissemination of European strong-motion data CD-ROM collection. European Council Environmental and Climate Research Programme, <http://www.isedc.cv.ic.ac.uk/>

- Ambraseys NN, Adams RD (2001) The seismicity of Central America – a descriptive catalogue. Imperial College Press, London
- Ambraseys NN, Douglas J (2003) Effect of vertical ground motions on horizontal response of structures. International Journal of Structural Stability and Dynamics 3:227–266
- Ambraseys NN, Douglas J, Sigbjornsson R, Berge-Thierry C, Suhadolc P, Costa G, Smit P (2004) European strong motion database – Volume 2. The Engineering and Physical Science Research Council of the United Kingdom GR-52114-01
- Ambraseys NN, Douglas J, Sarma SK, Smit PM (2005a) Equations for the estimation of strong ground motions from shallow crustal earthquakes using data from Europe and the Middle East: Horizontal peak ground acceleration and spectral accelerations. Bulletin of Earthquake Engineering 3:1–53
- Ambraseys NN, Douglas J, Sarma SK, Smit PM (2005b) Equations for the estimation of strong ground motions from shallow crustal earthquakes using data from Europe and the Middle East: Vertical peak ground acceleration and spectral accelerations. Bulletin of Earthquake Engineering 3:55–73
- Anderson DL (1989) Theory of the Earth. Blackwell Scientific Publications, Boston
- Andrus RD, Stokoe KH (1997) Liquefaction resistance based on shear wave velocity. In: NCEER workshop on evaluation of liquefaction resistance of soils. Salt Lake City, Utah, NCEER-97-0022
- Andrus RD, Stokoe KH (2000) Liquefaction resistance of soils from shear wave velocity. Journal of geotechnical and Geoenvironmental Engineering 126:1015–1025
- API (2005) Recommended practice for planning, designing and constructing fixed offshore platforms—working stress design, API RP 2A-WSD. American Petroleum Institute
- Arulanandan K, Scott RF (eds.) Verification of numerical procedures for the analysis of soil liquefaction problems (VELACS). Balkema
- ASTM D3999 – 91 Standard test methods for the determination of the modulus and damping properties of soils using the cyclic triaxial apparatus. American Society for Testing and Materials, annual book of ASTM standards 04.08
- ASTM D4015 – 92 Standard test method for modulus and damping of soils by the resonant-column method. American Society for Testing and Materials, annual book of ASTM standards 04.08
- ASTM D4428/D 4428m – 00 Standard test methods for crosshole seismic testing. American Society for Testing and Materials, annual book of ASTM standards 04.08
- ASTM D5777 – 00 Standard guide for using the seismic refraction method for subsurface investigation. American Society for Testing and Materials, annual book of ASTM standards 04.08
- ASTM 6391 – 99 Standard test method for field measurement of hydraulic conductivity limits of porous materials using two stages of infiltration from a borehole. American Society for Testing and Materials, annual book of ASTM standards 04.08
- Atkinson JH (2000) Non-linear soil stiffness in routine design. Geotechnique 50:487–507
- Atkinson JH, Bransby PL (1978) The mechanics of soils: An introduction to critical soil mechanics. McGraw Hill, London
- Baker GL, Gollub JP (1992) Chaotic dynamics, an introduction. Cambridge University Press, Cambridge
- Bakir BS, Ozkan MY, Ciliz S (2002) Effect of basin edge on the distribution of damage in 1995 Dinar, Turkey earthquake. Soil Dynamics and Earthquake Engineering 22:335–345
- Baldovin E, Paoliani P (1994) Dynamic analysis of embankment dams In: J.W. Bull (ed) Soil-structure interaction numerical analysis and modeling. E&FN Spon 121–125
- Barron RA (1948) Consolidation of fine grained soils by drain wells. Transactions ASCE 113:1718
- Bear J (1988) Dynamics of fluids in porous media. Courier Dover, New York
- Berrill JB, Christensen SA, Keenan RP, Okada W, Pettinga JR (2001) Case study of lateral spreading forces on a piled foundation. Geotechnique 51:501–517
- Benioff H (1934) The physical evaluation of seismic destructiveness. Bulletin of the Seismological Society of America 24:398–403
- Bielak J, Xu J, Ghattas O (1999) Earthquake ground motion and structural response in alluvial valleys. Journal of Geotechnical and Geoenvironmental Engineering, ASCE, 125:413–423

- Bishop AW (1955) The use of slip circle for stability analysis. *Geotechnique* 5:7–17
- Biot MA (1941) A mechanical analyzer for the prediction of earthquake stress. *Bulletin of the Seismological Society of America* 31:151–171
- Bjerrum L, Krinstad S, Kummeneje O (1961) The shear strength of fine sand. In: Fifth International Conference on Soil Mechanics and Foundation Engineering. Paris 1:29–37
- Blake LS (ed) (1989) Civil engineer's reference book, fourth edition. Butterworths
- Bolt BA (1969) Duration of strong motion. In: 4th World Conference on Earthquake Engineering, Santiago, Chile 1304–1315
- Bommer JJ, Elnashai AS (1999) Displacement spectra for seismic design. *Journal of Earthquake Engineering* 3:1–32
- Boore DM, Joyner WB, Fumal TE (1997) Equations for estimating horizontal response spectra and peak acceleration from western North America earthquakes: A summary of recent work. *Seismological Research Letters* 68:128–153
- Bouchon M, Barker JS (1996) Seismic response of a hill: The example of Tarzana, California. *Bulletin of the Seismological Society of America* 86:66–72
- Boulanger RW, Idriss IM (2007) Evaluation of cyclic softening in silt and clays. *Journal of Geotechnical and Geoenvironmental Engineering, ASCE*, 133:641–652
- Boussinesq J (1885) Application des potentiels a l'etude de l'équilibre et du Mouvement des Solides Elastiques, Gauthier-Villard, Paris
- Bozzolo D, Pamini R, Hutter K (1988) Rockfall analysis – a mathematical model and its test with field data. In: The Fifth International Symposium on Landslides, Lausanne 1: 555–560
- Bray JD, Travasarou T (2007) Simplified procedure for estimating earthquake-induced deviatoric slope displacement. *Journal of Geotechnical and Geoenvironmental Engineering* 133:381–392
- Britto AM, Gunn MJ (1987) Critical state soil mechanics via finite elements. Ellis Horwood, Chichester
- BS 5930 (1999) Code of practice for site investigation. British Standard Institution
- Burland JB (1989) Small is beautiful – the stiffness of soils at small strains. *Canadian Geotechnical Journal* 26:499–516
- Campbell KW (1981) Near source attenuation of peak horizontal acceleration. *Bulletin of the Seismological Society of America* 71:2039–2070
- Campbell KW (1997) Empirical near-source attenuation relations for horizontal and vertical components of peak ground acceleration, peak ground velocity, and pseudo-absolute acceleration response spectra. *Seismological Research Letters* 68:154–179
- Carrillo N (1962) Simple two- and three-dimensional cases in theory of consolidation of soils. *Journal of Mathematical Physics* 21
- Carver GA, McCalpin JP (1996) Paleoseismology of compressional tectonic environments. In: McCalpin JP (ed) Paleoseismology. Academic Press
- Castro G (1969) Liquefaction of sands. Harvard Soil Mechanics series 87, Harvard University, Cambridge, Massachusetts
- Celebi M (1993) Seismic response of two adjacent buildings, I: Data and analysis. *Journal of Structural Engineering* 119:2461–2492
- Celebi M, Safak E (1992) Seismic response of Pacific Plaza, I: Data and preliminary analysis. *Journal of Structural Engineering* 118:1547–1565
- Cetin KO, Seed RB, Kiureghian AD, Tokimatsu K, Harder Jr LH, Kayen RE, Moss RES (2004) Standard penetration test-based probabilistic and deterministic assessment of seismic soil liquefaction potential. *Journal of Geotechnical and Geoenvironmental Engineering, ASCE*, 130:1314–1340
- Chen P, Chen H (1989) Scaling law and its applications to earthquake statistical relations. *Tectonophysics* 166:53–72
- Chen H, Lee CF (2000) Numerical simulation of debris flows. *Canadian Geotechnical Journal* 37:146–160
- Chen W-F, Scawthorn C (2003) Earthquake engineering handbook. CRC Press

- Chugh AK (1985) Dynamic response analysis of embankment dams. *International Journal for Numerical and Analytical Methods in Geomechanics* 9:101–124
- Choudhary D, Sitharam TG, Rao KSS (2004) Seismic design of earth-retaining structures and foundations. *Current Science* 87(10):1417–1425
- Clough RW, Penzien J (1993) Dynamics of structures (2nd edition). McGraw-Hill, New York.
- Cornell CA, Winterstein SR (1986) Applicability of the Poisson earthquake occurrence model. In: Seismic hazard methodology for the central and eastern Unite States, EPRI Research Report NP-4726, Electric Power Research Institute, Palo Alto, California
- Cornforth DH (2005) Landslides in practice. Investigation, analysis, and remedial/preventative options in soils. Wiley
- Coulomb CA (1776) Essai sur une application des regles des maximis et minimis a quelques problemes de statique relatifs a l'architecture. Memoires de l'Academie Royale pres Divers Savants
- Dakoulas P, Gazetas G (1985) A class of inhomogeneous shear models for seismic response of dams and embankments. *Soil Dynamics and Earthquake Engineering* 4:166–182
- Dakoulas P, Gazetas G (2008) Insight into seismic earth and water pressures against caisson quay walls. *Geotechnique* 58:95–111
- Das BM (1985) Advanced Soil Mechanics. McGraw-Hill Book Co., Singapore
- Das BM (2004) Principles of foundation engineering. Thomson
- Davis RO, Selvadurai APS (1996) Elasticity and Geomechanics. Cambridge University Press
- Davis PM, Rubenstein JL, Liu KH, Gao SS, Knopoff L (2000) Northridge earthquake damage caused by geologic focusing of seismic waves. *Science* 289:1746–1750
- Davis RO, Selvadurai APS (2002) Plasticity and Geomechanics. Cambridge University Press
- Davies TR, McSaveney MJ (2002) Dynamic simulation of the motion of fragmenting rock avalanches. *Canadian Geotechnical Journal* 39:789–798
- Day RW (2002) Geotechnical Earthquake Engineering Handbook. McGraw Hill
- De Alba P, Chan CK, Seed HB (1975) Determination of soil liquefaction characteristics by large scale laboratory tests. Report EERC 75-14, Earthquake Engineering Research Center, University of California, Berkeley
- De Alba P, Seed HB, Retamal E, Seed RB (1987) Residual strength of sand from dam failures in the Chilean earthquake of March 3, 1985. Earthquake Engineering research Center Report No. UCB/EERC-87-11, University of California, Berkeley, California
- De Alba P, Seed HB, Retamal E, Seed RB (1988) Analyses of dam failures in 1985 Chilean earthquake. *Journal of Geotechnical Engineering, ASCE* 114:1414–1434
- Douglas J (2003) What is a poor quality strong-motion record? *Bulletin of earthquake Engineering* 1:141–156
- Douglas J (2004) Ground motion estimation equations 1964–2003. Reissue of ESEE Report 01-1: A comprehensive worldwide summary of strong-motion attenuation relationships for peak ground acceleration and spectral ordinates (1969 to 2000). Department of Civil & Environmental Engineering, Soil Mechanics Section, Report 04-001-SM, Imperial College, London, U.K.
- Douglas J (2006) Errata of and additions to: Ground motion estimation equations 1964–3003. Intermediary Report BRGM/RP-54603-FR
- Dowding CH, Rozen A (1978) Damage to rock tunnels from earthquake shaking. *Journal of Geotechnical Engineering Division, ASCE* 104:175–191
- Drucker DC, Gibson RE, Henkel DJ (1957) Soil mechanics and work hardening theories of plasticity. *Transactions ASCE* 122:338–346
- Duncan JM (1996) State of the art: Limit equilibrium and finite-element analysis of slopes. *Journal of Geotechnical Engineering, ASCE* 122:577–596
- Durrani AJ, Elnashai AS, Hashash YMA, Kim SJ, Masud A (2005) The Kashmir earthquake of October 8, 2005 – A quick look report. Mid-America Earthquake Center, University of Illinois at Urbana-Champaign
- Eckersley D (1990) Instrumented laboratory flow slides. *Geotechnique XV*:489–502
- Evans SG, Clague JJ, Woodsworth GJ, Hung O (1989) The Pandemonium Creek rock avalanche, British Columbia. *Canadian Geotechnical Journal* 26:427–446

- Eurocode 8 (2004) Design of structures for earthquake resistance (Parts 1 to 6)
- Fannin RJ, Wise MP (2001) An empirical-statistical model for debris flow travel distance. *Canadian Geotechnical Journal* 38:982–994
- Fearon RE, Chandler RC, Bommer JJ (2004) An investigation of the mechanism which control soil behavior at fast rates of displacement. In: Advances in geotechnical engineering, the Skempton conference 1:441–452. Thomas Telford, London
- Fenves GL, Serino G (1990) Soil-structure interaction in buildings from earthquake records. *Earthquake Spectra* 6:641–655
- Fenves GL, Filippou FC, Sze DT (1992) Response of the Dumbarton bridge in the Loma Prieta earthquake. Earthquake Engineering Research Center, College of Engineering, University of California at Berkeley, Report UCB/EERC-92/02
- Fenves GL, Desroches R (1994) Response of the Northeast connector in the Landers and Big Bear earthquakes. Earthquake Engineering Research Center, College of Engineering, University of California at Berkeley, Report UCB/EERC-94/12
- Ferretti A, Prati C, Rocca F (2001) Permanent catters in SAR interferometry. *IEEE Transactions on Geoscience and Remote Sensing* 39:8–20
- Field ME, Gardner JV, Jennings AE, Edwards BD (1982) Earthquake-induced sediment failures on a 0.25o slope, Klamath River delta, California. *Geology* 10:542–546
- Fielder G (1968) Estudio sismológico de la región de Caracas con relación al terremoto del 29 de Julio de 1967. Boletín Técnico, Instituto de Materiales y Modelos Estructurales, Universidad Central de Venezuela, Caracas 6:127–222
- Finlay PJ, Mostyn GR, Fell R (1999) Landslide risk assessment: Prediction of travel Distance. *Canadian Geotechnical Journal* 36:556–562
- Finn WDL (1991) Geotechnical aspects of microzonation. In: The 4th International Conference on Microzonation. Earthquake Engineering Research Institute, Stanford University, Palo Alto, California 1:199–259
- Finn WDL (1999) Evolution of dynamic analysis in geotechnical earthquake engineering. In: New approaches to liquefaction analysis. Transportation Research Board 99 Workshop, Washington
- Finn WDL, Fujita N (2002) Piles in liquefiable soils: Seismic analysis and design issues. *Soil Dynamics and Earthquake Engineering* 22:731–742
- Florin V A, Ivanov P L (1961) Liquefaction of saturated sandy soils. In: Proceedings of the 5th International Conference on Soil Mechanics and Foundation Engineering 1:107–111
- Fowler CMR (1990) The solid Earth, an introduction to global geophysics. Cambridge University Press, Cambridge, England
- Fredlund DG, Rahardjo H (1993) Soil mechanics for unsaturated soils. Wiley
- Galadini F, Hinzen KG (2006) Archaeoseismology: Methodological issues and procedure. *Journal of Seismology* 10:395–414
- Gazetas G (1987) Seismic response of earth dams; some recent developments. *Soil Dynamics and Earthquake Engineering* 6:3–47
- Gazetas G, Mylonakis G (1998) Seismic soil-structure interaction: New evidence and emerging issues. In: Geotechnical Earthquake Engineering and Soil Dynamics III – vol 2, ASCE Geotechnical Special Publication 75:1119–1174
- Gazetas G, Gerolymos N, Anastopoulos I (2005) Response of three Athens metro underground structures in the 1999 Parnitha earthquake. *Soil Dynamics and Earthquake Engineering* 25:617–633
- Genc C (1993) Structural and geomorphological aspects of the Catak landslide, NE Turkey. *Quarterly Journal of Engineering Geology* 26:99–108
- Gieck K, Gieck R (1997) Engineering Formulae – 7th edition, McGraw-Hill
- Goltz C (1998) Fractal and chaotic properties of earthquakes (lecture notes in Earth science). Springer Verlag
- Graves RW, Pitarka A, Somerville PG (1998) Ground-motion amplification in the Santa Monica area: Effects of shallow basin-edge structure. *Bulletin of the Seismological Society of America* 88:1224–1242

- Green RA, Terri GA (2005) Number of equivalent cycles concept for liquefaction evaluations – revisited. *Journal of Geotechnical and Geoenvironmental Engineering* 131:477–488
- Gutenberg B (1945) Magnitude determination for deep-focus earthquakes. *Bulletin of the Seismological Society of America* 35:117–130
- Gutenberg B, Richter CF (1936) On seismic waves. *Gerlands Bietraege zur Geophysik* 47:73–131
- Gutenberg B, Richter CF (1944) Frequency of earthquakes in California. *Bulletin of the Seismological Society of America* 34:1985–1988
- Gutenberg B, Richter CF (1956) Magnitude and energy of earthquakes. *Annali Geofisica* 9:1–5
- Hadjian A, Fallgen R, Lau L (1990) Imperial County services building revisited: A re-evaluation with pile-soil-structure interaction. In: The 4th U.S. National Conference on Earthquake Engineering, Palm Springs 3:835–844
- Hamada M, Yasuda S, Isayama R, Emoto K (1986) Study on liquefaction induced permanent ground displacements. In: Report of the Association for the Development of Earthquake Prediction in Japan, Tokyo, Japan
- Hancock J, Bommer JJ (2004) Predicting the number of cycles of ground motion. In: The 13th World Conference on Earthquake Engineering, Vancouver, Canada 1989
- Hans T, Kanamori H (1979) A moment magnitude scale. *Journal of Geophysical Research* 84:2348–2340
- Hansen JB (1970) A revised and extended formula for bearing capacity. *Danish Geotechnical Institute Bulletin* 28, Copenhagen
- Harder LFJr, Boulanger R (1997) Application of  $K\sigma$  and  $K\alpha$  correction factors. In: NCEER Workshop on Evaluation of Liquefaction Resistance of Soils, NCEER-97-0022
- Hardin BO (1978) The nature of stress-strain behavior of soil. In: *Earthquake Engineering and Soil Dynamics*, ASCE, Pasadena, California, 1:3–89
- Hardin BO, Drnevich VP (1972) Shear modulus and damping in soil: Design equations and curves. *Journal of Soil Mechanics and Foundations Division*, ASCE 98:667–692
- Hashiguchi K (2001) Description of inherent/induced anisotropy of soils: Rotational hardening rule with objectivity. *Soils and Foundations* 41:139–146
- Havenith HB, Strom A, Calvetti F, Jongmans D (2003) Seismic triggering of landslides, part B: Simulation of dynamic failure process. *Natural Hazards and Earth System Sciences*, 3:663–682.
- Heaton TH, Kanamori H (1984) Seismic potential associated with subduction in the north-western United States. *Bulletin of the Seismological Society of America* 73:933–941
- Head KH (2006) Manual of soil laboratory testing (3 parts). Whittles Publishing, London
- Heidari M, James RG (1982) Centrifuge modeling of earthquake induced liquefaction in a column of sand. In: Proceedings of Conference on Soil Dynamics and Earthquake Engineering. Balkema 1:271–281
- Hoek E (1983) Strength of jointed rock masses. *Geotechnique* 33:187–223
- Hoek E (1986) Rock fall: A computer program for predicting rock fall trajectories. Unpublished internal notes, Golder Associates, Vancouver
- Hoek E (1987) General two-dimensional slope stability analysis. In: Brown ET (ed) *Analytical and Computational Methods in Engineering Rock Mechanics*. Allen & Unwin, London
- Hoek E (2006) Analysis of rock fall hazards [http://www.rockscience.com/hoek/pdf/Chapter\\_9\\_of\\_Rock\\_Engineering.pdf](http://www.rockscience.com/hoek/pdf/Chapter_9_of_Rock_Engineering.pdf)
- Hoek E, Bray JW (1981) *Rock Slope Engineering* (revised 3rd ed). The Institution of Mining and Metallurgy, London
- Hogan SJ (1990) The many steady state responses of a rigid block under harmonic forcing. *Earthquake Engineering and Structural Dynamics* 19:1057–1071
- Horner PC (1981) *Earthworks*. Thomas Telford Ltd.
- Housner GW (1963) The behavior of inverted pendulum structures during earthquakes. *Bulletin of the Seismological Society of America* 53:403–417
- Housner GW et al. (1990) Competing against time, report to the Governor. Governor's Board of Inquiry, State of California
- Hungr O (1995) A model for the run out analysis of rapid flow slides, debris flows, and avalanches. *Canadian Geotechnical Journal* 32:610–623

- Hungr O, Morgenstern NR (1984) High velocity ring shear test on sand. *Geotechnique* 34: 415–421
- Hunt RE (2005) Geotechnical engineering investigation handbook. Taylor & Francis
- Huo H, Bobet A, Fernandez G, Ramirez J (2005) Load transfer mechanism between underground structure and surrounding ground: Evaluation of the failure of the Daikai station. *Journal of Geotechnical and Geoenvironmental Engineering ASCE* 131:1522–1533
- Hutchinson JN (1986) A sliding-consolidation model for flow slides. *Canadian Geotechnical Journal* 23:115–126
- IBC (2006) International Building Code. International Code Council Inc, Illinois
- Idriss IM (1985) Evaluating seismic risk in engineering practice. In: The 11th International Conference on Soil Mechanics and Foundation Engineering, San Francisco 1:255–320
- Idriss IM (1990) Response of soft soil sites during earthquakes. In: Duncan JM (ed) H.Bolton Seed Memorial Symposium. BiTech Publishers, Vancouver, British Columbia 2:273–289
- Inagaki H, Iai S, Sugano T, Yamazaki H, Inatomi T (1996) Performance of caisson type quay walls at Kobe port. *Soils and Foundations special issue* 119–136
- Ingold TS (1982) Reinforced Earth. Thomas Telford Ltd., London
- Ishibashi I (1992) Discussion to Effect of soil plasticity on cyclic response by M.Vucetic and R.Dobry. *Journal of Geotechnical Engineering ASCE* 118:830–832
- Ishihara K (1993) Liquefaction and flow failure during earthquakes. *Geotechnique* 43:351–415
- Ishihara K (1995) Soil behavior in earthquake geotechnics. Oxford
- Ishihara K, Nagase H (1985) Multi-directional irregular loading tests on sand. In: Khosla V (ed) Advances in the Art of Testing Soils under Cyclic Conditions. Geotechnical Engineering Division of ASCE Convention in Detroit, Michigan
- Ishihara K, Yasuda S, Yoshida Y (1990) Liquefaction induced flow failure of embankments and residual strength of silty sands. *Soils and Foundations* 30:69–80
- Ishihara K, Yoshimine M (1992) Evaluation of settlements in sand deposits following liquefaction during earthquakes. *Soils and Foundations* 32:173–188
- ISO (2004) ISO 19901-2:2004. Petroleum and natural gas industries—Specific requirements for offshore structures—Part 2: Seismic design procedures and criteria. International Standards Organization
- Jackson J (2001) Living with earthquakes – know your faults. *Journal of Earthquake Engineering* 5 special issue 1
- Jaky J (1944) The coefficient of earth pressure at rest. Magyar Mernok es Epitez Egylet Kozlonye
- Jardine RJ, Fourie AB, Maswoswse J, Burland JB (1985) Field and laboratory measurements of soil stiffness. In: Proceedings of 11th International Conference of Soil Mechanics and Foundation Engineering, San Francisco 2:511–514.
- Jefferies M, Been K (2006) Soil liquefaction, a critical state approach. Taylor & Francis
- Jewel RA (1990) Strength and deformation in reinforced soil design. In: Den Hoedt (ed.) the 4th International Conference on Geotextiles, Geomembranes and Related Products, Hague, Netherlands, Balkema 3:913–946
- Jibson R (1987) Summary of research on the effect of topographic amplification of earthquake shaking on slope stability. Report 87-268, U.S. Geological Survey, Menlo Park, California
- Jibson RW (1996) Using landslides for paleoseismic analysis. In: McCalpin J (ed) Paleoseismology. Academic Press
- Joyner WB, Boore DM (1981a) Peak horizontal acceleration and velocity from strong-motion records including records from the 1979 Imperial Valley, California, earthquake. *Bulletin of the Seismological Society of America* 71:2011–2038
- Joyner WB, Boore DM (1981b) Measurement, characterization, and prediction of strong ground motion. In: Earthquake Engineering and Soil Dynamics II – Recent Advances in Ground Motion Evaluation, Geotechnical Special Publication 20, ASCE, New York, 43–102
- Kawase H (1996) The cause of the damage belt in Kobe: The basin-edge effect, constructive interference of the direct S-wave with the basin-induced diffracted/Rayleigh waves. *Seismological Research Letters* 67:25–34

- Keefer DK (1984) Landslides caused by earthquakes. *Bulletin of the Geological Society of America* 95:406–421
- Keller EA (1986) Investigation of active tectonics; use of surficial earth processes. In: Wallace RE (chairman) *Active Tectonics: Studies in Geophysics*. National Academic Press, Washington DC 136–147
- Kenney TC (1959) Discussion. *Soil Mechanics and Foundation Division ASCE* 85:67–79
- Kim SR, Kwon OS, Kim MM (2004) Evaluation of force components acting on gravity type walls during earthquakes. *Soil Dynamics and Earthquake Engineering* 24:853–866
- King JL, Tucker BE (1984) Dependence of sediment-filled valley response on the input amplitude and the valley properties. *Bulletin of the Seismological Society of America* 74:153–165
- Korner HJ (1976) Reichweite und Grschwindigkeit von Bergsturzen und Fließschneelawien. *Rock Mechanics* 8:225–256
- Kramer SL (1996) *Geotechnical earthquake engineering*. Prentice Hall, New Yourk
- Kramer SL (2000) Dynamic response of Mercer Slough peat. *Journal of Geotechnical and Geoenvironmental Engineering ASCE* 126:504–510
- Kramer SL, Lindwall NW (2004) Dimensionality and directionality effects in Newmark sliding block analyses. *Journal of Geotechnical and Geoenvironmental Engineering ASCE* 130:303–315
- Kulhawy H, Mayne PW (1990) Manual of estimating soil properties for foundation design. Research Project 1493–6, Cornell University, Ithaca, New York
- Kumar J, Ghosh P (2006) Seismic bearing capacity for embedded footings on sloping ground. *Geotechnique* 56(2):133–140
- Kutter BL, Balakrishnan A (2000) Dynamic model test data from electronics to knowledge. In: *Centrifuge 98*, Balkema, Rotterdam 2:931–943
- Ladd CC, Foot R (1974) New design procedures for stability of soft clays. *Journal of Geotechnical Engineering Division ASCE* 100:763–786
- Lambe PW, Whitman RV (1979) *Soil mechanics – SI version*. Wiley
- Lee KL, Albaisa A (1974) Earthquake induced settlements in saturated sands. *Journal of Soil Mechanics and Foundation Division ASCE* 100:387–406
- Lee KL, Ficht JA (1976) Strength of clay subjected to cyclic loading. *Marine Geotechnology* 1
- Lee VW, Trifunac MD, Feng CC (1982) Effects of foundation size on Fourier spectrum amplitudes of earthquake accelerations recorded in buildings. *Soil Dynamics and Earthquake Engineering* 1:52–58
- Leick A (1995) *GPS Satellite Survey* (2nd edition). John Wiley & Sons Inc, New Yourk
- Leroueil S, Marques MES (1996) Importance of strain rate and temperature effects in geotechnical engineering. In: Sheahan TC, Kaliakin VN (eds) *Measuring and modeling time dependent soil behavior*. ASCE Geotechnical Special Publication No. 61, pp 1–60
- Liao SSC, Whitman RV (1986) Overburden correction factors for SPT in sand. *Journal of Geotechnical Engineering ASCE* 112:373–377
- Lin SY, Lin PS, Luo H-S, Juang CH (2000) Shear modulus and damping ratio characteristics of gravelly deposits. *Canadian Geotechnical Journal* 37:638–651
- Liu L, Dobry R (1997) Seismic response of shallow foundation on liquefiable sand. *Journal of Geotechnical and Geoenvironmental Engineering ASCE* 123:557–567
- Long NT, Guegan Y, Legeay G (1972) Etude de la terre armee a l'appareil triaxial. *Rapport de Recherche* 17, LCPC 6
- Loret B (1990) Geomechanical applications of the theory of multi-mechanisms. In: Darve F (ed.) *Geomaterials, constitutive equations and modeling*, Elsevier 187–211
- Lunne T, Robertson PK, Powell JJM (2001) *Cone penetration testing in geotechnical practice*. Spon Press, London
- Makris N, Badoni D, Delis E, Gazetas G (1994) Prediction of observed bridge response with soil-pile-structure interaction. *Journal of Structural Engineering* 120:2992–3011
- Maksimovic M (1988) General slope stability software package for micro computers. In: The 6th International Conference on Numerical Methods in Geomechanics, Innsbruck 3:2145–2150

- Maksimovic M (1989a) Nonlinear failure envelope for soils. *Journal of Geotechnical Engineering ASCE* 115:581–586
- Maksimovic M (1989b) On the residual shear strength of clays. *Geotechnique* 39:347–351
- Maksimovic M (1989c) Nonlinear failure envelope for coarse-grained soils. In: The 12th International Conference on Soil Mechanics and Foundation Engineering, Ro de Janeiro 1:731–734
- Maksimovic M (1992) New description of the shear strength for rock joints. *Rock Mechanics and Rock Engineering* 25:275–285
- Maksimovic M (1993) Nonlinear failure envelope for the limit state design. In: International Symposium on Limit State Design in geotechnical Engineering, Copenhagen, Session 2:131–140.
- Maksimovic M (1996a) The shear Strength components of a rough rock joint. *International Journal for Rock Mechanics and Mining Science* 33:769–783
- Maksimovic M (1996b) A family of nonlinear failure envelopes for non-cemented soils and rock discontinuities. *Electronic Journal of Geotechnical Engineering*
- Maksimovic M (2005) Mehanika tla (3rd edition). Gradjevinska knjiga a.d.
- Mandl G (2000) Faulting in brittle rocks. An introduction to the mechanics of tectonic faults. Springer
- Matsuda T, Ota Y, Ando M, Yonekura N (1978) Fault mechanism and recurrence time of major earthquakes in the southern Kanto district. *Bulletin of the Geological Society of America* 89:1610–1618
- McCalpin J (1996) Paleoseismology. Academic Press
- McClung DM (2001) Extreme avalanche run out: A comparison of empirical methods. *Canadian Geotechnical Journal* 38:1254–1265
- McDougall S, Hungr O (2004) A model for the analysis of rapid landslide motion across three-dimensional terrain. *Canadian Geotechnical Journal* 41:1084–1097
- McDougall S, Hungr O (2005) Dynamic modeling of entrainment in rapid landslides. *Canadian Geotechnical Journal* 42:1437–1448
- McGuire RK (1995) Probabilistic seismic hazard analysis and design earthquakes: Closing the loop. *Bulletin of the Seismological Society of America* 85:1275–1284
- Mendoza M, Romo M (1989) Behavior of building foundations in Mexico City during the 1985 earthquake: Second stage. In: Lessons Learned from the Mexico Earthquake, Publication 89-02, Earthquake Engineering Research Institute, 66–70
- Metropolis N, Ulam S (1949) The Monte Carlo method. *Journal of American Statistician Association* 44:335–341.
- Meymand PJ (1998) Shaking table scale model tests of nonlinear soil-pile-superstructure interaction in soft clay. PhD thesis, University of California, Berkeley
- MIL-HDBK (1997) Soil Dynamics and Special Design Aspects. U.S. Department of Defense Handbook 1007/3
- Mitchell JK, Soga K (2005) Fundamentals of soil behavior. Wiley
- Miura K, Yoshida N, Wakamatsu K (1995) Damage to fill embankment during the 1993 Kushiro-oki earthquake In: The 1st International Conference on Earthquake Geotechnical Engineering, Tokyo, Japan 2:1057–1062
- Miura K, Yoshida N, Nishimura M, Wakamatsu K (1998) Stability analysis of the fill embankment damaged by recent two major earthquakes in Hokkaido, Japan. In: The 1998 Geotechnical Earthquake Engineering and Soil Dynamics Specialty Conference, Seattle, Washington, ASCE Geo-Institute Geotechnical Special Publication 75, vol 2:926–937
- Mizuno H (1987) Pile damage during earthquakes in Japan (1923–1983). In Nogami (ed) *Dynamic Response of Pile Foundations*, ASCE, Geotechnical Special Publication 11:53–78
- Modaressi A, Boufelloh S, Evesque P (1999) Modeling of stress distribution in granular piles; Comparison with centrifuge experiments. *Chaos* 9:523–543
- Mononobe N (1936) Seismic stability of earth dams. In: The 2nd Congress on Large Dams, Washington, D.C. vol 4
- Mononobe N, Matsuo H (1929). On the determination of earth pressures during earthquakes. In: The World Engineering Congress

- Moss RES (2003) CPT-based probabilistic assessment of seismic sand liquefaction initiation. PhD Thesis, University of California, Berkeley
- Moss RES, Seed RB, Kayen RE, Stewart JP, Der Kiureghian A, Cetin KO (2006) CPT-based probabilistic and deterministic assessment of in situ seismic soil liquefaction potential. *Journal of Geotechnical and Geoenvironmental Engineering ASCE* 132:1032–1051
- Muir-Wood D (1990) Soil behavior and critical state soil mechanics. Cambridge University Press
- Murphy JR, O'Brien LJ (1977) The correlation of peak ground acceleration amplitude with seismic intensity and other physical parameters. *Bulletin of the Seismological Society of America* 67:877–915
- Newmark NM (1965) Effect of earthquakes on dams and embankments. *Geotechnique* 15:139–160
- Newmark NM, Hall WJ, Morgan JR (1977) Comparison of building response and free field motion in earthquakes. In: The 6th World Conference on Earthquake Engineering, New Delhi 2:972–977.
- Novak M, Grigg RF (1976) Dynamic experiments with small pile foundation. *Canadian Geotechnical Journal* 13:372–395
- Obermeier SF (1996) Using liquefaction-induced features for paleoseismic analysis. In: McCalpin J (ed) *Paleoseismology*, Academic Press
- Ohira A, Tazoh T, Dowa K, Shimizu K, Shimada M (1984) Observations of earthquake response behaviors of foundation piles for road bridge. In: The 8th World Conference on Earthquake Engineering, San Francisco III:577–584
- Ohsaki Y (1970) Effects of sand compaction on liquefaction during Tokachioki earthquake. *Soils and Foundations* 10:112–128
- Ohta T, Uchiyama S, Niwa M, Ueno K (1980) Earthquake response characteristics of structure with pile foundation on soft subsoil layer and its simulation analysis. In: The 7th World Conference on Earthquake Engineering, Istanbul 3:404–410
- Ohya S, Iwasaki T, Wakamatsu M (1985) Comparative study of various penetration tests in ground that underwent liquefaction during the 1983 Nihon-Kai-Chubu and 1964 Niigata earthquakes. In: The Workshop on In-Situ Testing Methods for Evaluation of Soil Liquefaction Susceptibility, San Francisco, California 1:56–88
- Okabe S (1926) General theory of earth pressures. *Journal of the Japan Society of Civil Engineering* 12:1
- Olson SM (2001) Liquefaction analysis of level and sloping ground using field case histories and penetration resistance. PhD Thesis, the Graduate College, University of Illinois at Urbana-Champaign
- Olson SM, Stark TD (2002) Liquefied strength ratio from liquefaction flow failure case histories. *Canadian Geotechnical Journal* 39:629–647
- Ovando-Shelley E, Romo MP, Contreras N, Giralt A (2003) Effects on soil properties of future settlements in downtown Mexico City due to ground water extraction. *Geofisica International* 42:185–204
- Papageorgiou AS, Kim J (1991) Study of the propagation and amplification of seismic waves in Caracas valley with reference to the 29th July 1967 earthquake: SH waves. *Bulletin of the Seismological Society of America* 81:2214–2233
- Parathiras A (1995) Rate of displacement effects on fast residual strength. In: Ishihara K (ed) the 1st International Conference on Earthquake Geotechnical; Engineering, Tokyo 1: 233–237
- Peck RB, Hanson WE, Thornburn TH (1974) Foundation Engineering (2nd ed.). John Wiley, New York
- Pei D, Papageorgiou AS (1996) Locally generated surface waves in Santa Clara Valley: Analysis of observations and numerical simulation. *Earthquake Engineering and Structural Dynamics* 25: 47–63
- Penzien J (2000) Seismically induced racking of tunnel linings. *Earthquake Engineering and Structural Dynamics* 29:683–691
- Pestana JM, Hunt CE, Goughnour RR (1997) FEQDrain: A finite element computer program for the analysis of the earthquake generation and dissipation of pore water pressure in layered

- sand deposits with vertical drains. Report EERC 97-15, College of Engineering, University of California, Berkeley, California
- Pitilakis K, Moutsakis A (1989) Seismic analysis and behavior of gravity retaining walls – the case of Kalamata harbor quay wall. *Soils and Foundations* 29:1–17
- Potts DM (2003) Numerical analysis: A virtual dream or practical reality? *Geotechnique* 53(6):535–573
- Poulos HG (1979) Group factors for pile-deflection estimation. *Journal of Geotechnical Engineering Division ASCE* 105:1489–1509
- Poulos SJ (1981) The steady state of deformation. *Journal of Geotechnical Engineering Division, ASCE*, 107:553–562
- Poulos HG, Davis EH (1980) Pile foundation analysis and design. John Wiley & Sons
- Puppala AJ, Griffin JA, Hoyos LR, Chomtid S (2004) Studies on sulphate resistant cement stabilization methods to address sulphate induced soil heave. *Journal of Geotechnical and Geoenvironmental Engineering ASCE* 130:391–402
- Rankine WJM (1857) On the stability of loose earth. *Philosophical Transcripts of the Royal Society, London*, 147(1):9–27
- Reid HF (1911) The elastic rebound theory of earthquakes. *Bulletin of the Department of Geology, University of California, Berkeley* 6:413–444
- Reiter L (1990) Earthquake hazard analysis – issues and insights. Columbia University Press, New York
- Richards R, Elms D (1979) Seismic behavior of gravity retaining walls. *Journal of the Geotechnical Engineering ASCE* 105:449–464
- Richards R, Huang C, Fishman KL (1999) Seismic earth pressure on retaining structures. *Journal of Geotechnical and Geoenvironmental Engineering ASCE* 25:771–778
- Richter CF (1958) Elementary Seismology. W.H. Freeman, San Francisco
- Rodriguez CE, Bommer JJ, Chandler RJ (1999) Earthquake-induced landslides: 1980–1997. *Soil Dynamics and Earthquake Engineering* 18:325–346
- Rollings RS, Burkes JP, Rollings MP (1999) Sulphate attack on cement-stabilized sand. *Journal of Geotechnical and Geoenvironmental Engineering ASCE* 125:364–372
- Ross GA (1968) Case studies of soil stability problems resulting from earthquakes. PhD Thesis, University of California, Berkeley, California
- Ruff L, Kanamori H (1980) Seismicity and subduction process. *Physics of the Earth and Planetary Interiors* 23:240–252
- Saada AS, Bianchini GF, Liang L (1994) Cracks, bifurcation and shear bands propagation in saturated clays. *Geotechnique* 44:35–64
- Sarma SK (1979) Stability analysis of embankments and slopes. *Journal of Geotechnical Engineering ASCE* 105:1511–1524
- Sarma SK (1994) Analytical solution to the seismic response of visco-elastic soil layers. *Geotechnique* 44:265–275
- Sarma SK, Chen YC (1995) Seismic bearing capacity of shallow strip footings near sloping ground. In: Elnashai A (ed) European Seismic Design Practice, Balkema, Rotterdam 505–512
- Sarma SK, Chen YC (1996) Bearing capacity of strip footings near sloping ground during earthquakes. In: The 11th World Conference on Earthquake Engineering paper 2078
- Sarma SK, Srbulov M (1996) A simplified method for prediction of kinematic soil-foundation interaction effects on peak horizontal acceleration of a rigid foundation. *Earthquake Engineering and Structural Dynamics* 25:815–836
- Sarma SK, Srbulov M (1998) A uniform estimation of some basic ground motion parameters. *Journal of Earthquake Engineering* 2:267–287
- Sarma SK, Tan (2006) Determination of critical slip surface in slope analysis. *Geotechnique* 56:539–550.
- Sasaki Y, Oshiki H, Nishikawa J (1994) Embankment failure caused by the Kushiro-Oki earthquake of January 15, 1993. In: The 13th International Conference on Soil Mechanics and Foundation Engineering, New Delhi, India 1:61–68

- Schaefer VR (ed), Ambranson LW, Drumheller JC, Hussin JD, Sharp KD (1997) Ground improvement, ground reinforcement, ground treatment developments 1987–1997. ASCE Geotechnical Special Publication 69
- Schnabel PB, Lysmer J, Seed HB (1972) SHAKE a computer program for earthquake response analysis of horizontally layered sites. Report EERC 72-12, Earthquake Engineering Research Center, University of California, Berkeley
- Schofield AN (1980) Cambridge Geotechnical Centrifuge Operations. *Geotechnique* 25:229–267
- Schofield AN (2005) Disturbed soil properties and geotechnical design. Thomas Telford
- Schofield AN, Wroth P (1968) Critical state soil mechanics. McGraw Hill, Maidenhead
- Scholz CH (1968) Micro fracturing and the inelastic deformation of rock in compression. *Journal of Geophysical Research* 73:1417–1432
- Scholz CH (1990) The mechanics of earthquakes and faulting. Cambridge University Press
- Scholz CH, Aviles C, Wesnousky S (1986) Scaling differences between large intraplate and interplate earthquakes. *Bulletin of the Seismological Society of America* 76:65–70
- Seed HB (1988) Design problems in soil liquefaction. *Journal of Geotechnical Engineering ASCE* 113(8):827–845
- Seed HB, Lee KL (1965) Studies of liquefaction of sands under cyclic loading conditions. Report TE-65-65, Department of Civil Engineering, University of California, Berkeley
- Seed HB, Lee KL, Idriss IM (1969) Analysis of Sheffield Dam failure. *Journal of the Soil Mechanics and Foundations ASCE* 95:1453–1490
- Seed HB, Idriss IM (1970) Soil modules and damping factors for dynamic response analyses. Report EERC 70-10, Earthquake Engineering Research Center, University of California, Berkeley
- Seed HB, Idriss IM (1971) Simplified procedure for evaluating soil liquefaction potential. *Journal of the Soil Mechanics and Foundations Division ASCE* 107:1249–1274
- Seed HB, Idriss IM, Makdisi F, Banerje N (1975) Representation of irregular stress time histories by equivalent uniform stress series in liquefaction analyses. Report EERC 75-29, Earthquake Engineering Research Center, University of California, Berkeley
- Seed HB, Murarka R, Lysmer J, Idriss IM (1976) Relationships of maximum acceleration, maximum velocity, distance from source and local site conditions for moderately strong earthquakes. *Bulletin of the Seismological Society of America* 66:1323–1342
- Seed HB, Idriss IM (1982) Ground Motions and Soil Liquefaction during Earthquakes. Earthquake Engineering Research Institute, Berkeley, California
- Seed HB, Tokimatsu K, Harder LF, Chung RM (1985) Influence of SPT procedures in soil liquefaction resistance evaluations. *Journal of Geotechnical Engineering ASCE* 111:1425–1445
- Seed RB, Harder LF (1990) SPT based analysis of cyclic pore pressure generation and undrained residual strength. In: Duncan JM (ed) H.Bolton Seed Memorial Symposium, University of California, Berkeley 2:351–376
- Seed RB, Cetin KO, Moss RES, Kemmerer AM, Wu J, Pestana JM, Riemer MF, Sancio RB, Bray RE, Kayen RE, Faris A (2003) Recent advances in soil liquefaction engineering: A unified and consistent framework. In: H.M.S. Queen Mary 26th Annual ASCE Los Angeles Geotechnical Spring Seminar, Long Beach, California
- Shepherd JB (1992) Current status of seismicity studies in the Greater and Lesser Antilles. *Journal of the Geological Society of Jamaica, Special Issue 12, Natural Hazards in the Caribbean*, 3–9
- Shepherd JB, Aspinall WP (1983) Seismicity and earthquake hazard in Trinidad and Tobago, West Indies. *Earthquake Engineering and Structural Dynamics* 11:229–250
- Sieh K, Jahns R (1984) Holocene activity of the San Andreas Fault in Wallace Creek, California. *Bulletin of Geological Society of America* 95:883–896
- Simons NE, Menzies BK (1977) A short course in foundation engineering. Butterworths Scientific
- Sivapullaiah PV, Sridharan A, Rames HN (2000) Strength behavior of lime-treated soils in the presence of sulphate. *Canadian Geotechnical Journal* 37:1358–1367
- Sharma S, Judd WR (1991) Underground opening damage from earthquakes. *Engineering Geology* (Amsterdam) 30:263–276
- Skempton AW (1957). Discussion: The planning and design of new Hong Kong airport. Proceedings of the Institution of Civil Engineers 7:305–307

- Skempton AW (1986) Standard penetration test procedures and the effects in sands of overburden pressure, relative density, particle size, aging and over consolidation. *Geotechnique* 36:425–447
- Skempton AW, Hutchinson JN (1969) Stability of natural slopes and embankment foundations. In: The 7th International Conference on Soil Mechanics and Foundation Engineering, Mexico City, State-of-the-Art Volume 291–340
- Slemmons DB (1982) Determination of design earthquake magnitudes for microzonation. In: The 3rd International Earthquake Microzonation Conference, Seattle, Washington 1:119–130
- SNAME (1997). Site specific assessment of mobile jack-up units, first edition with Rev. 1. The Society of Naval Architects and Marine Engineers pp 61–69
- Somerville PG, Saikoa C, Wald D, Graves R (1996) Implications of the Northridge earthquake for strong motions from thrust faults. *Bulletin of the Seismological Society of America* 86:S15–S125
- Somerville PG, Smith NF, Graves RW, Abrahamson NA (1997) Modification of empirical strong ground motion attenuation relations to include the amplitude and duration effects of rupture directivity. *Seismological Research Letters* 68:199–222
- Sousa J, Voight B (1991) Continuum simulation of flow failures. *Geotechnique* 41:515–538
- Srbulov M (1987) Limit equilibrium method with local factors of safety for slope stability. *Canadian Geotechnical Journal* 24:652–656
- Srbulov M (1988) Reply to discussion on: Limit equilibrium method with local factors of safety for slope stability. *Canadian Geotechnical Journal* 25:842
- Srbulov M (1991) Bearing capacity of a strip footing on brittle rock. *Rock Mechanics and Rock Engineering Journal* 24:53–59
- Srbulov M (1995) A simple method for the analysis of stability of slopes in brittle soil. *Soils and Foundations* 35:123–127
- Srbulov M (1997) On the influence of soil strength brittleness and nonlinearity on slope stability. *Computers and Geotechnics* 20:95–104
- Srbulov M (1999) Force-displacement compatibility for reinforced embankments over soft clay. *Geotextiles and Geomembranes* 17:147–156
- Srbulov M (2001) Analyses of stability of geogrid reinforced steep slopes and retaining walls. *Computers and Geotechnics* 28:255–268
- Srbulov M (2002) A note on peak foundation acceleration assessment. *European Earthquake Engineering* XVI 2:3–9
- Srbulov M (2003a) An estimation of the ratio between horizontal peak accelerations at the ground surface and at depth. *European Earthquake Engineering* XVII 1:59–67
- Srbulov M (2003b) The effect of vertical acceleration on permanent co-seismic displacements of soil slopes. *European Earthquake Engineering* XVII 2:56–62
- Srbulov M (2003c) On the fast damage propagation through marine soil offshore Newfoundland following Grand Banks earthquake of 1929. *European Earthquake Engineering* XVII 3:3–9
- Srbulov M (2004) Towards new generation of attenuation relationships for the horizontal peak ground acceleration prediction. *European Earthquake Engineering* XVIII 2:14–25
- Srbulov M (2005a) Simple physical models of sand liquefaction and flow failures induced by earthquakes. *European Earthquake Engineering*. XIX 3:25–37
- Srbulov M (2005b) Simplified analyses of soil lateral forces on retaining walls during earthquakes. *European Earthquake Engineering* XIX 3:38–48
- Srbulov M (2006a) A note on one-dimensional analyses of the peak horizontal accelerations near the edges of sediment basins. *European Earthquake Engineering* XX 1:43–47
- Srbulov M (2006b) The use of observational method for short-term seismic hazard assessment. *European Earthquake Engineering* XX 1:3–13
- Srbulov M (2006c) Simplified analysis of the peak horizontal acceleration of pile caps and caisson tops. *European Earthquake Engineering* XX 3:61–72
- Srbulov M (2006d) A simple discrete element model of gravity wall response to earthquakes. *European Earthquake Engineering* XX 2:21–31

- Srbulov M (2007a) A bouncing ball model of rock falls triggered by earthquakes. European Earthquake Engineering XXI 1:3–9
- Srbulov M (2007b) An elementary model of soil and rock avalanches, debris run-out and fast spreads triggered by earthquakes. European Earthquake Engineering (accepted for publication)
- Srbulov M (2007c) A note on possible influence of seismic wave propagation on tunnels, shafts and piles. European Earthquake Engineering XXI 1:35–40
- Srbulov M (2007d) Forensic geotechnical earthquake engineering for long-term seismic hazard assessment. European Earthquake Engineering XXI 3:21–28
- Srbulov M, Parathiras A (1995) The prediction of sliding in plastic soil during strong earthquakes. European Earthquake Engineering IX 2:23–36
- Stark TD, Choi H, McCone S (2005) Drained shear strength parameters for analysis of landslides. Journal of Geotechnical and Geoenvironmental Engineering ASCE 131:575–588
- Stephenson WJ, Williams RA, Odum JK, Worley DM (2000) High-resolution seismic reflection surveys and modeling across an area of high damage from the 1994 Northridge earthquake, Sherman Oaks, California. Bulletin of the Seismological Society of America 90:643–654
- Stephenson WJ, Lomnitz C (2005) Shear wave velocity profile at the Texcoco strong motion array site, Valley of Mexico. Geofisica Internacional 44:3–10
- Stewart IS, Hancock PL (1990) What is a faulty scarp? Episodes 13:256–263
- Stewart JP, Seed RB, Fenves GL (1998) Empirical evaluation of inertial soil-structure interaction effects. Report PEER-98/07, Pacific Earthquake Engineering Research Center, University of California, Berkeley, California
- Stewart JP, Chiou SJ, Bray JD, Graves RW, Somerville PG, Abrahamson NA (2001) Ground motion evaluation procedures for performance-based design. PEER Report 2001/09, Pacific Earthquake Engineering Research Center, College of Engineering, University of California, Berkeley
- Stewart JP, Choi Y, Graves RW (2005) Empirical characterization of site conditions on strong ground motion. PEER Report 2005/01, Pacific Earthquake Engineering Research Center, College of Engineering, University of California, Berkeley
- Stone WC, Yokel FY, Celebi M, Hanks T, Leyendecker EV (1987) Engineering aspects of the September 19, 1985 Mexico earthquake. NBS Building Science Series 165, National Bureau of Standards, Washington, D.C. 207
- Stroud MA (1988) The standard penetration test—its application and prediction. In: Penetration Testing in the UK. Proceedings of the Geotechnology Conference organized by the Institution of Civil Engineers, Birmingham, UK
- Tatsuoka F, Jardine RJ, Presti DLo, Benedetto HDi, Kodaka T (1997) Theme lecture: Characterizing the pre-failure deformation properties of geomaterials. In: Proceedings of the 14th International Conference on Soil Mechanics and Foundation Engineering 4: 2129–2163
- Taylor FB (1910) Bearing of the Tertiary mountain belt on the origin of the Earth's plan. Bulletin of the Geological Society of America 21:179–226
- Taylor RN (ed.) (1994) Geotechnical centrifuge technology. Blackie Academic & Professional, UK
- Terzaghi K (1925) Erdbaumechanik auf boden-physicalischhen grundlagen. Deuticke, Vienna.
- Terzaghi K, Peck RB, Mesri G (1996) Soil mechanics in engineering practice. Wiley
- Tika TE, Vaughan PR, Lemos LJ (1996) Fast shearing of pre-existing shear zones in soil. Geotechnique 46:197–233
- Timoshenko S, Goodier JN (1951) Theory of elasticity. McGraw Hill, New York
- Tokimatsu K, Seed HB (1987) Empirical correlation of soil liquefaction based on SPT N-value and fines content. Soils and Foundations 23:56–74
- Tominaga M, Nakata S, Kimura T, Shioya K (1989) Performances of soil – foundation systems in reclaimed industrial land during the Chibaken Toho-Oki earthquake in Japan, 1987. In: The 12th International Conference on Soil Mechanics and Foundation Engineering, Rio de Janeiro, Discussion Session on Influence of Local Conditions on Seismic Response, pp 67–72

- Trifunac MD, Hudson DE (1971) Analysis of the Pacoima Dam accelerograms – San Fernando earthquake of 1971. *Bulletin of the Seismological Society of America* 61:1393–1411
- Trifunac MD, Brady AG (1975) A study of the duration of strong earthquake ground motion. *Bulletin of the Seismological Society of America* 65:581–626
- USGS (1984) United States Geological Survey. Geotechnical investigations at strong motion stations in the Imperial Valley, California. Report OFR-84-562 TI85 901790, Menlo Park, California
- UBC (1997) Uniform building code: Structural engineering design provisions. International Conference of Building Officials, Pasadena, CA
- Ushiro T, Matsumoto Y, Akesaka N, Yagi N (1999) Study of accidents caused by rock fall in Kochi Prefecture. In: *Slope Stability Engineering*, Balkema, Rotterdam 2:1349–1354
- Vaid YP, Chern JC (1985) Cyclic and monotonic undrained response of saturated sands. In: Khosla V (ed) *Advances in the Art of testing Soils under Cyclic Conditions*. ASCE, New York 120–147
- Varnes DJ (1978) Slope movement types and processes. In: *Landslides, Analysis and Control*. Transportation Research Board Special Report 176, National Academy of Science, Washington D.C. pp 12–33
- Vucetic M, Dobry R (1991) Effect of soil plasticity on cyclic response. *Journal of Geotechnical Engineering ASCE* 117:89–107
- Wartman J, Bray JD, Seed RB (2003) Inclined plane studies of the Newmark sliding block procedure. *ASCE Journal of Geotechnical and Geoenvironmental Engineering* 129:673–684
- Wartman J, Seed RB, Bray JD (2005) Shaking table modeling of seismically induced deformations in slopes. *ASCE Journal of Geotechnical and Geoenvironmental Engineering* 131:610–622
- Wegener A (1915) *Die entstehung der kontinente und ozeane*. Vieweg, Braunschweig, Germany
- Weldon II RJ, McCalpin JP, Rockwell TK (1996) Paleoseismology of strike-slip tectonic environments. In: McCalpin (ed) *Paleoseismology*, Academic Press
- Wells DL, Coppersmith KJ (1994) New empirical relationships among magnitude, rupture length, rupture width, rupture area, and surface displacement. *Bulletin of the Seismological Society of America* 84:974–1002
- Werner SD, Beck JL, Levine MB (1987) Seismic response evaluation of Meloland Road Overpass using 1979 Imperial Valley earthquake Records. *Earthquake Engineering and Structural Dynamics* 15:249–274
- Whitman RV, Liao S (1985) Seismic design of retaining walls. Miscellaneous Paper GL-85-1, US Army Engineer Waterways Experimental Station, Vicksburg, Mississippi
- Wieczorek GF, Snyder JB, Waitt RB, Morrisey MM, Uhrhammer RA, Harp EL, Norris RD, Bursik MI, Finewood LG (2000) Unusual July 10, 1996, rock fall at Happy Isles, Yosemite National park, California, *Bulletin of Geological Society of America* 112:75–85
- Wilson DW (1998). Soil-pile-superstructure interaction in liquefied sand and soft clay. Ph.D. Dissertation, Department of Civil and Environmental Engineering, College of Engineering, University of California at Davis
- Wolf JP (1985) Dynamic soil-structure interaction. Prentice Hall, Englewood Cliffs, New Jersey
- Wolf JP (1994) Foundation vibration analysis using simple physical models. PTR Prentice Hall.
- Wolf JP, Deeks AJ (2004) *Foundation Vibration Analysis: A Strength-of-Materials Approach*, Elsevier, Amsterdam
- Wroth CP, Housby GT (1985) Soil mechanics – property characterization and analysis procedures. In: Proceedings of the 11th International Conference on Soil Mechanics and Foundation Engineering (ICSMFE), San Francisco 1:1–53
- Yamada G (1966) Damage to earth structures and foundations by the Niigata earthquake June 16, 1964, in JNR. *Soils and Foundations* 6:1–13
- Yamamoto JA, Lade PV (1997) Static liquefaction of very loose sands. *Canadian Geotechnical Journal* 34:905–917
- Yamamoto JA, Kaliakin VN (eds.) (2005) Soil constitutive models, evaluation, selection, and calibration. *Geotechnical Special Publication ASCE* 128
- Yegian MK, Ghahraman VG, Gazetas G (1994a) 1988 Armenia earthquake. I: Seismological, geotechnical and structural overview. *Journal of Geotechnical Engineering ASCE* 120:1–20

- Yegian MK, Ghahraman VG, Harutunyan RN (1994b) Liquefaction and embankment failure case histories, 1988 Armenia earthquake. *Journal of Geotechnical Engineering ASCE* 120:581–596
- Yim CS, Chopra AK, Penzien J (1980) Rocking response of rigid blocks to earthquakes. *Earthquake Engineering and Structural Dynamics* 8:565–587
- Youd TL, Idriss IM (2001) Liquefaction resistance of soil. Summary Report from the 1996 NCEER and 1998 NCEER/NSF Workshop on Evaluation of Liquefaction Resistance of Soils. *Journal of Geotechnical and Geoenvironmental Engineering ASCE* 127:297–313
- Youd TL, Hansen CM, Bartlett SF (2002) Revised multilinear regression equations for prediction of lateral spread displacement. *Journal of Geotechnical and Geoenvironmental Engineering ASCE* 128:1007–1017
- Zeng X, Steedman RS (2000) Rotating block method for seismic displacement of gravity walls. *Journal of Geotechnical and Geoenvironmental Engineering ASCE* 126:709–717
- Zienkiewicz OC, Morgan K (1983) Finite elements and approximation. John Wiley & Sons
- Zienkiewicz OC, Taylor RL (1989) The finite element method. In: Volume I Basic formulations and linear problems. McGraw-Hill
- Zienkiewicz OC, Taylor RL (1991) The finite element method. In: Volume 2 Solid and fluid mechanics: Dynamics and non-linearity. McGraw-Hill
- Zhang B, Papageorgiou AS (1996) Simulation of the response of the Marina District Basin, San Francisco, California, to the 1989 Loma Prieta earthquake. *Bulletin of the Seismological Society of America*. 86:1382–1400
- Zhang J, Andrus RD, Juang CH (2005) Normalized shear modulus and material damping ratio relationships. *Journal of Geotechnical and Geoenvironmental Engineering ASCE* 131:453–464
- Zhang J, Makris N (2001) Seismic response analysis of highway over crossings including soil-structure interaction. Pacific Earthquake Engineering Research Center (PEER) report 2001/02, University of California, Berkeley
- Zhongyou L (1984) Examples of rapid landslides in semi rock strata. In: The 4th International Symposium on Landslides 1:663–667

# Index

- 1857 to 2004 Parkfield earthquakes, 32  
1925 Santa Barbara earthquake, 130  
1940 Imperial Valley earthquake, 130  
1957 San Francisco earthquake, 131  
1964 Niigata earthquake, 122, 131  
1967 Caracas earthquake, 47  
1970 Peruvian earthquake, 107  
1971 San Fernando earthquake, 122, 176  
1978 Miyagi earthquake, 179  
1979 Imperial Valley earthquake, 175, 177  
1983 Kanagawa-ken Seibu earthquake, 175  
1983 Nihonkai-Chubu earthquake, 122, 131  
1984 Morgan Hill earthquake, 51  
1985 Chile earthquake, 132  
1985 Michoacan earthquake, 54, 199  
1986 Kalamata earthquake, 166  
1987 Chibaken-Toho-Oki earthquake, 132, 176  
1987 Whittier earthquake, 176, 178  
1988 Armenia earthquake, 48, 132  
1989 Loma Prieta earthquake, 50, 51, 54, 58, 177, 179  
1992 Big Bear earthquake, 180  
1992 Landers earthquake, 180  
1992 Petrolia earthquake, 178  
1993 Kushiro-oki earthquake, 133  
1994 Northridge earthquake, 51  
1995 Dinar earthquake, 52  
1995 Hyogoken-Nanbu earthquake, 52, 161, 196  
1999 Mount Parnitha earthquake, 196
- A**  
ABAQUS, 196  
Aberfan fast spread, 115  
acceleration amplification, 56  
Afghanistan-Pakistan zone, 43  
aftershocks, 62  
Aleutian trench, 43  
Alpine zone, 43
- archaeological data, 62  
artificial accelerograms, 41  
attenuation relationships, 33, 35  
avalanches, 107  
axial dashpot, 159  
axial spring, 159
- B**  
backbone curve, 15  
bearing capacity, 187  
Bedrina-1 rock fall, 103  
bending moment, xx, 198, 200, 201  
bi-direction simple shear tests, 20  
body wave magnitude, 30  
bracketed duration, 23  
brittle slope failures, 76  
bulk-up, 111
- C**  
Caracas basin, 47  
Caribbean Antilles, v  
Caribbean islands, 43  
Cascadia trench, 43  
Catakl slide, 97  
centrifuge test, 142, 191  
chaotic, vii, 29, 125  
Chiba warehouse, 176  
Chonan middle school, 132  
circular frequency, xxv, 55, 56  
clay undrained shear strength, 19  
closed form solution, 154  
co-seismic permanent displacement, 7, 90  
coefficient of water permeability, 26  
cohesion, 75  
computer programs, 142  
CONAN, 172, 174, 197  
consolidation, 205  
Coulomb lateral coefficient, 155  
Cowden till shear strength rate dependence, 21

critical acceleration, 86, 90, 99  
 critical damping, 10  
 cyclic friction angles, 128  
 cyclic shear strength, 20  
 cyclic shear strength of clay, 20  
 cyclic shear strength of sand, 20  
 cyclic shear strength of silt, 20  
 cyclic stress ratio, 121

**D**

Daikai station, 196  
 damping ratio, xxv, 16, 55, 56  
 Darcy's law, 206  
 databases of accelerograms and spectra, 40  
 Dead Sea zone, 43  
 deaggregation, 62  
 debris run outs, 107  
 deep foundation, 172  
 deterministic seismic hazard analysis, 60  
 Dinar basin, 52  
 discrete element model, 157  
 Duhamel's integral, 223  
 Dumbarton bridge, 149, 179  
 duration of strong ground motion, 23  
 dynamic soil-structure interaction, 141

**E**

earthquake intensity, 60  
 East Mediterranean sea trench, 43  
 effective overburden stress, 19  
 effective stress, 14  
 eleven storey apartment house, 179  
 energy balance, 112  
 entrainment, 111  
 epicentral distance, 31  
 epicentre, 2, 3, 5, 211  
 equation of motion, 108  
 equivalent disks, xxi, 173  
 equivalent harmonic motion, 25, 87  
 Eurasia plate, 43  
 excess pore water pressure, 21, 22, 26, 206  
 excess water pressure relief wells, 205

**F**

factor of safety, xviii, 74, 76  
 fast shear rates, 91  
 fault distance, 31  
 fault slip rate, 63  
 field trials, 203  
 field water pumping tests, 26  
 fill dams, 87, 88  
 FLAC, 166  
 flexural retaining wall, 169, 181  
 fling step, 44

flow spreads, 107  
 foreshocks, 62  
 foundation settlement, 191  
 four-Gauss-point integration, 4  
 Fourier series, 24, 47  
 frequency, 9  
 frictional angle in static condition, xxiv, 19  
 fundamental frequency, xxv, 10, 172, 184  
 fundamental period, 10  
 Futamata rock fall, 106

**G**

geomorphic studies, 67  
 global positioning system, 64, 65  
 global seismic hazard map, 58  
 GPS, 64, 65  
 gravelly cobble deposits, 17  
 gravity wall, 150, 156  
 ground slopes, 6  
 Gutenberg – Richter relationship, 62

**H**

Hachiro-Gata road embankment, 131  
 harmonic motion, 24, 55  
 Hollywood storage building, 176  
 hypocentre, 2, 3, 5, 211

**I**

Imperial Valley County services building, 149, 177  
 inertial interaction, 141  
 InSAR, 63  
 insignificant damage, 60  
 interferometric synthetic aperture radar, 63  
 Iran, 62

**J**

Japan trench, 43  
 Java trench, 43

**K**

Kalamata harbour quay wall, 166  
 Kanto district, 68  
 Kelvin-Voigt model, 46, 56, 109  
 Kerameikos station, 195  
 Kermadec-Tonga trench, 43  
 kinematic interaction, 141, 170  
 Kirovakan basin, 48  
 Kobe basin, 52  
 Kobe port caisson wall, 161  
 Kuril trench, 43

**L**

La Marquesa dam, 132

La Palma dam, 132  
layer vibration frequency, 56  
layer vibration period, 56  
limit equilibrium method, 74, 111, 212  
liquefaction, 69, 119, 120, 123, 125, 188, 190, 192, 201  
liquefaction flow distance, 137  
local magnitude, 30  
logic trees, 62  
London clay shear strength rate dependence, 21  
longitudinal seismic waves, 2  
Los Angeles basin, 51  
Love waves, 44  
lumped mass model, 144

**M**

Macquarie ridge, 43  
magnitude conversion, 30  
magnitude scaling factors, 122  
Maidipo slide, 95  
major tectonic plates, 41  
Marianas trench, 43  
Marina basin, 50  
material damping, xix, 3, 173  
mean annual rate of exceedance, 60  
Mediterranean region, 65  
Meloland road overpass, 175  
Merced lake bank, 131  
Mexico City, 54, 199  
Mexico trench, 43  
Moho surface, 35  
Mohr - Coulomb, 204  
Mohr – Coulomb, xxi, 76  
moment magnitude, 30  
Monastiraki station, 195  
Mononobe-Okabe, 155, 170  
Montague zone, 43  
MS Excel, 211

**N**

Nalband railway embankment, 132  
New Hebrides trench, 43  
non-linear shear strength criterion, 76, 111  
non-standard errors of uncorrected accelerograms, 40  
normal tectonic faults, 42, 67  
normally consolidated clay, 19  
North Anatolian fault, 58  
Northolt slope, 83, 212  
Northwest connector, 149, 180  
Norwalk buildings, 178  
number of equivalent cycles, xx, 23, 24

**O**

oblique tectonic faults, 42  
observational method, 62  
oedometer tests, 28  
Ohba-Ohashi road bridge, 175  
one-dimensional wave propagation, 47  
organic peat, 18  
over consolidated ratio, 20

**P**

Pacific Park Plaza building, 177  
Painter street bridge, 178  
paleoearthquakes, 67  
paleoseismic data, 62  
Pandemonium Creek rock avalanche, 112  
peak foundation acceleration, 145  
peak horizontal ground acceleration, 34  
peak horizontal ground displacement, xviii, 39  
peak horizontal ground velocity, xxii, 37  
peak horizontal velocity and acceleration ratio, 38  
peak shear strength, 75  
peak velocity to acceleration ratio, 25  
peak vertical ground acceleration, 35  
peak vertical to horizontal acceleration ratio, 37  
permanent ground displacements, 122  
Persian/Arabian Gulf, 43, 58  
Peru-Chile trench, 43  
Philippine plate, 43  
pile flexural failures, 201  
pile group, 172  
piled foundations, 169  
planar source model, 4  
point-source model, 1  
Poisson process, 32  
Poisson's model, 62  
Poisson's ratio, 3, 152  
post-seismic permanent displacements, 94  
predominant period, 24  
pressure relief wells, 207  
probabilistic seismic hazard analysis, 61  
punch through failure, 188

**Q**

QUAD4M, 52, 88  
Quaternary age, 17

**R**

radiation damping, 3  
radiocarbon dating, 68, 70  
Rayleigh waves, 44  
recurrence period, xxi, 63  
reinforced soil, 82

residual shear strength, 75  
 resonance, 10, 54, 141, 149  
 response spectrum, 10, 171, 222  
 return period, xxi, 60  
 reverse tectonic faults, 42, 68  
 ring shear apparatus, 91  
 rock falls, 99  
 rock stress-strain relationship, 63  
 rocking block, 124, 157  
 rolling cylinder model, 135  
 rotating cylinder model, 123, 125  
 rotational dashpot, 153  
 rotational spring, 153  
 route 272 embankment, 133  
 rupture directivity, 44

**S**

San Andreas fault, 58, 68  
 San Andreas zone, 43  
 San Francisco bay, 54  
 sand friction angles in cyclic condition, 21  
 sand shear strength rate dependence, 21  
 sand volcanoes, 70  
 Santa Clara basin, 51  
 SDOFO, 10, 11, 55, 169, 172, 173  
 Sea of Marmara, 58  
 sediment basin depth, 53  
 sediment-filled basins, 45  
 sedimentation time, 136  
 seismic codes, 40  
 seismic gaps, 58  
 seismic hazard map, 39  
 seismic wave propagation, 54  
 seismic wave refraction, 201  
 Sepolia station, 195  
 settlement, 191  
 SHAKE, 47, 109, 151, 198, 200  
 shaking table test, 9, 142  
 shallow foundation, 187, 189, 191  
 shear beam, 86  
 shear modulus, 15–17  
 Sheffield dam, 129  
 Shibecha-Cho embankment, 133  
 Shima rock fall, 105  
 short term seismic hazard, 60  
 Shum Wan Road debris run-out, 114  
 sills, 70  
 single degree of freedom oscillator, 10, 55, 169  
 sliding block, 7, 89, 157, 215  
 sliding wedge, 84, 214  
 slip predictable, 32

slope failures, 69  
 Snell's law, 201  
 soil deformation modulus, 192  
 soil friction angle, 75  
 soil impedance, 54  
 soil mixing, 204  
 soil plasticity index, 19  
 soil-cement grid walls, 205  
 Solfatara Canal dike, 130  
 space clustering, 58  
 SPT blow count, 121  
 standard penetration resistance, xx, 19  
 Stokes law, 136  
 stone columns, 203  
 stratigraphic studies, 67  
 strike-slip tectonic faults, 42, 68  
 subduction zones, 41  
 sulphate resistant cement, 205  
 surface wave magnitude, 30  
 system identification analysis, 142

**T**

Takatori station, 196  
 tectonic data, 62  
 tectonic energy, xviii, 1, 3, 4  
 tectonic fault, 2  
 Tertiary age, 17  
 three dimensional ground motion, 9  
 three-dimensional slope stability, 84  
 time clustering, 32, 41, 58, 59, 62, 71  
 time predictable, 32  
 topographic effects, 57  
 transversal force, xxii, 198  
 transversal seismic waves, 2  
 transversal wave velocity, 204  
 tunnel response, 195  
 two sliding blocks model, 94

**U**

Uetsu line railway embankment, 131  
 undrained shear strength, 119

**V**

vibration modes, 56  
 visco-elastic soil layers, 55  
 viscous damping, 46, 174  
 volumetric compressibility, 26

**W**

water viscosity, 136  
 West Mediterranean sea zone, 43